SECONDARY MOMENT EFFECTS ON SLENDER REINFORCED MASONRY WALLS

ADRIEN JOSEPH JAMES SPARLING

A DISSERTATION SUBMITTED TO THE FACULTY OF GRADUATE
STUDIES IN PARTIAL FULFILLMENT OF THE REQUIREMENTS FOR THE
DEGREE OF DOCTOR OF PHILOSOPHY

GRADUATE PROGRAM IN CIVIL ENGINEERING

YORK UNIVERSITY

TORONTO, ONTARIO

June 2022

Abstract

Slender masonry walls can be an effective loadbearing component of buildings that require high ceilings such as warehouses and gymnasiums. This type of construction is also efficient in terms of material usage and over-all construction costs. The proven long-term durability of existing masonry buildings makes this construction material an attractive option; however, the limited experimental testing on slender walls in out-of-plane flexure combined with high axial loads have led to conservative prescriptive restrictions on their design in Canadian and U.S. standards. The experimental testing presented herein aims to advance knowledge on Reinforced Masonry (RM) walls and introduces a novel method of reinforcement for new masonry wall construction. This novel method consists of applying Near-Surface Mounted (NSM) steel reinforcement rather than conventional embedded reinforcement. The first phase of the research included numerical Finite Element (FE) analysis and experimental testing of 3 m tall RM walls subjected to four-point out-of-plane loading; the second phase consisted of experimental testing of 8 m tall slender (slenderness ratio $kh/t = 42$) RM walls subjected to combined axial loading and four-point out-of-plane loading. For both phases, the flexural stiffness (EI) of the walls was assessed through multiple approaches (using reinforcement strain, surface strain, and out-of-plane displacement data), and compared to the stiffness calculated using the current Canadian masonry design standard (CSA S304-14) formulation. The equation for the effective flexural stiffness in the current design standard was observed to underestimate the stiffness response in most loading conditions, however it does not provide a consistently accurate value. An alternative method for calculating flexural stiffness was therefore proposed, which accounts for loss of stiffness from repeated loading, or accidental overload, as well as the effect of applied axial loads. Throughout this dissertation, the performance of RM walls with conventional embedded reinforcement is compared to the performance of walls with NSM steel bars. RM walls with NSM steel reinforcement exhibited higher flexural stiffness, and displacement ductility comparable to or exceeding that of RM walls with conventional reinforcement. In addition, a design example illustrated how NSM steel reinforcement can be beneficial for the design of walls with large secondary moment effects.

Dedication

This dissertation is dedicated to the High Bay Laboratory of the Bergeron Centre for Engineering Excellence (BCEE). In the summer of 2015, before starting my scholarly journey at York University, I had the privilege of visiting the BCEE and the High Bay Laboratory while it was still under construction. Over the course of my studies, starting in January 2016, it has been my honour to contribute to the evolution of the space from an empty shell, full of potential, into the state-of-the-art testing facility we have today. I have taken my trailblazing role seriously with the hopes that the infrastructure that I have designed for my own testing, as well as my example and my other contributions to the development of operational procedures, will contribute to quality and safe research activities into the future.

May the cold steel and rough concrete of the lab be fortunate to the researcher who follow.

Acknowledgements

Table of Contents

List of Tables

List of Figures

1 Introduction

Modern load-bearing masonry construction in North America is dominated by reinforced concrete unit masonry which allows the efficient use of resilient materials for the construction of a wide range of buildings. This remains a desirable form of construction since interior walls can often serve multiple purposes at once, for example: as load-bearing structural members, effective fire separations, and an aesthetically pleasing interior finish. In Canada, structural design in masonry is supported by the comprehensive CSA S304-14 Design of Masonry Structures (CSA 2019a) standard which provides guidance on all aspects of practical design. The current standard was developed based on research and testing of masonry assemblies, and many principles from reinforced concrete design have been adapted to masonry design; however, the influence of antiquated approaches to design can still be found in certain sections of the current standard. These can lead to over-conservatism in design. The clauses related to the design of very slender Reinforced Masonry (RM) walls contain very stringent prescriptive constraints.

This dissertation presents a review of formative and state-of-the art research on slender RM walls as well as a full-scale experimental testing program.

1.1 Background

Slender load-bearing masonry walls are often used in construction for buildings that require high ceilings and large uninterrupted spans between supports. When designing these structures, such as gymnasiums, indoor swimming pool facilities, and warehouses, it is often desirable to reduce the encroachment of vertical supporting members (columns and walls) into the floor space. Therefore, eliminating supporting projections from the walls (pilasters), and reducing the thickness of walls, while maintaining their vertical load carrying capacity are desirable features of load-bearing walls in these structures. The design of slender walls, which arise from these building constraints, requires careful consideration since their load-bearing capacity (vertical and out-of-plane) are often highly influenced by secondary moment effects. Whereas primary axial and out-of-plane loads on walls are determined directly based on dead and live loads, following the

requirements of applicable building codes, the secondary moment effects depend on both the externally applied loads and the properties of the wall – particularly the out-of-plane flexural stiffness.

Research and standards equations for the determination of flexural stiffness of RM walls appear to be relatively underdeveloped compared those related to compressive and flexural resistance. Calculation of member stiffness is most often used for serviceability limit state calculations for occupant comfort (displacements) and to avoid damage to non-structural components. Although these calculations are important, they do not affect the life-safety of a structure; in contrast, the determination of flexural stiffness of members for the calculation of secondary moments has a significant effect on the design of a member at the ultimate limit state. Overestimation of the flexural stiffness of a slender RM wall can result in the severe underestimation of total applied bending moments and conditions that could negatively affect the life-safety of a structure. This issue was highlighted in a recent ACI Tech Note (ACI Committee 551 2021). Conversely, over-conservatism can lead to uneconomical designs or even the effective exclusion of a structural system from consideration – as is often case for RM walls for warehouse structures in Canada.

Masonry design standards have largely been developed based on Reinforced Concrete (RC) design standards. In many cases this is appropriate given the similarities between the materials used in RC and RM, as well as their interaction: both make use of a brittle material (concrete or masonry units) to resist compressive forces, and a ductile material (steel reinforcing bars) to resist tensile forces. Both systems generally assume a fully cracked section when assessing the strength of reinforced flexural members; they also both typically permit the use of a hybrid moment of inertia (between the value for the intact section and the value for the fully cracked section) for the determination of flexural stiffness. There are, however, fundamental differences between the behaviour of RC and RM systems, which require differences in the design approaches in certain situations. For example, the modular size and shape of masonry units constrains the thickness and the increments of length to which members can be easily constructed. Masonry construction is also anisotropic, and designers must account for the orientation of forces relative to the mortar bedding plane for the design of beams. Most relevant to the design of slender walls is the inherent

Chapter 1 - Introduction

limitation to the location in which reinforcing bars can be placed. Whereas in concrete design, reinforcing bars can be located near the surface (covers generally range between 25mm and 75mm depending on the application), masonry walls are usually constructed with the reinforcing bars placed in the middle of the cross section. Very little room is available for variation from this placement given that the masonry grout must be able to fully surround a reinforcing bar to offer a proper bond. This placement of reinforcing bars limits their contribution to out-of-plane flexural stiffness in RM walls.

The research presented herein seeks to update the current understanding of the response of very slender RM walls under service loading conditions including axial and out-of-plane loading. This study includes testing of full scale 3 m tall RM walls and very slender 8 m tall RM walls, in addition to preliminary Finite Element (FE) analyses. The general research objective is to supplement and update existing formative data from tests conducted in the 1970s-80s (Yokel, Mathey, and Dikkers 1970; Hatzinikolas, Longworth, and Warwaruk 1978; ACI-SEASC Task Committee on Slender Walls 1982) and to complement other research focusing on slender reinforced masonry walls currently being conducted across Canada (Isfeld, Hagel, and Shrive 2019; Alonso et al. 2021).

Additionally, the application of Near-Surface Mounted (NSM) steel reinforcement using the Surface Reinforced Concrete Masonry Unit (SRCMU) masonry system (Hashemian 2015) is presented as a possible alternative or supplement to conventional reinforcement strategies for new concrete masonry wall construction. Tests of walls reinforced with NSM steel bars were included among the tests of 3 m tall and 8 m tall walls, along with RM walls reinforced using conventional techniques. These proof-of-concept tests explore the potential structural benefits of this system; study of the durability, fire-resistance or other additional resistance capabilities or limitations of this wall system are outside the scope of the current study but will require further attention prior to widespread adoption.

Chapter 1 - Introduction

1.2 Research Methodology

This report discusses the current state of practice of design of slender RM walls in Canada and includes a review of the literature that led to current design standards. It also includes a report on two test series conducted on reinforced masonry walls. The first is a series of out-of-plane loading tests conducted on 3 m tall RM walls, the second is a series of tests conducted on 8 m tall RM walls subjected to combined axial (vertical) loading and out-of-plane (horizontal) loading. The first series of tests is accompanied by preliminary FE analyses, which offer further insight in how future analyses and parametric studies could be conducted.

The literature review consisted of a search of scholarly scientific journal databases, as well as a search of the proceedings of masonry specialty conferences (Canadian Masonry Symposium and North American Masonry Conference). Formative research articles on slender reinforced concrete and masonry walls as well as contemporary research related to the out-of-plane strength and stiffness of reinforced masonry walls are included in the review. These include articles related to finite element analysis of slender masonry walls and the analysis of slender walls using North American and European standards. Literature regarding the application of NSM reinforcement for the strengthening of concrete and masonry structures is also discussed.

The testing apparatus for the 3 m tall and 8 m tall walls were designed based on those reported in the literature for similar tests. The support frames were constructed from structural steel members and the loading was applied using computer controlled hydraulic actuators. Testing was performed on full-scale masonry walls that were constructed using the materials and methods typical of RM construction in Canada. The masonry walls were constructed by a certified professional mason. The cross section and reinforcement pattern of the masonry walls tested were selected to facilitate the comparison of the performance of walls reinforced with conventionally embedded bars to walls reinforced with NSM steel bars. This was conducted in collaboration with the Canada Masonry Design Centre, which provided important perspectives on the

needs of the masonry construction industry. They also ensured the walls were representative of typical construction in Canada.

During testing, data were recorded using high sensitivity digital instruments connected to a sophisticated data acquisition system. This system allowed the readings from each instrument to be recorded simultaneously and at a high frequency throughout each test. The data collected during testing were analysed to assess the out-of-plane displacement as well as the curvature response of the walls to applied loads, thereby allowing the accurate determination of flexural stiffness. The response of the walls was compared to those expected from analysis using Canadian design standards and a rational analysis.

1.3   Research Objectives

The goal of this research was to assess the out-of-plane flexural stiffness response of RM walls. This research builds upon previously completed works (formative tests on slender RM walls) and fills gaps in areas where experimental data is lacking. Thereby, it will support further development of design strategies for slender RM walls. This includes a study of the elastic and post yielding response of RM walls subjected to out-of-plane loading, as well as with applied axial load exceeding 10% of the load capacity of the section. Insights achieved through this study will lead to more efficient and safe design of slender RM walls by reducing over-conservatism in the design approaches.

In addition, this study demonstrates the structural performance of RM walls with NSM steel reinforcement and compares it to conventional RM walls. The potential benefits of stiffer RM wall systems for the construction of slender walls, as well as the feasibility of using NSM steel reinforcement for new masonry constructions, is discussed.

A preliminary investigation of an approach to FE modeling and analysis of RM walls with NSM steel reinforcement is also included and the limitations associated with the use of 3-dimentional micro-modelling for such an application are highlighted.

Chapter 1 - Introduction

1.4　Research Novelty and Significance

1.4.1　Design equations and flexural stiffness response

The current Canadian and U.S. masonry design standards (CSA Group 2019a; TMS 2016) impose highly restrictive limits on the load capacity and flexural stiffness of slender reinforced masonry walls. These restrictive conditions are imposed in part due to a lack of experimental test data. This study of the out-of-plane stiffness of RM walls is intended to highlight aspects of the design standards that may be over-conservative. Testing of very slender walls with axial loads which are larger than those typically used for design provides a more fulsome view of the continuum of responses that slender RM walls may exhibit.

Additionally, there is a need for masonry wall systems, such as the SRCMU system, that can be an economical choice for applications where tall, unsupported structural walls, including those used in warehouses, gymnasiums, and certain "big box" stores, are required. Herein, out-of-plane flexural testing and analysis of the flexural stiffness of the SRMCU system are presented. The increased flexural stiffness provided by NSM steel reinforcement in the SRMCU system is quantified, illustrating its potential for improving structural efficiency in reinforced masonry design.

Examples of how the principles investigated over the course of this research could be applied in the design of a typical warehouse wall further illustrate the significance of this test series.

1.4.2　Tall wall testing

The masonry wall tests presented herein are among the tallest performed in North America. Walls of a comparable scale were tested under conditions of axial load only (Yokel, Mathey, and Dikkers 1970; Hatzinikolas, Longworth, and Warwaruk 1978), or in out-of-plane loading with only low levels of axial load (ACI-SEASC Task Committee on Slender Walls 1982). Contemporary tests available in the literature are of a smaller scale. Testing of marginally taller walls (8.5 m, compared to 8 m in the testing described herein) is currently being conducted at the University of Alberta (Alonso et al. 2021), however, only a limited range of axial load will be applied during those tests (similar to that used in the ACI-SEASC Task

Committee on Slender Walls (1982) series). There are also inherent limitations to the out-of-plane loading that can be applied using their airbag system; the displacement which are induced in the walls are not directly controlled, making it challenging to exceed the yield resistance of the walls.

For the testing series described herein, the out-of-plane loading was applied using a hydraulic actuator under displacement control, allowing the walls to be loaded to twice the yield displacement. This mode of testing, with strict control over the induced displacement, also permitted cyclic testing of each wall (within the elastic response range) with varying levels of applied axial load. This allowed an examination of the response of a cracked reinforced masonry section to combined axial and out-of-plane loading – this is particularly useful for informing design considerations since it is generally considered to be best practice to assume a cracked section when determining the flexural resistance of reinforced masonry (ACI Committee 551 2021). Although a wall may be designed not to fully crack when subjected to the factored design loads, an unexpected overload event that does not cause immediate failure could nonetheless cause additional cracking. In such cases, the extent of cracking and accompanying reduction in flexural stiffness may not be easily assessed. Since the reduction in flexural stiffness of a slender wall affects its resistance to applied loads (due to secondary moment effects), it is desirable to understand the effect of cracking on the stiffness response, and to adopt design practices wherein the cracked stiffness is used for the ultimate limit state design of slender walls.

Owing to the high level of control over the applied loads afforded by the test set-up that was designed for this testing series, out-of-plane loading cycles were completed during which the imposed axial load exceeded the elastic buckling load of a conventionally reinforced masonry wall and approached that of a wall with NSM steel reinforcement. Although other research programs studied the response of RM walls subjected to higher axial load (Yokel, Mathey, and Dikkers 1970; Hatzinikolas, Longworth, and Warwaruk 1978; Liu and Hu 2007), the testing herein appears to be unique in its combination of large axial loads and controlled out-of-plane loading. This addresses a gap in the research that exists between the testing of RM

walls under axial loading only and those that studied the out-of-plane response of RM walls with applied axial loading below 10% of the section capacity.

1.4.3   New masonry construction with NSM steel reinforcement

To date, the application of NSM reinforcement has been limited to the retrofitting of existing structures to increase the resistance to changing loading conditions, or to improve seismic resilience; the state of practice is well documented by de Lorenzis and Teng (2007). Existing examples of practical applications of NSM reinforcement have mostly incorporated fibre-reinforced polymer bars or tapes to avoid changing the stiffness of the existing structural members; however, the current study aims to take advantage of the increased stiffness afforded by NSM steel reinforcement to benefit the construction of slender masonry walls.

This approach follows other attempts to increase the flexural stiffness of RM walls by increasing the distance (moment arm) between the tension reinforcement and the centroid of compression in the masonry under flexural loading. These other strategies include the use of wider masonry units, or the introduction of pilaster elements into wall construction, and the placement of reinforcing bars near the inner face of the masonry unit. The use of NSM steel reinforcement takes the principle of increased flexural stiffness through increased distance between the tension reinforcement and the centroid of masonry in compression to its extreme by placing reinforcing bars as near to the surface as practicable. Each of these methods, however, has advantages and disadvantages related to structural performance, constructability, and durability which will require further research to fully assess. The current study focuses on the structural performance of NSM steel reinforcement compared to that of conventional embedded steel reinforcement methods.

1.5   Dissertation Layout

This dissertation presents a research study completed by the author from 2016 to 2022 and is divided thematically into chapters. Some of the chapters are based on previously published works; however, each one contains unique and novel content and elements adding further clarity or detail, as follows:

Chapter 1 - Introduction

Chapter 2 – Literature Review was developed based on the literature reviews which were conducted for the various publications which arose from this research (Sparling, Palermo, and Hashemian 2017; 2018; 2019; 2021; Sparling and Palermo 2021; 2022). It includes a discussion of relevant literature regarding the effect of secondary moments on slender structural elements in general, and on reinforced masonry walls. A detailed review of formative and contemporary literature regarding the strength and flexural stiffness of reinforced masonry walls is also included. Background information on the Surface Reinforced Masonry Unit (SRCMU) system and relevant literature on Near-Surface Mounted (NSM) reinforcement complete this section.

Chapter 3 – Numerical Modelling principally presents the outcomes of Finite Element (FE) analyses that were performed prior to testing of the 3 m tall RM walls presented in Chapter 4. These analyses were originally published in the proceedings of the 2017 Canadian Masonry Symposium (Sparling, Palermo, and Hashemian 2017) and the 2018 International Masonry Conference (Sparling, Palermo and Hashemian 2018), however the chapter also includes further elaboration on the uses and limitations of the approach presented.

Chapter 4 – Preliminary Testing describes the design and construction of 3 m tall RM walls as well as the steel frame and test set-up that was used for testing. The load-displacement and other primary responses measured during testing, first presented at the North American Masonry Conference (Sparling, Palermo, and Hashemian 2018) and in the Canadian Journal for Civil Engineering (Sparling, Palermo, and Hashemian 2021), are also presented in this chapter. The response of hollow and grouted walls with NSM steel reinforcement are contrasted against the response of conventionally reinforced walls.

Chapter 5 – Slender Wall Testing describes the design and construction of 8 m tall RM walls and the design of the steel test frame. This chapter also includes the load-displacement and other primary responses of the 8 m tall RM walls during testing, which have been submitted to ASCE for publication (Sparling and Palermo 2022). The performance of conventional RM walls is also compared to that of RM walls with NSM steel reinforcement.

Chapter 1 - Introduction

Chapter 6 – Analysis provides an interpretation of the primary data collected during testing of the 3 m tall and 8 m tall RM walls. It includes an assessment of the curvature and flexural stiffness response of the 3 m tall RM walls which was published in the Canadian Journal for Civil Engineering (Sparling, Palermo, and Hashemian 2021), as well as the axial load-moment resistance interaction, curvature, and flexural stiffness response of the 8 m tall RM walls. This section compares the results of various approaches for the determination of out-of-plane flexural stiffness and proposes a novel method of estimating the stiffness of reinforced masonry walls subjected to both axial and out-of-plane loads.

Chapter 7 – Application discusses how the experimental results and analyses presented in the dissertation could be used in practical design applications. It includes a discussion which was prepared as part of a published article (Sparling Palermo and Hashemian 2021) and elaborates on the topic of slender RM walls subjected to out-of-plane loads and substantial axial loading. This chapter also includes a design example highlighting the implications of the novel approach to the calculation of slender RM wall flexural stiffness as well as the potential of using NSM steel reinforcement in new RM wall construction.

Chapter 8 – Conclusion summarizes the findings presented in the dissertation.

Chapter 9 – Primary Contributions lists the main contributions arising from the research project.

Chapter 10 – Future Work provides an outline of proposed areas for future research.

Chapter 1 - Introduction

2   Literature Review

This chapter presents relevant formative research and a discussion of the latest developments in the areas that pertain to this dissertation. It includes a discussion of the development of modern analysis approaches for slender RM (Reinforced Masonry) walls and presents various techniques that have been proposed to increase the out-of-plane flexural stiffness or RM walls. Various approaches to FE (Finite Element) modeling of RM elements are also introduced.

2.1   Secondary Moment Effects

Secondary moment effects, also known as moment magnification or P-Δ effects, occur in slender structural elements subjected to axial compression. When a column, strut, or wall is loaded in compression, out-of-plane deformation (due to out-of-plane loads, eccentricity of the axial load, or imperfections) cause a secondary moment to develop as the product of the axial load "P" and the displacement "Δ". When the axial compression load is low, or when the column, strut, or wall is short, the product of P and Δ is low and does not significantly affect the behaviour. Conversely, if the aspect ratio is large (a height to thickness ratio h/t of 30 is often used as a threshold value), the secondary P-Δ moment can represent a large portion or even most of the induced moment. Figure 2.1 illustrates a possible loading condition for a simply supported wall resisting vertical roof loads (P) and out-of-plane distributed loading from wind (w).
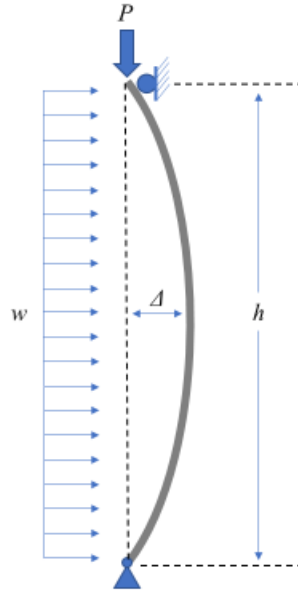
Figure 2.1: Simply supported slender wall subjected to wind loading

The moment at midspan (*M*) in this case may be calculated following Equation (2.1):

Equation 2.1
$$M = \frac{wh^2}{8} + P\Delta$$

The calculation of the displacement, *Δ*, is influenced by both the primary moment from the wind load and the secondary *P-Δ* effect. Since *Δ* depends on the total applied moment, including secondary effects, an exact solution is difficult to calculate. Solutions have been developed, using differential equations and an assumed displaced shape function for certain loading conditions, however satisfactory approximations can also be achieved through iteration. Approximate closed form equations based on the Euler critical buckling load are also commonly used; this closed form solution is referred to as the moment magnifier method, or moment magnification since it multiplies the primary moment by a factor to arrive at the total moment including *P-Δ* effects.

The Euler critical buckling load P_{cr} is the axial compression load at which a column, strut, or wall becomes unstable and may collapse elastically if any initial or induced out-of-plane displacement is present. For a linear-elastic member, P_{cr} is calculated using Equation (2.2):

Chapter 2 – Literature Review

Equation 2.2
$$P_{cr} = \frac{\pi^2 EI}{(kh)^2}$$

Where *EI* is the effective flexural stiffness of the member section and *kh* is the effective unbraced height.

Moment magnification equations based on the Euler critical buckling load have been developed for slender steel columns (Johnston 1966 p. 31) and for slender reinforced concrete columns (McGregor, Breen, and Pfrang 1970) as shown in Equation (2.3):

Equation 2.3
$$M = M_p \frac{C_m}{1 - \frac{P}{P_{cr}}} \geq M_p$$

Where M_p is the primary moment and C_m is a correction factor relating the case being considered to the uniform moment case (equal end moments).

In all cases, the accuracy of the determination of *P-Δ* effects is dependant on the flexural stiffness value *EI* – iterative calculations use the flexural stiffness to determine the deflection value at each iteration, and the moment magnifier method relies on an accurate stiffness value in the calculation of P_{cr}. Equation (2.3) appears in current editions of the Canadian and U.S. masonry design standards CSA S304-14 (CSA Group 2019a) and TMS 402/602-16 (The Masonry Society [TMS] 2016), except that in the U.S. standard, the C_m factor is conservatively taken as 1.

2.2 Slender Reinforced Masonry Walls

Masonry construction has a long history of design following empirical assumptions and rules of thumb. Following these principles, *P-Δ* effects may easily be avoided by maintaining a low aspect ratio; this strategy, however, leads to uneconomical design in the modern construction context. Yokel, Mathey, and Dikkers (1970) conducted a series of tests on slender plain and reinforced masonry walls to assess their response to high axial load and to provide guidance for engineering designers wishing to include tall masonry walls in their designs. They tested walls subjected to eccentric axial compressive loading with the base of the walls placed flat against the laboratory floor as illustrated in Figure 2.2. This set-up resulted in partial fixity at the base of the wall. The reinforced masonry walls were constructed from 140 mm x 190

Chapter 2 – Literature Review

mm x 190 mm hollow concrete masonry units and reinforced with two #5 bars (area of 200 mm^2 each). Three different wall heights (approximately 3.0 m, 4.9 m, and 6.1 m representing *h/t* ratios of 21, 35, and 44, respectively) and four axial load eccentricities (0, *t*/6, *t*/4, and *t*/3) were included in the testing matrix.
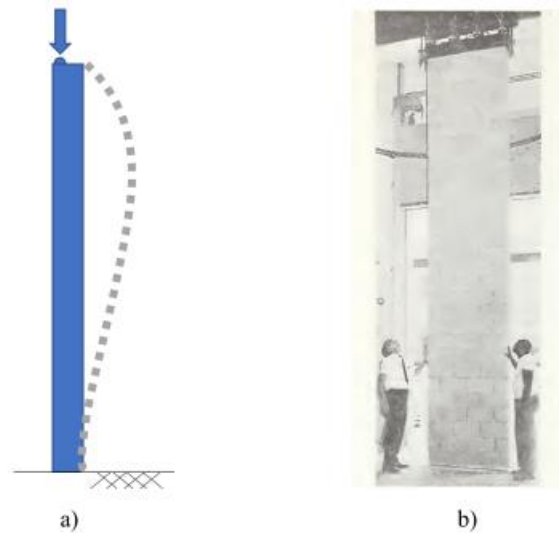
Figure 2.2: Eccentric vertical loading of a slender wall with the base bearing on flat ground: a) conceptual loading condition; and b) photograph from the experimental series (Yokel, Mathey, and Dikkers 1970)

In their analysis, the authors compare the axial load resistance of the walls to the theoretical axial load-moment (*P-M*) interaction curve. These theoretical curves were reduced by an appropriate factor to account for moment magnification of the 4.9 m and 6.1 m tall walls. The flexural stiffness, *EI,* used in the calculation of the critical buckling load was determined using Equation (2.4):

Equation 2.4 $$EI \ = \ \frac{E_i I_n}{2.5}$$

Where E_i is Young's modulus and I_n is the moment of inertia of the uncracked net section. The equation was based on an approximation used for the analysis of slender concrete columns. Although the analysis predicted the strength of the 4.9 m tall walls, it under-estimated the strength of the shorter reinforced walls and over-estimated the strength of the taller walls. The authors did not include an assessment of the total moment resistance including resisting the secondary moment and did not provide the load-displacement response. The indeterminate support conditions made the determination of the applied moment distribution difficult, and figures illustrating the deflected shape suggest the location of maximum displacement

Chapter 2 – Literature Review

changed during testing with increasing load. The authors also added that the flexural stiffness equation, Equation (4), might not be appropriate for the most extreme cases tested (6.1 m tall walls with eccentric axial loading at *t/4* or *t/3*) due to further losses of stiffness from cracking. It must also be noted that all these walls were tested at an early age; most walls were tested 10 to 14 days after construction.

Drysdale and Sallam (1976) also expressed difficulty in developing a rational method for the calculation of second-order effects. Their tests on plain and reinforced masonry walls, constructed from 140 mm thick CMUs and with a height of 2.8 m ($h/t = 20$), were performed with combined axial and out-of-plane loading. The walls were simply supported with varying degrees of axial load eccentricity (symmetrical supports with eccentricity values of 0, $t/6$, $t/3$, and $t/2$) and were tested in third-point out-of-plane loading. Results from the test were used to highlight the shortcomings of existing analysis methods (e.g., the use of a slenderness coefficient) for predicting the capacity of slender masonry walls. They suggested that a simplified moment magnifier method was needed for masonry design.

Another testing series on slender reinforced masonry walls was conducted by Hatzinikolas, Longworth, and Warwaruk (1978). This series included eccentric vertical load tests of walls in single and double curvature using pin connections both at the top and bottom, as illustrated in Figure 2.3.
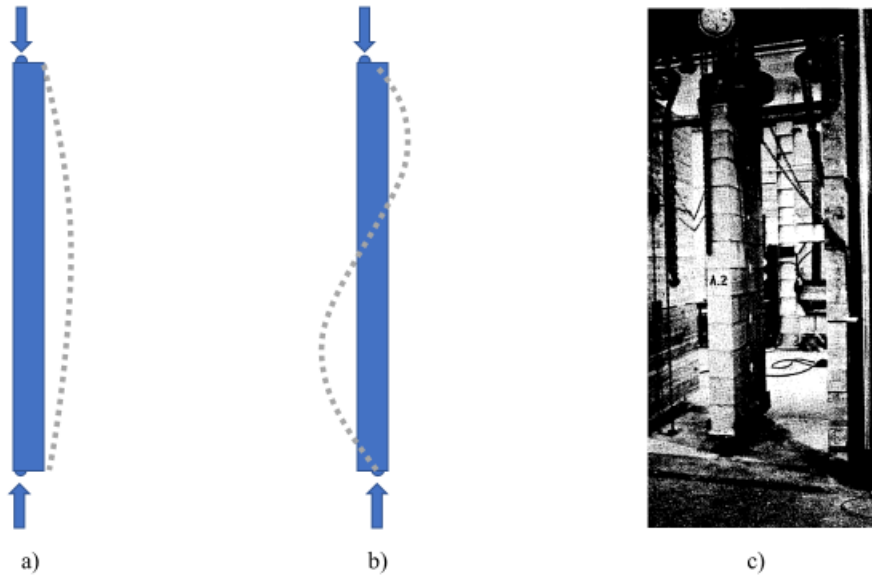
Figure 2.3: Slender walls in eccentric vertical loading: a) single curvature; b) double curvature; and c) photogram from the experimental series (Hatzinikolas, Longworth, and Warwaruk 1978)

The statically determinate set-up facilitated the analysis of their results. Equation (2.5) was developed to calculate the effective moment of inertia *I* based on the initial (uncracked) moment of inertia of the reinforced walls tested:

Equation 2.5
$$I = \left[\frac{1}{2} - \frac{e}{t}\right] I_n$$

Where *e* is the eccentricity of the axial load and *t* is the wall thickness. This equation yields a negative value, and can therefore not be used, for eccentricities greater than *t/2*. In practical applications of masonry, however, it is possible to have effective load eccentricity greater than *t*/2 if out of plane loading is applied (e.g., wind loading) or if vertical loads are applied though a ledger angle. Both conditions can be in play in the case of the slender exterior walls of warehouse-type structures.

The ACI-SEASC Task Committee on Slender Walls (1982) presented results of tests on slender reinforced masonry and concrete walls subjected to combined eccentric vertical loading and out-of-plane distributed loading. In these tests, vertical load was applied through a ledger angle offset from the top of the masonry section (eccentricity > *t/2*) to simulate a roof support connection that is typical of warehouse construction, and the out-of-plane load was applied using an air bag. This set-up allowed the researchers to determine the

Chapter 2 – Literature Review

flexural stiffness and moment resistance of the slender walls (7.2 m tall, *h/t* ranging from 30 to 51 for different block thicknesses) with axial load ranging from 5 kN/m to 13 kN/m. These loading conditions, illustrated in Figure 2.4 were selected to represent typical in-service loading.
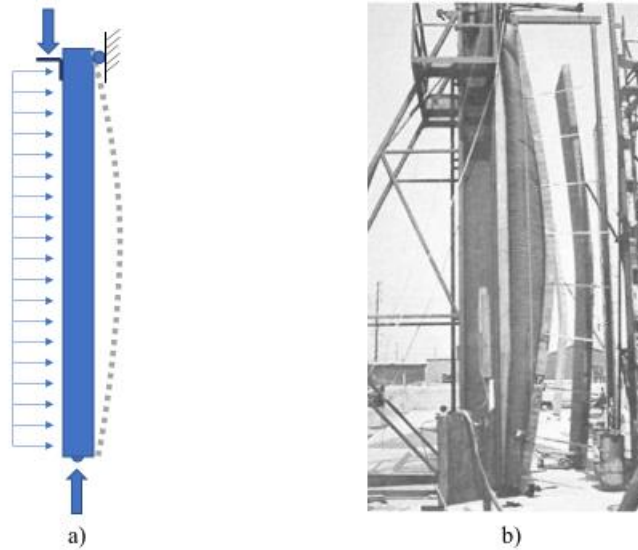
Figure 2.4: Slender wall subjected to combined axial and out-of-plane distributed loading: a) conceptual loading condition; and b) photograph from the experimental series (ACI-SEAS Task Committee on Slender Walls 1982)

The authors demonstrated a good fit between the experimental results and a bilinear response model wherein the initial displacement is controlled by the uncracked flexural stiffness and additional displacements are a function of the cracked flexural stiffness as shown in Figure 2.5. Their calculation of flexural stiffness was based on the transformed moment of inertia and Young's modulus of the masonry and steel materials for both the uncracked and cracked sections.

Chapter 2 – Literature Review
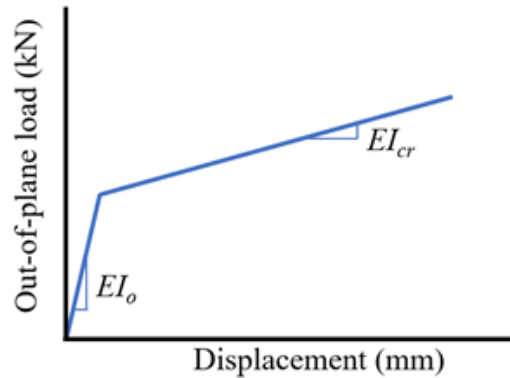
Figure 2.5: Bilinear response of reinforced masonry wall, adapted from ACI-SEASC Task Committee on Slender Walls (1982)

They also provided design examples which account for secondary effects using an iterative method to account for the *P-Δ* moment. Their displacement calculations were based on the simplifying assumption that the shape of the moment diagram (moment distribution along the height of the wall) would be similar for the case of the wall with out-of-plane uniformly distributed load only, and the combined out-of-plane and vertical loading. The displacement could therefore be calculated following Equation (2.6):

Equation 2.6
$$\Delta = \frac{5Mh^2}{48EI}$$

Where *M* is the maximum total moment at midspan including the moments induced by vertical load eccentricity and secondary moments from *P-Δ* effects (updated at each iteration to add the *P-Δ* effect from the previous iteration). The bilinear response is then established by calculating the displacement before and after cracking separately as shown in Equation (2.7):

Equation 2.7
$$\Delta = \frac{5M_{cr}h^2}{48EI_o} + \frac{5(M-M_{cr})h^2}{EI_{cr}}$$

Where M_{cr} is the cracked moment, and EI_{cr} is the flexural stiffness of the transformed cracked section.

More recent testing completed by da Porto, Mosele, and Modena (2011) studied the behaviour of slender reinforced cantilever walls with combined vertical and out-of-plane loading. These tests set out to compare the behaviour of reinforced slender clay masonry unit walls with different reinforcement arrangements. The

Chapter 2 – Literature Review

reversed cyclic out-of-plane load testing of the walls were completed with superimposed axial load provided by a large weight equivalent to 25 kN/m at the top of the wall, as illustrated in Figure 2.6. The authors used the data collected during testing to validate a finite element model consisting of multiple beam elements. Individual beam elements within the model were assigned the constitutive M-ϕ (Moment-curvature) properties of the walls derived based on testing of short specimens; very good agreement was reached between the model and observed behaviour.
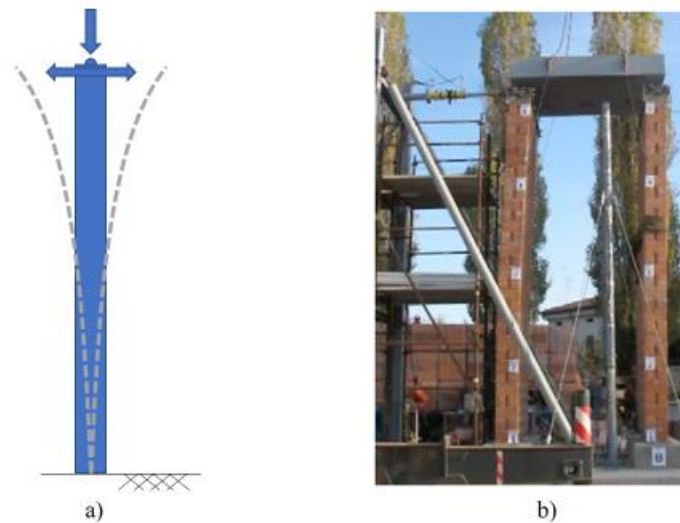
Figure 2.6: Illustration of slender cantilever wall with vertical and reversed cyclic out-of-plane loading: a) conceptual loading condition; and b) photograph from the experimental series (da Porto, Mosele, and Modena 2011)

The validated FEA model was then used to perform parametric analyses on the two wall types to determine the effect of increasing wall height (increasing slenderness) and increasing axial load. As expected, large differences in out-of-plane resistance were found with increasing wall height, for example a 5 m tall wall was shown to have an out-of-plane load resistance of 42 kN compared to 6 kN for a 12 m tall wall. However, the effect of the increasing shear span was not separated from the secondary moment effects (due to the vertical load and self-weight) in the analysis. Changes in vertical loading in the range of 5 kN/m to 30 kN/m resulted in a difference in out-of-plane resistance of up to 10%. Further work (Dona et al. 2019) based on the test data and related FE modeling and parametric analyses (Dona, Tecchio, and da Porto 2018) resulted in a proposed design method for slender RM walls for use within the design framework of the Euro Code.

Chapter 2 – Literature Review

Recent research efforts in Canada and the U.S. have focused on possible sources of over-conservatism in design standards that govern slender masonry walls. Mohsin and Elwi (2003) studied the effect of base fixity on the eccentric axial load capacity of slender RM walls. Although current Canadian standards (CSA Group 2019a) require that walls with a height to thickness ratio *h/t>30* must be analysed as simply supported members, the researchers found that applying a simulated support stiffness at the base of a slender wall (*h/t = 33.9*) could have a profound effect on the load resistance. Support stiffness of 1000 and 5000 kNm/rad resulted in increased axial load capacity of 26% and 55%, respectively, compared to a wall with a pin-connection at the base; increasing the support stiffness to 10 000kNm/rad only resulted in a further 7.8% increase in load capacity compared to the case with a support stiffness of 5000 kNm/rad. Liu and Hu (2007) evaluated the out-of-plane flexural stiffness of RM walls subjected to eccentric axial loading through measurement of the curvature (strain on the tension and compression side) during loading. They found that the current formulation for effective flexural stiffness EI_{eff} greatly underestimated the test results, thus they proposed a new formulation. Whereas the current CSA formulation for the effective flexural stiffness is expressed as shown in Equation (2.8), Liu and Hu (2007) proposed Equation (2.9) as an alternative. This alternative equation was developed as a tri-linear model representing the lower-bound of flexural stiffness values determined during analysis:

Equation 2.8
$$EI_{eff} = E_m \left[0.25I_o - (0.25I_o - I_{cr}) \left(\frac{e - e_k}{2e_k} \right) \right], \quad E_m I_{cr} \le EI_{eff} \le 0.25 E_m I_o$$

Equation 2.9
$$EI_{eff}/EI_o = \begin{cases} 0.7, \ 0 \le e/t \le 0.1 \\ 1 - [2.375 - (0.0175h/t)](e/t), \ 0.1 \le e/t \le 0.4 \\ [0.05 + .007h/t], \ e/t > 0.4 \end{cases}$$

A different approach to the calculation of EI_{eff} was proposed by Bilotta Rios and Cruz Noguez (2021), who used a regression analysis to develop Equation (2.10):

Chapter 2 – Literature Review

Equation 2.10

$$EI_{eff} = \begin{cases} 6.021x10^6P + 5.92x10^5A_s + 1.075x10^7f'_m + 1.0632x10^7\left(\dfrac{h}{t}\right) - 4.75x10^8, & \rho < 1.5 \\[3mm] 2.07x10^6P + 5.77x10^5A_s + 5.052x10^7f'_m + 2.157x10^7\left(\dfrac{h}{t}\right) - 6.602x10^8, & \rho \geq 1.5 \end{cases}$$

Where P is expressed in kN, A_s in mm², and f'_m in MPa, and the resulting EI_{eff} is in kNmm².

Outcomes from the "*CANUS: Harmonization of Canadian and American Masonry Structures Design Standards Project*" included a wide range of recommendations for changes to the Canadian (CSA Group 2019a) and U.S. (TMS 2016) masonry design standards which are outlined in a report by Dutrisac and Banting (2021), as well as a series of conference papers presented at the 2021 Canadian Masonry Symposium. Several recommendations regarding the design of slender RM walls are outlined in (Sustersic et al. 2021), some of which are currently being addressed by various Canadian research groups. Most relevant among these are recommendations regarding the need for more research to justify a simpler and more accurate formulation for the effective flexural stiffness EI_{eff} and to re-examine the limits on axial load imposed on RM walls with a slenderness ratio *h/t > 30*. These are among the principal goals of a research group from the University of Alberta (Alonzo et al. 2021; Gonzalez et al. 2021) as well as the research presented herein.

Other research examining the response of RM walls subjected to axial load and reversed cyclic out-of-plane loading (Mahmood, Gheni, and ElGawady 2021), and the blast resistance of RM walls (Salem et al. 2021) are also helping to demonstrate the strength and resilience of RM assemblies to out-of-plane loads.

2.3   Improving the flexural Stiffness of Masonry Walls

Conventional reinforced masonry construction makes use of cementitious grout to bond reinforcing bars into the hollow cells of standard Concrete Masonry Unit (CMU) assemblies as shown in Figure 2.7. Given that hollow CMUs are approximately 50% void, the grouting process effectively doubles the weight of masonry assemblies when compared to the hollow assembly. Additionally, this method of reinforcing walls

Chapter 2 – Literature Review

usually places reinforcing bars at or near the wall's out-of-plane neutral axis. This practice severely limits the cracked out-of-plane flexural stiffness of a wall and limits a designer's ability to control horizontal cracking.
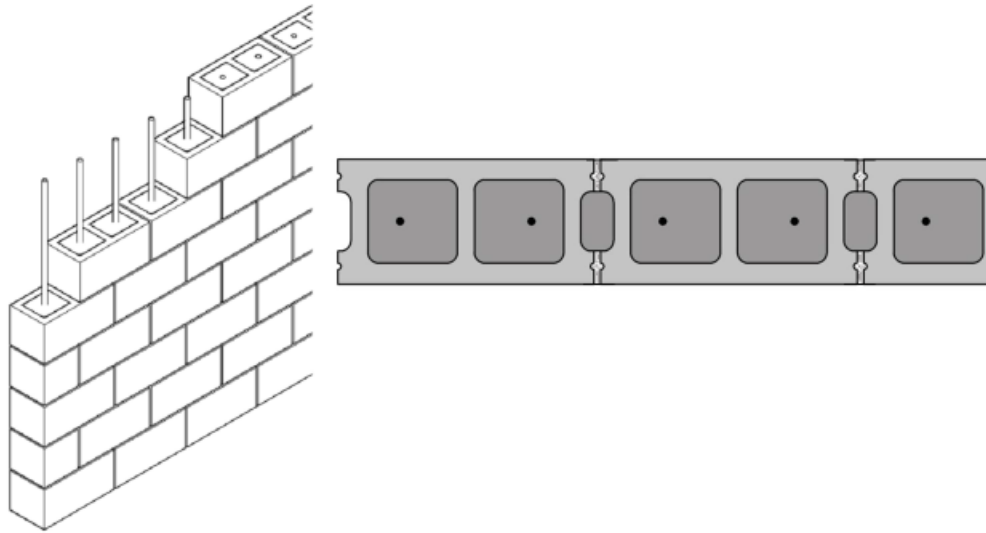
Figure 2.7: Conventional reinforcement of a CMU wall (Sparling 2015)

To maximize the effectiveness of vertical reinforcing bars, Abboud, Hamid, and Harris (1996) tested a staggered placement of reinforcing bars – alternating placement of reinforcing bars near the inner surface of opposing face shells as illustrated in Figure 2.8 a). They found that a 30% increase in strength as well as improved flexural stiffness could be achieved through this method. This approach is now being investigated numerically by Gonzalez et al. (2021), with full-scale experimental testing to follow. In another study, da Porto et al. (2010) nearly tripled the out-of-plane load capacity of a reinforced clay brick masonry wall subjected to combined axial and out-of-plane loading by using a tied rebar cage configuration with only double the area of reinforcement of the control wall. The use of a tied rebar cage has been explored in Canada by Entz et al. (2017) and tested in full scale by Pettit et al. (2019); they found that placing the reinforcement near the inner surface of the CMUs resulted in increased flexural stiffness, as well as a small increase in strength, but did not report further benefits from tying the reinforcement into a cage. The use of post-tensioning of the main vertical reinforcement to restrict the out-of-plane displacement has also been studied by Bean Popehn, Schultz, and Drake (2007). Their findings demonstrated an increase in moment

Chapter 2 – Literature Review

resistance and flexural stiffness with increasing pre-stressing axial load; they also illustrated that restraining the pre-stressing tendons can greatly improve the response compared to unrestrained tendons.
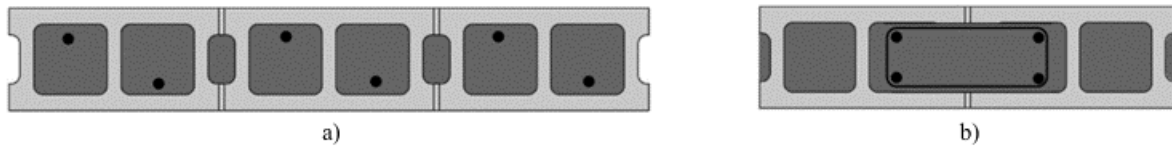
Figure 2.8: Staggered reinforcement layouts: a) adapted from Abboud, Hamid, and Harris (1996), and b) tied cage adapted from Entz et al. (2017)

Although Near-Surface Mounted (NSM) reinforcing materials have been used to improve the strength of existing masonry structures, most of these focus on improving the earthquake-resilience of unreinforced masonry structures (Dizhur, Griffith, and Ingram 2014); it has not yet been adopted as a reinforcement method for new RM walls. The use of NSM wires or bars as the primary reinforcement for new masonry structures was first proposed by Sentrop (1928); in the patent application, no test results or strength calculations were present, however it was claimed that a wall of significant strength could be achieved following the proposed method. A similar construction method was later explored by Hashemian (2017) and Sparling (2015), who illustrated, through calculations and small-scale tests, that increased moment resistance could be achieved using NSM reinforcement, for cases of masonry walls with applied axial loading. The current study continues the examination of the benefits of using NSM steel reinforcement for the construction of RM walls.

2.4   NSM Reinforcement

Modern Near-Surface Mounted (NSM) reinforcement was developed as a method of retrofitting deficient concrete, masonry, or wood structures to improve their resistance. This method was first reported by Asplund (1949), who retrofitted a deficient bridge deck by applying additional steel reinforcing bars within cut grooves and bonding them in place with a cement grout. NSM reinforcement has since gained popularity as a method of reinforcing existing structures to improve their capacity to resist various types of loading (de Lorenzis and Teng 2007; Parvin and Shah 2016). The technique provides similar performance as surface-mounted sheets and strands but with the benefit of protecting the reinforcing material from surface

abrasions. This technique has also been found to resist degradation related to environmental conditions (Fernandes, et al. 2018; Al-Jaberi, Myers, and ElGawady 2018a), and it can be applied in a way that largely preserve a structure's original aesthetics. The applications of NSM reinforcement that are documented in the literature focus on circumstances where increased strength and displacement capacity are desirable, but where increased stiffness could have deleterious effects (i.e., attracting additional loading to the structural member). FRP tapes and strands, which have relatively high strength and low stiffness compared to steel, are ideal in these situations. Current applications are relatively expensive due in part to the need to cut shallow grooves in the members to be reinforced and the technique is often used to improve the strength and resilience of historical unreinforced masonry structures.

NSM reinforcement has gained popularity for retrofitting of structures to increase their strength and displacement capacities, and now appears as a repair method in the Canadian Highway Bridge Design Code, in its provisions for fibre-reinforced structures (Mufti et al. 2007). NSM reinforcement has been widely studied as a retrofit method for various structural systems and construction materials including concrete, masonry, and timber. A common approach for applying this technique to unreinforced masonry elements is known as "structural repointing", where a masonry bed-joint is partially removed and a reinforcing bar, tape, or strand is then inserted and bonded in place using mortar. Laboratory studies have shown the potential improvements to compressive and shear strengths afforded by "structural repointing"; Valluzzi, Binda, and Modena (2005) demonstrated that 50% of the compressive strength of brick masonry wallets could be recovered with structural repointing after testing to failure, and Casacci et al. (2019) established that the shear capacity of brick masonry wallets could be increased by 46% with the addition of basalt bars. These and other studies have led to the application of this type of retrofit solution to existing Unreinforced Masonry (URM) structures, particularly those of historical significance (Valluzzi, Binda, and Modena 2005; Dizhur, Griffith, and Ingham 2014; Marcus et al. 2019).

A similar technique was tested by Carney and Myers (2003) to improve the blast-resistance of URM walls, wherein the stack-bonding pattern of the walls allowed for NSM GFRP reinforcement to be placed

Chapter 2 – Literature Review

vertically through the mortar head-joints. For specimens where anchorage was provided, the NSM reinforcing bars resulted in a 40% increase in resistance to the applied out-of-plane pressure compared to unreinforced specimens. Galati, Tumialan, and Nanni (2006), using a variety of FRP materials and a 4-point out-of-plane loading system on masonry walls, achieved up to a 14-fold improvement in strength compared to unreinforced walls. A further development to this technique, known as "reticolatus", has recently been proposed by Borri et al. (2009) and further tested by Borri et al. (2014). This new technique, which places reinforcing strands within horizontal and vertical mortar joints and connects them in a lattice pattern, has demonstrated effectiveness for the improvement of in-plane shear and out-of-plane flexural strengths and resiliency of masonry walls, specifically those constructed from irregularly shaped stones.

In other studies, grooves were cut horizontally at the mortar joints, and/or vertically through the surface of masonry units to apply NSM reinforcement and increase the strength and/or resiliency of masonry walls under seismic loading (Dizhur Griffith, and Ingram 2014; Konthesingha et al. 2015; Derakhshan et al. 2018). Al-Jaberi, Myers, and ElGawady (2018b) explored the application of NSM GFRP reinforcement to steel-reinforced concrete masonry wallets, resulting in some cases, in doubling the out-of-plane flexural strength. Others have explored the use of cementitious adhesives as an alternative to epoxy as a method of bonding NSM reinforcing bars to structural assemblies. It has been suggested that cementitious materials such as high strength self-consolidating cementitious adhesives (Al Saadi, Mohammed, and Al-Mahaidi 2017), or cementitious paste adhesive (Al-Jaberi, Myers, and El Gawady 2018b; Galati et al. 2006) can be used to achieve a bond that is comparable or superior to that of epoxy. Each of these studies focused primarily on improvements to strength and drift/displacement capacities of existing structures; however, the potential benefits of applying NSM reinforcement technology to new masonry construction remains largely unexplored.

2.5   Numerical Modeling of Slender Masonry

Numerical modeling for analysis of masonry structures is challenging due to the heterogenous and anisotropic nature of the bulk material. To effectively reproduce the behaviour of masonry structures in a

numerical model, one of three general approaches may be followed: Macro-modelling, micro-modelling, or modeling using a combination of macro- and micro-elements. Macro-modelling approaches treat the masonry as a homogenous material with the global properties of the brick/block, mortar, and grout (if applicable) assembly. This approach is the least computationally complex of the three, but it can lead to unrealistic responses due the heterogenous nature of masonry; behaviours arising from the weak fracture planes (along mortar joints) or which arise from the interaction of dissimilar materials may be missed. Conversely, micro-modelling seeks to assign unique properties to each constituent material (mortar, masonry bricks/block, grout, etc.) to account for the effect of their interactions on the global behaviour of the masonry assembly. Drawbacks to micro-modelling include the increased computational complexity of these models due to the larger number of elements needed. Difficulties also arise in setting the properties of each of the constituent materials since the properties of the mortar and grout that are placed within a masonry assembly are often very different from those recorded from testing of samples cast in industry-standard non-porous molds (e.g., 50 x 50 x 50 mm mortar cubes and 100 x 200 mm grout cylinders specified in the CSA A179-14 (CSA Group 2019b) standard). It is well-known that the strength of mortar and grout is significantly higher in the finished assembly than when cast in non-porous molds due to the effect of moisture wicking into the dry and porous masonry units, thereby reducing the water to cement ratio (Drysdale and Hamid 2005, 164, 171). It is important, with the micro-modelling approach, not only for the properties of the individual materials to match the physical materials, but also for the bulk behaviour of the model which arises from the interaction of its component parts to match the bulk behaviour of the masonry assembly. Hybrid models aim to bring the benefits of both micro- and macro-modelling by modeling the individual materials separately, where appropriate, while reducing the computational complexity of the model by combining other portions of a model; however, this approach can incur problems of compatibility between portions of a model and result in modeling artefacts that may affect the analysis outputs.

Liu and Dawe (2003) developed a FE model for reinforced concrete masonry walls based on a macro-modelling approach using simple beam-column elements. The moment-curvature (M-φ) relationship for the

elements was determined analytically using a non-linear compressive stress-strain equation for the masonry material and by applying the principles of strain compatibility and equilibrium. Their analysis accounted for large displacements to properly model the behaviour of slender walls, and the model was successfully validated against the maximum applied load, depending on the wall thickness and load eccentricity, achieved in previous experimental studies. The modeling approach was then used for a parametric study of slender walls. The FE model developed by da Porto, Mosele, and Modena (2011) also consisted of beam elements with an assigned non-linear M-φ relationship. The M-φ relationship was developed based on equilibrium and compatibility of the reinforced section using elastic-perfectly plastic constitutive models for both the masonry and reinforcement material. The resulting models were validated against the load-displacement response from the group's full-scale test, then used to generate a parametric study of cantilevered slender walls with changing wall geometry and axial loading parameters. Although the response of the walls was recorded beyond the point of maximum out-of-plane load resistance, neither the tests nor the numerical models captured the ultimate mode of failure of the walls. Gonzalez et al. (2021) and Alonso et al. (2021) used a similar macro-modelling approach to develop a model based on beam-column elements in their pre-testing analysis of slender RM walls. These models were successfully validated against the load-displacement response of multiple previously reported tests of slender RM walls with combined axial and out-of-plane loading including Liu and Hu (2007) and the ACI-SEASC Task Committee on Slender Walls (1982). Ahmed et al. (2021) opted for a micro-modelling approach for their analyses of slender unreinforced hollow masonry walls subjected to eccentric axial loading, which accurately replicated the axial load resistance of walls with slenderness ratios (h/t) ranging from 10 to 40. Micro-modelling has also been favoured by researchers studying the bond properties of NSM reinforcement (Valluzzi, Binda, and Modena 2005; Chen, Chen, and Teng 2016) to examine the complex bond behaviour observed in experimental studies (Galati, Tumialan, and Nanni 2006; Al-Saadi, Mohammed, and Al-Mahaidi 2017; Maljaee, Ghiassi, and Lourenco 2018). The modeling by Valuzzi, Binda, and Modena (2005) accurately simulated the cracking pattern of masonry under compression and confirmed the effectiveness of the NSM reinforcement by transferring tensile stresses from the masonry to the reinforcement; however,

their simulations did not provide accurate results of the ultimate compressive strength of previously tested and repaired masonry prisms (repair work done by structural repointing with NSM FRP). Chen, Chen, and Teng (2016) provided a detailed discussion of the importance of intermediate cracking and crack propagation for modeling the bond behaviour between FRP materials and concrete; their numerical modeling work provided a very good fit to the observed behaviour from their bench-scale test specimens. Since walls reinforced with NSM bars, tapes or strands often fail through a debonding mechanism, this bond is an important feature of most FE models.

2.6   Summary of Literature Review

The formative experimental tests by Yokel, Mathey, and Dikkers (1970); Hatzinikolas, Longworth, and Warwaruk (1978); and by the ACI-SEASC Task Committee on Slender Walls (1982) were instrumental to the transition from empirical design methods for slender RM walls to modern methods based on rational analysis. However, these testing series focused mainly on the most common design conditions, leaving large gaps in the current literature. As the structural requirements of buildings has evolved, including the need for taller exterior walls and increasing spans between supports for warehouse structures, and construction practices change, contemporary research is needed to advance knowledge. Recent experimental studies have each focused on distinct sub-areas of research, including the effect of base fixity on axial load capacity (Mohsin and Elwi 2003) and the effective out-of-plane flexural stiffness of slender walls (Lui and Hu 2007; Bilotta Rios and Cruz Noguez 2021). A few reinforcement methods which could improve the out-of-plane flexural stiffness of RM walls have also been proposed, including staggered reinforcement (Abboud, Hamid, and Harris 1996; Entz et al. 2007), and NSM steel reinforcement (Hashemian 2017, and Sparling 2015). The testing presented herein includes the first full-scale tests on hollow RM walls with NSM steel reinforcement, as well as rare contemporary data from testing of very slender walls ($kh/t = 42$) subjected to combined axial and out-of-plane loads.

Current available research literature on NSM reinforcement presents it as a reinforcement method for retrofitting of structures, with a strong focus on the use of FRP as the reinforcement material. Certain

principles from the existing research literature may be applicable to NSM steel reinforcement of new masonry construction, however the higher stiffness of the steel reinforcement can result in a different bond behaviour.

Finite element analyses of slender walls available in the research literature have focused on conventional methods of reinforcement bonding (grouting within the hollow cells of masonry). The finite element analysis presented in this dissertation investigates a possible modelling approach for this novel reinforcement technique for new RM construction. Further investigation is required to determine how best to represent the complex behaviour of NSM reinforcement bonding, which is usually addressed though micro modelling (Valluzzi, Binda, and Modena 2005; and Chen, Chen, and Teng 2016), within models of slender RM walls that are typically developed using a macro-modelling approach (Liu and Dawe 2003; da Porto, Mosele, and Modena 2011; Gonzalez et al. 2021; and Alonso et al. 2021).

3 Numerical Modeling

The research presented in this dissertation began with a numerical investigation of the behaviour of hollow masonry walls reinforced with NSM steel bars, following successful small-scale proof of concept testing which took place at the University of Manitoba (Sparling 2015). During the planning phase for testing on 3 m tall, Reinforced Masonry (RM) walls, Finite Element (FE) models of the RM materials were developed using a micro-modelling approach and validated against the data from the proof-of-concept testing. The models were then used to analyze the 3 m tall walls subjected to monotonic out-of-plane loading to anticipate their behaviour during testing. They were further refined following testing of the constituent materials (masonry prisms in uniaxial compression and steel reinforcing bars in direct tension). The FE analyses took place after construction, but prior to testing of the reinforced masonry walls.

3.1 Preliminary Modeling Approach (adapted from Sparling, Palermo, and Hashemian 2017)

Various FE modeling approaches were considered for this research study. These included 1- and 2-dimensional models as well as the 3-dimensional modelling approach that was eventually adopted. Given the presence of thin concrete components (webs of CMUs) within the masonry wall sections, and the unique cracking pattern that arises due to the NSM reinforcement system, a detailed 3-dimensional approach was selected. By using the ATENA 3-D Finite Element Analysis software package (Červenka Consulting 2016), the CMUs, mortar joints, and masonry grout could be assigned different material properties, and the reinforcing bars could be placed as discrete 1-D reinforcing elements within the models in a way that accurately reflected their position within the walls as built. Furthermore, the constitutive models for the material properties of the CMU concrete, masonry mortar, and grout could simulate the non-linear stress-strain response of this type of material as well as the cracking response.

3.1.1 Material models

Individual material properties were assigned to the CMUs, mortar beds, grout, and reinforcing steel to accurately represent the interaction of these various materials that constitute a reinforced masonry wall system. The CMUs, mortar, and grout were modeled using a 3-dimensional non-linear cementitious constitutive model. Steel reinforcement elements were modeled as 2-dimensional truss elements with a bilinear stress-strain relationship. Support and loading elements (steel plates) were modeled using a 3-dimensional, linear-elastic isotropic constitutive model. A summary of the properties assigned to the various materials is provided in Table 3.1. These properties were selected based on previously recorded data (Sparling 2015) and on recommended values from Drysdale and Hamid (2005).

Table 3.1: Constitutive Models - Summary of Properties

Material	Constitutive model type	Properties
Concrete masonry unit	3-D non-linear cementitious	$f'_c = 25$ MPa $E = 18.5$ GPa $f_t = 2.3$ MPa $v = 0.2$
Mortar	3-D non-linear cementitious	$f'_c = 10$ MPa $E = 12$ GPa $f_t = 0.8$ MPa $v = 0.2$
Grout	3-D non-linear cementitious	$f'_c = 12$ MPa $E = 18.5$ GPa $f_t = 1.3$ MPa $v = 0.2$
Steel plate	3-D linear-elastic isotropic	$E = 200$ GPa $v = 0.3$
Steel reinforcing bar	2-D bilinear	$f_y = 400$ MPa $E = 200$ GPa

To limit the complexity of the models, a perfect bond was applied between adjacent elements. However, to avoid over-estimating the tensile strength of mortar joints, the tensile strength of the mortar material was set to lie within the range of tensile bond strength reported in Drysdale and Hamid (2005). In this way, the

masonry units were effectively bonded to each other with the bond strength typical of a masonry-mortar bond. A perfect bond was assumed between the steel reinforcing bars and the surrounding material.

3.1.2   Model validation

The geometric properties of the FE models were simplified from the specimens, as built. These specimens were constructed from 6 stack-bonded SRCMU masonry units and reinforced within two 10M reinforcing bars, one within the central groove of each face (tension and compression side), as shown in Figure 3.1 a) and b). The simplifications resulted in a reduction in the number of elements necessary to model the geometry, and to allow the meshing of the models using only brick-type elements. The wall specimen was separated into 6 components; these components consisted of the following: compressive CMU face shell, tensile CMU face shell, mortar joints in tension, CMU webs, steel reinforcement, and steel supports and load spreader beams. An image of the specimens as well as a representation of the assembled FE model is provided in Figure 3.1 c), d), and e).
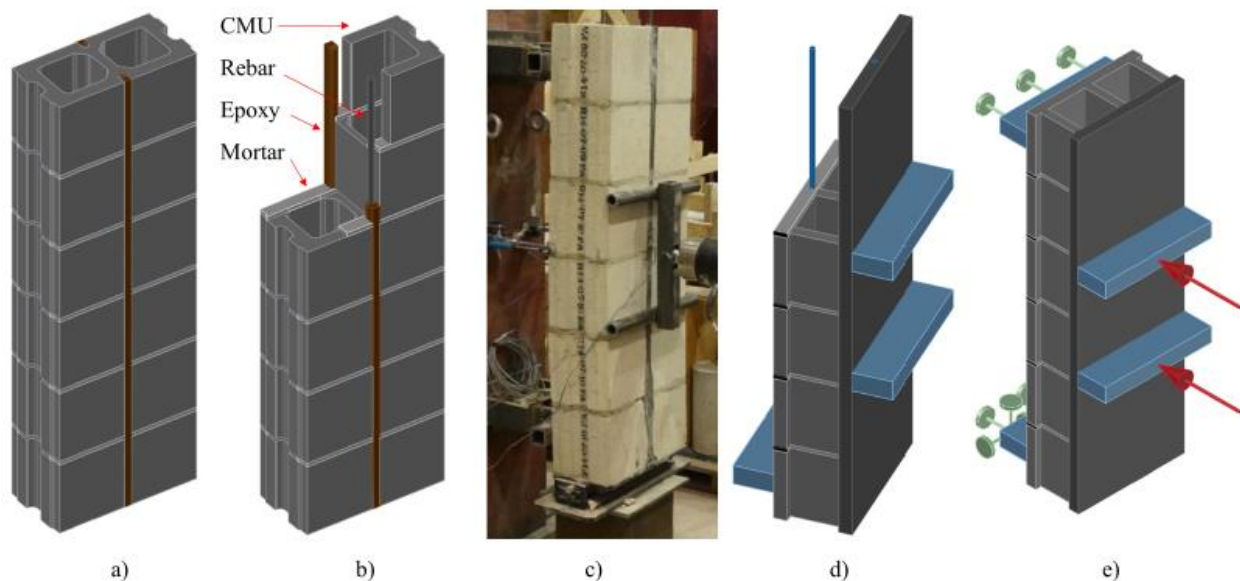
Figure 3.1: Small reinforced flexural specimens: a) conceptual illustration; b) annotated cutaway; c) photo of specimen from previous study (Sparling 2015); d) FE model cutaway; and e) specimen load and support conditions

The compressive face shells of the specimen were modeled as a single monolithic component with the properties of the concrete masonry unit. This component, therefore, had a thickness of 32 mm, a width of 390 mm, and a height of 1190 mm. Since no tensile cracks are expected on the compression face of the wall

Chapter 3 – Numerical Modeling

specimen, the behaviour was expected to be governed by the properties of the CMU. Although localized compression and rotation at the mortar joints is possible, that effect was not considered in this analysis.

The tensile face of each wall specimen was modelled as successive courses of CMU face shells and horizontal mortar beds. The CMU face shell elements each had a thickness of 32 mm, a width of 390 mm and a height of 190 mm, while the mortar beds had the same thickness and width, but a height of only 10 mm. These successive layers of material with different tensile strength create the preferential planes of horizontal cracks typical of masonry construction.

The CMU webs spanning from the compressive face to the tensile face were modeled as three separate components for each CMU. These components each had a thickness of 26 mm, a length of 126 mm, and a height of 190 mm. They were spaced to match the location of webs of the CMUs. There was, therefore, no vertical continuity between the webs of successive courses, as was the case in the specimens as built.

The reinforcement was modeled using truss elements perfectly bonded to the FE mesh of the CMU face shell material on the compression side, and to the face shell and mortar material on the tension side. These elements were positioned at the same location as in the test walls: laterally centred and embedded 20 mm from the surface of the wall on both the tension and compression side. As perfect bonding was assumed between the reinforcing material and the wall, neither the groove nor the epoxy bonding material was included in the model.

The mesh sizes for the various components of the models were selected to be as coarse as possible while limiting the aspect ratio of elements to a maximum of 2:1 for the CMU material. All components were therefore meshed with elements having a maximum length in any direction of 40 mm. This size results in an aspect ratio greater than 2:1 for elements in the mortar joints; however, since they are expected to crack at relatively low load levels, their larger aspect ratio was not expected to have a significant influence on the analysis results. The models were analyzed under monotonic loading at third points along the specimen height as illustrated in Figure 3.1 c) in increments of 0.5 mm until failure.

The load-displacement results, under third-point loading, of the analysis and the data from Sparling (2015) are shown in Figure 3.2. Specimens F1, F2, and F3 were replicate hollow RM specimens, each constructed from six stack bonded SCRMU units with a single steel reinforcing bar bonded into the central 20 mm x 30 mm grooves on both exterior faces. Up to a load of approximately 12 kN, the numerical load-displacement curve captures the un-cracked flexural stiffness of the masonry assembly; however, during testing, the mortar joints separated from the CMUs at the onset of loading and the un-cracked response was not observed. This was attributed to the weak CMU-mortar bond achieved in the specimens due to the method by which the units were manufactured. Agreement between the results at loads above 15 kN suggests that the selected constitutive models, model geometry, and element mesh accurately simulate the cracked flexural behaviour of the reinforced masonry assemblies. It should, however, be noted that the FEA model predicted failure due to crushing of the masonry in compression, whereas the observed failure was diagonal shear tension in the CMU webs in the shear span region (between the upper or lower support and the nearest loading point).
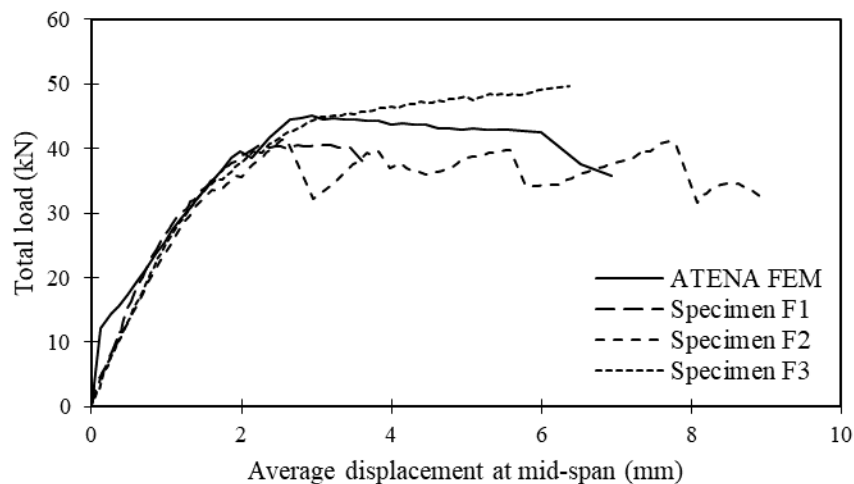
Figure 3.2: Load-displacement response of ATENA FE analysis and reinforced walls from Sparling (2015)

3.1.3 Modelling of 3m walls

The wall models in this section were developed to predict the behaviour of the 3 m tall walls presented in Chapter 4; more information on the materials, construction, and testing for those walls is available in that

Chapter 3 – Numerical Modeling

chapter. Finite element models were developed based on the test wall specimens that were constructed. These walls each had the same total cross-sectional area of reinforcement, however the placement of the reinforcing bars and the number of grouted cells varied as indicated in Table 3.2 and illustrated in Table 3.3. The constructed cross-sections were selected to compare the behaviour of walls with conventional and NSM steel reinforcement, and isolate the effect of grouting. The designation of each wall indicates whether the wall is reinforced conventionally (C) or with NSM steel reinforcement (N), whether it is grouted (G) or hollow (H), as well as the height of the wall (in mm). For example, wall NG3200 was reinforced with NSM steel bars, was fully grouted, and measured 3200 mm in height.

Table 3.2: 3 m wall cross section properties

Wall ID	Tension Reinforcement Ratio[a]	Grouted cells [x/6]	Bar size (quantity)	Depth to tension reinforcing bar [mm]	Area of steel in tension [mm^2]
CG3200	0.26%	6	10M (6)	95	600
NG3200	0.13%	6	10M (6)	170	300
CH3200	0.26%	2	20M (2)	95	600
NH3200	0.13%	0	10M (6)	170	300
[a] Ratio of the area of steel in tension to the gross area of the masonry section					

Table 3.3: Conceptual rendering of RM wall cross sections

Wall ID	Cross section
CG3200	
NG3200	
CH3200	
NH3200	
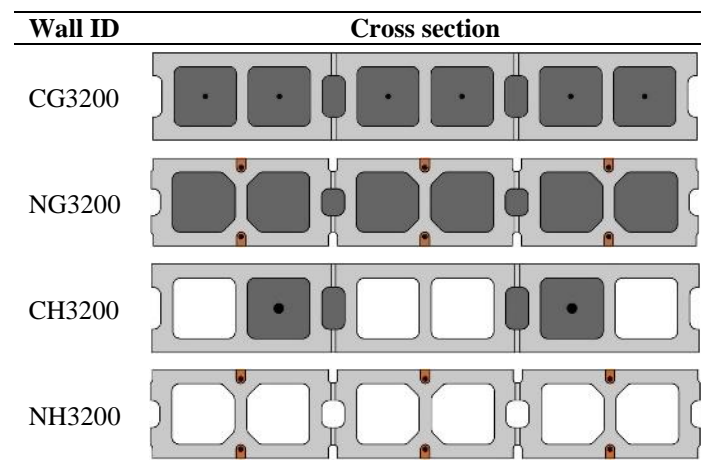
The models of the 3 m tall walls were developed in a similar way as the models of the 1.2 m specimens from Sparling (2015). The face shell element in compression had a thickness of 32 mm, a width of 1200 mm, and a height of 3190 mm (matching the full length and height of the walls as built). The CMU face

35

Chapter 3 – Numerical Modeling

shell elements on the tension side each had a thickness of 32 mm, a width of 1200 mm and a height of 190 mm, and the mortar beds had a height of 10 mm. Head joints were not expected to greatly impact the behaviour of the walls and were therefore not included in the FE models.

Grouted cells, where applicable, were modelled with elements spanning the entire grouted width including adjacent webs, and the full height of the walls. To simplify the models, the CMU webs were deleted from locations containing grout since the average mechanical properties in those areas were expected to closely resemble that of the grout. One-dimensional truss elements were positioned within the face shells, or grouted cells, as applicable, corresponding to the location of the reinforcing bars within each of the walls. These reinforcing elements were perfectly bonded to the material within which they were placed, similar to the models of the smaller specimens.

A graphical representation of the cross-section of each masonry wall alongside a representation of how it was modeled in ATENA 3D is provided in Figure 3.3. The elements were assembled as shown - the bottom support and first course of each wall is represented.
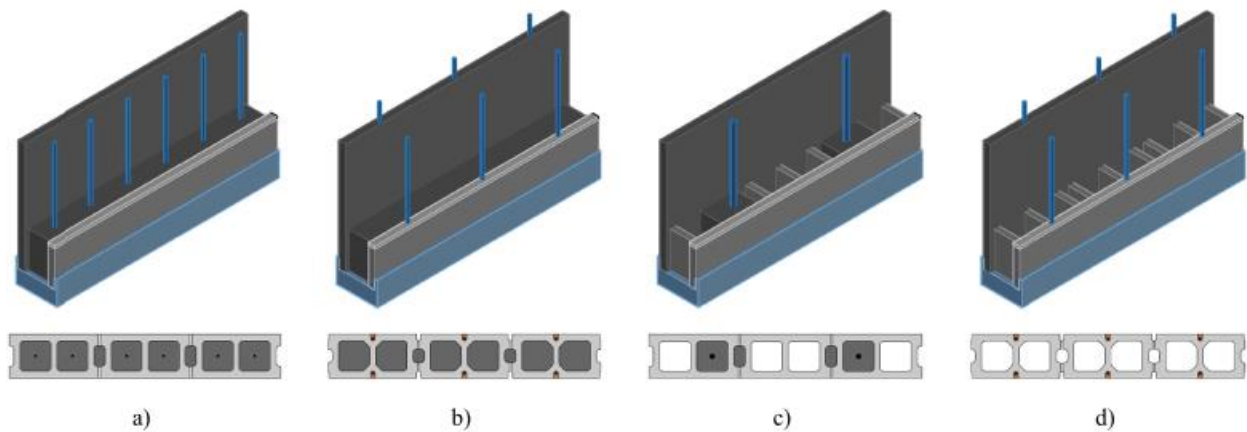
Figure 3.3: Cutaway of FE modes for RM walls: a) CG3200; b) NG3200; c) CH3200; and d) NH3200

To simulate the test conditions (simple support), the bottom pin connection was developed by restraining the line of nodes at the centre of the bottom support plate against all translation (horizontal and vertical movement), without restricting rotation. Similarly for the top support, the line of nodes at the centre of the top support plate was restrained against horizontal translation (in-plane and out-of-plane), however rotation

Chapter 3 – Numerical Modeling

and vertical translation were left unrestrained to generate a roller type support. The out-of-plane loading was applied at two discrete points. These points were located at the centre of very stiff steel elements which could distribute the load across the horizontal length of the wall models. Point loads were used to simplify the process of assessing the applied load (since the models were run in displacement control, the total applied load was simply the sum of load resistance at the two loading points), and to avoid additional constraint to the displaced shape of the loaded model. Applying a displacement-controlled line load would prevent the wall from bowing or rotating about the vertical axis. An illustration of the geometry of the FE model is provided in Figure 3.4.
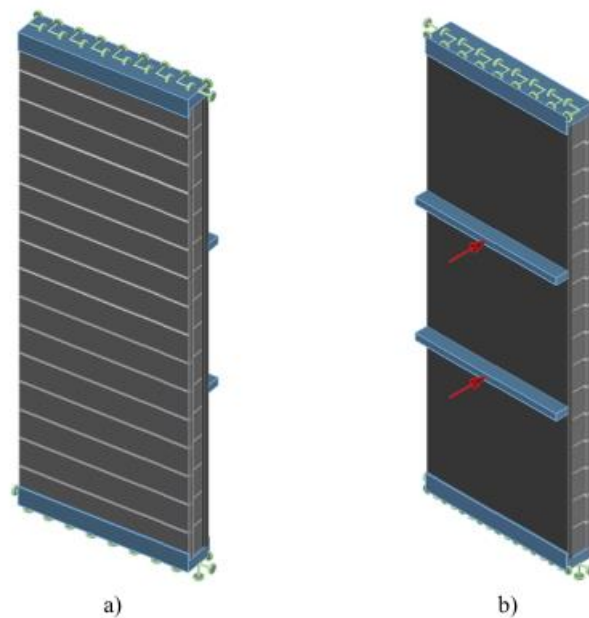
Figure 3.4: Isometric illustration of FE model including loading points and support conditions: a) tension side; and b) compression side

3.1.4   Analysis results

The load-displacement results from the FE analyses for the two fully grouted 3 m tall walls and two hollow walls of the present study are shown in Figure 3.5 and Figure 3.6, respectively. Note that the wall models are identified similarly to the test specimens with the added prefix "M-" to indicate the results presented are those of a FE model as well as a suffix (e.g., "a") to identify the series of the FE model. These results highlight the difference in behaviour between walls with conventionally placed reinforcing bars, and those

Chapter 3 – Numerical Modeling

with NSM steel reinforcement. The shape of the load-displacement curves for grouted walls shown in Figure 3.5 closely matches that of grouted walls tested by Abboud, Hamid, and Harris (1996), suggesting that the material model used to represent the grout reasonably simulates the behaviour. [Note that the yield point in Figure 3.5 and Figure 3.6 corresponds to the load at which the strain in the reinforcing bars first exceeded 0.2%]
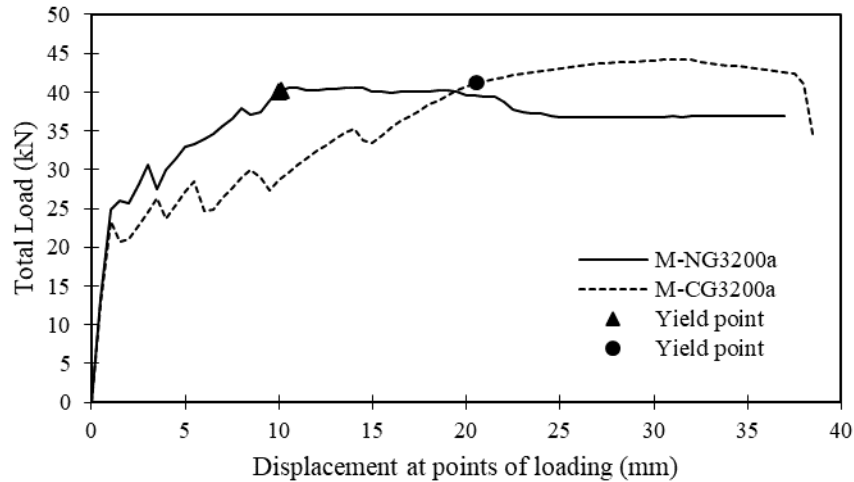
Figure 3.5: Load-displacement response for grouted wall models M-CG3200a and M-NG3200a
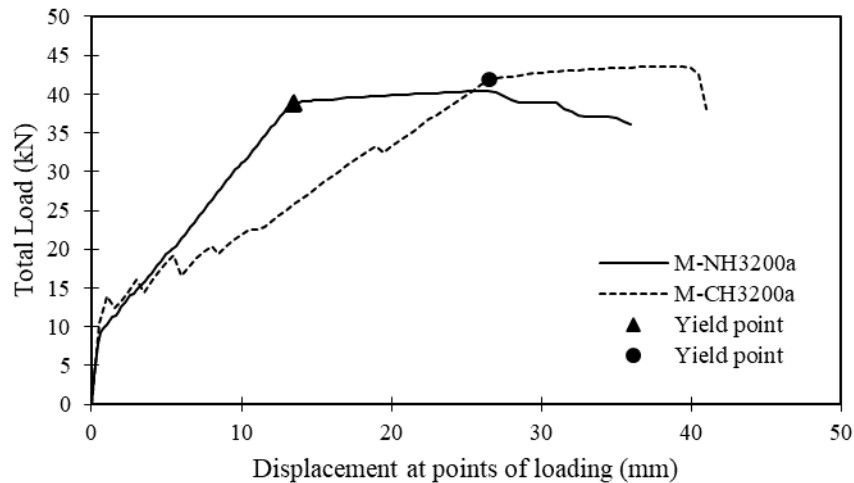
Figure 3.6: Load-displacement response for hollow wall models M-NH3200a and M-CH3200a

Wall models M-CG3200a and M-NG3200a (Figure 3.5) exhibited similar flexural behaviour up to approximately 60% of the ultimate load, during which the behaviour was controlled by the tensile strength of the grout (un-cracked behaviour). For loads beyond 60% of ultimate, the sections began to crack and

Chapter 3 – Numerical Modeling

flexural behaviour was controlled by the reinforcing bars. After cracking, the wall model with conventional reinforcement, M-CG3200a, exhibited lower flexural stiffness than M-NG3200a. Furthermore, the reinforcing bars began to yield in tension after a displacement at the loading points of 10 mm for M-NG3200a, whereas the reinforcing bars in Wall M-CG3200a yielded after 20 mm of displacement.

Similar differences exist between the responses of wall models M-CH3200a and M-NH3200a (Figure 3.6). The un-cracked flexural stiffness of the walls is similar, however M-CH3200a exhibited lower post-cracking flexural stiffness. The onset of yielding of the reinforcing bars also occurs at a higher displacement for M-CH3200a (27 mm) than M-NH3200a (13 mm). Additionally, since these walls contain less cementitious materials in tension, the cracking load is less than half that of the fully grouted walls.

Another notable difference between the conventionally reinforced walls and those with NSM reinforcement is the level of cracking in the walls at the onset of yielding of the longitudinal steel in tension. The onset of yielding generally represents the point at which further deformation is not recoverable. It therefore represents the maximum load level at which the structure could be expected to maintain its functionality.

Figure 3.7 illustrates the displaced shape of the four models magnified 5-fold at the onset of yielding. Locations with high tensile stress are depicted in red, locations with high compressive stress are shown in blue. The black lines indicate cracks wider than 0.2 mm.
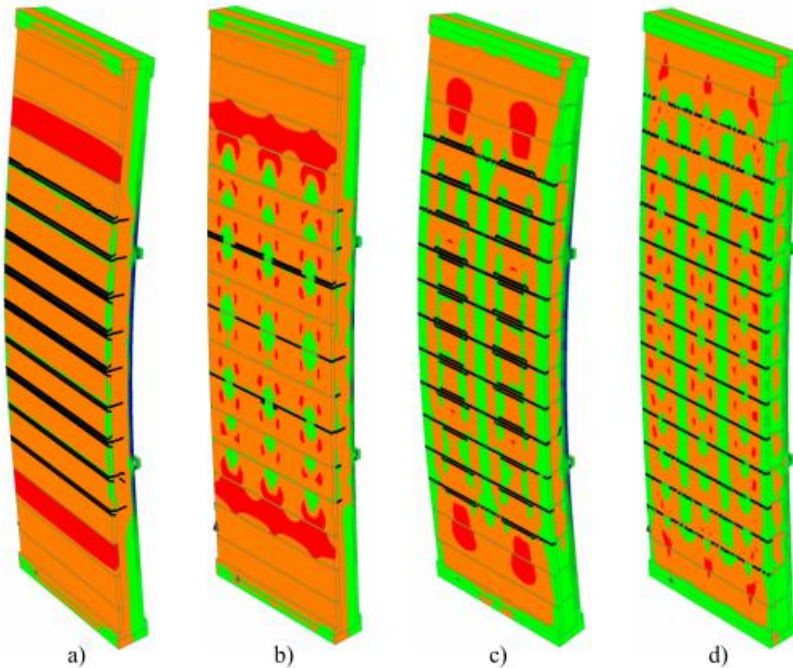
Figure 3.7: Normal Stress and Crack Pattern at Onset of Yielding: a) M-CG3200a; b) M-NG3200a; c) M-CH3200a; and d) M-NH3200a

Comparing the behaviour of M-CG3200a to that of M-NG3200a, and the behaviour of M-CH3200a to that of M-NH3200a, the walls reinforced with NSM steel bars exhibit lower stress in the masonry and decreased severity of cracking at the onset of yielding.

The walls with NSM reinforcement have an ultimate strength within 10% of that of equivalent conventionally reinforced walls. However, the FE analyses suggest that the NSM-reinforced walls exhibit approximately half the level of displacement of conventionally reinforced walls at the onset of yielding of the longitudinal reinforcement in tension.

3.2   Model Refinement (Adapted from Sparling, Palermo, and Hashemian 2018)

Following the testing of the materials used in the walls, the FE models were refined, and the material properties adjusted to fit those of the constructed walls. Models of the masonry prisms were analysed to confirm the properties of the masonry blocks, mortar, and grout. Models of the reinforced masonry walls were then analysed to determine the sensitivity of the walls to variations in stiffness and strength of the constitutive steel and concrete materials.

Chapter 3 – Numerical Modeling

3.2.1   Material properties and validation

Sparling (2015) correlated the strength of CMUs and prisms to the cylinder strength (f'_c) of the concrete used to manufacture the CMUs. Those results suggest that for normal strength Type S mortar, a CMU made from concrete with a cylinder strength, f'_c, of approximately 32 MPa should result in a hollow masonry prism strength of 22 MPa. This correlation between concrete block strength and the f'_c value of the constituent concrete for the CMUs is not typically assessed because the nature of the concrete used in CMU production is not conducive to casting conventional concrete cylinders, and the finished CMUs are not large enough for standard sized cores to be extracted from them. However, the correlation established by Sparling (2015) was used to inform the selection of an appropriate f'_c value for the CMUs in the FE models.

The correlation between the f'_c value for the constituent concrete material and the prism strength was verified through FE modeling of the masonry prisms. These 5-course prisms were casted in a pseudo-running bond pattern and tested in uniaxial compression, as illustrated in Figure 3.8 a) (further discussion of the materials tests is provided in Chapter 4). The CMUs for the FE model of masonry prism tests were simplified to a combination of two face shell portions 32 mm thick linked by three webs, each with a thickness of 26 mm. Mortar joints were modeled as 3-D macro-elements with a thickness of 10 mm. Half-block courses were achieved by reducing the length of face shells into two equal pieces of 190 mm length, separated by a 10 mm mortar joint, as in the physical specimens. The outermost webs of the cut blocks had a thickness of 8 mm.

Chapter 3 – Numerical Modeling
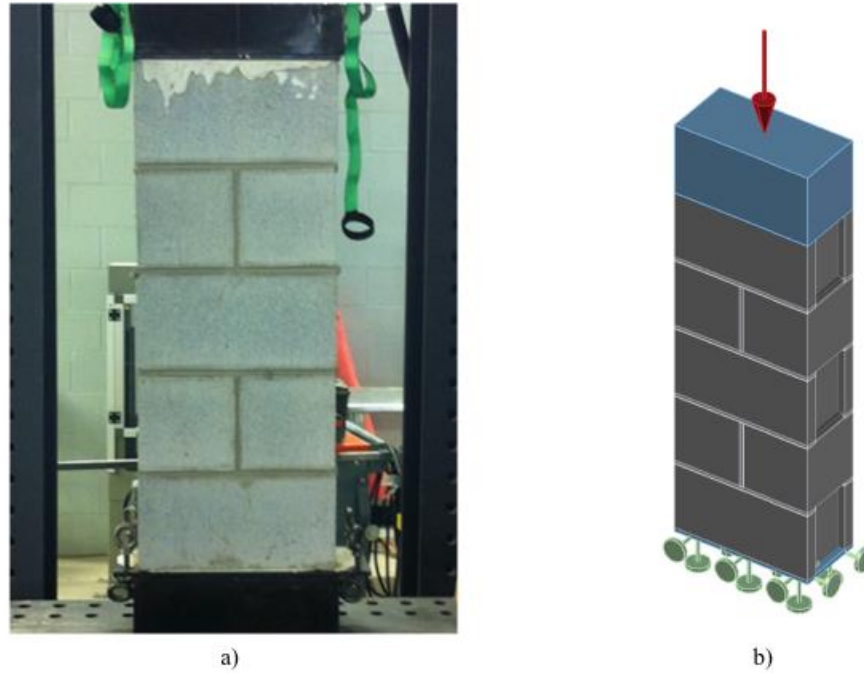
Figure 3.8: 5-course masonry prism with pseudo running bond pattern: a) conventional block prism; and b) FE model

Figure 3.9 provides a comparison of the simplified cross sections used in the FE models with the minimum

cross sections of the concrete blocks. The grouted cells, when applicable, were modeled by the addition of

concrete macro-elements filling in the space between the webs and face shells of the concrete blocks.
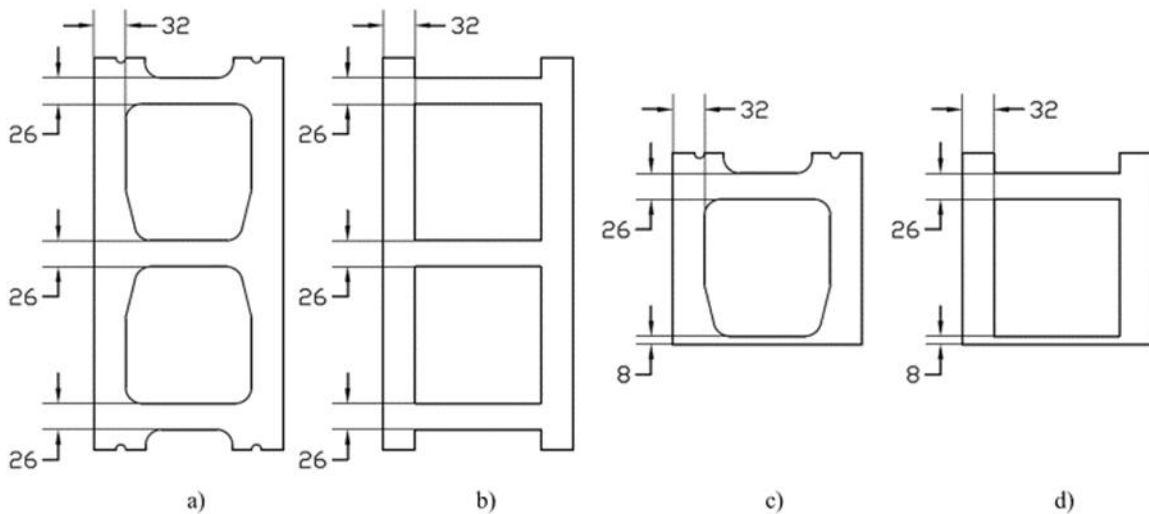
Figure 3.9: Cross section of the CMUs and FE model: a) Minimum CMU cross section; b) simplified FE block cross section; c) minimum CMU half-block cross section; and d) simplified FE half-block cross section (dimensions in mm)

The bottom surface was fully restrained to simulate the lower (stationary) platens of the test frame. On the

upper side of the prism, an additional macro-element with the mechanical properties of steel was placed

Chapter 3 – Numerical Modeling

such that a concentrated point load could be applied at the centroid of its top surface. The thickness of the top plate was set at 200 mm to limit its deformation during loading as illustrated in Figure 3.8 b). Loading was performed by incrementally increasing displacements at the centroid of the top plate until the analysis solution diverged beyond the default criteria.

The properties of the mortar and grout were maintained for all prism models and were based on the default characteristics of ATENA's 3D non-linear concrete model given the f'_c values determined from material testing. Strength and elastic modulus values used in the grout and mortar models as well as two trial values for the CMUs are shown in Table 4. The base f'_c value for the CMUs was based on the average hollow conventional prism strength of 23 MPa (see Chapter 4 material testing) and the correlation between prism strength and CMU f'_c from Sparling (2015). The f'_c value for the CMU-grooved block was similarly calculated using the average hollow grooved prism strength. Note that Young's modulus values assigned to the material constitutive model were determined using Equation (3.1) taken from the CSA standard A23.3:19 Design of concrete structures (CSA 2019c).

Equation 3.1 $$E = 4500\sqrt{f'_c}$$

Table 3.4: Compressive properties of mortar and grout for FE analysis

Material	f'_c [MPa]	E [MPa]
Grout	20.1	20 200
Mortar	16.4[a]	18 200
CMU – base value	32	25 500
CMU – grooved block	18	19 100
[a] Assuming $f'_c = 0.85 f_{cu}$		

Figure 3.10 provides the stress-strain responses for the FE models of masonry prisms with the CMU material having the base value. Figure 3.10 also provides the initial elastic modulus of tested grouted and hollow prisms made from conventional blocks (see Chapter 4). The lines representing the elastic moduli are extended to the average maximum stress of that population of prisms. Good correlation between the experimental and numerical results is achieved with the CMU base values for the conventional hollow prisms. However, the decrease in strength and axial compressive stiffness of the tested prisms with the

Chapter 3 – Numerical Modeling

43

addition of the grout is not accurately simulated. This is likely due to difficulties in accurately modelling the interaction between the grout and masonry blocks that causes the observed lower strength in grouted prisms. This lower strength is reportedly due to differences in the Poisson's ratio as well as subtle geometric effects (Drysdale and Hamid 2005).
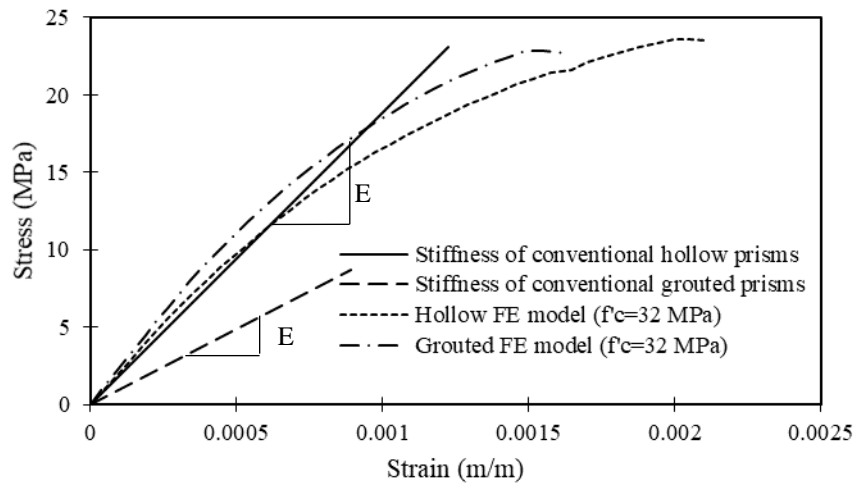
Figure 3.10: Stress-strain response of FEA prism models for f'c =32 and average initial stiffness of conventional prism tests

Figure 3.11 shows the initial axial compressive stiffness of the hollow prism tests and the stress-strain response of the hollow FE models. It illustrates that although the grooved prisms had a lower strength than the conventional prisms, the stiffness was similar. The prism model with the "CMU – grooved block" (f'_c = 18 MPa) properties had a similar strength to that of the grooved prisms tested; however, the stiffness captured by the model was lower than what was observed during testing.

Chapter 3 – Numerical Modeling
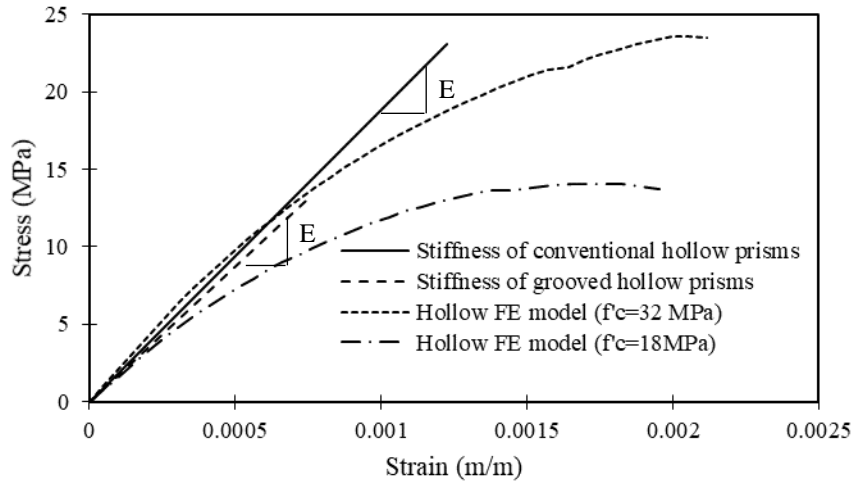
Figure 3.11: Stress strain responses of hollow prism FE models and initial stiffness of hollow prism tests

Figure 3.12 provides the stress-strain behaviour from the FE models of the grouted prisms and shows the axial compressive stiffness of the grouted prism tests; it highlights the importance of the interaction between the grout and the CMUs. For both the conventional CMU (f'_c = 32 MPa) prism model and the grooved CMU (f'_c = 18 MPa) prism model, the strength and stiffness captured by the grouted models were over 200% of what was observed during the tests.
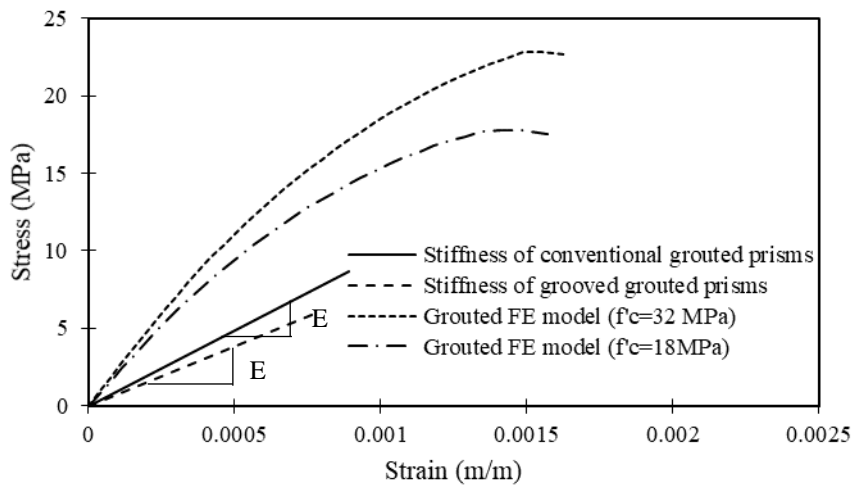
Figure 3.12: Stress strain responses of grouted prism FE models and initial stiffness of grouted prism tests

When modeling a hollow masonry prism, it is important to account for the shape factor of the masonry unit when setting the f'_c value assigned to the constituent material of the CMUs. The FE model analyses completed as part of this research support the correlation between f'_c of the masonry units and the strength

Chapter 3 – Numerical Modeling

of hollow prisms with type S mortar observed by Sparling (2015); however, the use of the measured compressive strength (from grout cylinder tests) for the material properties of masonry grout resulted in an over-estimation of the strength and axial compressive stiffness of grouted prisms. The results from modeling of the masonry prisms suggests more work is needed to develop a method of accurately modeling the interaction between the CMU, mortar, and grout within masonry specimens in compression.

3.2.2   Wall modeling and results

The refined FE models of the 3 m tall flexural walls were constructed by replicating the pattern of masonry units, mortar, and grout, where applicable, from the prism test FE models to form models of half the height of the full walls as built; these wall models are identified by the suffix "b". The top of each wall model (middle of the walls as built) was restrained against vertical movement and rotation, the bottom of each model was restrained against horizontal translation only (not rotation or vertical translation) at the location of the bottom pin support of the walls as built. Reinforcing bar truss elements were placed at the locations of the reinforcing bars within the walls as built and given the properties provided in Table 3.1. The reinforcing bar elements were perfectly bonded to surrounding materials. For the conventionally reinforced wall models, the CMU cells containing a reinforcing bar line element were filled with a 3-D grout macro-element.

Figure 3.13 illustrates the development of the models, where the cementitious materials are shown in shades of grey, the steel supports and reinforcing bars are shown in blue, and external support and applied load are shown in green and red, respectively. The fully meshed finite element model is also shown; the nominal element size was 30 mm.

Chapter 3 – Numerical Modeling
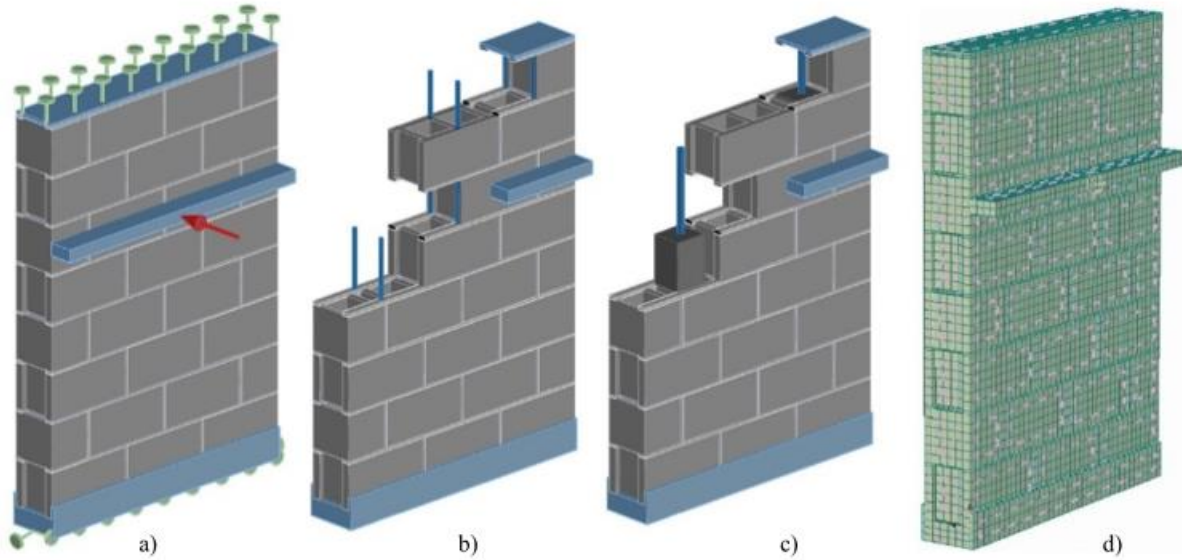
Figure 3.13: FE model of a reinforced masonry wall: a) Wall model support and load conditions; b) Hollow wall model with NSM reinforcement cutaway; c) Partially grouted conventionally reinforced wall model cutaway; and d) Meshed finite element model

When the strength of the CMUs is set to the "CMU base" value (see Table 3.4), a high level of ductility is observed in Wall M-CH3200b (partially grouted, conventional reinforcement) and Wall M-NH3200b (hollow, NSM reinforcement). As evident in Figure 3.14, these two wall configurations have similar strength; the marginally lower strength of the wall with NSM reinforcement is due to the effective moment arm of the reinforcing steel in M-NH3200b being approximately twice that of M-CH3200b, whereas M-CH3200b has twice the reinforcing steel in tension. Additionally, M-NH3200b exhibited twice the cracked flexural stiffness of M-CH3200b. This result, however, presupposes that the conventional and grooved blocks have the same axial compressive properties.

Chapter 3 – Numerical Modeling
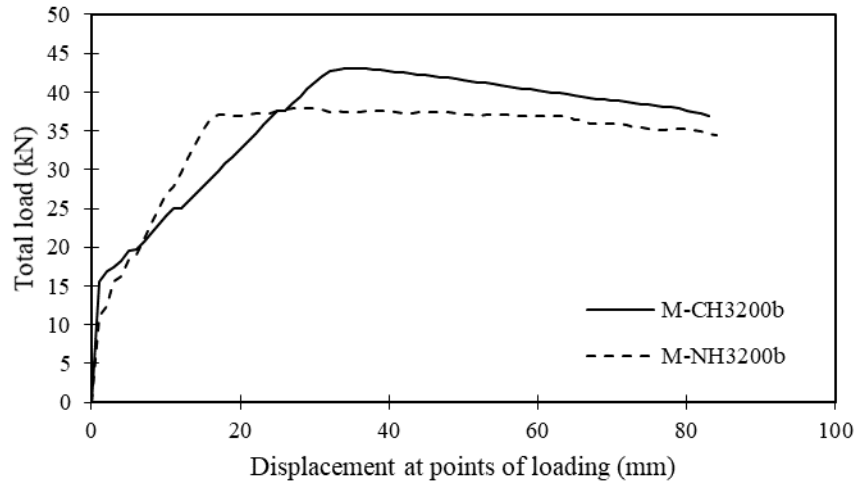
Figure 3.14: Load-displacement behaviours of FE models M-CH3200b and M-NH3200b

3.2.3   Parametric study (Adapted from Sparling, Palermo, and Hashemian 2018)

Four variations of the M-NH3200b model were analysed. Each variation considered the sensitivity of the model to altered material properties or loading conditions. The differences between each variation and the base M-NH3200b model are summarized in Table 3.5. The first variation was selected to determine the impact of the probable lower bound of effective CMU strength and stiffness that could result from using grooved blocks. The second and third variations were selected to assess the impact of marginal changes in reinforcement ratio or the mechanical properties of available reinforcing bars. The fourth variation was selected to increase the ratio of applied shear to applied moment and assess the wall's sensitivity to the shear stress.

Table 3.5: NH3200 FE model variations

Wall ID	Model variance
M-NH3200b I	Block strength reduced to 18MPa, E of 19 100 MPa (CMU – grooved block)
M-NH3200b II	Steel yield strength and stiffness increased by 20%
M-NH3200b III	Steel stiffness reduced by 20%
M-NH3200b IV	Distance from the lower support to the applied load reduced by 33%

The load-displacement analysis results for the wall models from Table 3.5 are shown in Figure 3.15. The changes in material properties did not result in a significant change in strength or ductility. Furthermore, the wall system seems to be significantly more sensitive to changes in the properties of the reinforcing steel

Chapter 3 – Numerical Modeling

than the CMUs. By reducing the span between the applied loads and the wall supports, it becomes apparent that the shear resistance of Wall M-NH3200b is significantly higher than that required under the experimental test conditions.
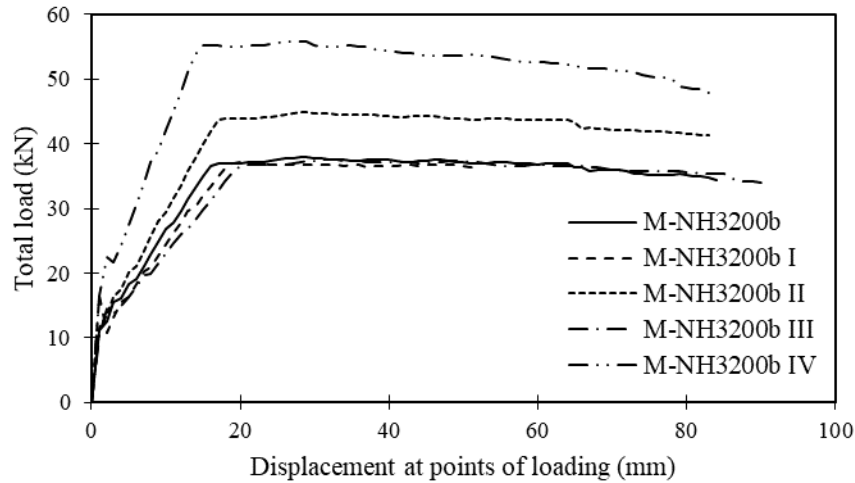
Figure 3.15: Load-displacement responses of FE models of NH3200 variations

3.2.4 Comparison with 3 m wall results

Only one of the wall FE models can be directly compared to the experimental results. Only Walls CH3200 (partially grouted) and NH3200 (hollow) with conventional and NSM steel reinforcement were modeled with the updated material properties from testing of the masonry prisms, mortar, and reinforcing steel. Both walls failed prematurely during testing (see Chapter 4 for discussion), and only the wall with NSM reinforcement exhibited a reliable response that allowed fair comparison with the FE model up to the onset of yielding. Figure 3.16 provides a comparison of the response of the FE model and experimental response of Wall NH3200 with NSM steel reinforcement. The FE model exhibits a higher initial flexural stiffness and cracking moment compared to the experimental response; however, in general there is agreement until the sudden failure of the experimental wall.

Chapter 3 – Numerical Modeling
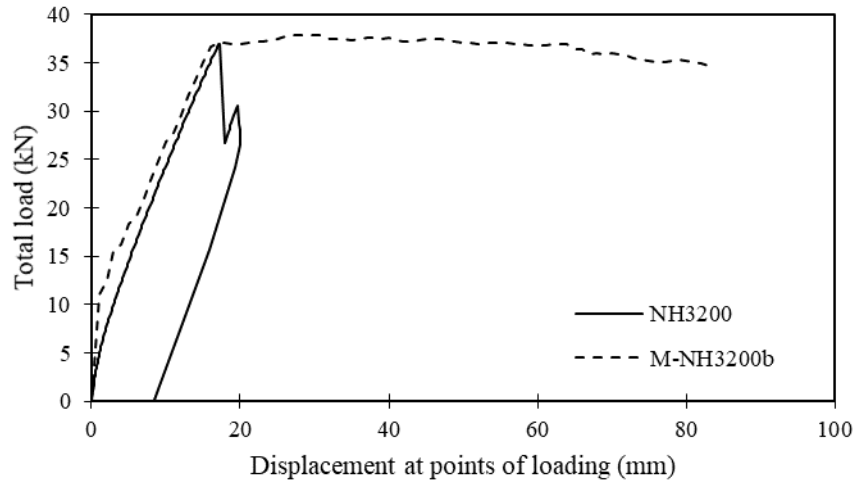
Figure 3.16: Response of hollow masonry wall with NSM steel reinforcement, FE model and experimental response

Other than the initial failure of Wall NH3200, which was due to a problem with the alignment of the top roller connection and lack of reinforcement in the top course of masonry, the FE models generally underestimated the ductility of the walls. None of the FE models exceeded a displacement of 90 mm before a loss of convergence in the analysis (causing it to halt), however, the grouted RM test walls displaced beyond 400 mm (see Chapter 4) prior to failure.

3.3   Discussion (Adapted from Sparling, Palermo, and Hashemian 2018)

A micro-modelling approach is very appealing as a strategy for FE analysis of masonry assemblies; however, it introduces challenges such as ensuring the interaction between each component material is representative and simulates the macroscopic behaviour of the masonry assembly. In addition, the in-situ material properties of the mortar and grout are difficult to establish due to the non-porous moulds used for casting samples for standard material testing. Further refinement of the FE models is required to accurately capture the interaction between the masonry grout and CMUs, particularly for the post-yielding response of reinforced walls. The bond behaviour of the reinforcing steel within the grooves will also require further detailed analysis, although the perfect bond assumption appears to have resulted in acceptable response.

In summary, based on the analyses performed, the load-displacement behaviour (specifically ductility) of the masonry walls with NSM reinforcement is not strongly affected even by large variations in the

properties of the CMUs. Given that the walls studied are relatively lightly reinforced, the reinforcing steel governs the flexural behaviour. However, where axial loads are introduced to walls tested in flexure, the axial and shear strengths of the CMUs, mortar, and grout may have a larger impact on overall behaviour as well as modes of failure.

3.4   Future Work

The main challenge in applying this method of FE analysis for RM walls arises due to the increasing complexity of models as they grow in size. The nominal size of individual finite elements must remain small to maintain an aspect ratio of less than 2:1 and must be assembled in a way that preserves compatibility at the points of contact between the regions being assembled. Hardware and software limitations made it impractical for the fully grouted walls to be analyzed using the detailed modeling method described in Section 3.2. Modeling even hollow RM walls with a slenderness ratio approaching that of the walls described in Chapter 5 of this dissertation would be similarly challenging. A different simplified modelling approach may therefore be desirable despite the drawbacks. For slender RM walls, the use of a simplified modelling approach may be further justified by considering that instability failures are often caused by secondary moment effects within the elastic response range. Accurately modelling the elastic response of a structural member is generally simpler than modelling the plastic response.

As discussed in Chapter 2, 1-dimensional (beam or beam-column type) elements can be effectively used, within FE models that account for large displacement, to predict the response of slender RM walls. For wall sections for which the axial load and moment-curvature responses, as well as the axial load-moment interaction, are known, these properties can be assigned to the beam elements. Properly constructed models will then simulate the axial and out-of-plane response of the wall; however, the response of wall elements must be known prior to using the model - as was the case for the FE study by da Porto, Mosele, and Modena (2011). This makes it difficult to apply the technique broadly unless it is integrated with another method for determining the flexural response properties of RM sections. A fibre model can also be used to approximate the section properties (Alonso et al. 2021).

Chapter 3 – Numerical Modeling

Alternatively, a 2-dimensional modeling approach could be considered, wherein the cross section is discretized along the vertical and out-of-plane directions, but not in-plane. This would reduce the complexity of the model compared to the 3-dimensional analysis, however constraints on the aspect ratio of the elements could still make the analysis of slender walls very complex. It would also maintain many of the drawbacks of a 1-dimensional analysis, including lacking a representation of the variations in behaviour of the wall along its plane, and challenges related to representing the behaviour of the thin concrete webs of CMUs within the modeled section.

4   Preliminary Testing: 3 m Tall Walls

The experimental testing program for this research began with out-of-plane testing of single-storey Reinforced Masonry (RM) walls. The purpose of this series of tests was to compare the behaviour of conventional RM walls to walls with NSM steel reinforcement. To accomplish this, the masonry walls and the testing frame had to be designed and constructed, and testing protocols developed. The experimental approach followed in this phase was generally based on a previous work reported by Abboud, Hamid, and Harris (1996), and adapted to the specific requirements of the walls being tested and the available materials and equipment.

As this was the first series of tests performed on full-scale structural members in the Bergeron Centre for Engineering Excellence's (BCEE) high bay laboratory, several delays and other problems were encountered. These included delays in the manufacturing and delivery of the testing frame due to the procurement process that had to be followed, and delays caused by wait times for necessary training for operating the various apparatus needed for construction and testing. Although a few problems arose during testing, these did not detract from the overall success of the testing series at characterising the load-displacement and moment-curvature response of the RM walls.

4.1   Test Frame Development

As these tests on 3 m tall masonry walls were the first full-scale experiments on structural members performed in the high bay laboratory of the BCEE, the design of the testing frame considered possible future testing needs in addition to the needs of this testing series. To save on materials and cost, elements of the wall testing frame were re-purposed to construct a vertical loading frame for prism testing, and each component included additional perforations to facilitate reconfiguration to suit the needs of future tests.

To meet the needs of this first testing series, rigid frames were needed that would accommodate the loading conditions, shown in Figure 4.1, for axial loading of 1 m tall masonry prisms, and out-of-plane loading of 3 m tall RM walls.
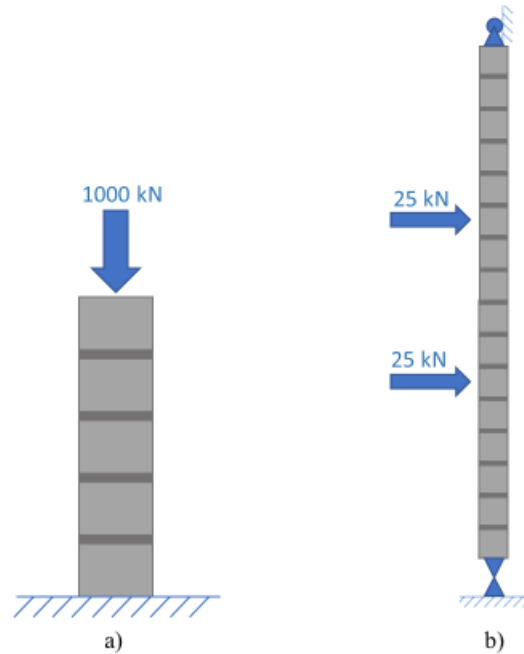
Figure 4.1: Conceptual loading conditions: a) masonry prism in uniaxial compression, and b) RM wall in 4-point out-of-plane loading

4.1.1 Prism testing frame

The self-reacting loading frame for the prism tests was designed to accommodate one of the laboratory's large vertical hydraulic actuators (1 400 kN capacity). The main vertical columns for this set-up were produced from W310x107 steel sections; these were selected based on their use in other structural test frames at the University of Ottawa and provided more than adequate axial load capacity. These columns were perforated symmetrically on both flanges with a spacing of 75 mm to accommodate connection using 1" (25.4 mm diameter) structural bolts – opting to use US customary sizing of bolts for improved availability of materials and increments of multiples of 25 mm for the spacing of perforations for compatibility with SI and US customary measurements. The same structural steel section type (W310x107) was used in the design of the transfer beams, and bolted connections between the transfer beams and columns were designed such that the frame had a factored ultimate strength greater than the load capacity

Chapter 4 – Preliminary Testing: 3 m Tall Walls

of the large actuator. The crosshead and base plate of the set-up were constructed from a larger W360x216 steel section, similar to those used in the design of other brackets, donated to the high bay laboratory. Figure 4.2 a) provides an annotated schematic of the loading frame for uniaxial testing of the masonry prisms. The support columns were anchored into the high bay's strong floor to prevent any movement during testing.
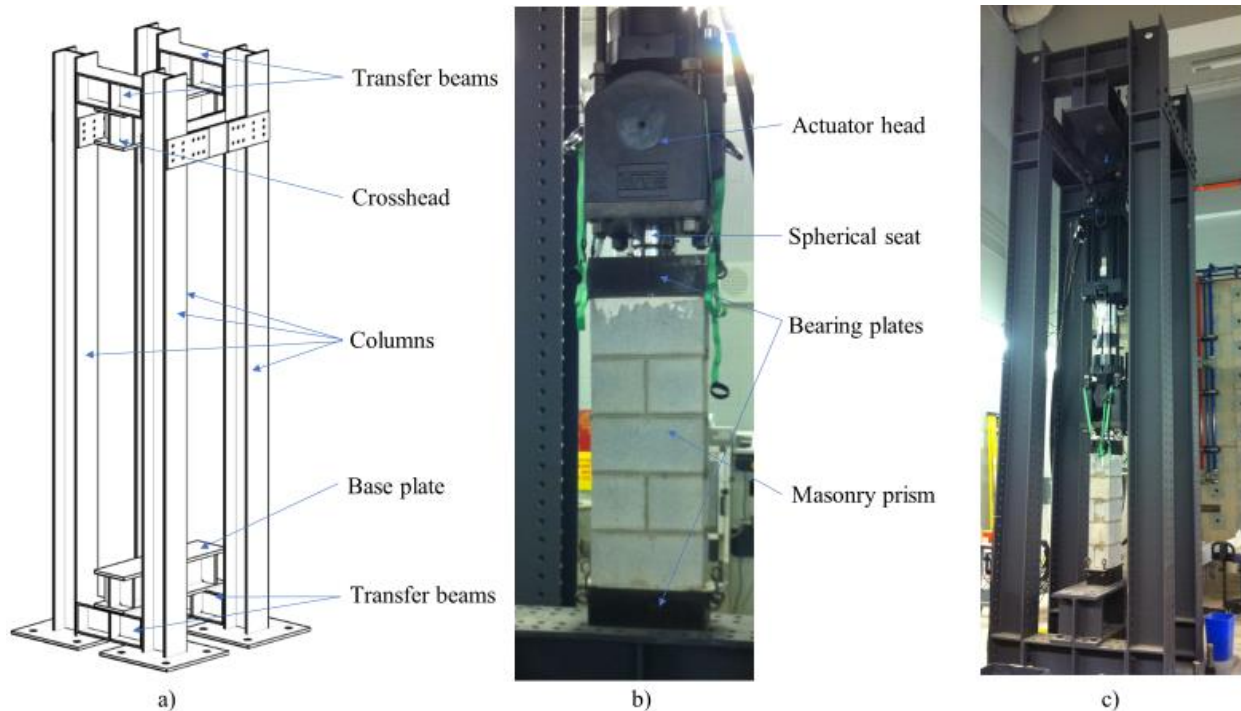
Figure 4.2: Axial loading frame: a) annotated drawing of bare frame; b) bearing plates for prism tests; and c) prism test in progress

Bearing plates and a spherical seat were also designed and manufactured to conform to the requirements of CSA S304 (CSA Group 2019a) for testing of masonry prisms. This ensured smooth and flat bearing surfaces were provided during the tests and that the load was applied uniformly over the surface of the prisms, as shown in Figure 4.2 b). The prism testing frame was disassembled after the prism tests as the columns were used to construct the wall testing frame.

4.1.2   Wall testing frame (adapted from Sparling, Palermo, and Hashemian 2021)

Various test methods for masonry walls subjected to out-of-plane flexure are described in the literature. These include vertical test set-ups designed exclusively for the application of eccentric axial loading without additional out-of-plane loading (Yokel, Mathey, and Dikkers 1970; Hatzinikolas, Longworth, and

Warwaruk 1978; Liu and Hu 2007), and the application of out-of-plane loading through airbags (ACI-SEASC Task Committee on Slender Walls 1982; Dawe and Aridru 1992; and Babaeidarabad, De Caso, and Nanni 2014) or an actuator (e.g., Abboud, Hamid, and Harris 1996; Bean Popehn, Schultz, and Drake 2007), or by testing walls in a horizontal orientation (e.g., Galal and Sasanian 2010 and Al Jaberi et al. 2018b). A vertical test frame with idealized support conditions was selected, and designed based on the set-up described by Abboud, Hamid, and Harris (1996). This set-up was selected to minimize the risk of damaging the walls, which could arise while rotating them into a horizontal position, and to effectively simulate the behaviour of walls under service conditions.

Wherever possible, elements from the prism testing frame were reused for the construction of the wall testing frame. This frame consisted of two main support columns (repurposed from the prism testing frame), anchored at the base into the laboratory strong floor, and tied back to the strong wall near the position of the top support for the test walls as shown in Figure 4.3. The pin and roller support connections for the walls were fastened to support beams running between columns. The support beams were sized to fulfill the needs of the out-of-plane tests on 3 m tall walls but were also checked to ensure they could be used for future wall tests that would include axial load (although plans for that testing were not yet crystalized). The pin and roller support connection assemblies were constructed from steel plates and high-capacity pillow-block bearings, as shown in Figure 4.4, which allowed the 32 mm-diameter solid steel support axles to rotate freely during testing. The connections to the top and bottom of the walls were achieved using capping channels that were fitted in place using plaster grout to avoid stress concentrations. These connection assemblies resulted in highly idealized pin and roller supports, and allowed free rotation of the bottom support, and free rotation and vertical displacement of the top support.

Chapter 4 – Preliminary Testing: 3 m Tall Walls
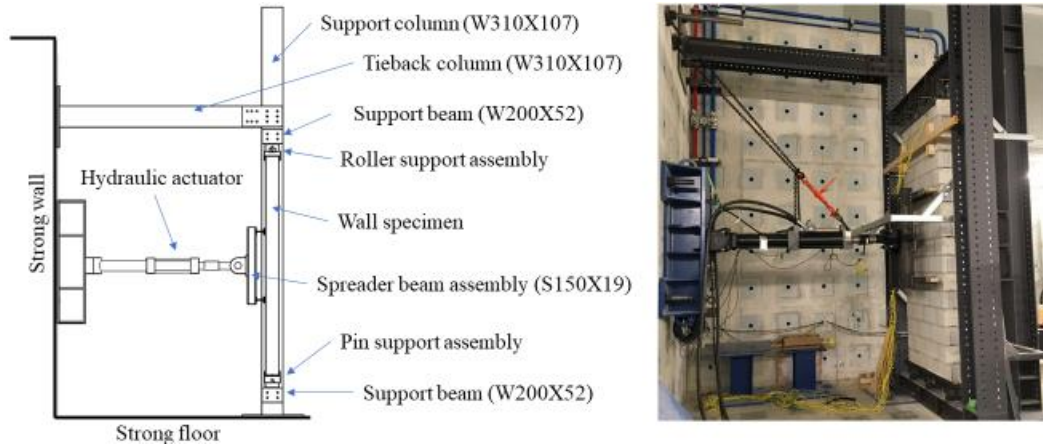
Figure 4.3: Test frame for 4-point out-of-plane flexural loading (Sparling, Palermo, and Hashemian, 2021)
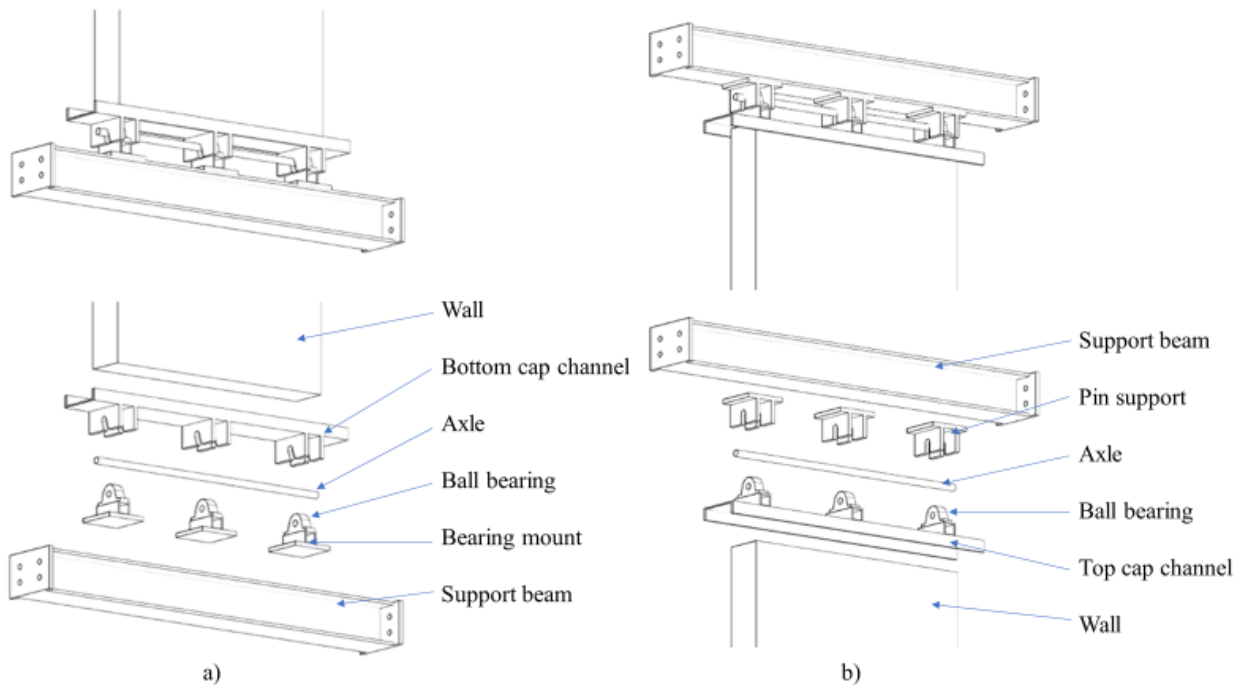
Figure 4.4: Detail of support connections using pillow-block bearings: a) Bottom support assembly and b) Top support assembly

Out-of-plane loads were applied using a hydraulic actuator, mounted to the laboratory strong wall, which was maintained in a centered horizontal orientation using chains as shown in Figure 4.3. The load from the spherically seated actuator head was distributed to two horizontal line loads using a simple frame as shown in Figure 4.5. The line loads were applied to the walls through 20 mm-diameter steel rollers, onto steel plates mounted directly to the wall surface with a structural adhesive. The vertical spacing between the centroid of the support rollers and the nearest line load was 1200 mm, whereas the vertical spacing between the two line loads was 1000 mm.

Chapter 4 – Preliminary Testing: 3 m Tall Walls
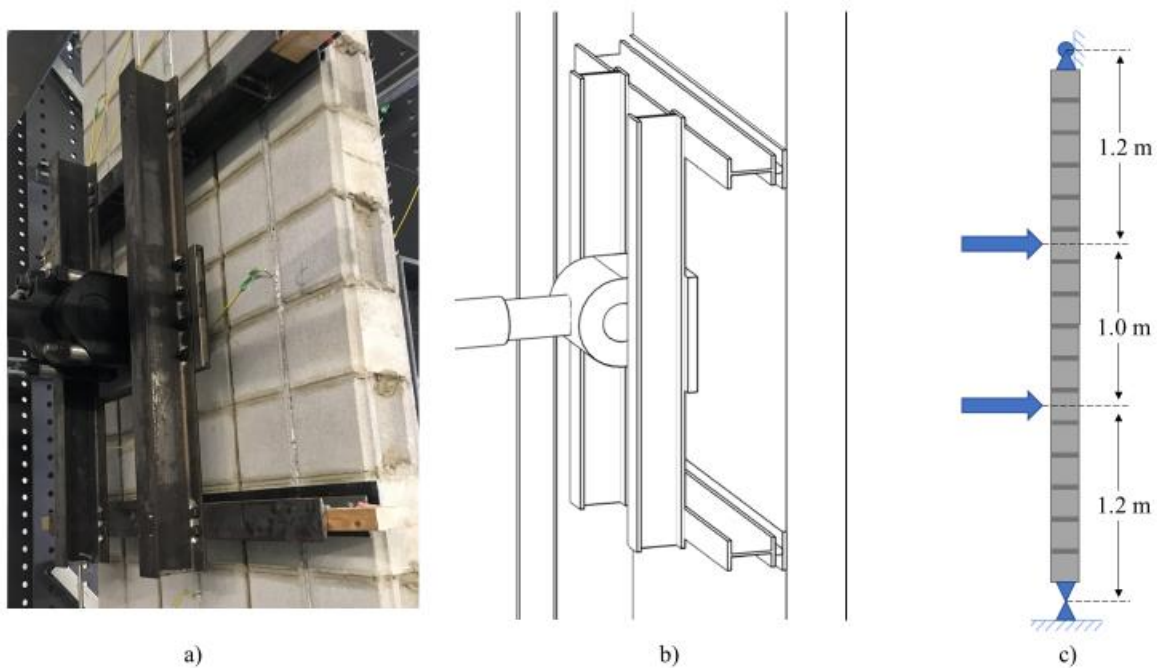
Figure 4.5: Wall loading configuration: a) photograph; b) computer aided rendering; and c) idealized conceptual illustration

4.2   Wall Construction (adapted from Sparling, Palermo, and Hashemian 2021)

In this part of the study, four RM wall cross-sections were selected with the same gross total cross-sectional area of reinforcement of 600 mm^2, but with different reinforcement layouts and grouting. These are the same cross sections as those presented in Chapter 3. For the walls with NSM reinforcement, half of the reinforcing bars were placed near the compression face, thus their gross tension reinforcement ratio was lower. These walls were constructed using specially fabricated grooved units, known as Surface-Reinforced Concrete Masonry Units (SRCMU). When placed in a running bond (50% overlap of successive courses) they form walls with continuous vertical grooves (spaced at 200 mm on centre), as illustrated in Figure 4.6, into which the reinforcing bars were placed using the NSM technique.

Chapter 4 – Preliminary Testing: 3 m Tall Walls
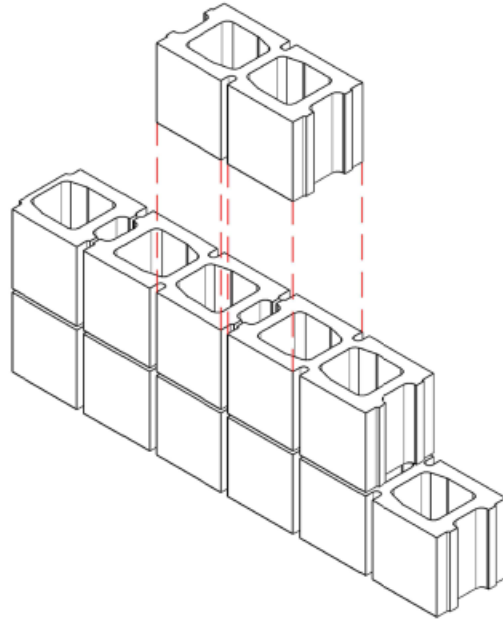
Figure 4.6: Alignment of SRCMUs in running bond pattern resulting in continuous vertical grooves (Sparling, Palermo, and Hashemian 2019)

A summary of the features of each cross section, along with a conceptual view, is provided in Table 2 and Table 3 of Chapter 3. The designation of each wall indicates whether the wall is reinforced conventionally (C) or with NSM steel reinforcement (N), whether it is grouted (G) or hollow (H), as well as the height of the wall (in mm). Wall CG3200 was reinforced with six, 10M, steel reinforcing bars located centrally within each grouted cell of the wall; NG3200 and NH3200 were also reinforced with six 10M bars, however three bars each were distributed near the tension and compression faces, embedded at a depth of 20 mm using the NSM technique. CH3200 was reinforced with two, 20M, bars placed in the second and fifth cell of the wall, respectively. This configuration is representative of a continuous wall with bars placed at 600mm on centre. Walls CG3200 and NG3200 were fully grouted, CH3200 was grouted only in the reinforced cells, and NH3200 remained hollow. Each wall was constructed from 190 mm CMUs to a length of 1.2 m and height of 3.2 m, consisting of 16 alternating courses of three stretcher units, and courses composed of two stretcher units and two half-units cut from stretcher units. The wall height and thickness are representative of typical single-storey wall construction and the 1.2 m length of the walls allows for regular placement of reinforcing bars at various spacing intervals. The resulting slenderness ratio (*h/t*) for all four walls was 16.8.

Chapter 4 – Preliminary Testing: 3 m Tall Walls

The top course of Wall NH3200 failed prematurely during testing; this course was removed, and the resulting 3.0 m tall wall is referred to herein as Wall NH3000 (slenderness ratio of 15.8).

The four walls were constructed by a professional mason. This was followed by reinforcement and grouting, where applicable, of the walls and prisms by pouring grout from the top into the open cells (high-lift grouting). Grout was mixed in volume-proportioned batches and poured in from the top of the walls in a single lift. Clean-out holes at the base of the walls were checked to ensure the grout reached the bottom of the cells.

The vertical grooves on the surface of Walls NG3200 and NH3200 were cleared of mortar during construction. The NSM reinforcing bars were installed into the grooves by first placing a bead of epoxy at the bottom of a groove, then pressing the bar into the epoxy, and adding a topping layer. The epoxy was recessed by 10 mm to optimize material usage, and to demonstrate that a topping layer of mortar could be added, if desired, as an aesthetic consideration. Photographs from the construction process are available in Appendix A.

4.3   Material Testing (adapted from Sparling, Palermo, and Hashemian 2021)

The masonry units used in this testing series were 15 MPa (nominal strength) stretcher hollow CMUs cast by a commercial block manufacturer. The blocks were 190 mm units with "pear-shaped" cells as shown in Figure 4.7 a), with outer dimensions of 190 mm x 190 mm x 390 mm. The hollow CMUs used in the construction of the SRCMU walls were cast to produce units with vertical surface grooves (20 mm wide and 30 mm deep) to accept the NSM reinforcement. They were cast using the same manufacturing equipment and concrete mix as the conventional CMUs using a modified mold. The mold was customized from a standard CMU mold by the block manufacturer to produce the desired grooves shown in Figure 4.7 b). The half-units required to complete the alternate running-bond courses were produced by cutting stretcher units through the central web, resulting in 190 mm x 190 mm x 190 mm blocks.

Chapter 4 – Preliminary Testing: 3 m Tall Walls
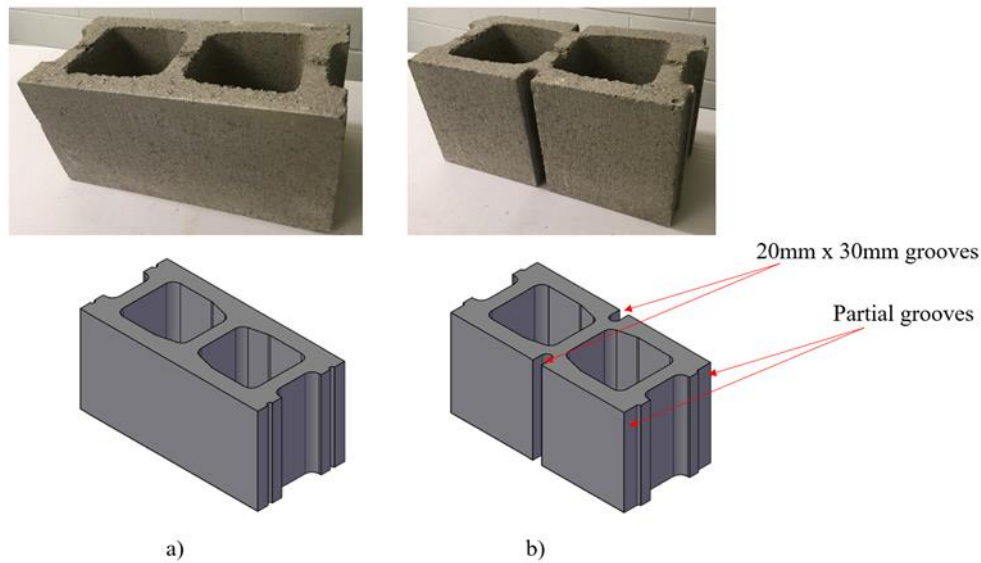
Figure 4.7: Concrete masonry units: a) conventional unit with "pear shaped" cells, and b) SRCMU with surface grooves for NSM reinforcement (Sparling, Palermo, and Hashemian, 2021)

The mortar used in the construction of the masonry walls was produced from a performance-specified pre-blended Type S bagged mortar mix to which water was added by the mason until the desired workability was reached. Mortar samples consisting of 50 mm x 50 mm x 50 mm cubes were prepared for axial compressive testing in accordance with CSA A179 (CSA Group 2019b). These samples were tested in uniaxial compression using a constant loading rate of 0.25 MPa/sec; the resulting average mortar cube strength following testing of the walls (24 months age) was 15.5 MPa.

The grout was proportioned by volume to meet the requirements of CSA A179 (CSA Group 2019a) for coarse grout with a Portland lime cement:pea gravel:sand ratio of 1:2:3 by volume. The grout was mixed in batches of 0.2 m^3 in a vertical axis stationary concrete mixer, and water was added until the desired slump of 275 mm was achieved. Samples of each batch of grout were taken to cast 100 mm x 200 mm cylinders for axial compressive testing in accordance with CSA A179 (CSA Group 2019b). These samples were tested in uniaxial compression using a constant loading rate of 0.25 MPa/sec; the resulting average grout cylinder strength following testing of the walls (12 months age) was 29.0 MPa.

The epoxy used for mounting the NSM reinforcement was a low-sag sanded structural epoxy with a manufacturer-specified 7-day tensile strength of 24.8 MPa and modulus of elasticity of 4 500 MPa. Reinforcing steel bar coupons were tested in direct tension following the provisions of ASTM E8. The average mechanical properties of each bar type are provided in Table 4.1.

Table 4.1: Reinforcing bar properties from ASTM E8 testing (reported by Sparling et al. 2018)

Physical and mechanical properties	400W 10M rebar	400W 20M rebar
Nominal cross-sectional area	100 mm^2	300 mm^2
Elastic modulus	172 000 MPa	182 000 MPa
Yield strength	432 MPa	440 MPa
Strain hardening strain	3.0 %	2.2 %
Ultimate strength	567 MPa	592 MPa
Strain at ultimate strength	15 %	15 %

A series of five-course masonry prisms were constructed in pseudo running bond, consisting of subsequent courses of a single stretcher unit and courses composed of two half-units, as shown in Figure 4.8, concurrently with the construction of the walls. Only face-shell mortar bedding was applied. Ten prisms were constructed for each type of masonry unit (conventional and SRCMU), five of which were filled with grout. The prisms were tested under axial compression following the provisions of CSA S304-14 (CSA Group 2019a). The modulus of elasticity and compressive strength for each type of prism are listed in Table 4.2. For the grouted prisms, the gross cross-sectional area was used to calculate the modulus of elasticity and strength, whereas for the hollow prisms, the net mortar bedded area (face-shell only, and accounting for the reduced area due to the presence of surface grooves, where applicable) was used.

Figure 4.8: Masonry prisms made from conventional units during construction

Chapter 4 – Preliminary Testing: 3 m Tall Walls

Block type	Grouted (yes/no)	E [MPa]	Coefficient of variation	f'_m [MPa]	Coefficient of variation
Conventional	Yes	9 800[a]	5.6%	8.7[b]	2.5%
Grooved	Yes	7 700	6.1%	6.1	7.3%
Conventional	No	18 900	4.2%	23.1	3.3%
Grooved	No	17 500	12.9%	13.0	5.6%
[a] Average of 3 prisms					
[b] Average of 4 prisms					

4.4   Wall Testing

The test walls were constructed in November 2016, however delays arising from design, purchasing, and delivery of the testing frame, as well as the scheduling of necessary training resulted in testing of the walls between July and September 2018. This section outlines the testing procedure, including anomalies that occurred during testing, as well as the instrumentation that was used.

4.4.1   Instrumentation and procedure (adapted from Sparling, Palermo, and Hashemian 2021)

Displacements, reinforcing bar strains, and the applied load were monitored simultaneously at a frequency of 10 Hz for the duration of the tests. The strains in the reinforcing bars were captured by Electronic Strain Gauges (ESG) that were mounted to the reinforcing bars. For the walls with NSM reinforcement, strain gauges were located to capture strains along the height of the wall on both the tension and compression side of the wall, at various distances from the nearest mortar joint. The bars within the conventionally reinforced walls were fitted with gauges along the height of the walls, 45 mm from the nearest mortar joint.

The strain gauge layout for each wall is provided in Figure 4.9. For Walls CG3200 and CH3200, strain gauges were mounted to the reinforcing bars along the height of the walls, 45 mm from the nearest mortar bed joint. For Walls NG3200 and NH3200, with NSM reinforcement, strain gauges were installed on the reinforcing bars near the tension and compression faces. The distance of each strain gauge from the nearest mortar bed joint is listed in Table 4.3.

Chapter 4 – Preliminary Testing: 3 m Tall Walls
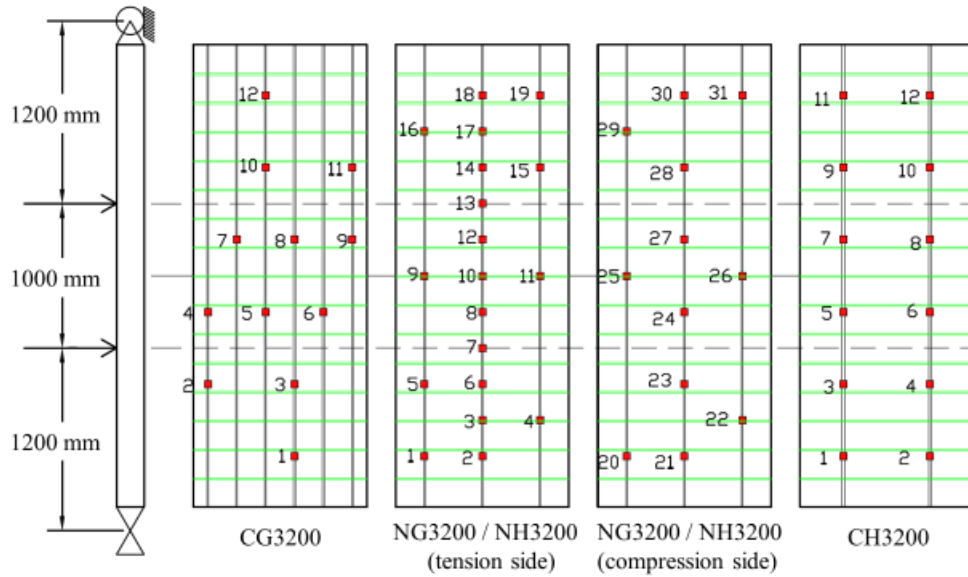
Figure 4.9: Strain gauge location for walls CG3200, NG3200, CH3200, and NH3200

Table 4.3: Strain gauge distance to nearest bed-joint - NSM reinforced walls NG3200, NH3200, and NH3000

Strain gauge ID	Distance to nearest bed-joint (mm)	Compression or Tension face (C or T)
3,4,9,10,11,16,17	0	T
1,2,5,6,8,12,14,15,18,19	45	T
7,13	90	T
22,25,26,29	0	C
20,21,23,24,27,28,30,31	45	C

Cable differential transducers recorded the out-of-plane displacement of the tensile face of the wall along two lines along the height of the wall. Displacements were monitored at 600 mm, 1200 mm, 1700 mm, 2200 mm, and 2800 mm from the centroid of the bottom support, as well as at the supports as illustrated in Figure 4.10. The applied load was measured by the load cell of the actuator.

Chapter 4 – Preliminary Testing: 3 m Tall Walls
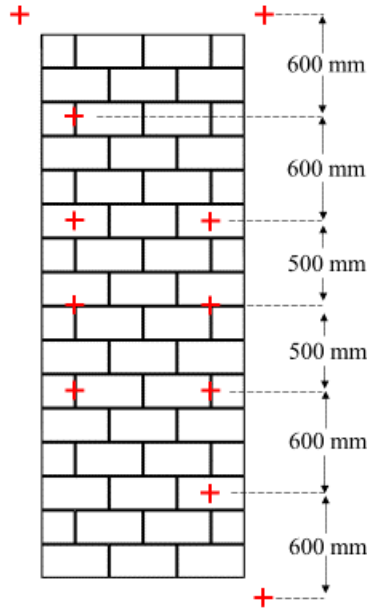
Figure 4.10: Location of transducers recording out-of-plane displacement for 3m tall walls

Each wall was loaded monotonically at a rate of 1 mm/min until the estimated global yield point of the wall (inflection point in the load-displacement response), such that the elastic displacement portion of the test occurred over approximately 30 minutes. This rate was selected to allow for close visual monitoring of the elastic behaviour of the wall. Once the estimated yield point was exceeded, the loading rate was increased to 2 mm/min until a drop of at least 20% in the lateral resisting load was observed. This increased loading rate for the plastic portion of the test was selected to reduce the total duration such that testing could be completed in one day. Deviation from this loading protocol was necessary during testing of certain walls due to various anomalous testing conditions, as discussed in Section 4.2.2.

4.4.2   Problems during testing (adapted from Sparling, Palermo, and Hashemian 2021)

The initial design of the top roller support accommodated a maximum vertical travel of 50 mm. This amount of vertical travel was sufficient to accommodate the out-of-plane displacement that was anticipated based on the FE model analysis completed prior to testing. The out-of-plane displacement of Wall CG3200, however, exceeded the expected displacement by 300%, resulting in the vertical travel limit of the top roller support being reached during testing. To address this, the load was removed, and the top roller support assembly was lowered to increase the maximum permissible vertical travel. Thereafter, the loading was

Chapter 4 – Preliminary Testing: 3 m Tall Walls

reapplied. These steps were repeated three additional times prior to reaching the final failure displacement of the wall (rupture of reinforcing bars). Strain and displacement data collected from each subsequent loading cycle were added end-to-end to the previous cycle to develop the full response sequence. Each loading cycle was assumed to initiate when the total out-of-plane load exceeded 2 kN, and terminate, on the unloading branch, when the load reached 2 kN. After the completion of testing CG3200, the top roller support was modified to accommodate 100 mm of vertical travel for subsequent tests. This allowed the remaining wall tests to proceed uninterrupted. The original and modified roller support assemblies are shown in Figure 4.11 a) and b), respectively.
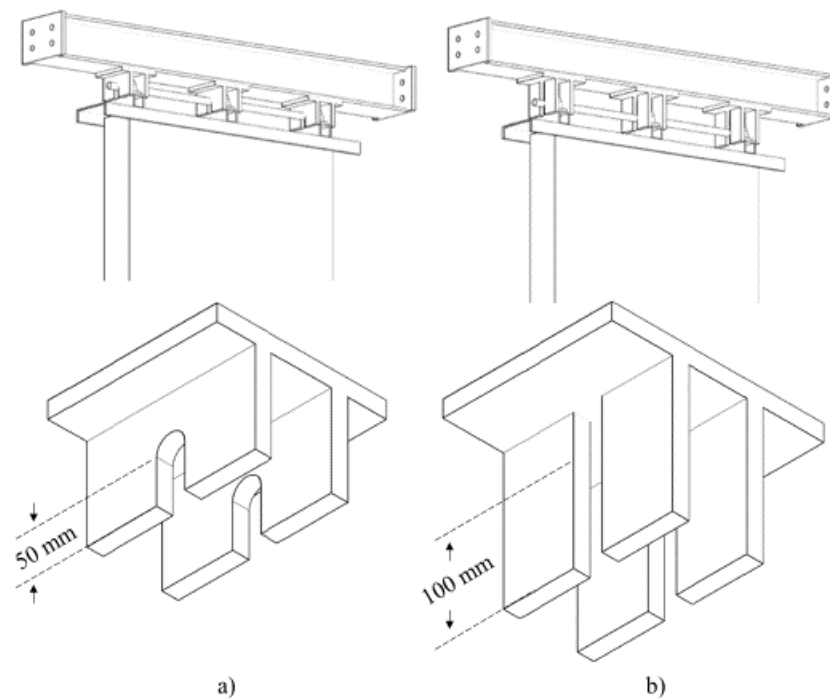
Figure 4.11: Roller support forks: a) original support for allowing 50 mm of vertical displacement and b) modified support for allowing 100 mm of vertical displacement

Wall CH3200 exhibited asymmetric curvature along its height, and low strength and flexural stiffness throughout testing. During the test, a crack developed in the top course as shown in Figure 4.12 a), which resulted in relative movement of the wall with respect to the top support roller. Following the test, the face-shells of the wall covering the grouted cells were removed. This examination revealed that one of the reinforcing bars had not been fully encased in grout during the reinforcing process, despite the fact that some grout had reached the bottom course, as shown in Figure 4.12 b); however, the reinforcing bars were

Chapter 4 – Preliminary Testing: 3 m Tall Walls

fully embedded in the upper 8 courses. Data collected from strain gauges and displacement transducers mounted to the upper portion of the wall (where both reinforcing bars were fully grouted in place) were used for comparison with the behaviour of the other 3 m tall walls.
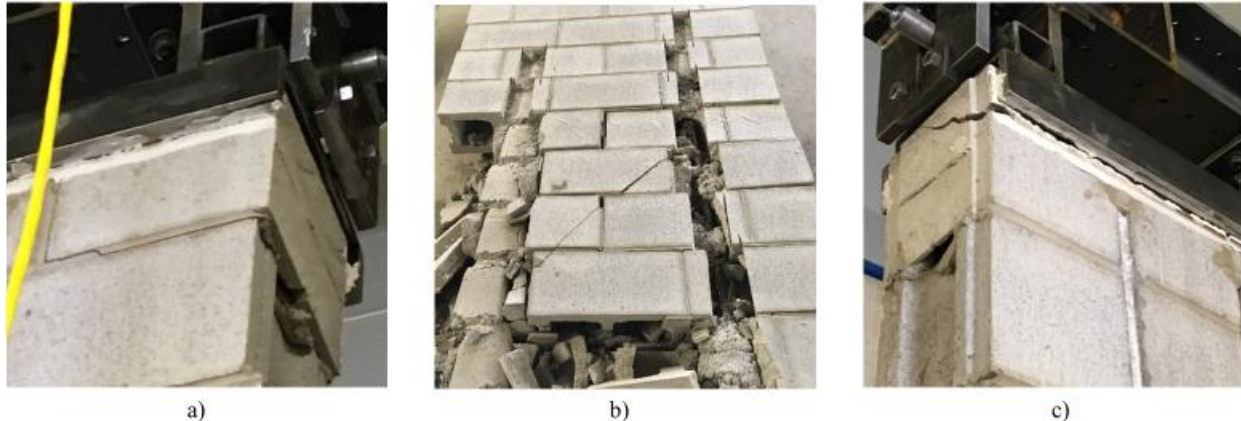
Figure 4.12: Anomalies during testing: a) crack in top course of Wall CH3200; b) incomplete grouting of reinforced cells in Wall CH3200; and c) crack in top course of Wall NH3200

Upon initial loading of Wall NH3200, the CMUs in the top course cracked prior to yielding of the tension reinforcement, as shown in Figure 4.12 c). The probable cause of this damage is the misalignment of the top capping channel (connected to the top support roller-axle) and the top supporting fork, resulting in flexural/shear stress concentration at one end of the wall. The strain gauge data revealed that the reinforcing bars did not exceed their yield strain prior to this crack, and no visible damage was apparent outside the top course of SRCMUs. Testing of the wall resumed after the NSM reinforcing bars were cut flush with the second course from the top, while the top course was removed. Testing on the resulting 2.99 m tall wall (referred to as Wall NH3000 herein) was conducted using the same test set-up and procedure as the other walls, while lowering the actuator, load distribution frame, and surface displacement transducers to apply the loading and measure out-of-plane displacements symmetrically.

4.5   Response

This section presents the primary response of the 3 m tall RM walls subjected to four point out-of-plane loading as measured by the available instruments during the tests. This includes the load-displacement

Chapter 4 – Preliminary Testing: 3 m Tall Walls

response and displaced shape, cracking response, and reinforcing bar strain response. Further analysis and discussion of these data are presented in Chapter 6 – Analysis.

4.5.1   Load-displacement responses (adapted from Sparling, Palermo, and Hashemian 2021)

The full load-midspan displacement response of the five wall tests are illustrated in Figure 4.13; the response for the first 100 mm of displacement is provided in Figure 4.14. Note that Wall CH3200 failed prematurely due to incomplete bonding of the reinforcement in the lower portion of the wall (since only one of the two reinforcing bars was properly anchored, the wall developed approximately half of its expected strength and flexural stiffness), and the top course of wall NH3200 failed during initial loading and prior to yielding of the main reinforcing bars. With the exception of wall CH3200, and the initial loading of wall NH3200, the walls exhibited similar strength and significant displacement capacities.
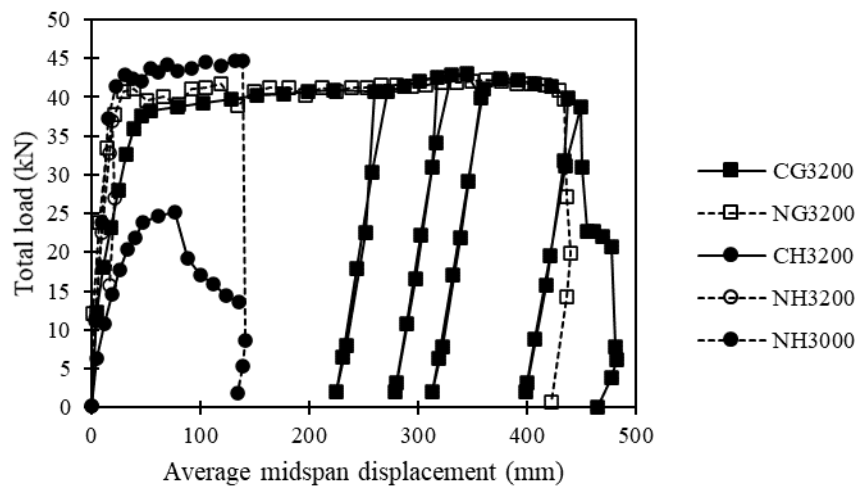
Figure 4.13: Load-midspan displacement response of 3 m tall RM walls
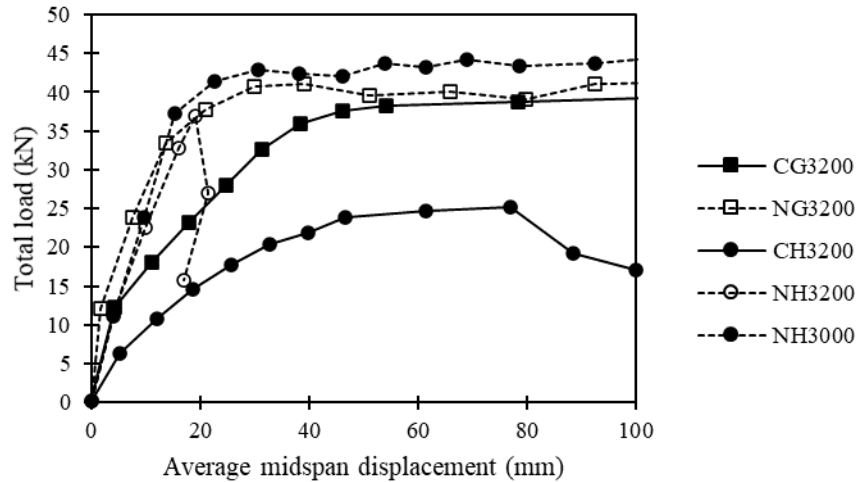
Figure 4.14: First 100 mm of the load-midspan displacement response of 3 m tall RM walls

Table 4.4 summarizes salient points of the load-midspan displacement response for each wall. First yield was based on the strain gauge data and corresponded to the point at which the yield strain of a reinforcing bar was first exceeded. [Note: the reinforcement yield strain was not exceeded in wall CH3200, nor upon initial loading of wall NH3200] The global yield point was defined as the displacement corresponding to the point of intersection of a secant through the point at 75% of the nominal (peak) load with a horizontal line drawn from the nominal load point (Priestley and Park 1987). The nominal load was defined as the maximum recorded load during testing, while the load at ultimate displacement corresponded to a 20% drop in load from the nominal load. The global yield loads of walls CG3200, NG3200, NH3200, and NH3000 were comparable, with the corresponding displacement of wall NG3200, NH3200, and NH3000 approximately half that of the conventionally reinforced wall CG3200. The ultimate displacement of the fully grouted walls exceeded that of the hollow walls.

Chapter 4 – Preliminary Testing: 3 m Tall Walls

Wall ID	First Yield		Global Yield		Nominal Load		Ultimate Displacement		M_r
	P [kN]	Δ_{max} [mm]	P [kN]	Δ_{max} [mm]	P [kN]	Δ_{max} [mm]	P [kN]	Δ_{max} [mm]	[kNm]
CG3200	34.7	35.1	36.8	36.0	43.2	337.9	38.8	448.5	25.9
NG3200	40.5	18.3	38.4	16.9	42.3	47.8	39.8	433.2	25.4
CH3200	-	-	21.7	38.7	25.4	72.8	20.5	86.4	15.2
NH3200	-	-	34.9	17.5	37.0	18.9	36.9	19.0	22.2
NH3000	42.1	18.0	42.7	18.3	44.8	129.5	44.7	139.3	24.6

4.5.2 Displacement profile

Typical displacement profiles of the walls at 20 kN of lateral load (approximately 50% of nominal load) and at the global yield point are illustrated in Figure 4.15 a) and b), respectively. At 20 kN of load, greater displacements were recorded in the conventionally reinforced Walls CG3200 and CH3200 compared to Walls NG3200 and NH3200 with NSM reinforcement; however, among walls with similar reinforcement, the fully grouted walls exhibited less displacement than the hollow walls. As the walls were partially cracked when 20 kN of load was applied, the flexural stiffness of the walls was affected both by the grout and by the placement of the reinforcement. The displacement profile at the global yield point for walls CG3200, NG3200, CH3200, and NH3200, shown in Figure 4.15 b), illustrates their symmetric curvature concentrated at the mid-span; however, walls NG3200 and NH3200, with NSM reinforcement, exhibit reduced displacements compared to Wall CG3200 and CH3200, with conventional reinforcement. At the global yield point, the wall sections are fully cracked, and the flexural stiffness is governed by the reinforcement; little or no stiffening influence from the grout is observed.
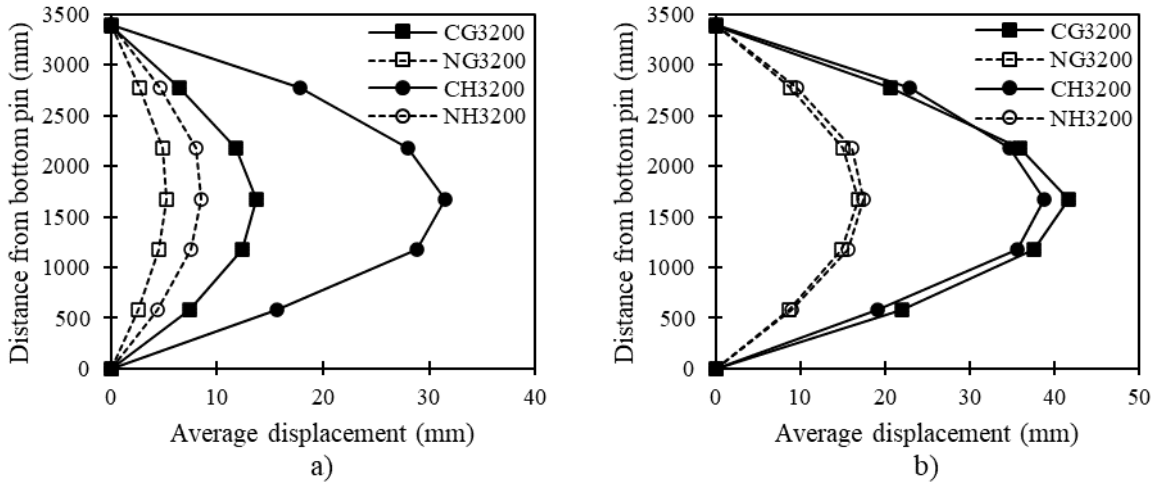
Figure 4.15: Wall displacement profile: a) at 20kN load; and b) at global yielding

Beyond the yield point, additional curvature in the walls was even more concentrated near the midspan as the reinforcing bars in that area yielded. The displacement profile of the Walls CG3200, NG3200, CH3200, and NH3000 at their ultimate displacement is shown in Figure 4.16.
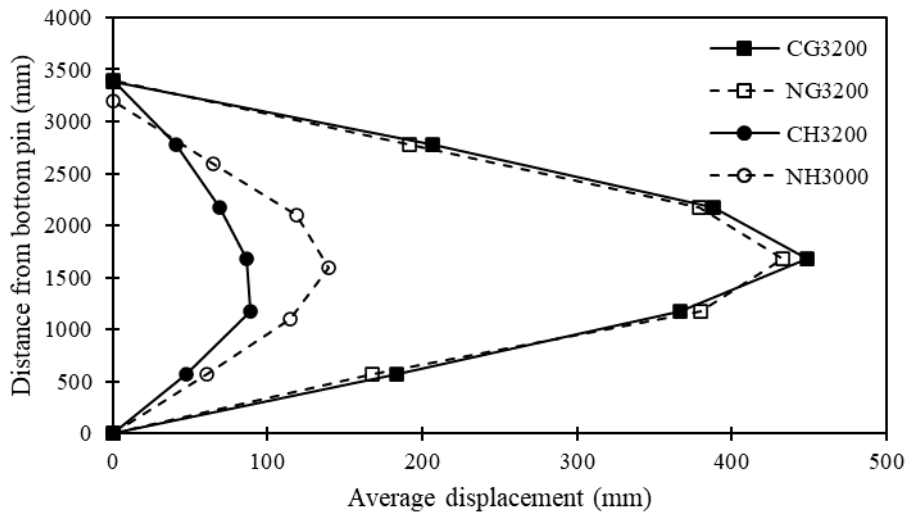
Figure 4.16: Wall displacement profile at the ultimate displacement

Variations in the displaced shape of the tested walls are highlighted in Figure 4.17 wherein the displacements have been normalized by dividing them by the value of the displacement recorded at 600 mm from the bottom pin support. The displaced shape of the walls is generally unchanged for applied loads ranging from 20 kN to the global yield point. For loads below 20kN, the displaced shape is more variable, since it is more likely to be influenced by random differences in cracking in the upper or lower half of the

wall. The asymmetric displaced shape of wall CH3200 at the ultimate applied load is due to the lack of bonding of one of the reinforcing bars as discussed in Section 4.4.2.
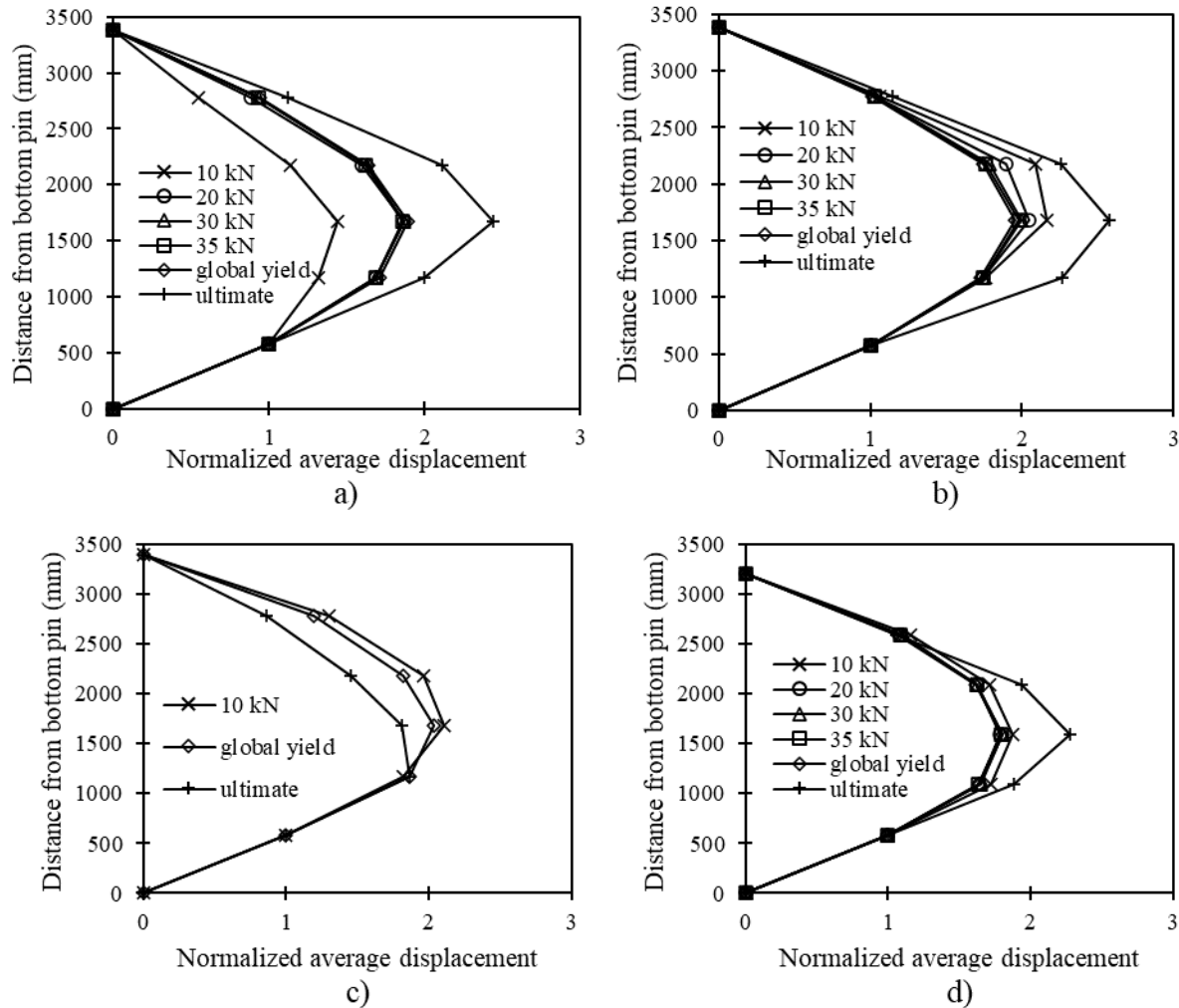
Figure 4.17: Normalized displaced shape of walls at various levels of out-of-plane loading: a) CG3200; b) NG3200; c) CH3200; and d) NH3000

4.5.3   Cracking

Surface cracking was monitored visually throughout testing. All walls developed horizontal cracks along the mortar bed-joints on the tension face prior to yielding as shown in Figure 4.18. The width of these cracks was not measured during testing, however Walls NG3200 and NH3000 (as well as NH3200) with the NSM steel reinforcement exhibited much thinner cracks around the global yield point compared to the

Chapter 4 – Preliminary Testing: 3 m Tall Walls

conventionally reinforced Walls CG3200 and CH3200 due to their higher flexural stiffness and lower displacement.
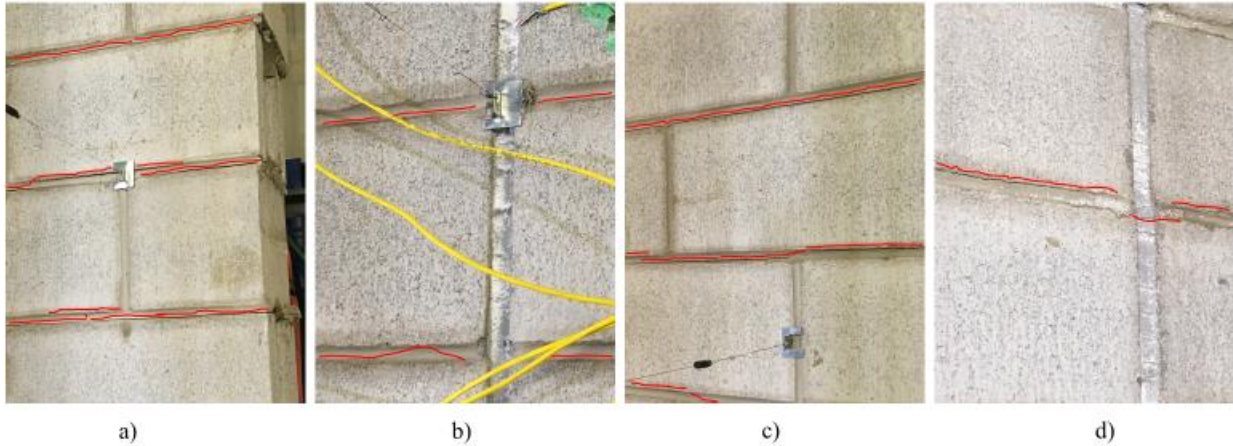
Figure 4.18: Cracking of reinforced masonry walls near the midspan at the global yield point: a) CG3200, b) NG3200, c) CH3200, and d) NH3000

The walls also exhibited compression and rotation of the bed-joints on the compression face at larger displacement levels. As shown in Figure 4.19, the level of compression and rotation of CG3200 near the ultimate displacement caused localized spalling of the CMUs even though the eventual mode of failure of that wall was the tensile rupture of the reinforcing bars.

Figure 4.19: Compression and rotation of mortar joints at the ultimate displacement: a) CG3200, and b) NG3200

Furthermore, the NSM-reinforced walls developed the distributed herring-bone cracks shown in Figure 4.20 a), similar to those reported in other NSM tests (e.g., Galati, Tumialan, and Nanni 2006; Rashid Oehlers, and Seracino 2008; and Al Jaberi, Myers, and ElGawady 2018b).

Walls CG3200, NG3200, and NH3000 exhibited a well-defined elastic response, followed by large plastic deformation prior to failure. Yielding in the walls was confirmed based on the defined inflection point in the load-displacement response, and from the strain gauge data, which also exhibited a defined inflection point in the load-strain response and recorded strains exceeding the yield strain. No significant external damage was observed in the walls at yielding, except for horizontal tension cracks in the bed-joins within the zone of maximum moment.

A sudden reduction in load capacity marked the onset of failure for the five tests. In wall CG3200, failure was associated with the rupture of the reinforcement, which was visible through the wide bed-joint crack opening depicted in Figure 4.20 b). Walls NG3200 and NH3000 failed through de-bonding of the NSM reinforcement and cracking of the masonry units, as is evident in Figure 4.20 c) and d), respectively. Walls CH3200 and NH3200 failed prior to yielding of the reinforcement due to lack of reinforcement bonding and cracking of the top course of CMUs, respectively. Figure 4.21 depicts walls CG3200, NG3200, CH3200, and NH3000 at the ultimate displacement.
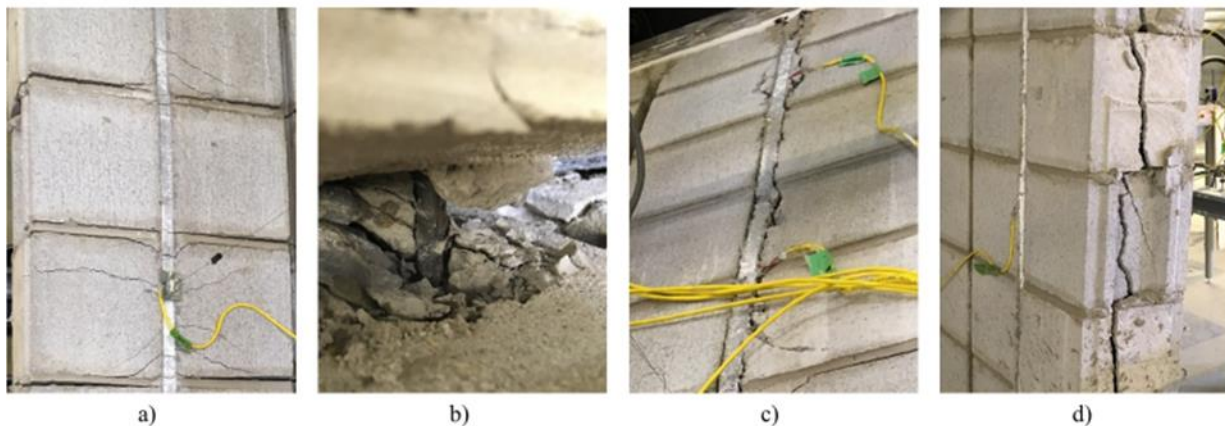
Figure 4.20: Damage to reinforced masonry walls during testing: a) herring bone cracks in wall NG3200); b) reinforcing bar fracture in wall CG3200; c) debonding of NSM reinforcement in wall NG3200; and d) cracking of CMU webs in NH3000

Chapter 4 – Preliminary Testing: 3 m Tall Walls

<div align="center">a)   b)   c)   d)</div>
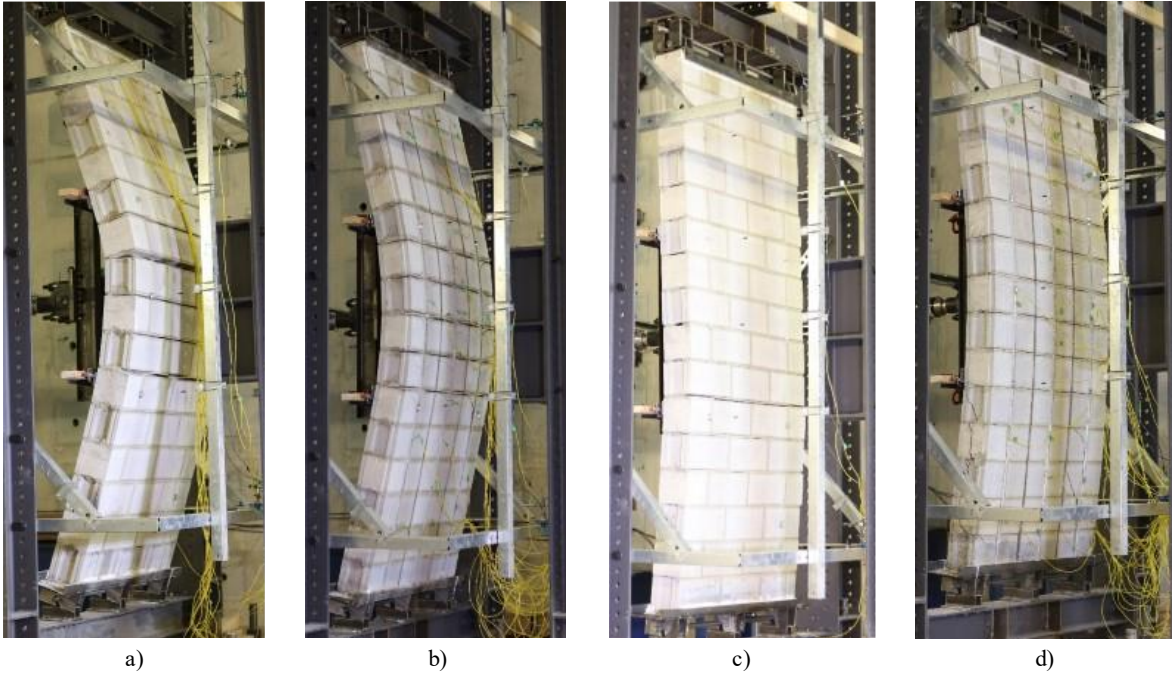
Figure 4.21: Wall specimens at the ultimate displacement: a) CG3200; b) NG3200; c) CH3200; and d) NH3000

4.5.4 Strain response

The reinforcing bar strain response varied both with the local applied moment (a function of the applied load and of the distance from the supports and from the loading points) as well as with the distance of the strain gauge from the nearest mortar joint. Scatter in the strain response, however, made it difficult to interpret the response of individual strain gauges. For example, Figure 4.22 illustrates the strain response of gauges located at mortar joints (Gauges 4, 10, and 16) and gauges located at the centre of SRCMUs (Gauges 7 and 13) for Wall NH3000 until the first yield. For each gauge, the strain response is plotted against the local moment at the gauge, which, for Gauges 4, 13, and 16 was lower than the maximum moment in the wall since those gauges were located outside the constant moment region.

Chapter 4 – Preliminary Testing: 3 m Tall Walls
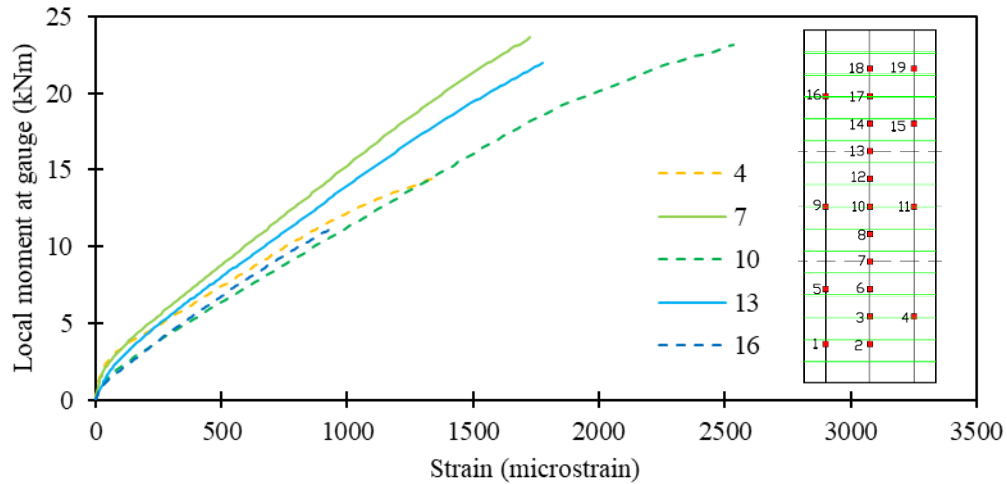
Figure 4.22: Strain response at select strain gauges within Wall NH3000

To make the data easier to interpret, the strain data were grouped according to their position relative to the

nearest mortar joint (groups of strain gauges listed in Table 4.3) and an average was taken. This average

was achieved by combining the strain gauge data into a single set per group (the data for all gauges from a

group of gauges with the same distance from the nearest mortar joint formed one set) and arranging the data

in order of increasing local moment at the gauge. A rolling average of 10 moment-strain data points was

then taken. In this way, the readings from multiple gauges from different parts of the wall (experiencing a

different range of applied moment) were combined, as shown in Figure 4.23.
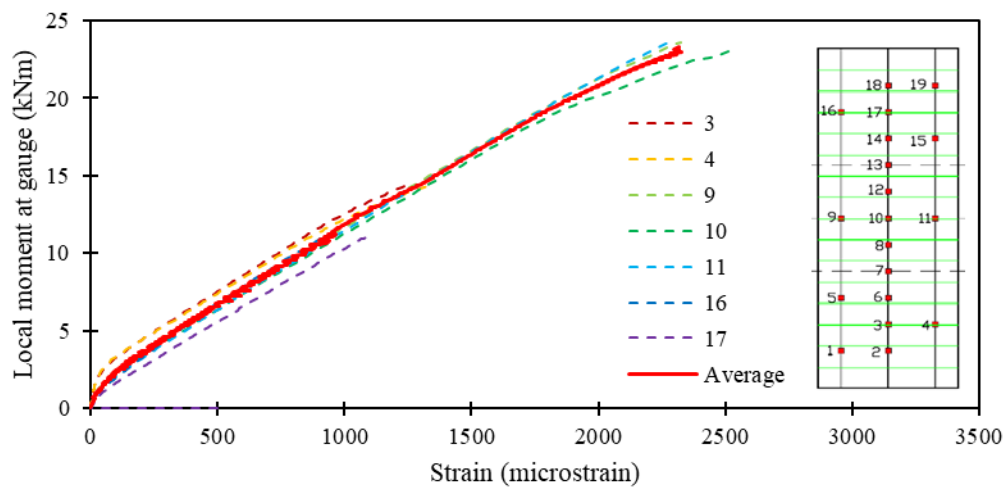
Figure 4.23: Strain response of wall NH3000 strain gauges located at mortar joints until the point of first yielding

Chapter 4 – Preliminary Testing: 3 m Tall Walls

For Walls CG3200 and CH3200, all the strain gauges were located 45mm from the nearest mortar joint. Figure 4.24 shows the response from individual strain gauges as well as the average strain response for Wall CG3200; scatter in the moment-strain response is more evident in CG3200 in comparison to the NSM-reinforced walls NG3200, NH3200, and NH3000. A probable cause for this effect is the variability in the cracking path through the grouted cells of the conventionally reinforced walls which, in turn, resulted in differences in the distance of the cracks relative to the position of the strain gauges.
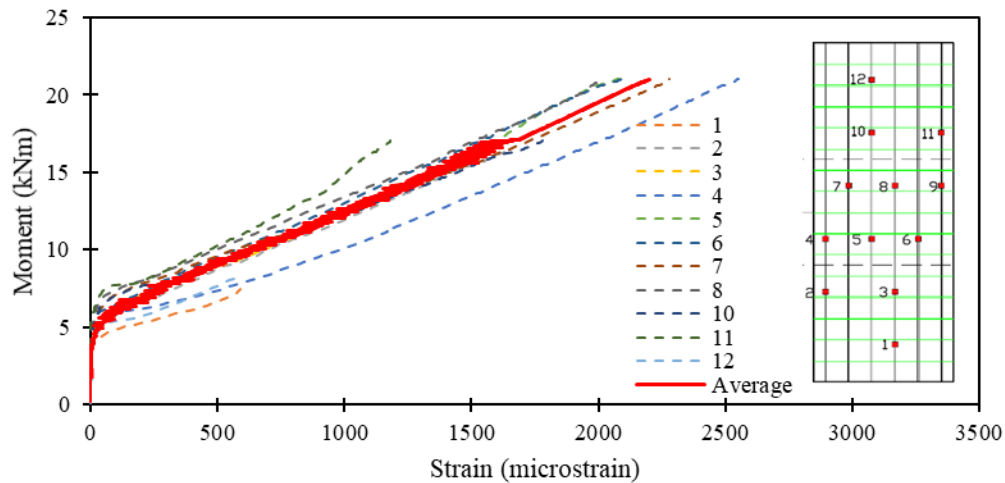
Figure 4.24: Moment-strain response of Wall CG3200

Figure 4.25 a) provides the average moment-strain response of wall NG3200 for gauges grouped by distance from the nearest mortar bed-joint (0mm, 45mm, or 95mm) and by location on the tension face (T), or compression face (C). Figure 4.25 b) illustrates the average moment-strain response for the reinforcing bars in walls NH3200 and NH3000. In all cases, higher strain values are observed near the mortar bed joints, where cracks typically initiate.

Chapter 4 – Preliminary Testing: 3 m Tall Walls
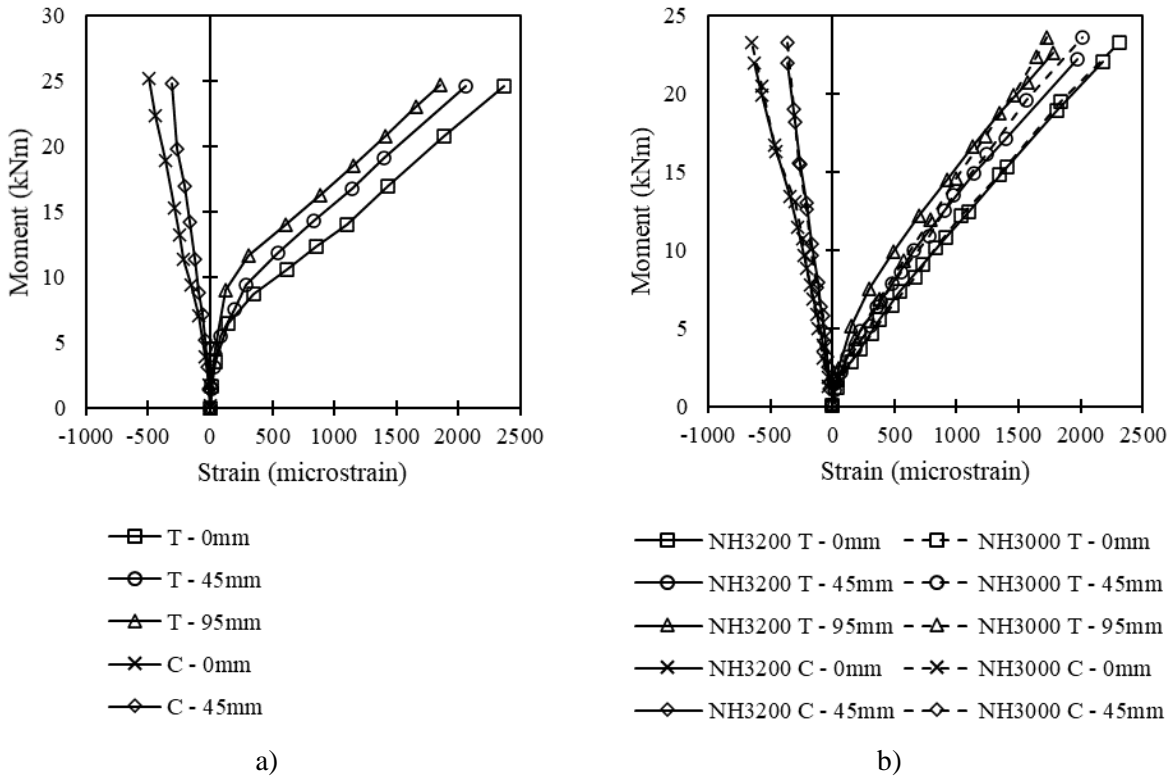
Figure 4.25: Average moment-strain response 0mm, 45mm, and 95mm from the nearest bed joint on the tension (T) or compression (C) face: a) wall NG3200; and b) walls NH3200 and NH3000

Figure 4.26 compares the moment-strain response of the hollow and grouted walls with NSM reinforcement. Regardless of distance from the nearest bed-joint, lower strains are evident in the fully grouted wall, NG3200, than in those with no grouting for a given level of applied moment; however, the strains in reinforcing bars under tension for these walls appear to be converging at load levels approaching the yielding moment. Bar strains on the compression side of these walls with NSM reinforcement appear to diverge at load levels approaching the yield moment.

Chapter 4 – Preliminary Testing: 3 m Tall Walls
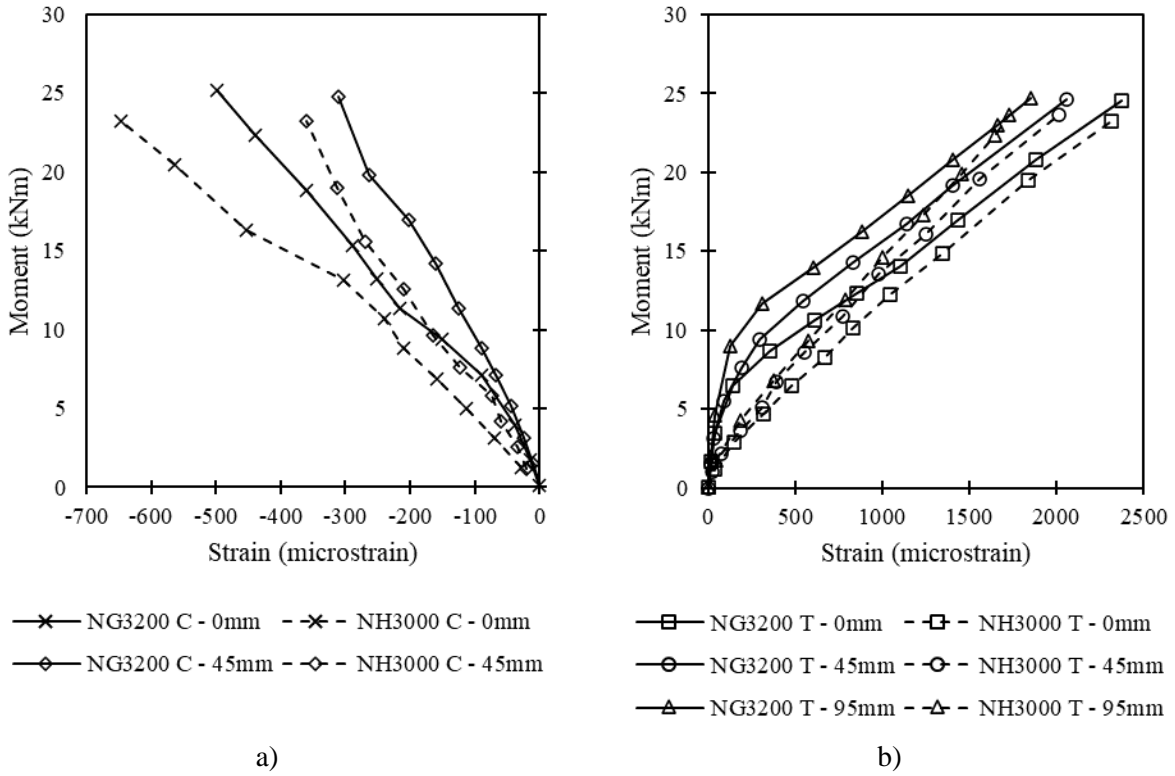
Figure 4.26: Comparing the average moment-strain response of grouted and hollow Walls NG3200 and NH3000: a) strain gauges on the compression face; and b) strain gauges on the tension face

For wall CH3200, the strain gauge data confirmed that the unbonded portion of one of the bars did not fully contribute to resisting the applied moment. As shown in Figure 4.27, strain gauges 2, 4, and 6, which were connected to the unbonded portion of the bar, do not show increasing strain once the applied moment exceeded 7 kNm. Conversely, the strains recorded at strain gauges 1, 3, and 5, located on the fully bonded bar and adjacent to the unbonded section, were higher than those recorded at other bonded regions of the wall since that bar had to sustain the same moment (stresses) as was distributed to two bars elsewhere in the wall. The average strain used for comparison with the response of the other walls was therefore calculated based on the response of Strain Gauges 7 to 12 only (from the upper portion of the wall wherein the reinforcing bars were fully grouted).

Chapter 4 – Preliminary Testing: 3 m Tall Walls
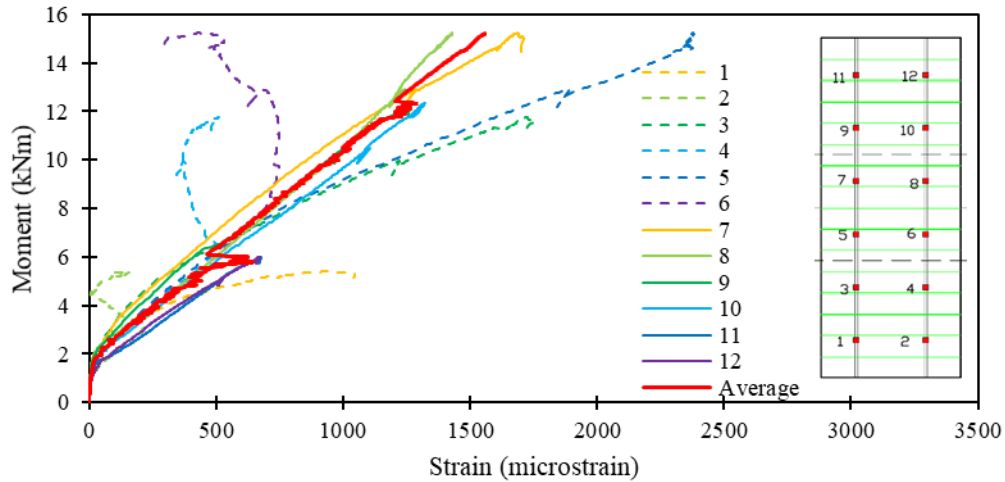
Figure 4.27: Moment-strain response of wall CH3200

The moment-average strain response up to the global yield point at 45mm from the nearest mortar bed-joint for each wall is illustrated in Figure 4.28. Whereas the initial flexural stiffness of grouted Walls CG3200 and NG3200 is shown to be similar, reflected by low reinforcing bar strain for moment values up to 5 kNm, the strain response of the walls with NSM reinforcement, and the walls with conventional reinforcement diverged with increasing moments. As the applied moment approached the yield moment, the strain response of Walls NG3200, NH3200, and NH3000 was similar; the strain response of Walls CG3200 and CH3200 also appeared to converge with increasing applied moment.
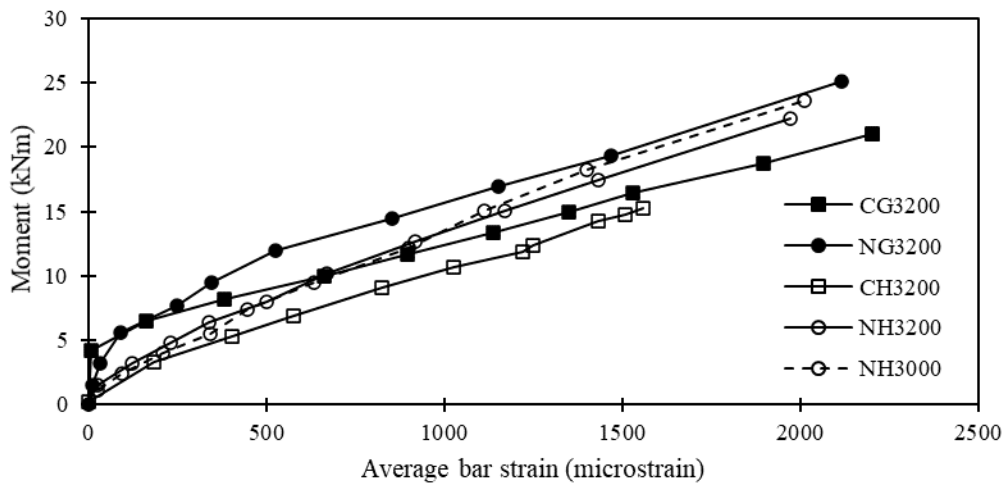
Figure 4.28: Moment-strain response of 3 m tall walls at 45mm from the nearest bed joint

Chapter 4 – Preliminary Testing: 3 m Tall Walls

4.6   Summary of Results from Testing 3 m Tall Walls

Testing of 3 m tall RM walls provided a successful demonstration of the capability of the high bay structures laboratory in the BCEE to conduct structural load tests on full-scale reinforced structural members.

Walls reinforced with conventionally embedded and NSM steel bars (gross tension reinforcement ratio of 0.26% and 0.13%, respectively) exhibited defined periods of elastic and plastic response when subjected to third-point out-of-plane loading. The conventionally reinforced walls and those with NSM reinforcement had similar maximum flexural resistance ranging from 22.2 kNm to 25.9 kNm, with the exception of the partially hollow wall with conventional reinforcement which had a lower flexural resistance of 15.2 kNm due to incomplete bonding of the reinforcement.

The experimental displacement profile of the walls indicates that, at an applied load of 20 kN, the walls with NSM reinforcement experienced lower displacements than those with conventionally embedded reinforcement. Under this load level, the fully grouted walls had lower displacements than the similarly-reinforced hollow walls. At the global yield point, the displacement profile of the two NSM-reinforced walls were nearly identical.

With the exception of the partially hollow wall with conventional reinforcement (which had a lower flexural resistance due to incomplete bonding of the reinforcement), each wall experienced significant plastic response prior to failure. The conventionally-reinforced fully grouted wall failed by rupture of the reinforcing bars, whereas the NSM-reinforced walls failed by debonding of the reinforcement and fracture through the masonry units.

The tension reinforcing bar strain response of the fully grouted walls was lower than that of the hollow walls under low applied loads; however, the strain response of the grouted and hollow walls with NSM reinforcement converged at load levels approaching yielding. The strain response of the fully grouted and partially grouted walls with conventional reinforcement also appeared to converge with increasing applied moment.

Chapter 4 – Preliminary Testing: 3 m Tall Walls

5 Slender Wall Testing: 8 m Tall Walls (adapted from Sparling and Palermo 2022)

During this second phase of testing, very slender Reinforced Masonry (RM) walls were constructed and tested under conditions of combined out-of-plane and axial loading. This testing series was developed from and executed based on the experience gained through the preliminary testing series on the 3 m tall walls reported in Chapter 4. The walls and testing frame were designed and constructed to maximize the use of the height available for testing within the Bergeron Centre for Engineering Excellence's (BCEE) high bay structural testing laboratory. Four walls were constructed to 7.8 m in height; two of these were constructed with conventional Concrete Masonry Units (CMUs) and reinforced similarly to wall CH3200, and the other two were constructed from the grooved Surface Reinforced Concrete Masonry Units (SRCMU) and reinforced similarly to wall NH3200, as described in Chapter 4. This chapter discusses the testing and primary response of these slender RM walls to combined axial and 4-point out-of-plane loading. This includes the following: a discussion of the design of the testing frame, results of material testing, the primary load-displacement response of the walls, and the cracking response. Although the walls were constructed in the fall of 2019, testing was delayed by 9 months in part due to the access restrictions related to the COVID-19 Pandemic.

5.1 Testing Frame Development

The testing frame was designed as an extension of the frame constructed for the preliminary testing series (3 m walls described in Chapter 4); the column extensions were fabricated from the same structural steel section as the main columns, and the horizontal support beams and tie backs were reused. The testing frame was designed as a hybrid of the set-ups described by Abboud, Hamid and Harris (1996) and the ACI-SEASC Task Committee on Slender Walls (1982). Axial loading using a lever beam, as described by the ACI-SEASC Task Committee on Slender Walls (1982), as opposed to the direct loading approach used by

others (Yokel, Mather and Dikkers 1970; Hatzinikolas, Longworth, and Warwaruk 1978; Mohsin and Elwi 2003; Isfeld et al. 2019), was selected to minimize the overhead space requirement for applying the load. A vertically oriented actuator was used to apply the load on the lever beam rather than a hanging weight (as was used by the Task Committee on Slender Walls (1982)) to allow a greater range of applied loads as well as better control.

The frame, shown in Figure 5.1, includes a pin connection at the base of the walls and a roller connection (restraining horizontal displacement, but permitting axial expansion and contraction) at the top. The pin and roller connections were achieved using the same pillow block mounted bearings and 35 mm diameter steel axles as the preliminary tests, but in a different configuration, as shown in Figure 5.2. Additional supporting bearings were added at the bottom pin connection to resist the increased vertical load that would be applied during the test. At the top roller support, the central portion of the roller was replaced by a solid steel fulcrum bolted directly to the wall coupling channel to resist the concentrated load applied by the loading beam. Resistance to out-of-plane displacement of the top roller support was achieved through an elongated version of the roller support fork assembly described in Chapter 4 on either side of the axial loading point (fulcrum). The frame was anchored to the laboratory strong-floor and strong wall at the base of the vertical support columns and through horizontal tiebacks, respectively.

Chapter 5 – Slender Wall Testing: 8 m Tall Walls
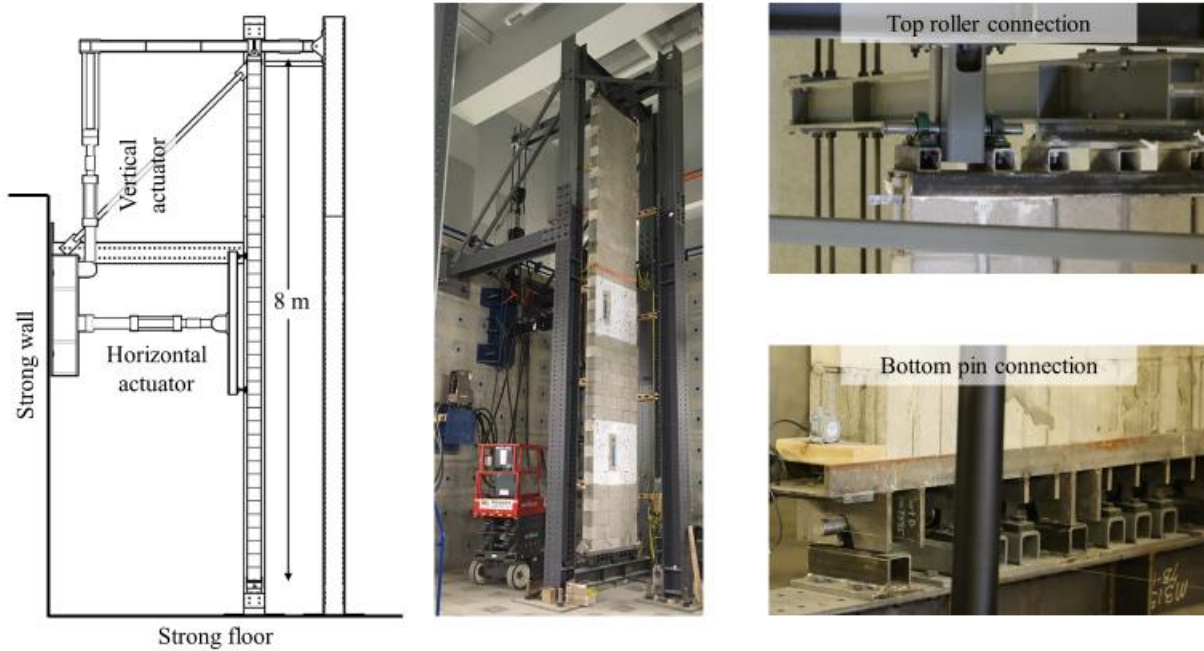
Figure 5.1: Slender wall testing frame
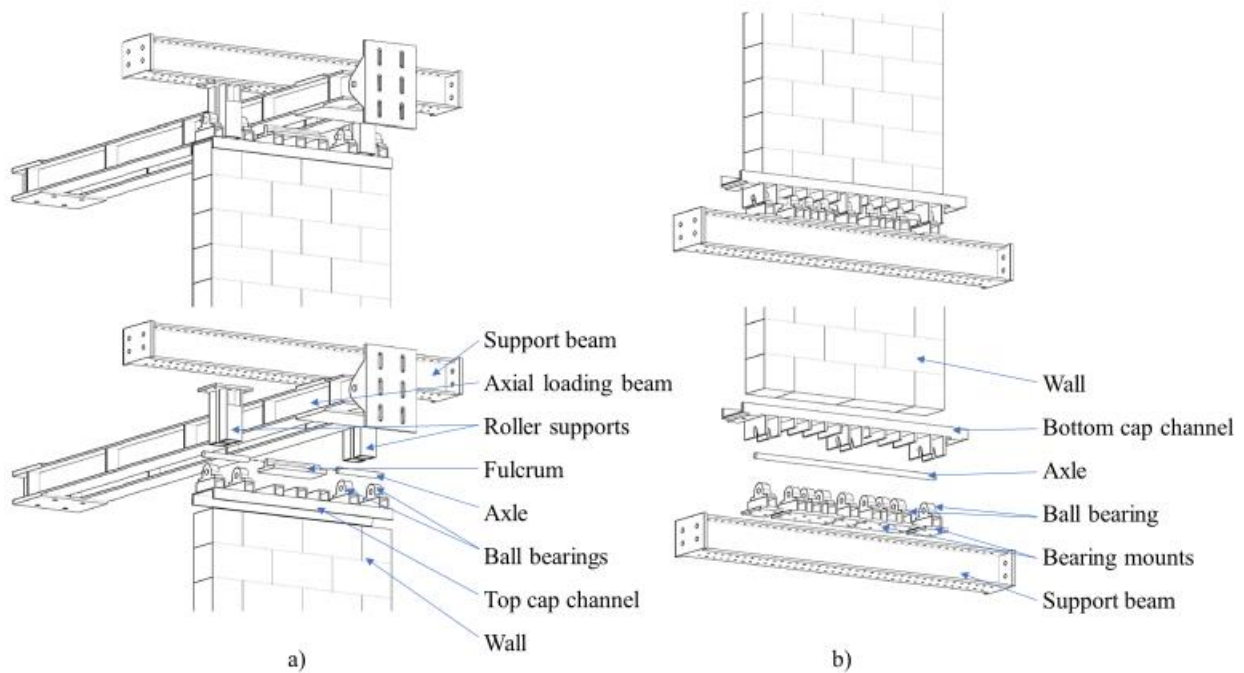
Figure 5.2: Detail of support connections using pillow block bearings: a) top roller connection and b) bottom pin connection

The out-of-plane-loading was applied using a horizontally oriented hydraulic actuator which was anchored to the laboratory strong wall. Spreader beams mounted to the head of the actuator were used to distribute the load from the actuator to two equal line loads spaced 2 m apart and centred about the mid-height of the

Chapter 5 – Slender Wall Testing: 8 m Tall Walls

test wall as shown in Figure 5.3. The out-of-plane load was applied in a displacement-controlled mode, as opposed to a load-controlled mode, such that a loss of out-of-plane load resistance (due to concrete crushing, yielding of reinforcement, secondary moment effects, or a combination) would not result in a runaway loading condition.
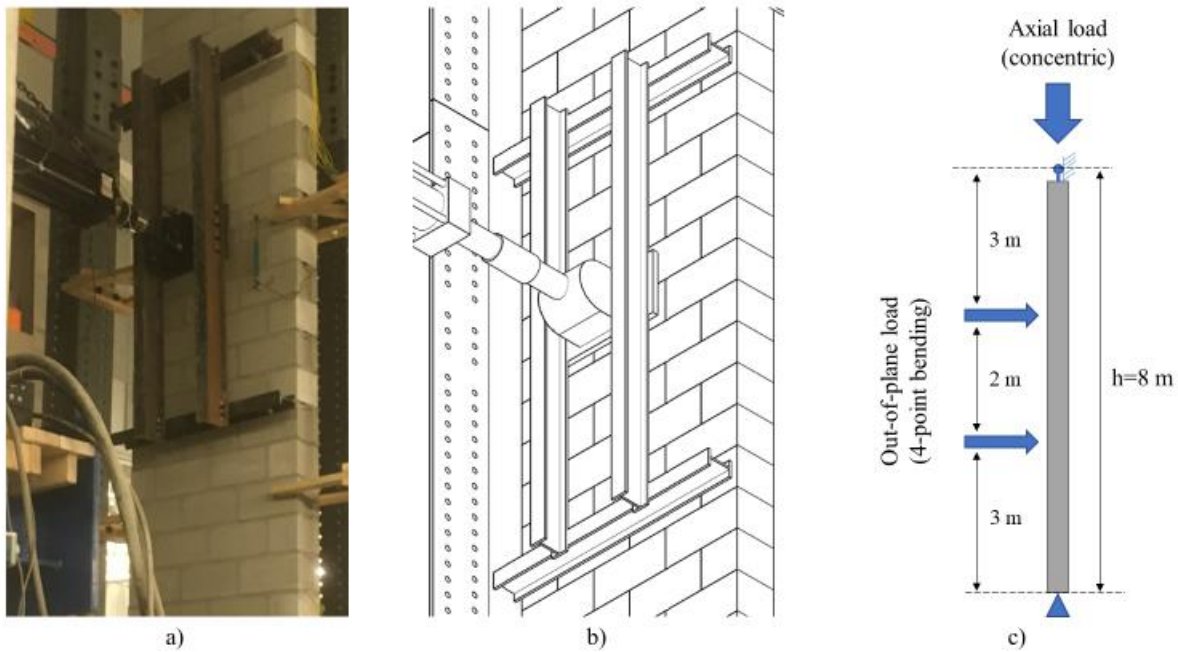
Figure 5.3: Wall loading configuration: a) photograph of spreader beams; b) computer aided rendering of spreader beams; c) conceptual loading condition

Axial load was applied using a lever beam assembly connected at one end to a steel column and at the other end to a vertically oriented hydraulic actuator. Load was applied to the top of the wall through a steel fulcrum at a distance of 935 mm from the lever beam-column pin connection as shown in Figure 5.4. With this setup, the axial load at the top of the wall was 3.7 times the load recorded by the vertically oriented actuator. The resulting load condition is illustrated in Figure 5.3 c).

Chapter 5 – Slender Wall Testing: 8 m Tall Walls
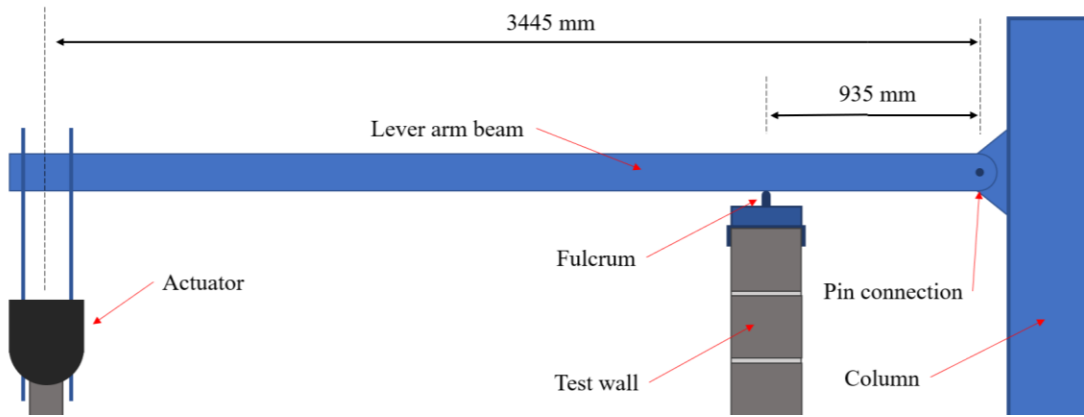
Figure 5.4: Configuration of axial loading system

Diagonal ties, highlighted in Figure 5.5, were included in the design of the frame to reduce unwanted movements during testing. Long steel bracing ties connected the top of the steel column extensions to the tie-back beams near the connection to the strong wall to restrict out-of-plane movement of the top of the walls during testing. Short ties connected the top of the column supporting the pin connection for the lever beam, to the columns supporting the masonry wall; these ties ensured the loading configuration remained consistent with that shown in Figure 5.4 throughout the tests.
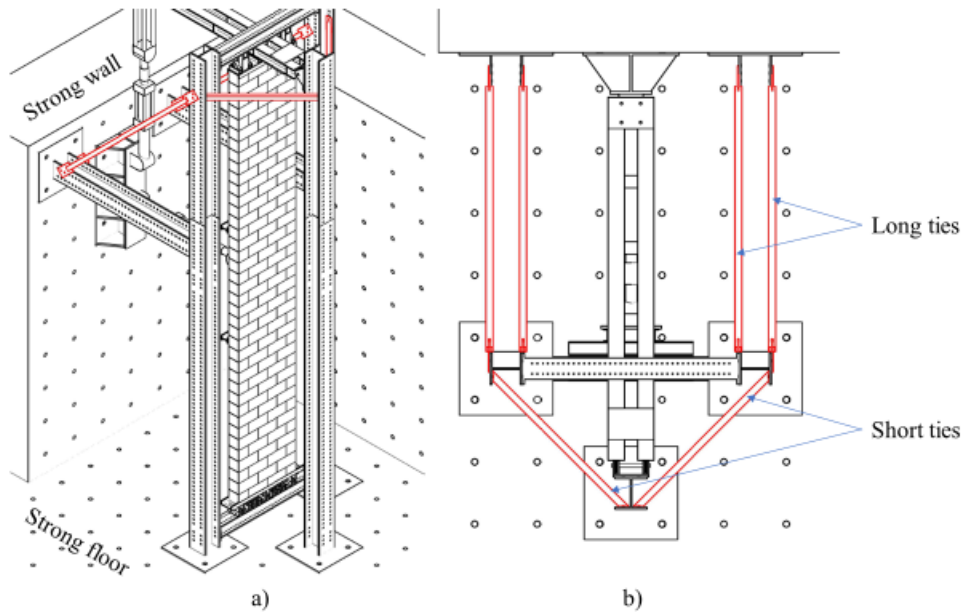
Figure 5.5: Structural ties for the tall wall loading frame highlighted in red: a) isometric view; and b) plan view

Chapter 5 – Slender Wall Testing: 8 m Tall Walls

Constraints in the testing frame did not allow the applied load to be measured directly during testing; however, a verification of the loading system was conducted using a portion of one of the wall specimens as shown in Figure 5.6. The response from tests of the loading arm, shown in Figure 5.7, indicates that frictional effects at the connections resulted in minor losses and uncertainty in the applied axial load. Multiple loading and unloading cycles were performed as part of this verification test to ensure the response was consistent. The applied load measured at the fulcrum using a load cell deviated from the 3.7:1 ratio relative to the load measured at the actuator by approximately ±9 kN throughout the range of applied loads from 20 kN to 200 kN.
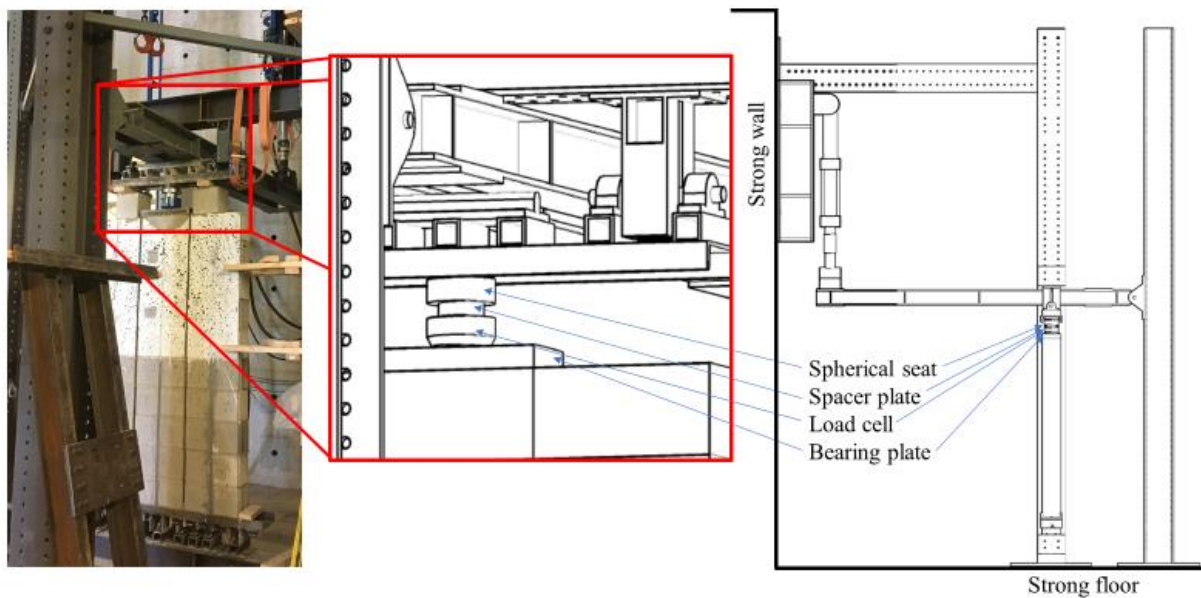
Figure 5.6: Axial load verification test set-up

Chapter 5 – Slender Wall Testing: 8 m Tall Walls
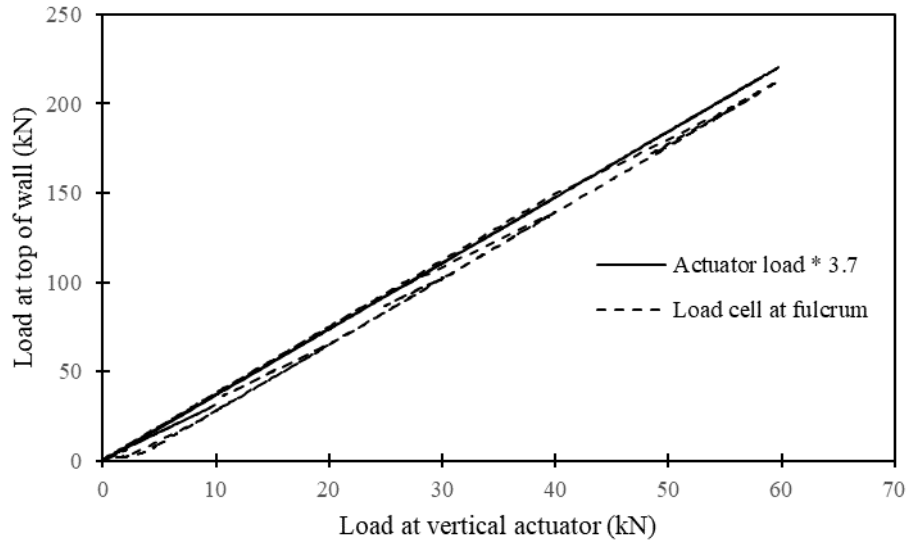
Figure 5.7: Imposed axial load verification test

The vertical actuator was programmed to maintain a constant load (load control) during each test such that it would automatically adjust its stroke (displacement) to accommodate small changes to the wall chord (height), including small expansion at early stages (due to cracking) and contraction due to large displacement; these phenomena are illustrated in Figure 5.8. Using load control, however, introduced the risk of uncontrolled displacement if the vertical load resistance of a test wall was lost (due to buckling or crushing of the masonry); this risk was mitigated by introducing a limit to the displacement of the actuator, at which point the applied load would be cut off (system interlock). For each test cycle, this stroke limit was set at a value approximately 10 mm larger than that required to accommodate the expected change in chord length based on an elastic analysis; this setting was further refined, following the first loading cycles of the test series, based on observed trends in the response.
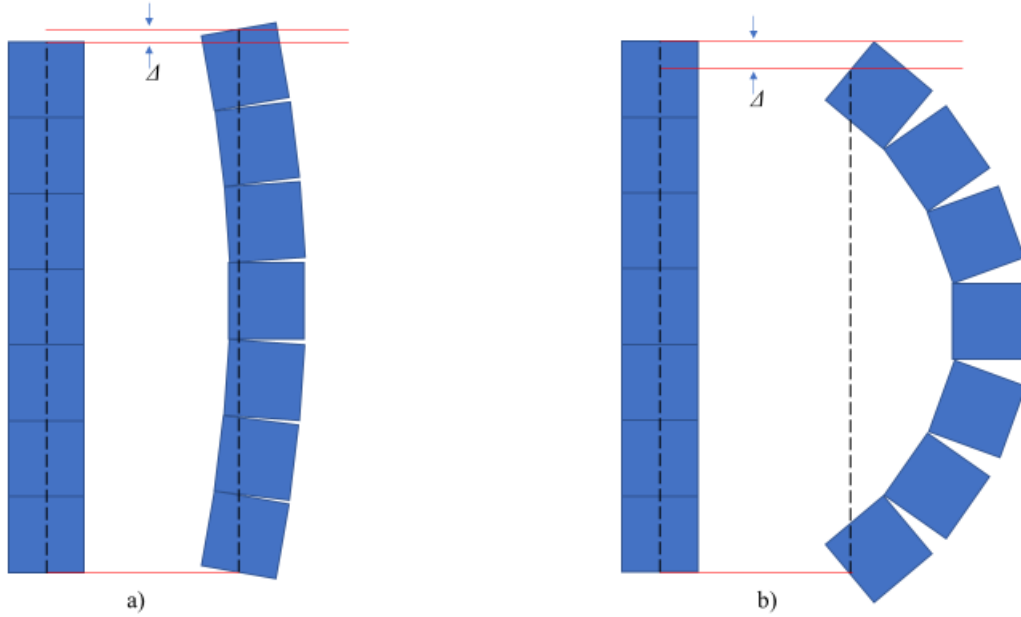
Figure 5.8: Vertical displacement, Δ, at top support due to changes in the chord length: a) expansion; and b) contraction

5.2   Wall Construction

The walls in this chapter were constructed by a professional mason using the same methods and material types as those described in Chapter 4 for the construction of the 3 m tall walls. These walls were constructed in running bond to a length of 1.2 m and a height of 7.8 m (39 courses). Two walls were conventionally reinforced by embedding steel reinforcing bars in grout-filled cells (Walls CH7800a and CH7800b), and the remaining walls were reinforced by placing steel reinforcing bars near the surface (Walls NH7800a and NH7800b). These two pairs of walls were constructed similarly to Walls CH3200 and NH3200, respectively. The reinforcement layouts and the reinforcement processes are illustrated in Figure 5.9.

Chapter 5 – Slender Wall Testing: 8 m Tall Walls
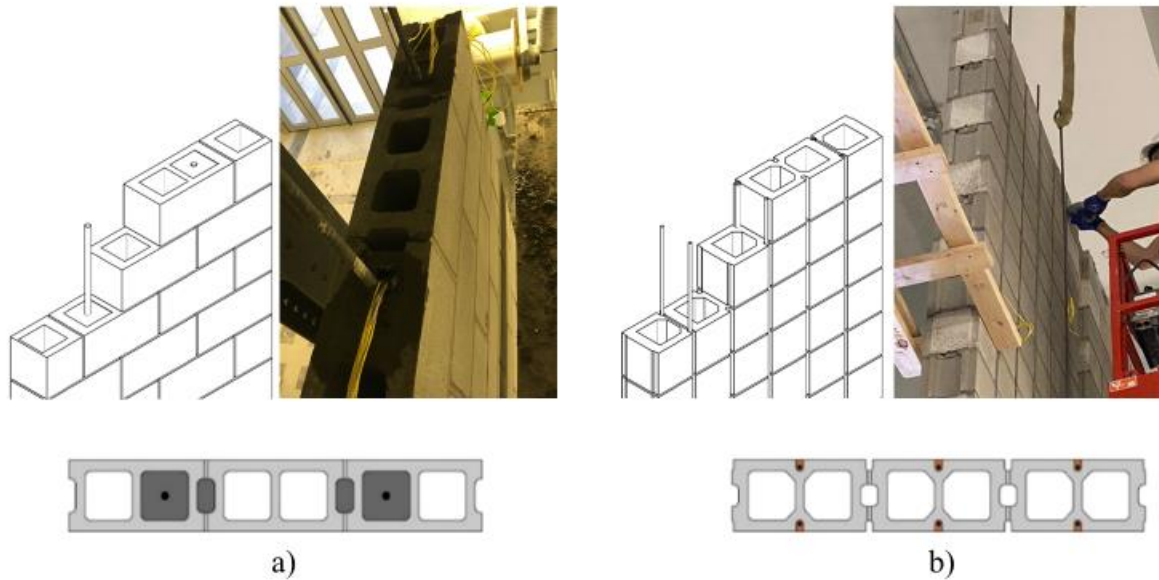
Figure 5.9: Cross sections and placement of reinforcement: a) conventional reinforcement (CH7800x); and b) NSM steel reinforcement (NH7800x)

The 20M reinforcing bars for Walls CH7800a and CH7800b were lap spliced to avoid grout lifts exceeding 3 m. Continuous 10M deformed steel bars were used for the NSM reinforcement of walls NH7800a and NH7800b. The top and bottom courses of each wall were reinforced horizontally with a hooked 10M reinforcing steel bar and fully grouted. For the conventional walls, only cells containing a reinforcing bar were grouted; the walls with NSM reinforcement were hollow, except for the top and bottom courses. Joint reinforcement was placed in the bed joints of every third course of masonry (600 mm on centre); for the walls with NSM reinforcement, the wires were bent such that they would not obstruct the grooves to be reinforced. Bar positioners were placed within the cells to be reinforced as the walls were built. The maximum compression resistance of these wall sections can be calculated based on Equation (5.1) from CSA S304-14 (CSA Group 2019a) as follows:

Equation 5.1 $\qquad P_{rmax} = 0.8[0.85\phi_m f'_m A_e]$

Neglecting the material resistance factor and using the specified *f'_m* values for grouted and ungrouted hollow 15 MPa CMU masonry with Type S mortar from CSA S304-14 (CSA Group 2019), 10 MPa for hollow and 7.5 MPa for grouted masonry, the nominal unfactored maximum load resistance for the conventional

and NSM reinforced walls is 760 kN and 520 kN, respectively. This calculation of maximum unfactored load resistance does not account for the effect of steel reinforcement in compression, nor for slenderness effects.

The walls were constructed in three stages to allow lap-splicing and grouting of the conventionally reinforced walls. During construction, the walls were arranged in a line such that the mason could build all four walls concurrently using a single mason's line. Following each construction stage (intervals of approximately 3 m of wall height), the walls were braced against steel columns which were anchored into the laboratory strong floor, and the conventional reinforcement was grouted in place for Walls CH7800a and CH7800b. Clean-out holes at the base of each wall stage, as well as at intermediate points, facilitated the cleaning and inspection of the hollow cells prior to grouting. At the end of each construction stage, the reinforcing bars were lowered into place (threaded through the bar positioners). Instrumentation wires connected to the reinforcing bar strain gauges were routed to exit the walls at both ends of the wall at the top of each stage. Free-standing construction scaffolding was erected concurrently as the walls were constructed. Walls NH7800a and NH7800b remained unreinforced (except for the top and bottom courses of masonry which were reinforced horizontally with a single hooked 10M bar and grouted solid for all four walls) until the construction was completed. Continuous 10M bars spanning the full height of the walls were applied to the NSM reinforced walls. The same procedure was used as for the 3 m tall walls NG3200 and NH3200 in Chapter 4, except that the overhead crane was used to lift the reinforcing bars into place. Photos illustrating the construction process are available in Appendix B.

Twelve standard masonry prisms (5 courses high) were constructed concurrently with the walls; six prisms were constructed from the conventional CMUs and six from the SRCMUs. All prisms were prepared in a pseudo running bond pattern as described in Chapter 4. Three of the conventional prisms and three of the SRCMU prisms were filled with masonry grout, concurrently with grouting of the walls.

Chapter 5 – Slender Wall Testing: 8 m Tall Walls

5.3   Material Testing

Samples of the reinforcing steel bars used in the construction of the walls were tested in direct tension following ASTM E8 (ASTM International 2016). For both bar sizes (10M and 20M), three samples were fitted with the same type of strain gauge as used in the walls during testing. Given that the application of strain gauges requires local modification of the bar (grinding and sanding to create a smooth surface), three additional bar samples were tested without strain gauges to assess the variation in mechanical properties with the application of strain gauges. For both sample types, an extensometer clip gauge was used to measure strain (in addition to the strain gauges, where applicable). The mechanical properties for the steel reinforcing bars with and without strain gauges are listed in Table 5.1. The number of test replicates was not sufficient to determine statistical significance; however, the difference in average yield stress and Young's Modulus was less than 2%. [Note that the strain gauges have a nominal gauge factor accuracy of $\pm$ 1%.] The yield strength of the 10M bars was higher than expected. This was the result of using a 0.2% offset to establish the yield point given that the stress-strain response of the bar did not have a defined yield point and was characterized by a rounded response curve.

Table 5.1: Reinforcing steel bar properties

Property	Bar type – bare bar		Bar type - with strain gauge	
	10M	20M	10M	20M
Nominal section area	100 mm^2	300 mm^2	100 mm^2	300 mm^2
Yield stress	544 MPa	440 MPa	536 MPa	439 MPa
Young's modulus	199 GPa	191 GPa	197 GPa	191 GPa
Maximum stress	682 MPa	587 MPa	674 MPa	587 MPa

The five-course masonry prisms (grouted and ungrouted) were tested under axial compression following the same procedure as described in Chapter 4. Three individual masonry units each of the conventional and SRCMU shape were also tested in axial compression following the same procedure as the prisms. Average strength and axial compressive stiffness for each type of prism, based on the effective cross-sectional area, are reported in Table 5.2. The average strength based on the net minimum cross-sectional area of the conventional and SRMCU units was 25.3 MPa and 21.0 MPa, respectively. The age at testing of the masonry units and prisms was approximately the same as that of the walls; whereas the walls were tested

Chapter 5 – Slender Wall Testing: 8 m Tall Walls

at 14 to17 months of age, the prisms were tested at 18 months of age, and the masonry units were tested in the same month as the prisms.

Table 5.2: Strength and Young's modulus of masonry prisms

Prism type	Average strength (MPa)	Average Young's modulus (MPa)
Conventional prism: hollow	17.5	22 872
Conventional prism: grouted	11.3	14 413
SRCMU prism: hollow	18.3	18 919
SRCMU prism: grouted	11.0	14 676

Mortar and grout samples were cast during the construction of the masonry walls and tested in compression at 28 days with a loading rate of 0.25 MPa/sec. The 28-day strength of the mortar cubes (50 mm x 50 mm x 50 mm) and grout cylinders (100 mm x 200 mm) was 27.3 MPa and 14.5 MPa, respectively. Grout cylinders were also tested at 18 months of age, resulting in an average strength of 16.8 MPa. The NSM steel reinforcement was applied using the same type of epoxy as used for the construction of the 3 m tall walls described in Chapter 4.

5.4   Wall Testing

The test walls were constructed in November 2019, however delays in testing were encountered due to the COVID-19 pandemic; access restrictions limiting the working hours during the pandemic also affected the testing schedule. The slender RM walls presented herein were tested between February and June 2021. This section outlines the testing procedure, including anomalies that occurred during testing, and the instrumentation that was used to record the response of the slender RM walls.

5.4.1   Instrumentation

Each reinforcing bar was fitted with strain gauges to monitor strains during testing. These gauges were located to correspond with mortar joints in the finished walls as shown in Figure 5.10; Walls CH7800a and CH7800b were fitted with 20 strain gauges, while NH7800a and NH7800b were fitted with 23 strain gauges. Placement of the gauges at the mortar joints allowed the monitoring of locations where the maximum strain was expected, since horizontal cracking of RM walls subjected to flexure about their

Chapter 5 – Slender Wall Testing: 8 m Tall Walls

horizontal axis initiates preferentially at the mortar joints. Every horizontal mortar joint within the region of maximum moment (2 m portion of the walls' height centred about the mid-height) contained at least one strain gauge; gauges were sparser in the region between the loading points and the supports where the applied moment was lower. Note that for Walls NH7800a and NH7800b, gauges were placed on both the tension and compression faces given the external placement of the reinforcement.
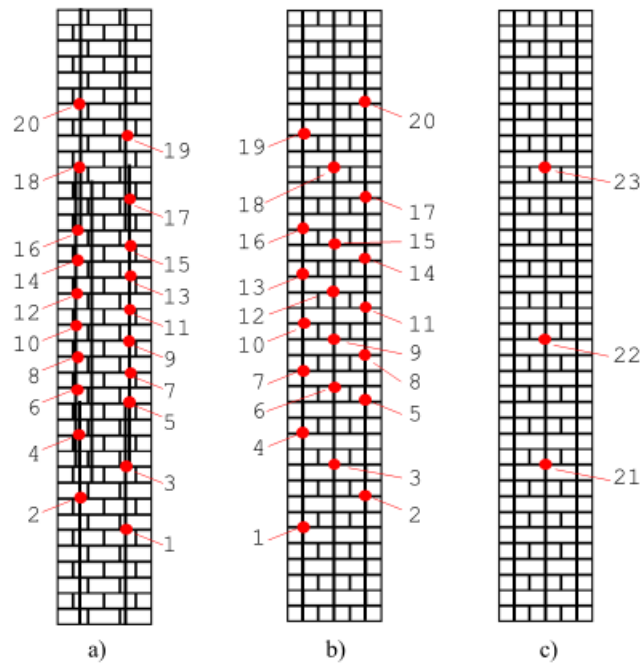
Figure 5.10: Strain gauge locations: a) Walls CH7800a and CH7800b; b) Walls NH7800a and NH7800b, tension side; and c) Walls NH7800a and NH7800b, compression side

The applied out-of-plane load was recorded using the load cell from the horizontal actuator, and the superimposed axial load was taken as proportional to the load recorded by the vertically oriented actuator as discussed in Section 5.1. Cable displacement transducers recorded the out-of-plane displacement of the walls at 1 m intervals along their height and at the top and bottom axles (roller and pin supports) as shown in Figure 5.11 a). Additionally, linear displacement transducers were mounted on the surface of the walls near the mid-span and between bottom line load and bottom support (on both tension and compression faces) to record surface strains over a gauge length spanning two mortar joints (400 mm) as shown in Figure 5.11 b).

Chapter 5 – Slender Wall Testing: 8 m Tall Walls
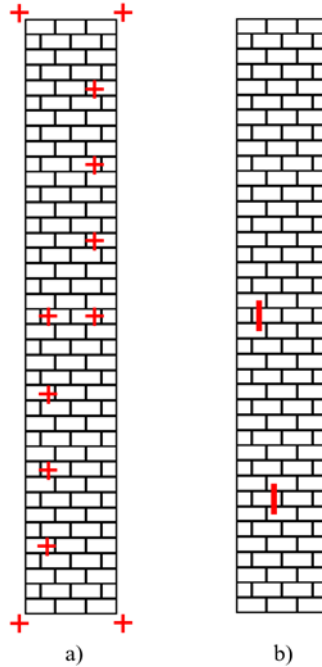
Figure 5.11: Location of displacement transducers: a) out-of-plane displacement cable transducers; and b) in-plane linear transducers

5.4.2 Loading protocol

For each loading cycle, an axial load was maintained while the horizontal load was applied under displacement control until a maximum strain reading of 1800 µm/m (90% of the nominal yield strain) was observed in one of the strain gauges. This target maximum strain ensured the reinforcing bars remained within the linear elastic response range over their entire length. The out-of-plane load was then removed, followed by the imposed axial load prior to the next loading cycle (at a different axial load level). The out-of-plane loading rate for Walls CH7800a and CH7800b, with conventional reinforcement, was 5 mm/min to achieve a target test duration between 15 and 30 minutes. The stiffer Walls NH7800a and NH7800b, with NSM reinforcement, were loaded at a rate of 3 mm/min.

The sequence of axial loads for each wall is listed in Table 5.3. The conventionally reinforced walls were loaded to a maximum axial load of 150 kN (20% of the nominal axial load capacity); this load level caused a gradual decrease in out-of-plane load resistance with increasing displacement while the reinforcing bar strain remained below the yield point (onset of elastic buckling). The walls with NSM reinforcement were subjected to imposed axial loads of up to 250 kN (48% of the nominal axial load capacity), the maximum

Chapter 5 – Slender Wall Testing: 8 m Tall Walls

load that could be applied using the lever beam setup. The last loading cycle for each wall applied out-of-plane loading beyond the yield point of the reinforcing steel to assess the plastic response. The conventionally reinforced walls were loaded with the same axial load of 60 kN to assess whether the minor differences in response observed during the elastic loading cycles would be reflected in the plastic response. The walls with NSM reinforcement had a near-identical elastic response, and different axial loads were assigned for their plastic load cycles to observe the effect of different axial load on the post-yielding behaviour.

Different sequences of loading cycles (sequence of sustained axial loads for each cycle of out-of-plane loading as shown in Table 5.3) were selected such that the effect of stress history on the response of the walls could be observed. For each pair of walls, one was tested with increasing applied axial load from cycle to cycle, and one was tested with decreasing applied axial load. For Walls CH7800b, NH7800a, and NH7800b, the first loading cycle was repeated as the penultimate loading cycle, before the plastic load cycle, to compare the response of the undamaged walls to the response of the same wall to the same loading conditions following multiple cycles of loading to 90% of the reinforcement yield strain.

Table 5.3: Sequence of axial loas for out-of-plane loading cycles

Load cycle number	Applied axial load for wall tests (kN) [axial stress (MPa)][a]			
	CH7800a	CH7800b	NH7800a	NH7800b
1	0 [0.0]	150 [1.14]	0 [0.0]	250 [3.25]
2	20 [0.15]	140 [1.06]	20 [0.26]	240 [3.01]
3	40 [0.30]	130 [0.98]	40 [0.51]	220 [2.82]
4	60 [0.45]	120 [0.91]	60 [0.77]	200 [2.56]
5	80 [0.61]	100 [0.76]	80 [1.03]	180 [2.31]
6	100 [0.76]	80 [0.61]	100 [1.28]	160 [2.05]
7	130 [0.98]	60 [0.45]	120 [1.53]	140 [1.79]
8	140 [1.06]	40 [0.30]	140 [1.79]	120 [1.53]
9	150 [1.14]	20 [0.15]	160 [2.05]	100 [1.28]
10	60 [0.45] [b]	0 [0.0]	180 [2.31]	80 [1.03]
11	-	150 [1.14]	200 [2.56]	60 [0.77]
12	-	60 [0.45] [b]	220 [2.82]	40 [0.51]
13	-	-	240 [3.01]	20 [0.26]
14	-	-	250 [3.25]	0 [0.0]
15	-	-	0 [0.0]	250 [3.25]
16	-	-	60 [0.77] [b]	120 [1.53] [b]

[a]Axial stress is the applied axial load divided by A_e
[b]Axial loads during plastic loading cycles

5.4.3 Problems and anomalies

During the second loading cycle of wall CH7800a, with applied axial load (20 kN), improper tuning of the vertical actuator control system caused sinusoidal fluctuations in the applied axial load throughout the test as shown in Figure 5.12 a). Adjustment of the actuator's settings allowed a constant axial load to be maintained during subsequent loading cycles as shown in Figure 5.12 b). [Note that the horizontal displacement shown in the figures was induced by loading from the horizontal actuator during testing.]

Chapter 5 – Slender Wall Testing: 8 m Tall Walls
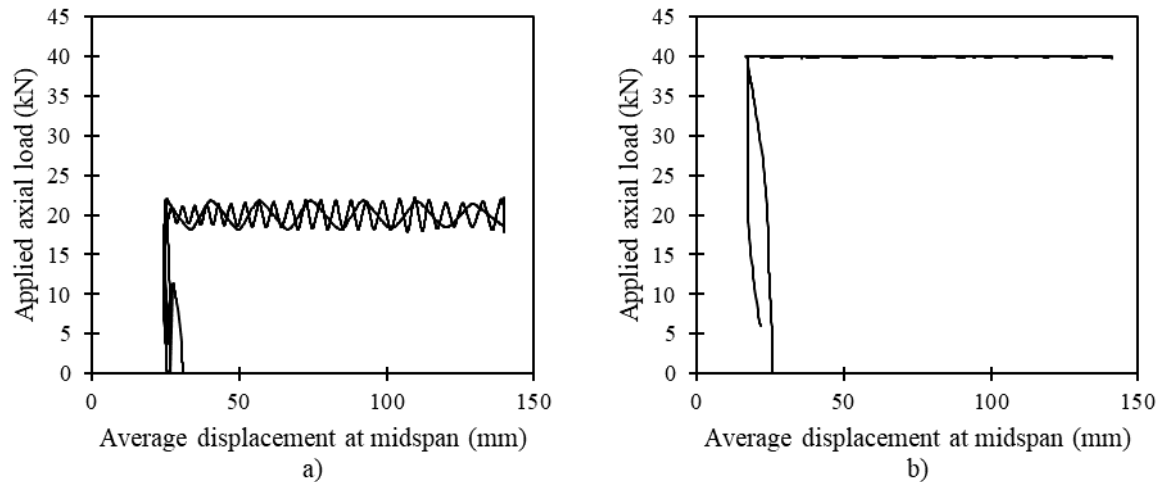
Figure 5.12: Axial load during testing of wall CH7800a: a) 20kN; and b) 40 kN

Programming errors caused minor irregularities in the loading of the wall CH7800a after yielding of the reinforcing bars. During the plastic load cycle, with 60 kN of applied axial load, and after the yield displacement was exceeded, the out-of-plane load and axial load each cut out for different reasons; however, these disruptions did not appear to affect the structural response of the wall as shown in Figure 5.13. The maximum stroke (displacement) of the vertical actuator had been set at 30 mm below the starting position of the actuator head to avoid uncontrolled buckling of the wall, however this displacement was reached during the controlled plastic loading phase, as the chord height of the wall was reducing due to the large displacement. The axial load was immediately re-established and set to the appropriate value without interruption to the out-of-plane loading. Later in the test, the horizontal actuator arrived at the limit of its programmed displacement before the end of the test, and the out-of-plane load was cut off. The out-of-plane loading program was then reset and reengaged without interrupting the applied axial load. The data acquisition system continued recording data throughout the interruptions in loading and confirmed that no adverse effects or responses were produced in the test wall. For subsequent tests, the displacement of the vertical actuator was monitored closely, and the limit to the stroke was adjusted during testing to avoid unexpected loss of axial load, while maintaining safeguards against sudden buckling. Careful attention was also paid during the programming of the horizontal actuator to ensure the maximum expected displacement of the wall could be reached without interruptions.

Chapter 5 – Slender Wall Testing: 8 m Tall Walls
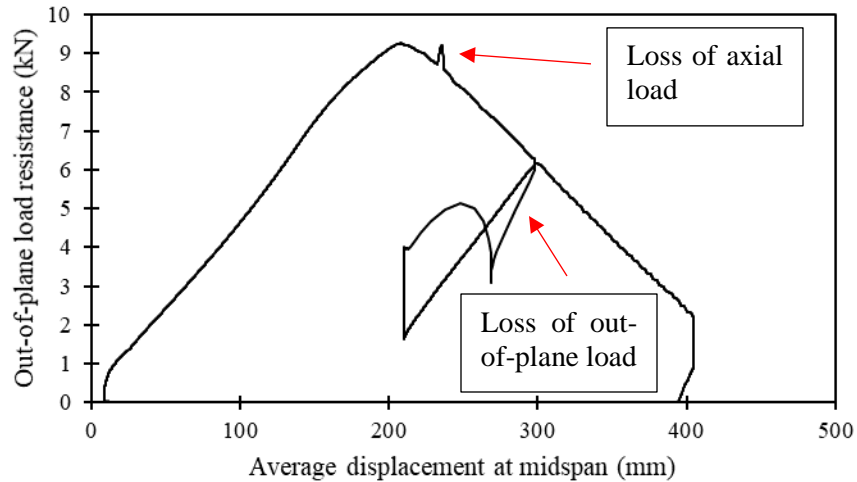
Figure 5.13: Load-displacement response of the wall CH7800a: plastic loading cycle with 60 kN of applied axial load

During testing of Wall NH7800b, one of the strain gauges (strain gauge 8, located at 3400 mm from the base of the wall) recorded strains exceeding others in the plastic region of the wall as show in Figure 5.14. This gauge was used to set the limit strain for load cycles 1 to 6 (applied axial load of 250 kN, 240 kN, 220 kN, 200 kN, 180 kN, and 160 kN); this resulted in a lower maximum displacement achieved during these test cycles in comparison with the other wall with NSM reinforcement (Wall NH7800a). For the remaining elastic cycles, the next largest strain reading was used. The difference in the reinforcement strain and wall displacement achieved during these cycles affected the cyclic response of the wall. Additional energy dissipation (wider displacement response loop) was observed during the loading cycle with 140 kN of applied axial load, compared to the preceding and subsequent cycles. Since the first loading cycle with 250 kN of applied axial load did not reach the same maximum strain as the repeated (penultimate) cycle with the same applied axial load, a greater difference between the response to these two cycles was observed, comparted to what may have otherwise occurred if the same maximum reinforcement strain had been achieved for both cycles.

Chapter 5 – Slender Wall Testing: 8 m Tall Walls
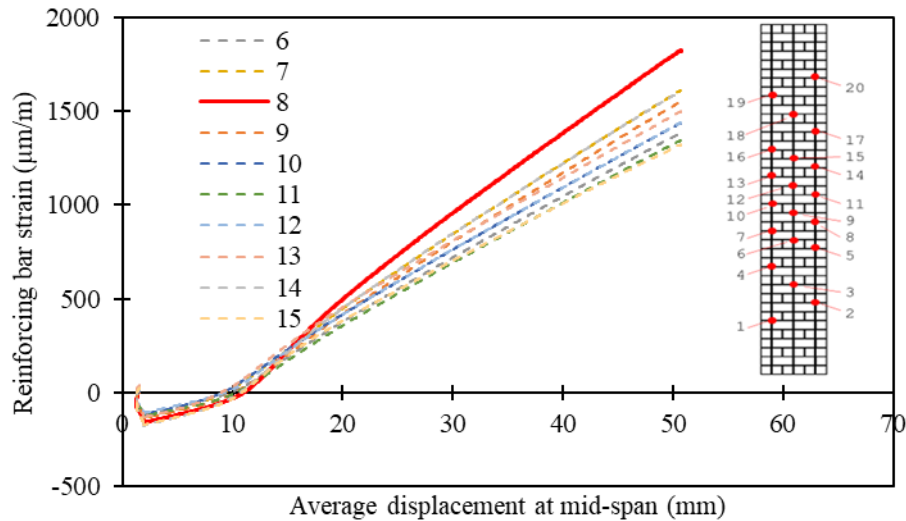
Figure 5.14: Response of strain gauges located within the region of maximum moment for wall NH7800b with 240 kN of applied axial load

5.5 Response

This section presents the primary response of the 8 m tall slender RM walls subjected to out-of-plane loading with superimposed axial load as measured by the available instruments during the tests. This includes the load-displacement response and displaced shape, cracking response, and reinforcing bar strain response. Further analysis and discussion of these data are presented in Chapter 6 – Analysis.

5.5.1 Load-displacement response

The out-of-plane load-displacement response of the walls for the entire range of applied axial loading is illustrated in Figure 5.15 (conventional reinforcement) and Figure 5.16 (NSM reinforcement). [Note that the unloading and reloading of CH7800a in the post-elastic range was the result of an error as noted in Section 5.4.3] The displacement was based on the average readings recorded by the cable transducers located at the mid height of the walls. The red arrows in the figures indicate the observed trend in the out-of-plane load resistance with increasing applied axial load. For example, Wall CH7800a exhibited increasing out-of-plane load resistance with increasing applied axial load up to a displacement of approximately 80 mm; however secondary moment effects resulted in a decreasing trend in out-of-plane load resistance with increasing applied axial load as the displacement approached the yield displacement.

Chapter 5 – Slender Wall Testing: 8 m Tall Walls

The elastic response of the walls was approximately linear at low levels of imposed axial load; however, a bilinear response was observed with increasing axial load. Only minor variations in the displacement at which the reinforcement strain reached the target value of 1800 μm/m were observed with changing imposed axial load for each of the walls. Table 5.4 indicates the load and displacement at the peak of the elastic loading cycles (when the maximum reinforcement strain reached 1800 μm/m) for each wall.
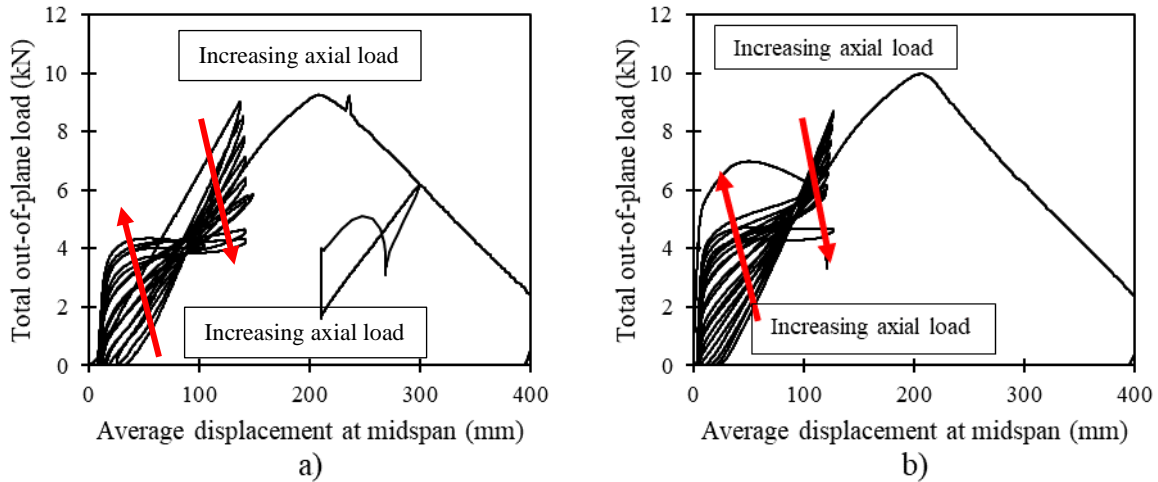
Figure 5.15: Out-of-plane load-displacement response of conventionally-reinforced walls: a) CH7800a; and b) CH7800b
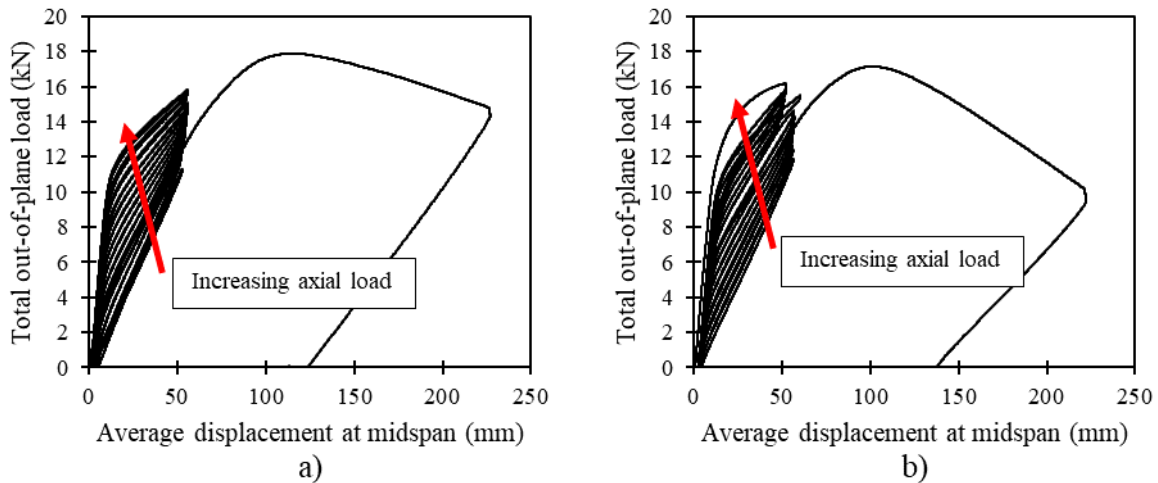
Figure 5.16: Out-of-plane load-displacement response of NSM reinforced walls: a) NH7800a; and b) NH7800b

Chapter 5 – Slender Wall Testing: 8 m Tall Walls

Table 5.4. *Maximum load and corresponding displacement from elastic loading cycles (at max reinforcement strain of 18000 μm/m)*

Axial load (kN)	Displacement at midspan (mm)				Total out of plane load (kN)			
	CH7800		NH7800		CH7800		NH7800	
	a	b	a	b	a	b	a	b
0	137	127	52 [53][a]	55	9.0	8.7	12.0 [11.3][a]	11.8
20	140	126	52	55	8.5	8.2	12.2	12.4
40	141	125	53	55	7.8	7.7	12.5	12.7
60	142	123	54	55	7.1	7.2	13.0	13.1
80	142	122	55	55	6.4	6.9	13.4	13.5
100	142	122	55	56	5.7	6.6	13.6	13.9
120	-	121	55	56	-	6.2	13.9	14.3
130	141	120	-	-	4.6	6.0	-	-
140	141	119	55	56	4.3	5.9	14.3	14.6
150	104[b]	115 [126][a]	-	-	4.1[b]	5.9 [4.6][a]	-	-
160	-	-	56	47	-	-	14.6	13.9
180	-	-	56	49	-	-	14.8	14.5
200	-	-	56	50	-	-	15.1	14.9
220	-	-	56	50	-	-	15.5	15.3
240	-	-	56	51	-	-	15.7	15.8
250	-	-	56	51 [58][a]	-	-	15.8	16.2 [15.5][a]

[ ][a] Results from a repeat cycle
[b] Test halted before the target maximum reinforcement strain was achieved

5.5.2 Displacement recovery

Each wall exhibited strong recovery (80% to 95%) following the elastic loading cycles. Displacement recovery was affected by the application of axial load. To illustrate this behaviour, Figure 5.17 shows the effect of the axial load on the displacement response at midspan of CH7800a. Following the load cycle with 80 kN of axial load, the out-of-plane and axial loads were removed resulting in a residual displacement of approximately 23 mm. During the subsequent loading to 100 kN of axial load, the displacement at midspan recovered to 10 mm as the axial load approached 40 kN (without any applied out-of-plane load). Thereafter no further recovery in the displacement was observed as the axial load was ramped up to 100 kN. Similarly, following the out-of-plane loading cycle with 100 kN of applied axial load, the residual displacement was approximately 10 mm upon removal of the out-of-plane load. Thereafter, the residual out-of-plane displacement increased when the axial load approached approximately 20 kN, returning to 23 mm of displacement when the axial load was fully removed.

Chapter 5 – Slender Wall Testing: 8 m Tall Walls
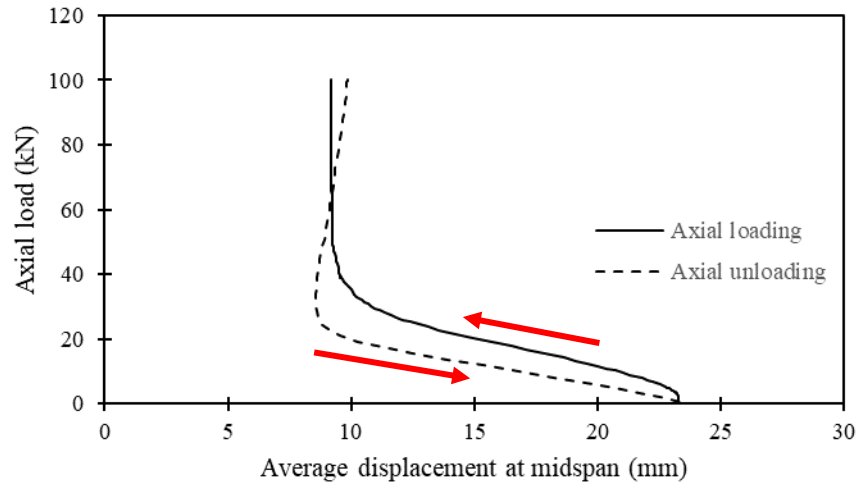
Figure 5.17: Displacement recovery with increasing axial load for wall CH7800a (no applied out-of-plane load)

5.6   Plastic Response

The total out-of-plane load- and moment-displacement responses of the walls when loaded beyond the yield point are illustrated in Figure 5.18. For these tests, the yield displacement, Δ_y, is defined as the mid-span displacement at which the average recorded strain of the reinforcing bars in the region of maximum moment reached the yield strain (yield strain determined from bar coupon testing), and the ultimate displacement, Δ_{ult}, is the displacement corresponding to a drop of 20% from the peak out-of-plane load or the maximum displacement achieved during the plastic loading cycle (whichever is less). The displacement and corresponding out-of-plane load resistance of the walls at Δ_y and at Δ_{ult} are provided in Table 5.5 and Table 5.6, respectively. Plastic loading of the walls demonstrated a displacement ductility (Δ_{ult}/Δ_y) of 1.3 and 1.5 for the conventionally reinforced Walls CH7800a and CH7800b, respectively; in contrast, the NSM reinforced Walls NH7800a and NH7800b had a ductility of 2.6, and 2.0, respectively.

Chapter 5 – Slender Wall Testing: 8 m Tall Walls
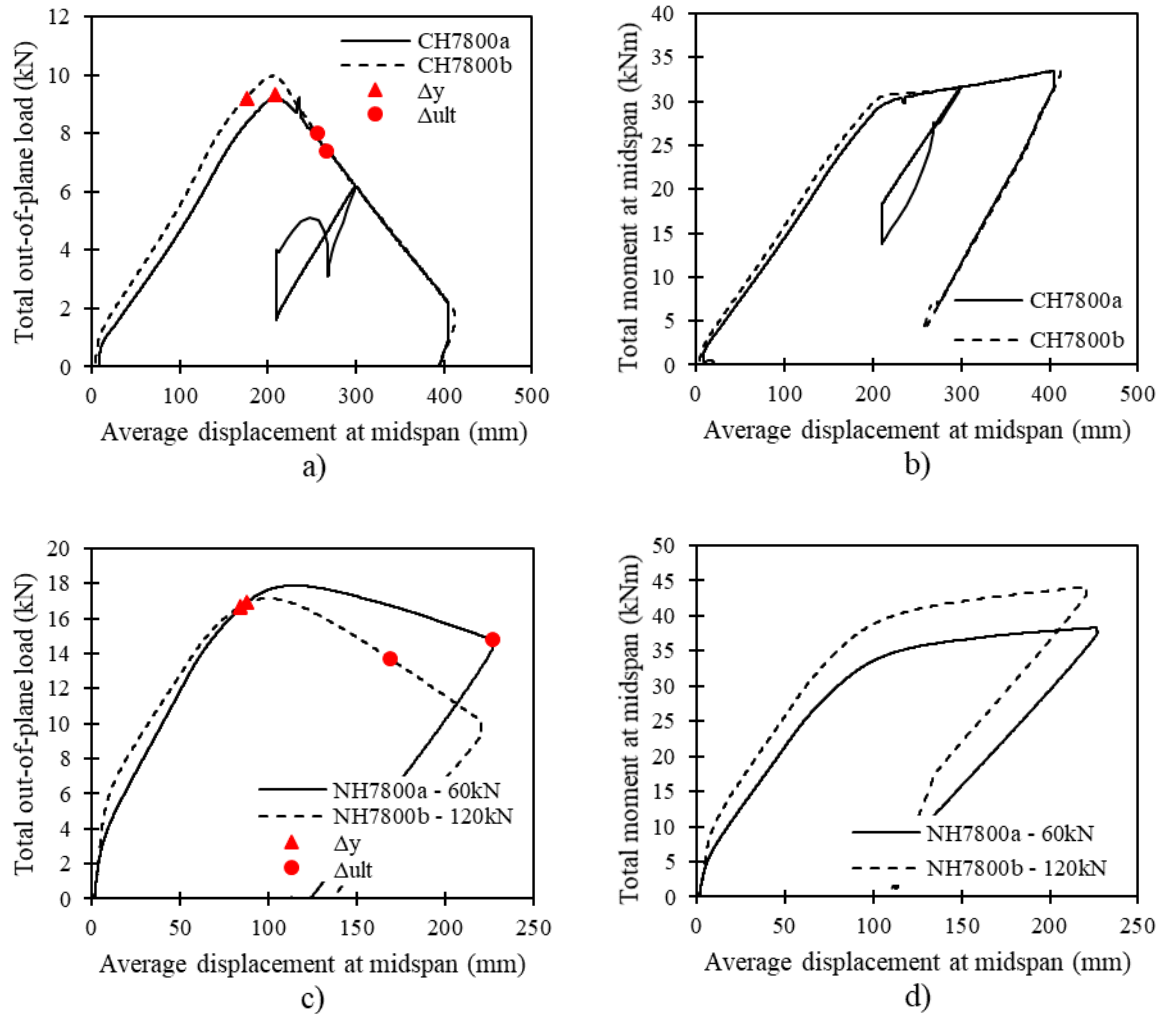
Figure 5.18: Post yielding response of masonry walls: a) load-displacement response of conventionally reinforced walls with 60kN of imposed axial load; b) moment-displacement response of conventionally reinforced walls with 60kN of imposed axial load; c) load-displacement response of NSM reinforced walls with 60kN and 120 kN of imposed axial load; and d) moment-displacement response of NSM reinforced walls with 60kN and 120 kN of imposed axial load

Table 5.5. Displacement and load at global yielding

Axial load (kN)	Midspan displacement at yielding, Δ_y (mm)				Total out-of-plane load at Δ_y (kN)			
	CH7800		NH7800		CH7800		NH7800	
	a	b	a	b	a	b	a	b
60	208	176	88	-	9.3	9.2	16.9	-
120	-	-	-	84	-	-	-	16.7

Note: the yield displacement Δ_y is the displacement at which the average strain of the bars in tension in the region of maximum moment exceeds the yield strain for that bar type (2300 µm/m for the 20M bars, 2700 µm/m for the 10M bars)

Table 5.6. Displacement and corresponding load at the ultimate displacement

Axial load (kN)	Maximum midspan displacement, Δ_{ult} (mm)				Corresponding total out-of-plane load at Δ_{ult} (kN)			
	CH7800		NH7800		CH7800		NH7800	
	a	b	a	b	a	b	a	b
60	267	256	227	-	7.4	8.0	14.8	-
120	-	-	-	169	-	-	-	13.7

The walls with conventional reinforcement (CH7800a and CH7800b) were both loaded with the same axial load (60 kN) for the plastic loading cycle. Prior to yielding, CH7800b exhibited higher strength and flexural stiffness compared to CH7800a; however, both the load and moment resistances of the walls converged as the walls exceeded the yield point. Both walls exhibited an increase in moment resistance beyond yielding consistent with the post-yielding behaviour of the reinforcing steel bars, however the out-of-plane load resistance decreased by 80% as the displacement at midspan reached twice the yield displacement due to $P\text{-}\Delta$ effects.

Wall NH7800b was loaded beyond the yield point with twice the axial load that was applied to the other walls. Both Wall NH7800a and Wall NH7800b, with NSM reinforcement, exhibited higher strength and flexural stiffness compared to the walls with conventional reinforcement and reached their yield point at approximately half the displacement at midspan. The peak out-of-plane load resistance of NH7800b was approximately 4% lower than NH7800a due to the larger $P\text{-}\Delta$ effects; however, the moment resistance at yielding of NH7800b was approximately 9% higher than NH7800a due to the increased axial load on the cross-section. Beyond yielding, the moment resistance of NH7800b remained higher than NH7800a; however, the out-of-plane load resistance of NH7800b decreased more steeply than NH7800a due to $P\text{-}\Delta$ effects being larger with the greater axial load. As NH7800a and NH7800b reached twice the yield displacement; there was a 17% and 41% decrease in total out-of-plane load resistance, respectively.

5.6.1 Differences between duplicate walls

Minor differences in the responses were observed between duplicate walls (CH7800a vs. CH7800b and NH7800a vs. NH7800b). Although some of these differences may be attributed to the different order of

Chapter 5 – Slender Wall Testing: 8 m Tall Walls

loading conditions (ascending or descending order of imposed axial load) and the resulting difference in stress history (damage) at the time of a particular loading cycle, minor variations in the placement of reinforcing bars are also a contributing factor. Bar positioners were used to facilitate centering of the reinforcing bars within the cells of walls CH7800a and CH7800b during grouting as shown in Figure 5.19. Measurements taken from the walls after testing indicate that the position of these bars deviated by up to 14 mm from the centre of the wall. The constraints of the grooves cast into the SRCMU blocks limited the deviation from the desired NSM bar position, resulting in a maximum deviation from the desired position (centred at 20 mm from the wall surface) of 6.5 mm. For walls CH7800a and CH7800b, the maximum deviation of 14 mm represents approximately 15% of the effective depth from the extreme compression fibre to the centroid of the reinforcement and could have a significant effect on the flexural stiffness and strength. The maximum variation in the position of the NSM reinforcement represents less than 5% of the effective depth to the tension reinforcement and therefore is less likely to have affected the flexural strength and stiffness response.
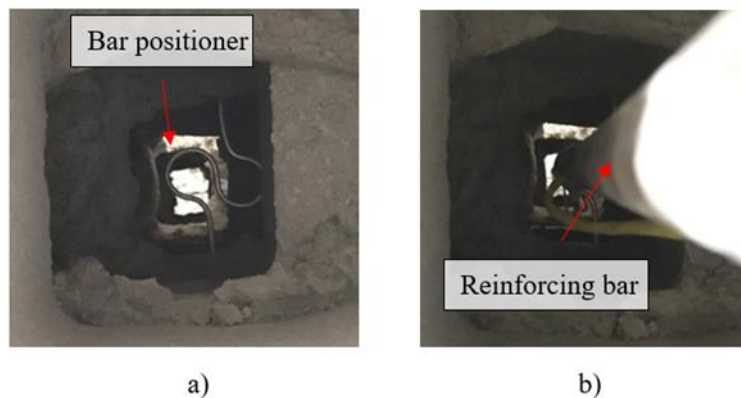
Figure 5.19: Bar positioners to maintain the reinforcing bars within the centre of the wall cross-section during grouting: a) before placing the reinforcing bar; and b) after placing the reinforcing bar

5.6.2 Cracking

The cracking patterns for all four walls were similar within the elastic displacement range; visible cracks consisted exclusively of horizontal cracks at the interface between mortar and the CMUs. These cracks were finer for the walls with NSM reinforcement due to the lower displacement and higher flexural stiffness and did not appear to continue through the epoxy as shown in Figure 5.20. Crack opening width was

Chapter 5 – Slender Wall Testing: 8 m Tall Walls

estimated from the readings of the surface-mounted linear transducers, which spanned two mortar joints (400mm) near the midspan of the walls. Dividing the transducer extension by a factor of two suggests an average crack opening width of 0.75 mm for wall CH7800b and 0.35 mm for NH7800b as the reinforcing bar strain reached 1800 µm/m (for all axial load levels).
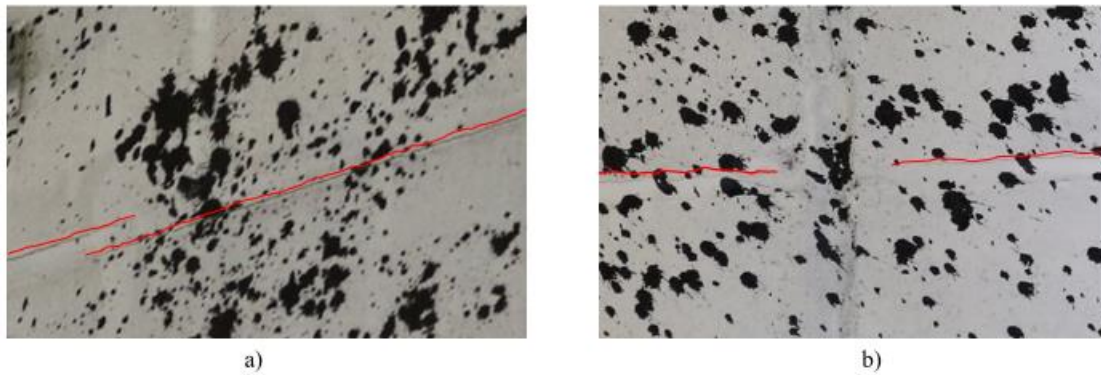
Figure 5.20: Horizontal cracking at the mortar joints near the midspan at 90% of the nominal reinforcement yield strain: a) Wall CH7800b; and b) Wall NH7800b

Beyond the yield point, the cracks at the mortar joints of the conventionally reinforced walls widened with increasing displacement, reaching an average width of over 5 mm as shown in Figure 5.21 a). The walls with NSM reinforcement developed herring bone cracks along the reinforcing bars in addition to the horizontal cracks at the mortar joints, as shown in Figure 5.21 b). The maximum average width of the horizontal cracks in the NSM walls was 2.4 mm.
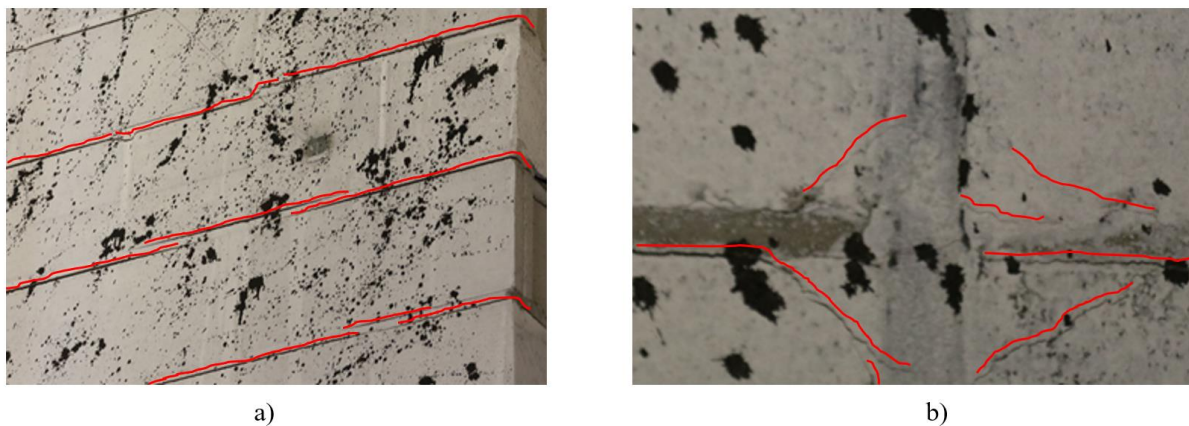
Figure 5.21: Cracking of walls at twice the yield displacement: a) horizontal mortar joint cracks in Wall CH7800a; b) herring bone cracking in Wall NH7800a

Chapter 5 – Slender Wall Testing: 8 m Tall Walls

5.6.3 Displaced shape of the walls

The displaced shape of the walls when the maximum reinforcement strain reached 1800 μm/m is illustrated in Figure 5.22. To facilitate the comparison of the shape, the displacements were normalized by the displacement at 1000 mm from the bottom pin connection for each wall. There is no apparent difference between the displaced shape of the walls with conventional or NSM reinforcement; however, with increasing axial load, there appears to be more severe curvature at the midspan compared to the shape of the walls without applied axial load. This trend is illustrated in Figure 5.23 for wall NH7800a; however similar trends were observed for each of the walls tested.
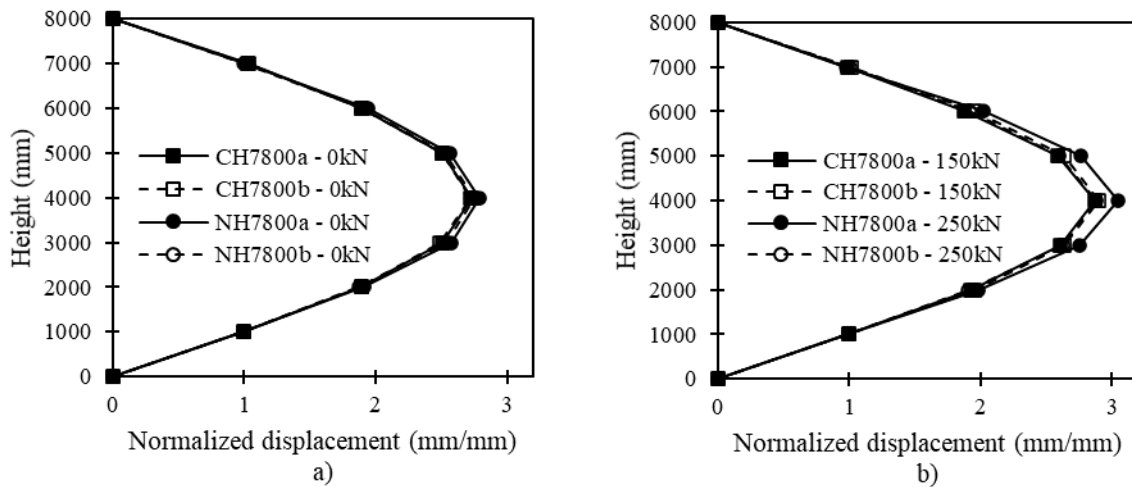
Figure 5.22: Displaced shape of walls at reinforcement strain of 1800μm/m: a) 0 kN applied axial load; and b) maximum applied axial load

Chapter 5 – Slender Wall Testing: 8 m Tall Walls
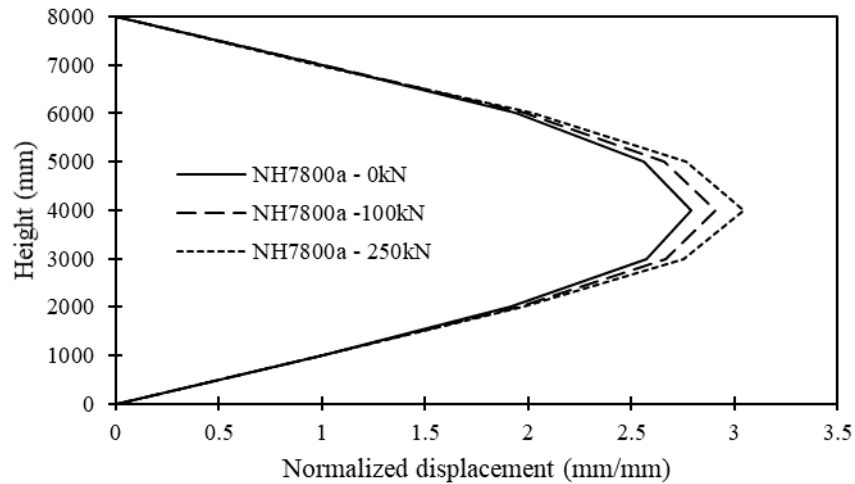
Figure 5.23: Displaced shape of wall NH7800a at reinforcement strain of 1800 μm/m with various applied axial loads

Both a parabola and a sine curve provide a good fit to the displaced shape of the walls, however the sine curve follows the displaced shape more closely for the walls loaded in the elastic range, as shown in Figure 5.24.
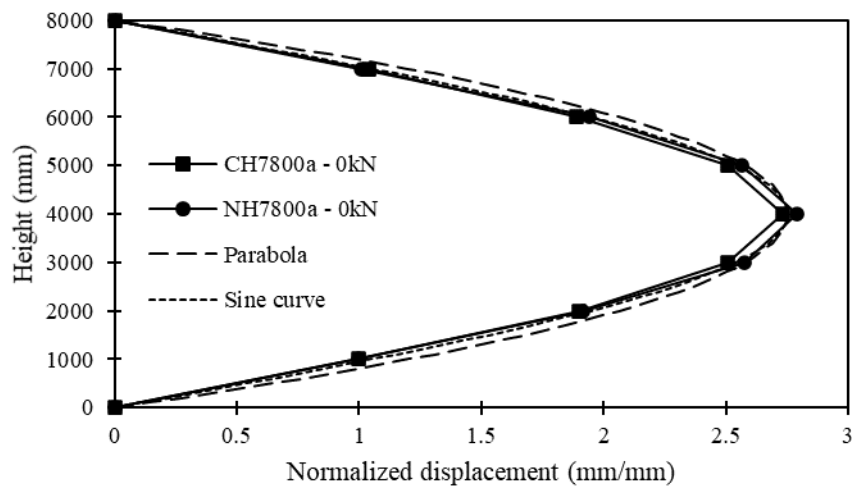
Figure 5.24: Displaced shape of walls at reinforcement strain of 1800μm/m with 0 kN applied axial load, overlaid with sine curve and parabola

When the walls were loaded beyond the yield point, the curvature became more concentrated at the midspan in the region where yielding was occurring, as shown in Figure 5.25.

Chapter 5 – Slender Wall Testing: 8 m Tall Walls
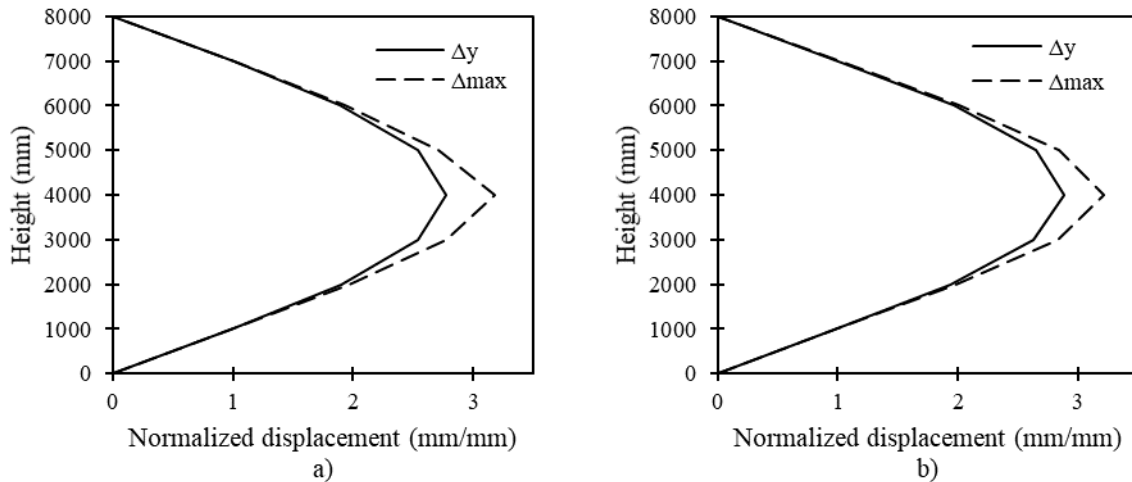
Figure 5.25: Displaced shape at the yield point and at the maximum achieved displacement with 60 kN of axial load: a) wall CH7800a; and b) wall NH7800a

5.6.4 Primary and secondary moments

During testing, the primary moments were induced by out-of-plane loading and secondary moments were caused by the product of out-of-plane displacements and axial load (from the imposed load and from self weight): the *P-Δ* effect. For walls with large axial loads, the secondary moment effects can dominate the response at higher displacements. Figure 5.26 shows the primary, secondary, and total moment responses of walls CH7800b and NH7800b with 100 kN of imposed axial load. As strain in the reinforcing bars of Wall CH7800b approached 1800 μm/m, the secondary moment accounted for 59% of the total moment at midspan, and the remainder of the moment was the result of the primary moment. In contrast, the secondary moment accounted for only 23% of the total moment at the same reinforcement strain level for Wall NH7800b. This difference is attributed to the lower displacement of NH7800b. Comparing the moment response of the walls at the same maximum reinforcement strain (1800 μm/m), the ratio of secondary to total moment for walls with conventional reinforcement (CH7800a and CH7800b) was approximately 250% that of the walls with NSM reinforcement (NH7800a and NH7800b) for all applied axial load cases. The higher flexural stiffness resulting from the placement of the reinforcing bars using the NSM technique resulted in lower displacements, in turn reducing the secondary moment effects.

Chapter 5 – Slender Wall Testing: 8 m Tall Walls
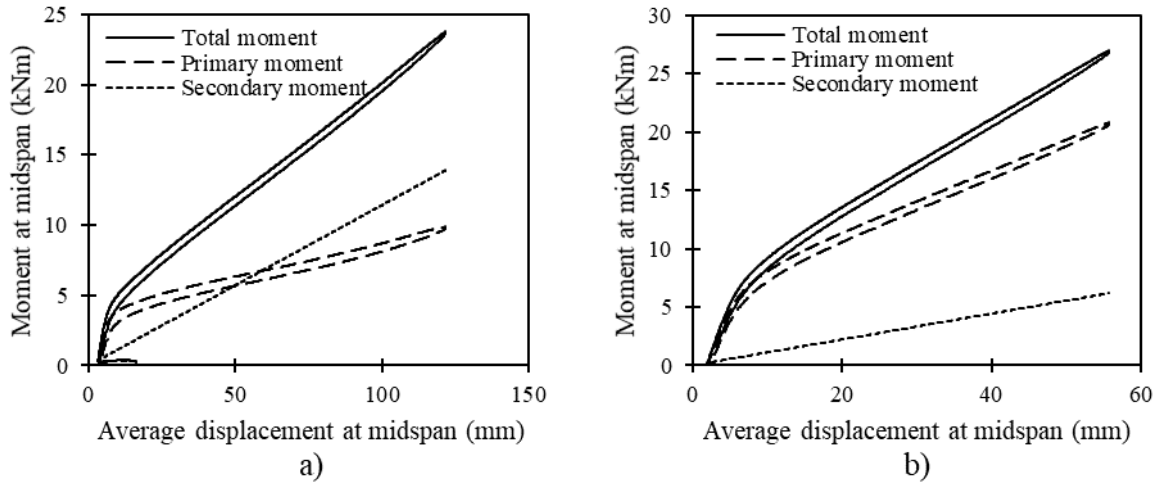
Figure 5.26: Primary, secondary, and total moment response: a) wall CH7800b with 100 kN of imposed axial load; and b) wall NH7800b with 100 kN of imposed axial load

It should be noted, however, that for the results in Figure 26 the secondary moment from self weight was calculated by lumping the weight of the masonry above the midspan at the top of the walls (where the imposed axial load was applied). This is a conservative method for calculating the secondary moment and is often recommended for design (Hatzinikolas and Korany 2005; Drysdale and Hamid 2005; Amrhein and Lee 1984). An accurate calculation of the secondary moment from self weight at a given point along the height of the wall requires the location of the centre of gravity of the masonry above the section being considered. An exact calculation of this value is cumbersome; however, an approximation can be achieved by using an idealized shape function. For a wall with a sinusoidal displaced shape of height π and a maximum displacement of 1, shown in Figure 5.27 a), the displacement x as a function of height y may be calculated using Equation (5.2).

Equation 5.2 $\qquad x = sin(y)$

Chapter 5 – Slender Wall Testing: 8 m Tall Walls
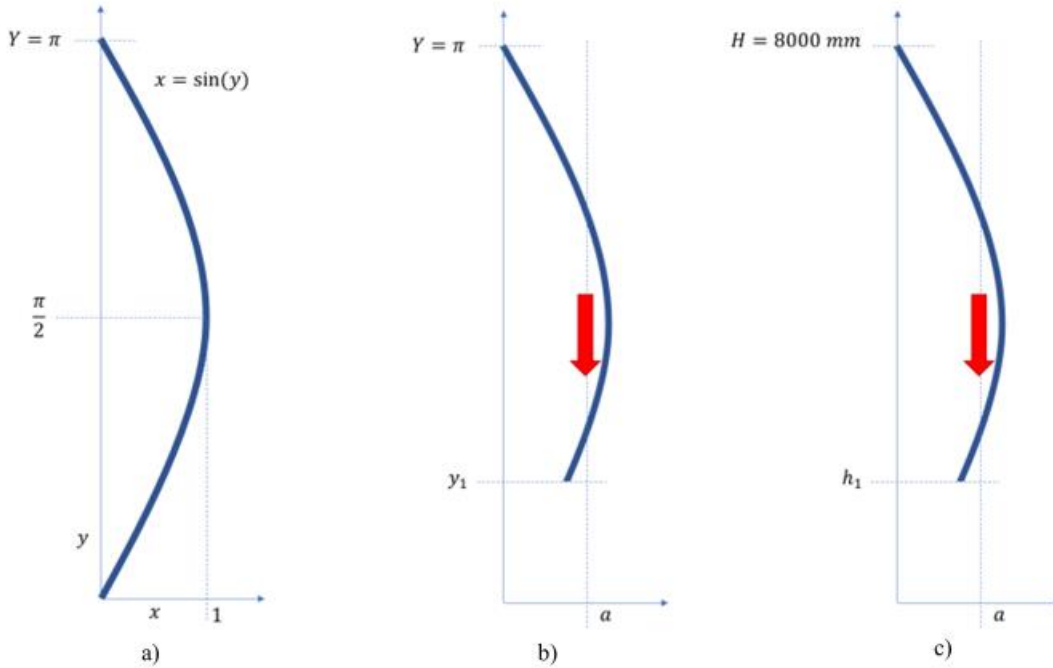
Figure 5.27: Idealized shape of thin wall: a) displaced wall of height π; b) centre of gravity of wall above y₁; and c) centre of gravity of wall above h₁ for 8m tall wall

The moment of a segment of the thin wall from a point along its height, y_i, to the top of the wall, Y, about an arbitrary axis a, as shown in Figure 5.27 b), can be calculated using the integral in Equation (5.3). The centre of gravity is located along the axis a for which the moment is nil.

Equation 5.3
$$M = \int_{y_i}^{Y} \sin(y) - a \; dy$$

Carrying out the integration as shown in Equation (5.4), the moment M about the arbitrary axis a can then be calculated using the definite integral as shown in Equation (5.5). By setting $M=0$ and isolating a, the location of the centre of gravity a_i of the thin wall segment above y_i is established (Equation (5.6)).

Equation 5.4
$$\int \sin(y) - a \; dy \; = \; -\cos(y) - ay + C$$

Equation 5.5
$$M = \int_{y_i}^{\pi} \sin(y) - a \; dy = -\cos(Y) - a \, Y + \cos(y_i) + a \, y_i$$

Equation 5.6
$$a_i = \frac{-\cos(Y) + \cos(y_i)}{Y - y_i}$$

Chapter 5 – Slender Wall Testing: 8 m Tall Walls

By solving Equation (5.6) at the midspan, the centre of gravity of a half-wall is located at 63.7% of the midspan displacement. This value differs from the value used by the ACI-SEASC Task Committee on Slender Walls (1982) who assumed a value of 66.7% for their walls subjected to a uniformly distributed load, which corresponds to the centre of gravity of half of a parabola.

To estimate the secondary moment due to self weight at the location of each strain gauge, the variables in Equation (5.6) are transformed to fit an 8 m tall wall, illustrated in Figure 5.27 c), as follows:

$$Y = H \frac{\pi}{8000}$$

$$y_i = h_i \frac{\pi}{8000}$$

Using this approach, the location a_i of the centre of gravity of the masonry above the section h_i was determined at the elevation of each strain gauge. Table 5.7 lists the value of a_i for a unit displacement at midspan ($\varDelta_{max} = 1$). Using this information, the ratio of the distance from the origin to the centre of gravity of the wall above to the displacement $a_i/\varDelta_i$ can be used to calculate the moment from the self weight through Equation (5.7).

Table 5.7: Location of the centre of gravity of the wall above various sections

h_i	$a_i/\varDelta_{max}$	$\varDelta_i/\varDelta_{max}$	$a_i/\varDelta_i$
6700	0.250	0.489	0.511
6300	0.322	0.619	0.519
5900	0.389	0.734	0.530
5500	0.453	0.831	0.544
5100	0.510	0.908	0.562
4900	0.537	0.938	0.573
4700	0.562	0.962	0.584
4500	0.586	0.981	0.597
4300	0.607	0.993	0.612
4100	0.627	0.999	0.628
3900	0.645	0.999	0.646
3700	0.662	0.993	0.666
3500	0.676	0.981	0.690
3300	0.689	0.962	0.716
3100	0.700	0.938	0.746
2900	0.708	0.908	0.780
2500	0.720	0.831	0.866
2100	0.725	0.734	0.987
1700	0.722	0.619	1.166
1300	0.712	0.489	1.457

$$M_i = W_i(\Delta_i - a_i)$$

Or

Equation 5.7 $$M_i = W_i\Delta_i\left(1 - \frac{a_i}{\Delta_i}\right)$$

Where W_i is the weight of masonry above section h_i. This allows the moment from self weight to be accurately calculated for each section of interest along the height of the walls without the need to input displacement data from other locations. The displacement at the locations of interest $\varDelta_i$ (at mortar joints with a strain gauge), inputted into Equation (5.7), is determined by linear interpolation between the locations of measured displacement data. Figure 5.28 illustrates the secondary moment from self weight during the first loading cycle of Wall CH7800.

Chapter 5 – Slender Wall Testing: 8 m Tall Walls
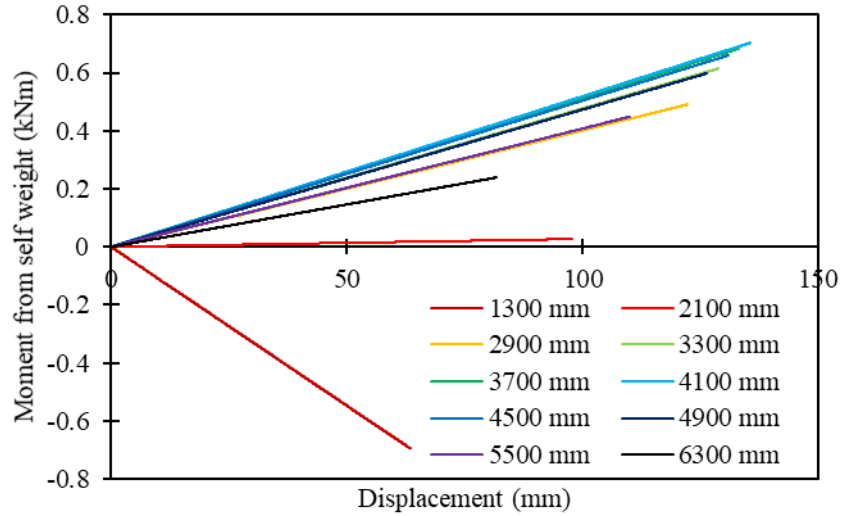
Figure 5.28: Secondary moment from self weight for the first loading cycle of Wall CH7800a (continuous data) at various locations along the wall height

This secondary moment from self-weight of the wall reduced the total moment at 1300 mm from the bottom pin connection of Wall CH3700a for the first loading cycle (with no applied axial load) by 11% as shown in Figure 5.29. For other loading cases and locations along the wall height, the effect of the secondary moment from the self-weight was less – typically contributing between 1 and 5% of the total moment.
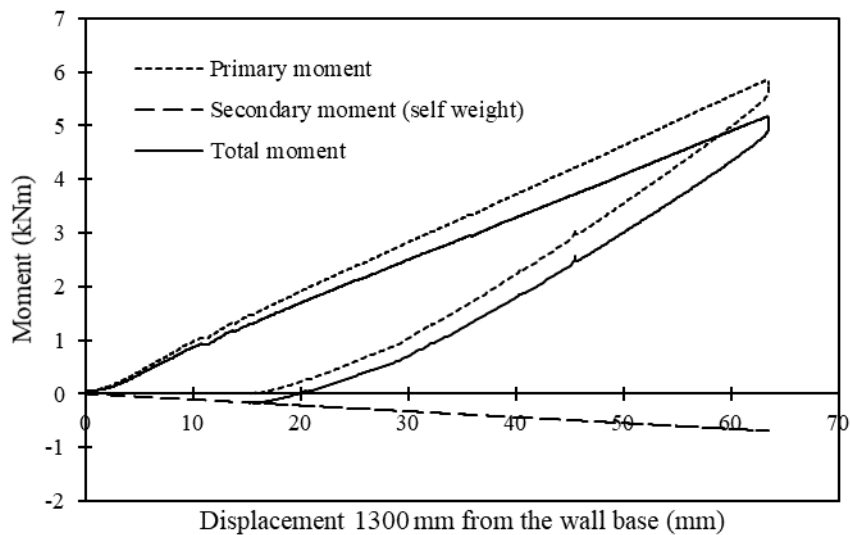
Figure 5.29: Primary, secondary, and total moment for Wall CH7800a at 1300mm from the base: first loading cycle with no applied axial load

The total moment-reinforcement strain response of the walls was bi-linear within the elastic response range of the walls as illustrated in Figure 5.30. The strain response was similar throughout the height of the walls;

Chapter 5 – Slender Wall Testing: 8 m Tall Walls

however, for the conventionally reinforced walls, there was a wider range in the values of the strain response. This may be due, in part, to the path of cracking through the grout material being more variable compared to cracking through the much thinner layer of epoxy surrounding the steel bars used for the NSM reinforcement. This results in greater variability in the distance from the gauge to the nearest crack for the walls with conventional reinforcement.
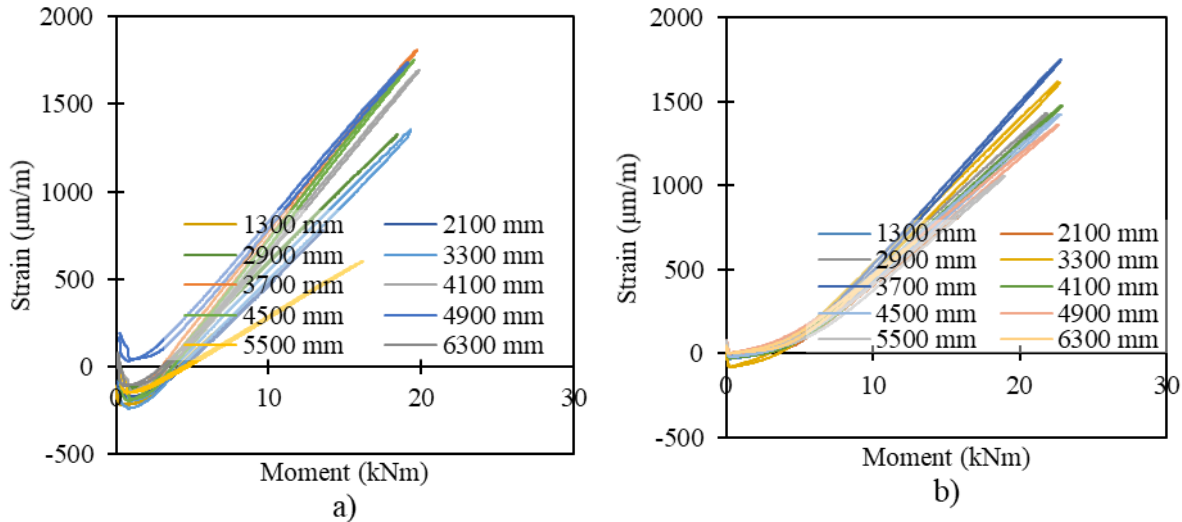
Figure 5.30: Moment-strain response with 60kN of applied axial load at various sections along the height: a) Wall CG7800a; and b) Wall NG7800a

5.7 Summary of Results from Testing 8 m Tall Walls

Testing of 8 m tall slender RM walls reached the limit of the available height in the high bay laboratory for testing of structural members. The success of these tests contributes to the limited available literature on testing of full-scale slender RM walls subjected to combined axial and out-of-plane loads.

Both the conventionally reinforced walls and the walls reinforced with NSM steel bars exhibited strong elastic recovery after loading cycles during which a maximum reinforcement strain of 1800 µm/m were reached. Each wall also exhibited a ductile response when loaded beyond the yield point of the reinforcement.

The walls with NSM reinforcement had approximately half the displacement response of the walls with conventional reinforcement as the reinforcing bars reached 1800 µm/m. Although the moment resistance

Chapter 5 – Slender Wall Testing: 8 m Tall Walls

of each wall was similar, the out-of-plane load resistance of the walls with NSM reinforcement was greater due to the reduced P-Δ effects.

The displacement ductility of the conventionally reinforced walls, based on the out-of-plane load response, ranged from 1.3 to 1.5 with 60 kN of applied axial load. The walls with NSM reinforcement had a displacement ductility of 2.6 and 2.0 with applied axial loads of 60 kN and 120 kN, respectively. The greater effective ductility of the walls with NSM reinforcement arises from the decreased P-Δ effects which allows the maintenance of high out-of-plane load resistance.

With increasing axial load, each wall developed a bilinear load-displacement and moment-displacement response.

With an applied axial load of 150 kN, the walls with conventional reinforcement exhibited signs of elastic buckling (decreased out-of-plane load resistance with increasing displacement without yielding of the reinforcement). The walls with NSM steel reinforcement were subjected to imposed axial loads up to 250 kN without any signs of elastic buckling.

The displaced shape of the walls at low levels of axial load resembled a sine curve. With increasing applied axial load, additional curvature is concentrated at the mid-span, where moments are magnified the most. Using the idealized sinusoidal displaced shape, the secondary moment from self-weight was determined for points of interest along the height of the walls. This revealed that there was more variation in the moment-strain response of the walls with conventional reinforcement compared to the walls with NSM steel reinforcement.

6 Analysis

Following testing of the 3 m tall and 8 m tall Reinforced Masonry (RM) walls, extensive data analysis was conducted to characterize the curvature and flexural stiffness response of these walls. The focus of this chapter is to provide insights regarding how the flexural stiffness of RM walls changes depending on the applied axial and out-of-plane loads. Current reinforced masonry design standards in Canada and in the United States impose stringent prescriptive requirements for the design of very slender masonry walls due to a lack of experimental data from tests on slender walls subjected to a combination of high axial loads and high out-of-plane loads. Although this experimental program only considers a limited range of reinforcement configurations and a single gross reinforcement ratio, important insights have been gained. These insights include the effect of axial load on the flexural stiffness of walls, how cracking affects flexural stiffness, as well as how increased stiffness of RM walls through NSM steel reinforcement can improve the load resistance of slender walls. A discussion of the masonry materials used for both testing series is also included.

6.1 Material Testing and Behaviour

The same type of materials was used for the construction of RM walls for the two testing series (3 m tall and 8 m tall walls), however some variability in the properties were observed. For example, a difference between the strength of the prisms constructed from conventional masonry units and those constructed from SRCMUs was observed for the prisms which accompanied the testing of the 3 m tall walls (discussed in Chapter 4). This difference was not observed in the initial testing of SRCMUs reported by Sparling (2015) and was attributed to the small thickness of concrete adjacent to the grooves in the commercially-cast units. The minimum thickness of concrete separating the inner edge of the central groove and the hollow cells was reduced by approximately 20% from the original design of the unit to avoid additional modifications to the block molds used for manufacturing. The difference between the units used for this experimental series and those cast at the University of Manitoba (Sparling 2015) is shown in Figure 6.1. Another possible

explanation is that there could have been a difference in the strength achieved between different casting runs – although the SRCMUs and conventional CMUs were produced by the same manufacturing plant, they may not have been produced in the same casting run.
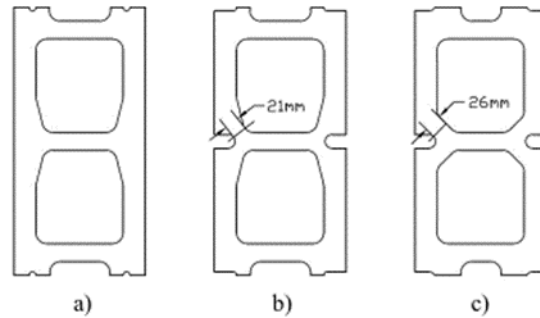
Figure 6.1: Cross section of masonry units: a) Conventional CMU; b) grooved SRCMUs used in the current study; and c) grooved SRCMUs used at the University of Manitoba (Sparling 2015)

The difference in prism strength was, however, not as large in the material tests that accompanied the 8 m tall wall tests. The conventional CMUs and SRCMUs for this series of wall tests were cast at the same time – they were shipped to site unsorted on pallets containing triplet block sets that were cast simultaneously (a single mold produced one conventional stretcher CMU, one bull-nosed splitter unit, and one SRCMU). The material properties derived from prism testing for both wall test series are presented in Table 6.1. Testing of individual masonry units also suggest that there was little difference between the strength of the conventional CMUs and the SRCMUs. Further experimental testing is required to determine the effect of the surface grooves on the compressive strength of SRCMUs.

Table 6.1: Prism test properties accompanying 3 m tall and 8 m tall wall tests

Prism type	Average prism strength 3 m walls / 8m walls (MPa)	Average Young's modulus 3 m walls / 8m walls (Mpa)
Conventional prism: hollow	23.1 / 17.5	18900 / 22 872
SRCMU prism: hollow	13.0 / 18.3	17500 / 18 919
Conventional prism: grouted	8.7 / 11.3	9800 / 14 413
SRCMU prism: grouted	6.1 / 11.0	7700 / 14 676

Differences in the mortar and grout strength (cast in non-porous molds) were also observed between the two test series, however these are unlikely to have significantly impacted the strength of the prisms, or the behaviour of the walls (Drysdale and Hamid 2005). Differences in the properties of the reinforcing steel

119

Chapter 6 – Analysis

bars were also observed, as indicated in Table 6.2. The difference between the yield stress and Young's modulus of the 10 M bars is attributed in part to the material handling process by the supplier; whereas the 10 M bars used for the 3 m tall walls tests had a defined yield plateau in their stress-strain response, those used in the construction of the 8 m tall walls had a curved stress-strain response. Figure 6.2 illustrates the difference in the stress-strain response of these two types of bars. The curved stress-strain response of the 10 M bars used in the construction of the 8 m tall walls could have been caused by mechanical straightening of the bars (yielding in tension) which could have pushed the bars to the onset of strain hardening; both bar types nonetheless had a very ductile strain response.

Table 6.2: Reinforcing bar properties accompanying 3 m tall and 8 m tall wall tests

| | Bar type | |
| | 10M | 20M |
Property	3 m walls / 8 m walls	3 m walls / 8 m walls
Nominal section area	100 mm	300 mm
Yield stress	432 / 540 Mpa	440 / 440 Mpa
Young's modulus	172 / 198 Gpa	182 / 191 Gpa
Maximum stress	567 / 678 Mpa	592 / 587 Mpa

Note: 0.2% offset method was used for the determination of the yield stress for the 10M bars in the 8 m tall walls
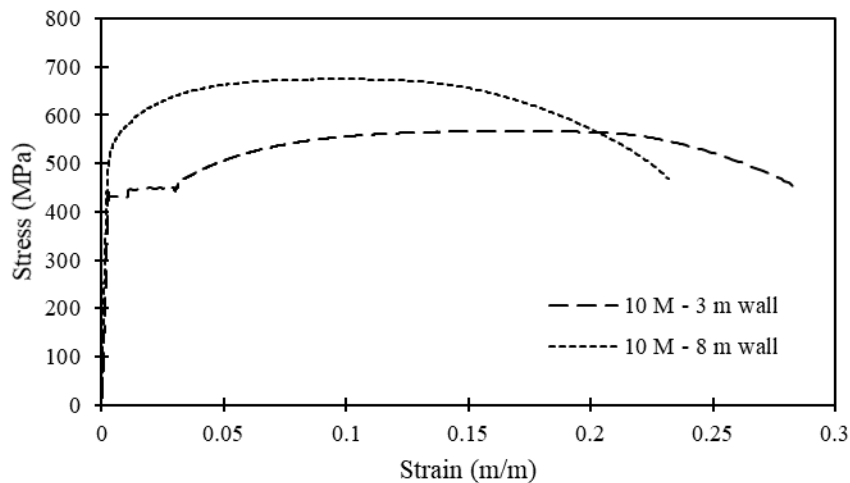
Figure 6.2: Stress-strain response of 10M reinforcing bars used in the construction of the 3 m tall and 8 m tall walls

6.2 Curvature Response

Curvature is the structural response of a member to bending. Curvature over a given length of a member leads to rotation and displacement. Resistance to curvature leads to flexural stiffness or rigidity against bending. Various instruments were applied to the RM walls during testing to measure curvature, and thereby assess the flexural stiffness of these structural members. Depending on the instrument used (strain gauge, out-of-plane displacement transducer, displacement transducer measuring strain on the wall surface), different approaches were required to convert the data into the curvature response.

6.2.1 Determining curvature from reinforcement strain

Curvature of a structural member section may be defined based on the strain profile at a given location. The placement of strain gauges in the walls with NSM reinforcement (NG3200, NH3200, NH3000, NH7800a and NH7800b) near the tension and compression faces of the walls, enabled a direct calculation of the curvature from the strain profile (dividing the difference in the strain between the two faces by the distance between the two reinforcing curtains) as shown in Figure 6.3. In certain cases, an average strain response was used to determine the curvature; in such cases, the average of the strain data points for gauges in tension or compression were taken along a single line through the cross section (at a mortar joint, or a set distance from a mortar joint). Alternately, the average of the data from multiple gauges (in tension or compression) located in the region of maximum moment located at the same distance from the nearest mortar joint was taken.

Chapter 6 – Analysis
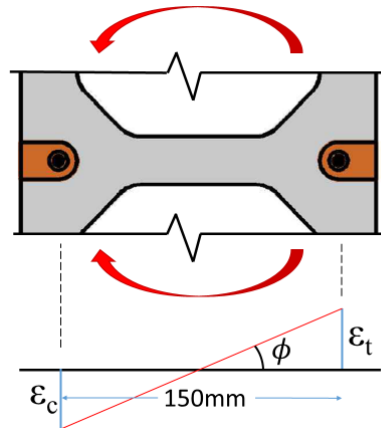
Figure 6.3: Measuring curvature from NSM reinforcement strain

For the 3 m tall walls with conventional embedded reinforcement (CG3200, CH3200), two methods were investigated to estimate the curvature. Both methods are based on a linear-elastic response for the steel and masonry. This is acceptable given that the intent is to establish the flexural stiffness prior to yielding, while the materials are responding in the elastic range. In Method 1, data from the strain gauges on the bars in the centre of the wall was used as the starting point for compatibility and equilibrium calculations, as illustrated in Figure 6.4 a). The compression force developed in the masonry and the tensile force in the reinforcement were calculated using the axial compressive stiffness of the masonry and the tensile properties of the reinforcing steel (from material testing presented in Chapter 4), respectively. This method assumes that there is no contribution from the masonry in tension and neglects the effect of the self-weight; at higher moments approaching yielding, these assumptions are more accurate.

Chapter 6 – Analysis

Left side (a):

$$C_m = \frac{E_m \varepsilon_{mc} c b}{2}$$
$$T_s = E_s \varepsilon_s A_s$$
$$\varphi = \frac{\varepsilon_{mc}}{c} = \frac{\varepsilon_s}{d - c}$$
$$0 = C_m - T_s$$
$$M_a = T_s \left(d - \frac{c}{3}\right)$$

Right side (b):

$$C_m = \frac{E_m \varepsilon_{mc} c b}{2}$$
$$T_s = E_s \varepsilon_s A_s$$
$$T_m = \frac{E_m \varepsilon_{tm}(d_2 - c) b}{2}$$
$$\varphi = \frac{\varepsilon_{mc}}{c} = \frac{\varepsilon_s}{d - c} = \frac{\varepsilon_{mt}}{d_2 - c}$$
$$0 = C_m - T_s - T_m$$
$$M_a = C_m \left(d - \frac{c}{3}\right) + T_m \left(d - c - 2\left(\frac{d_2 - c}{3}\right)\right)$$

a)   b)
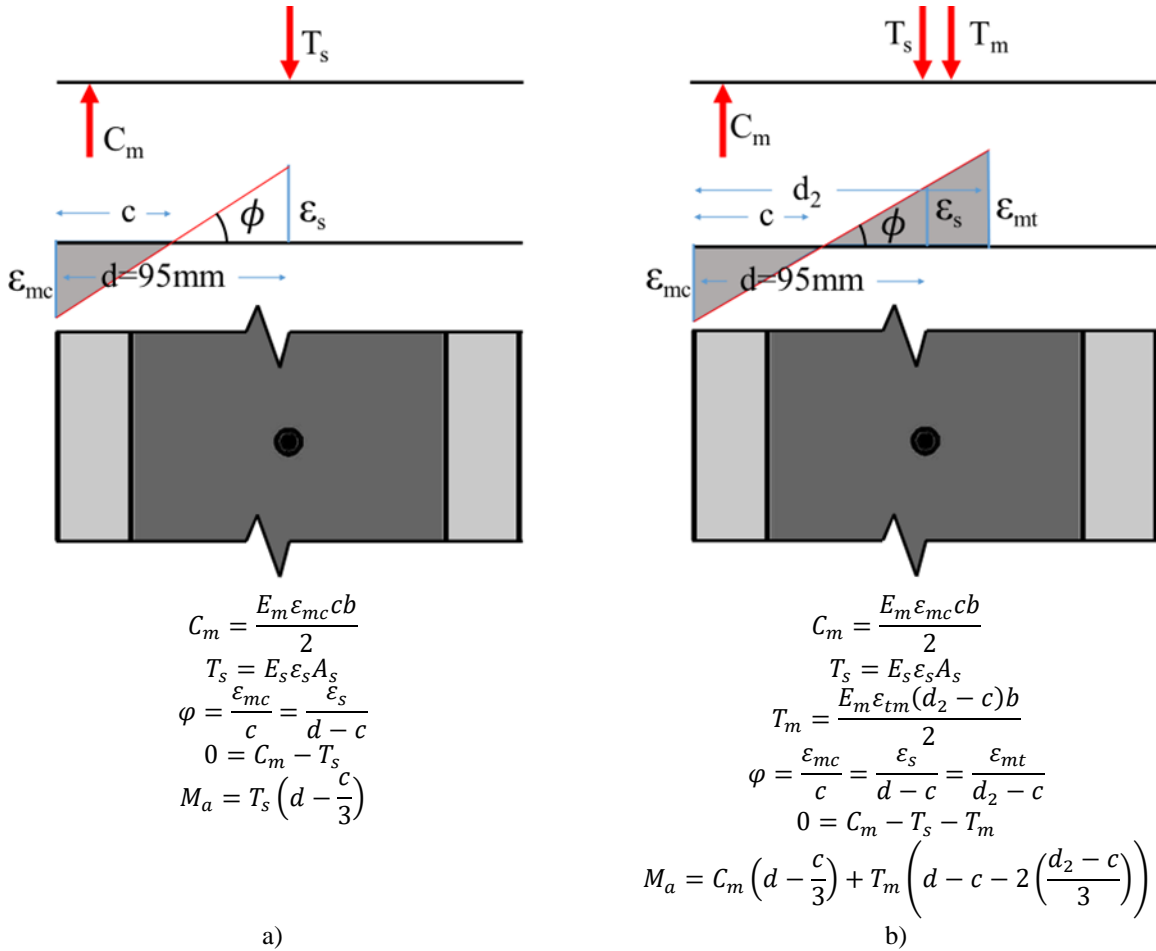
Figure 6.4: Determination of curvature for Walls CG3200 and CH3200: a) Method 1; and b) Method 2

Given that the applied moment in the walls were larger than the calculated moment resistance based on the assumptions in Method 1, specifically at lower levels of moment, Method 2 was developed to account for the contribution of the masonry in tension. In this method, strain compatibility is maintained, but the additional criterion of moment equilibrium at the location of the strain gauge is included by accounting for the contribution of a portion of the masonry in tension as illustrated in Figure 6.4 b). In this method, the section curvature and depth to maximum stress in tension (d_2) are varied iteratively until conditions of equilibrium of forces and moments are satisfied. For Walls CG3200 and CH3200, Method 1 resulted in a smaller curvature, whereas the consideration of tension in the masonry led to an increase in section curvature. [Note: The reduced effective area in the web of CH3200 due to the hollow cells is addressed in Methods 1 and 2 by using a 2-layered approach wherein the face shell and web regions were considered separately]

Chapter 6 – Analysis

A similar approach to Method 1 was adopted to estimate the curvature of the 8 m tall RM walls with conventional reinforcement (CH7800a and CH7800b), however the effects of the applied axial load and self weight were accounted for. This method is illustrated in Figure 6.5. Method 2 was not applied to the analysis of the 8 m tall walls since the cyclical nature of the testing reduced or eliminated the effect of tensile stress in the masonry material at the location of mortar joints (where the strain gauges were located).
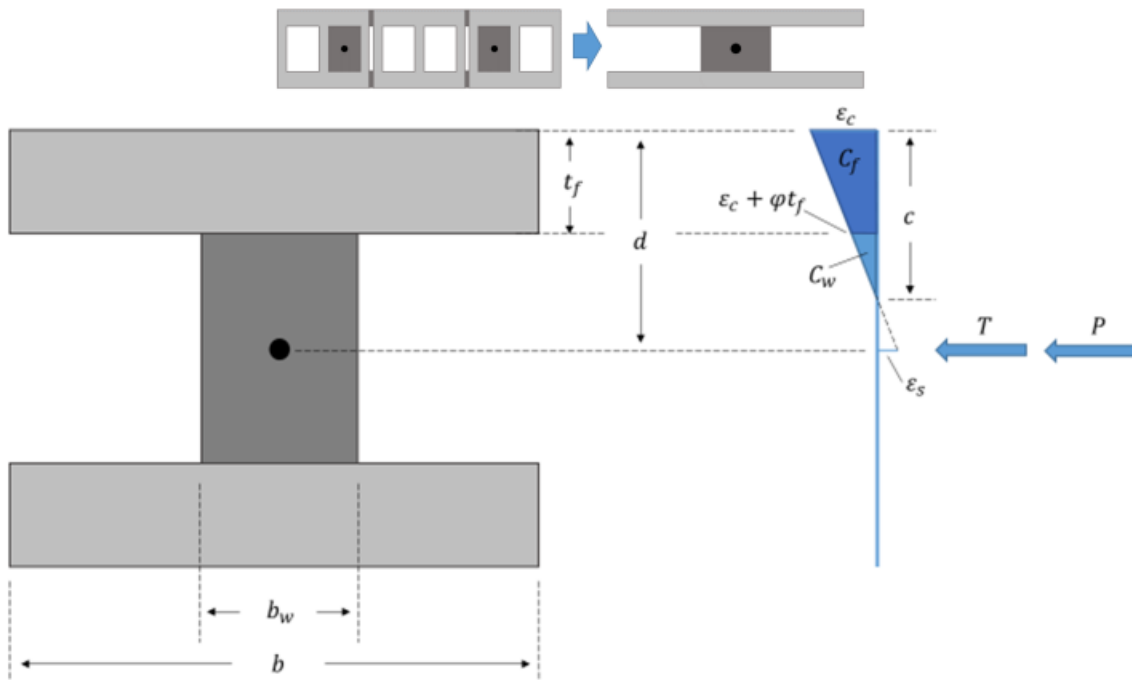
Figure 6.5: Cracked section flexural response of conventionally reinforced, partially grouted masonry wall with applied axial loading

The section curvature may be defined as shown in Equation (6.1). The depth from the extreme compression fibre to the neutral axis c that results in a solution to Equation (6.6), given the relations and definitions established in Equations (6.2) to (6.5), was determined iteratively for each strain value, ε_s recorded during testing.

Equation 6.1 $\qquad \varphi = \dfrac{\varepsilon_s}{d-c}$

Equation 6.2 $\qquad \varepsilon_c = \varepsilon_s - \varphi d$

Chapter 6 – Analysis

Equation 6.3
$$C_f = \begin{cases} c \le t_f, & \dfrac{\varepsilon_c E_c bc}{2} \\ c > t_f, & \left(\dfrac{2\varepsilon_c + (\varphi t_w)}{2}\right) E_c bt_f \end{cases}$$

Equation 6.4
$$C_w = \begin{cases} c \le t_f, & 0 \\ c > t_f, & \dfrac{(\varepsilon_c + \varphi t_f) E_c b_w (c - t_f)}{2} \end{cases}$$

Equation 6.5
$$T = A_s E_s \varepsilon_s$$

Equation 6.6
$$0 = P + T + C_f + C_w$$

Calculation of the moment using Equation (6.7) compared to the applied total moment during testing revealed that this method overestimates the moment resistance, however the two values converge with increasing applied moment (and increasing reinforcement strain).

Equation 6.7
$$M_a = \begin{cases} c \le t_f, & C_f\left(d - \dfrac{c}{3}\right) \\ c > t_f, & (\varepsilon_c + \varphi t_f) E_c bt_f \left(d - \dfrac{t_f}{2}\right) + \left(\dfrac{\varphi t_f{}^2 b}{2}\right)\left(d - \dfrac{t_f}{3}\right) + C_w\left(d - c + \dfrac{2(c - t_f)}{3}\right) \end{cases}$$

6.2.2 Determining curvature from average surface strain

For each of the 8 m tall walls (CH7800a, CH7800b, NH7800a, and NH7800b), surface strain on the tension and compression faces of the walls were monitored during the tests using displacement transducers over a gauge length of 400 mm as discussed in Chapter 5. Curvature in the walls was calculated by dividing the difference in the strain on the tension and compression side of the walls by the distance between the strain measurements. The layout of the instruments and the procedure for calculating curvature is illustrated in Figure 6.6. This set-up was used to determine the average curvature over two courses of masonry units which can be calculated using Equation 6.8.

Chapter 6 – Analysis
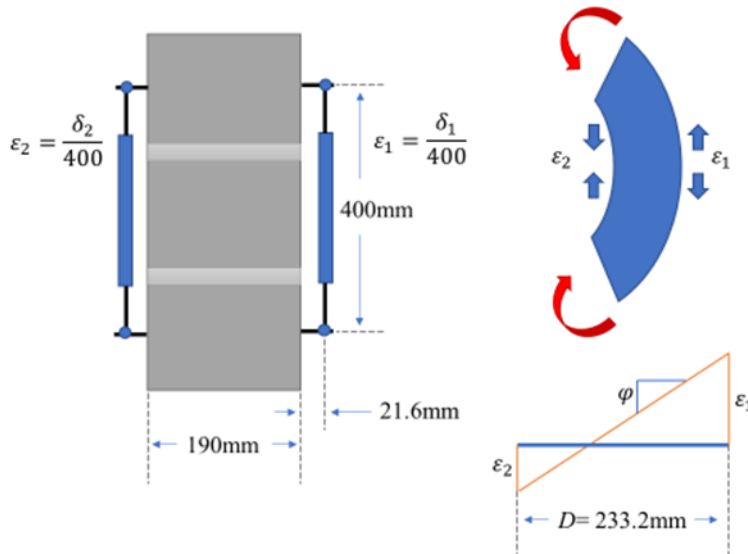
Figure 6.6: Determination of curvature from surface strains

Equation 6.8 $\qquad \varphi = \frac{\varepsilon_1 - \varepsilon_2}{D}$

The results from this measure of curvature can however be skewed since the displacement transducers measure the chord displacement between the connection points and not the displacement along the curved surface of the walls as it displaces. As illustrated in Figure 6.7 a), the horizontal distance D between gauges reduces to a value D' as the curvature of the section increases.
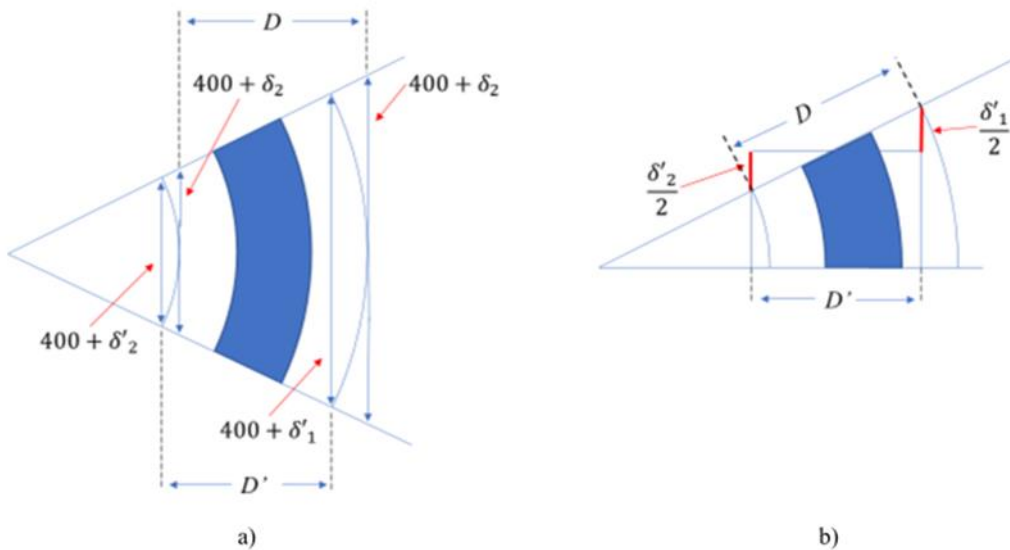
Figure 6.7: Measuring curvature using surface displacement transducers: a) Skewing of curvature measurement; and b) correction of measurement

Chapter 6 – Analysis

Assuming a circular curvature, the updated distance *D'* can be calculated using Equation 6.9 as illustrated in Figure 6.7 b).

Equation 6.9
$$D' = \sqrt{D^2 - \left(\frac{\delta'_1}{2} - \frac{\delta'_2}{2}\right)^2}$$

However, this effect is negligible over the range of curvature measured in the elastic loading cycles, and represented a change in *D'* of only 0.06% relative to the original *D* value of 233.2 mm even at the maximum curvature achieved during the plastic loading cycles of the conventionally-reinforced walls: at the midspan of Wall CH3200b at the maximum displacement during the plastic loading cycle with 60kN of applied load, δ'_1 reached 13 mm and δ'_2 reached -3 mm resulting in a value of *D'* of 233.06 mm). The original value of *D* (233.2 mm) was therefore used throughout the analyses of the results.

6.3   Flexural stiffness Response of 3 m Tall Masonry Walls

The flexural stiffness of an RM wall section under flexural loading is known to be influenced by the magnitude of the applied axial and flexural loads. In this section, data collected from strain gauges, as well as displacement transducers are used to examine the local and global flexural stiffness response of the 3 m tall RM walls. These results are compared to the global flexural stiffness response prescribed by the CSA S304-14 (CSA Group 2019a) design provisions, as well as a simple rational analysis of the wall sections.

6.3.1   Flexural stiffness from reinforcing bar strain

Flexural stiffness was evaluated by dividing the moment by the curvature (curvature estimated using the strain gauge data and Methods 1 and 2 for Walls CG3200 and CH3200, and by direct calculation using strain gauge data for Walls NG3200, NH3200, and NH3000) at the same location. Figure 6.8 a) and b) provide stiffness values near the mid-span up to the onset of yielding in the grouted walls, and in the partially grouted and hollow walls, respectively. [Note that for Wall NH3200, only the strain gauges in the upper half of the wall, where full grouting was achieved, were used in the curvature and flexural stiffness calculations].

Chapter 6 – Analysis
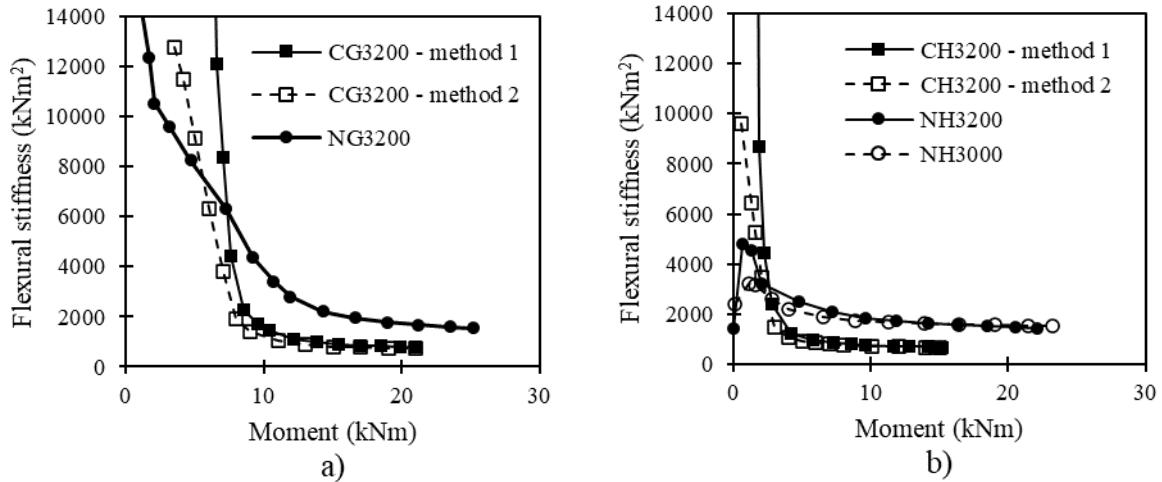
Figure 6.8: Moment-stiffness response near the mid-span (45mm from nearest bed-joint): a) fully grouted walls CG3200 and NG3200; and b) hollow walls CH3200, NH3200 and NH3000

The results demonstrate that the flexural stiffness decreases with increasing moment, and the variability in calculated flexural stiffness also decreases with increasing moment. As is evident for Wall NH3200 in Figure 6.9, the variability in stiffness is attributed, in part, to the location of the strain measurement along the height of the walls, and relative to the nearest mortar bed joint. At measurement points (numbered strain gauges as illustrated in Figure 6.10) located at the same relative position with respect to the mortar bed-joints, loading points, and supports, higher flexural stiffness is observed at the bottom of the wall compared to the top. This effect is attributed to the additional axial load at the base of the wall due to the self-weight. Flexural stiffness, regardless of the position along the height of the wall, converges to the cracked stiffness under increasing applied moment; however, the lower cracked stiffness observed at the location of mortar bed-joints is attributed to the effect of the lower stiffness of the mortar material.
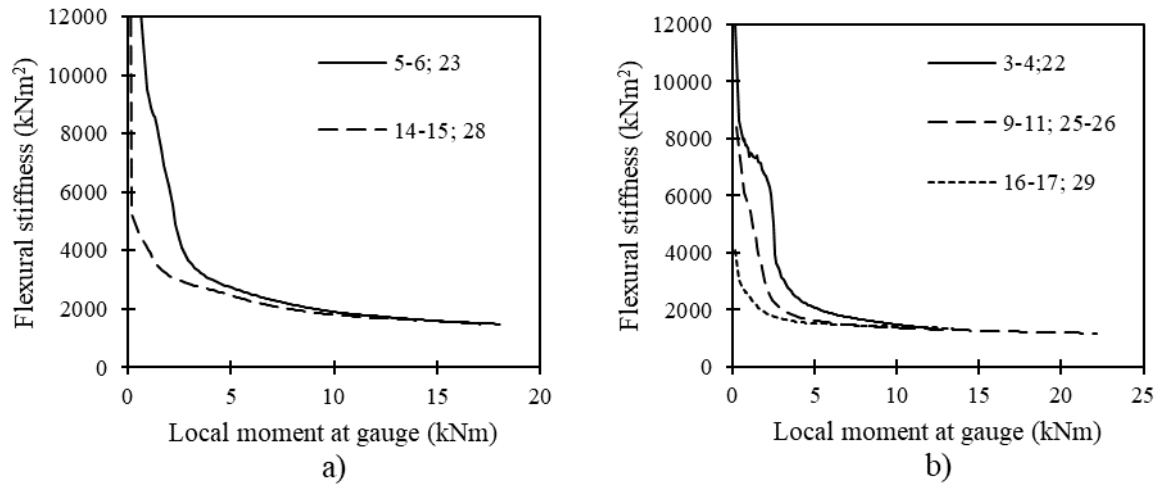
Figure 6.9: Moment-stiffness response calculated from NH3200 strain response: a) at 45mm from the nearest bed-joint; and b) at the location of mortar bed-joints, along the height of the wall
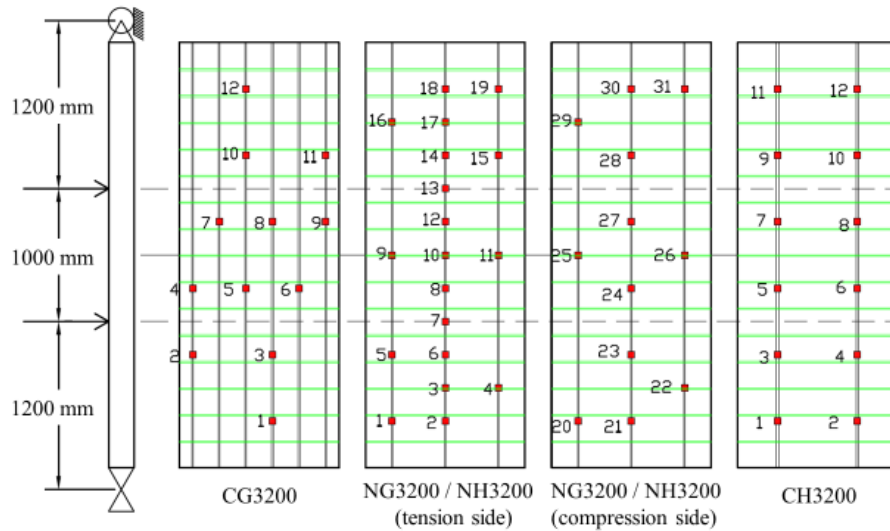
Figure 6.10: Strain gauge location for 3 m tall walls

With the exception of Walls NH3200 and NH3000, the flexural stiffness calculated from the reinforcing bar strains at low levels of applied moment trend toward or exceed the theoretical uncracked flexural stiffness ($E_m I_o$). The lower initial flexural stiffness of NH3200 and NH3000 is attributed to the lack of grouting. Given the weak bond afforded by mortar in tension, it is probable that the full section of the masonry wall is not engaged in resisting curvature near the mortar joints.

For both conventional and NSM reinforcement configurations, grouted walls maintained very high flexural stiffness under higher moments than the hollow and partially grouted walls; however, under increasing

Chapter 6 – Analysis

loads, the flexural stiffness of the grouted and hollow walls converge rapidly for both the NSM and conventional reinforcement configurations. The flexural stiffness at global yielding for each wall is listed in Table 6.3. The flexural stiffness of the grouted walls is approximately 10% higher than that of the similarly reinforced hollow walls, and the flexural stiffness of the walls with NSM reinforcement is approximately double that of similarly grouted conventionally reinforced walls.

Table 6.3: Flexural stiffness of walls at the global yield point, calculated from strain gauge data

Vertical distance from nearest bed-joint (mm)	Stiffness at global yield point (kNm²)				
	CG3200	NG3200	CH3200	NH3200	NH3000
45	715	1606	683	1451	1482
0	-	1320	-	1193	1063

6.3.2 Global flexural stiffness response from displacements

Whereas the flexural stiffness response determined from the strain readings from the reinforcing bars is only valid in the immediate proximity of the measurement, it is desirable in design applications to determine the global flexural stiffness which is representative of the entire wall. The global flexural stiffness was determined by using the experimental displacement data up to yielding and classical beam theory for displacement of a beam under conditions of four point bending as follows:

Equation 6.10
$$\Delta_{max} = \frac{Pa}{48EI}(3h^2 - 4a^2)$$

Where P is the total out-of-plane load, a is the distance from the support to the nearest load, and h is the full height of the wall. From Equation (6.10), the global flexural stiffness, EI, at a given load can be calculated based on the corresponding displacement as follows, where Δ_{max} is the displacement at midspan:

Equation 6.11
$$EI = \frac{Pa}{48\Delta_{max}}(3h^2 - 4a^2)$$

Flexural stiffness based on Equation (6.11) for Walls CG3200, NG3200, NH3200, and NH3000 is illustrated in Figure 6.11. For Wall CH3200, given that the reinforcement was not bonded over the entire height of the wall and challenges that arose with the top support connection, the displacement of the

Chapter 6 – Analysis

measured points on the upper half of the wall were used to calculate the flexural stiffness provided in Figure 6.11. For this case, the flexural stiffness was calculated from the following formula, for displacements occurring in the range of $x \leq a$:

Equation 6.12 $$EI = \frac{Px}{12\Delta_x}(3la - 3a^2 - x^2)$$

For a given load *P*, and flexural stiffness *EI*, the expected ratio of the displacements at the three measurement points is known. Considering that the top portion of the wall lacked restraint against accidental rotation and displacement due to the incomplete bonding of reinforcement in the lower portion of the wall and damage to the top course (as discussed in Chapter 4), an offset rotation and displacement was determined for each set of displacement readings. These offsets were used to correct the displacement data at each load increment such that the ratio of the three measured displacement points (at 1700, 1200, and 600 mm from the top support) matched that predicted by classical beam theory (i.e., 100%, 90.6%, and 54.2%, respectively, of the mid-span displacement). The variation in offset rotation and displacement with increasing applied load are illustrated in Figure 6.12 a) and b), respectively.
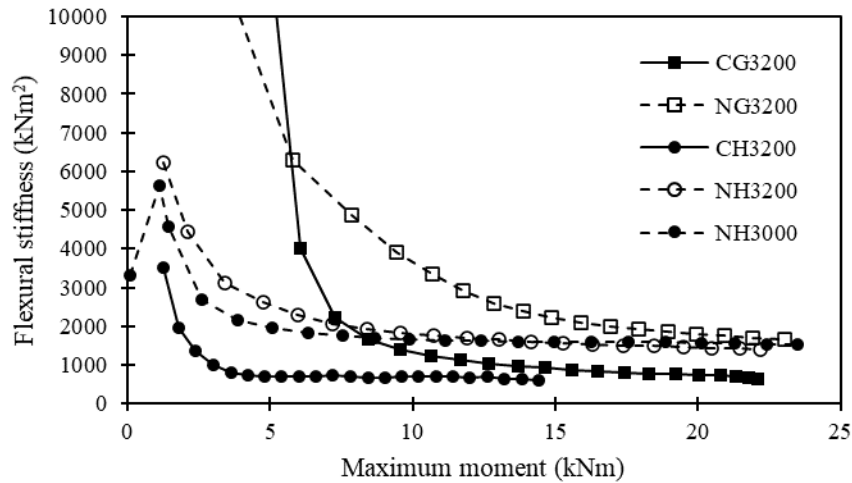
Figure 6.11: Average flexural stiffness based on displacement and out-of-plane load – classical beam theory

Chapter 6 – Analysis
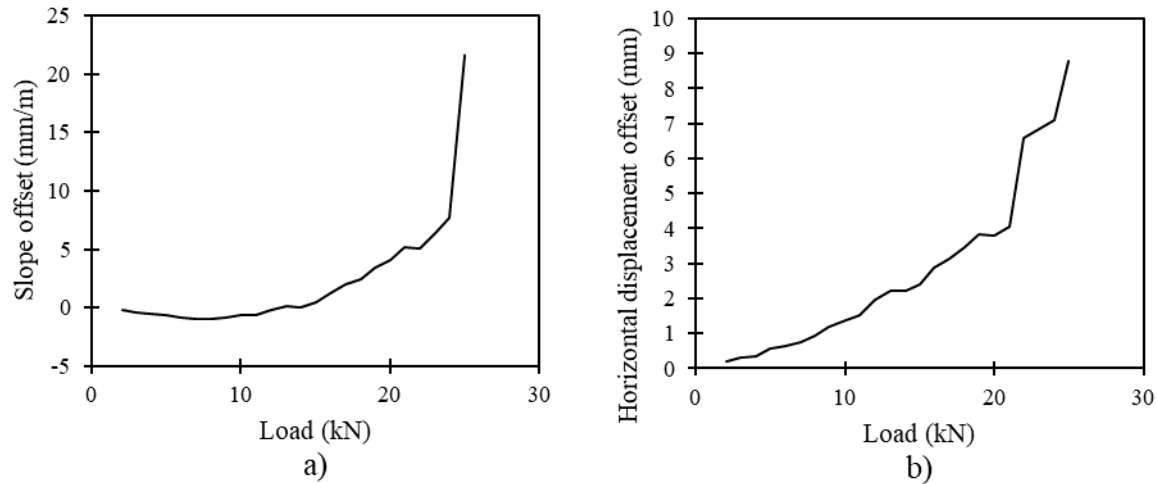
Figure 6.12: Correcting offsets for CH3200 displacements: a) rotation offset; and b) displacement offset

Using this approach, the displacement data was corrected using the correcting plane defined by the rotation

and displacement offset from Figure 6.12, as illustrated in Figure 6.13.
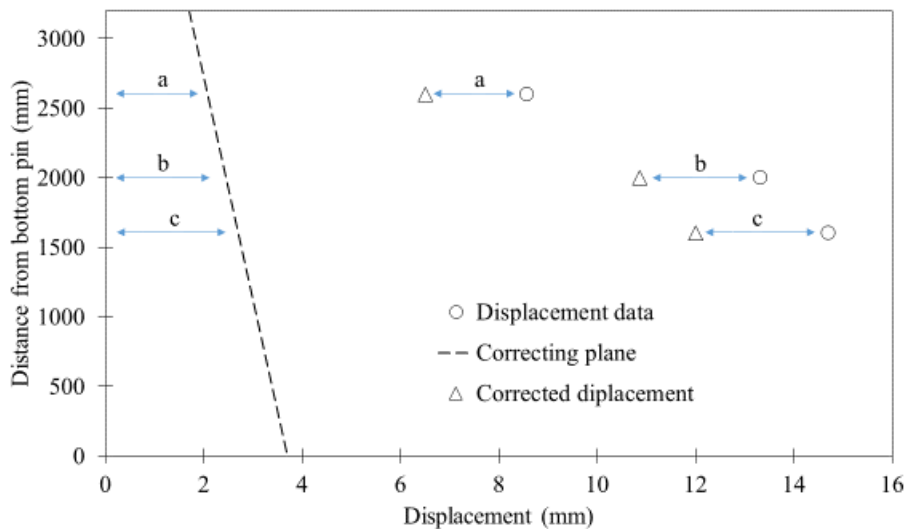
Figure 6.13: Correcting the displacement data of the top of Wall CH3200 using the correcting plane

6.3.3   Global flexural stiffness response – CSA standard provisions and rational analysis

The CSA S304-14 (R2019) Standard for Design of Masonry Structures (CSA Group 2019b) prescribes that

a single global effective flexural stiffness value, EI_{eff}, should be used to calculate displacements under

loading. This stiffness is calculated at the mid-span based on the section properties according to Equation

(6.13) (CSA Group 2019a, Cl 10.7.4.4):

Chapter 6 – Analysis

Equation 6.13
$$EI_{eff} = E_m \left[0.25I_o - (0.25I_o - I_{cr}) \left(\frac{(e - e_k)}{2e_k} \right) \right]$$

Where:

$E_m I_{cr} < EI_{eff} < 0.25 E_m I_o$

e_k = kern eccentricity (S_e / A_e)

e = virtual eccentricity (M_{fp} / P_f)

Using the main assumptions integrated into the CSA S304-14 approach, a rational analysis of the flexural stiffness for each wall was also performed. These assumptions are consistent with those described in Method 1 for the determination of curvature (compatibility of strains and equilibrium of forces), with the addition of accounting for the axial load from self-weight when determining the equilibrium of forces. For increasing values of strain in the reinforcing bars, the corresponding moment resistance of the section was calculated in Equation (6.14).

Equation 6.14
$$M_r = \frac{E_m \varepsilon_m bc}{2} \left(d - \frac{c}{3} \right)$$

Applying the test conditions (external loading and self-weight) at mid-span, the flexural stiffness response was determined for each wall according to S304-14 (Equation (6.13)), and the rational analysis method consistent with Method 1.

6.3.4 Moment-stiffness response – comparison of methods

Figure 6.14 provides the moment-stiffness responses for each 3m tall RM wall near the mid-span as determined by the various methods presented in this section. These methods include the following: a Rational Analysis based on Method 1 to determine the curvature; the method from CSA S304-14 using Equation (6.13); Stiffness from Displacement as described in Section 6.3.2; and stiffness determined using the strain gauge response as described in Section 6.3.1 (using Strain Gauges (SG) 7 to 9 for CG3200, SG 12 and 27 for NG3200, NH3200, and NH3000, and SG 7 and 8 for CH3200). Given that the strain readings

Chapter 6 – Analysis

at the mid-span mortar bed-joint in Walls NG3200, NH3200, and NH3000 underestimate the global flexural stiffness behaviour of the walls, and for consistency, flexural stiffness calculated from strain readings 45mm above the 9th bed-joint (1800mm from the bottom roller) are presented. The CSA S304-14 standard equation provides similar results to the rational analysis, neglecting tension stiffening effects of the masonry on the reinforcing bars; however, both approaches underestimate the flexural stiffness response under low out-of-plane loads. Flexural stiffness calculated from the strain readings near the mid-span is found to be a good predictor of the global flexural stiffness response of the walls given that it provides a similar value as the stiffness calculated from displacement. At applied loads approaching zero, the flexural stiffness calculated based on strain (Method 2), displacement, and rational analysis trend toward the theoretical uncracked flexural stiffness indicated in Table 6.4; at load levels approaching the yield moment, the stiffness trends towards the theoretical cracked flexural stiffness for all methods of calculation.

Chapter 6 – Analysis
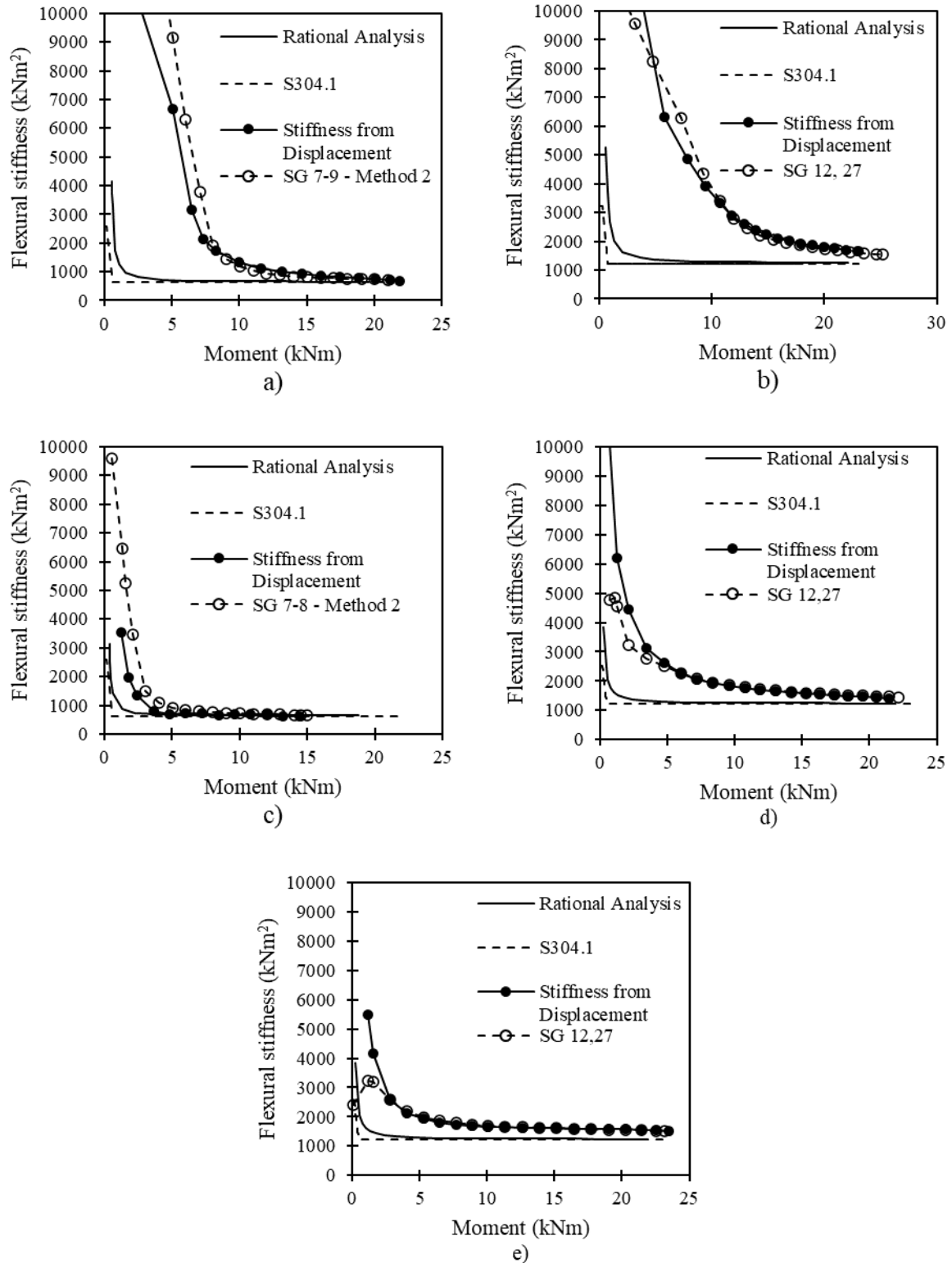
Figure 6.14: Moment-stiffness various methods of calculation: a) CG3200; b) NG3200; c) CH3200; d) NH3200 and e) NH3000

Chapter 6 – Analysis

Wall ID	Calculated stiffness (kNm^2)	
	E_mI_o	E_mI_{cr}
CG3200	12 243	637
NG3200	12 841	1 233
CH3200	10 314	637
NH3200	9 945	1 233
NH3000	9 945	1 233

6.4 Flexural stiffness Response of 8 m Tall Walls

In this section, the effect of axial load on the out-of-plane load and moment resistance of 8 m tall RM walls is examined. Changes in the behaviour of the walls between the first and subsequent loading cycles are also discussed. Data collected from strain gauges, as well as displacement transducers which measured out-of-plane displacement and average surface strains (tensile and compressive) are used to examine the local and global flexural stiffness response of the 8 m tall RM walls when subjected to combined axial and out-of-plane loads. These results are compared to the global flexural stiffness response prescribed by the CSA S304-14 (CSA Group 2019a) design provisions, as well as a simple rational analysis of the wall sections.

6.4.1 Load- and moment-displacement behaviour with changing axial load

The load-displacement response of the walls with varying applied axial load is illustrated in Figure 6.15. In general, for out-of-plane displacements below 50 mm, there is an increase in flexural stiffness and load resistance for all walls with increasing applied axial load. For Walls CH7800a and CH7800b, larger displacements, over 120 mm at mid span, were imposed to achieve the target strain in the reinforcing bars of 1800 µm/m. As the displacement in CH7800a and CH7800b increased beyond approximately 70 mm, a decreasing trend in the out-of-plane load resistance was observed with increasing applied axial load. This decrease is attributed to the effect of the secondary moment which is greater with larger displacements.

Chapter 6 – Analysis
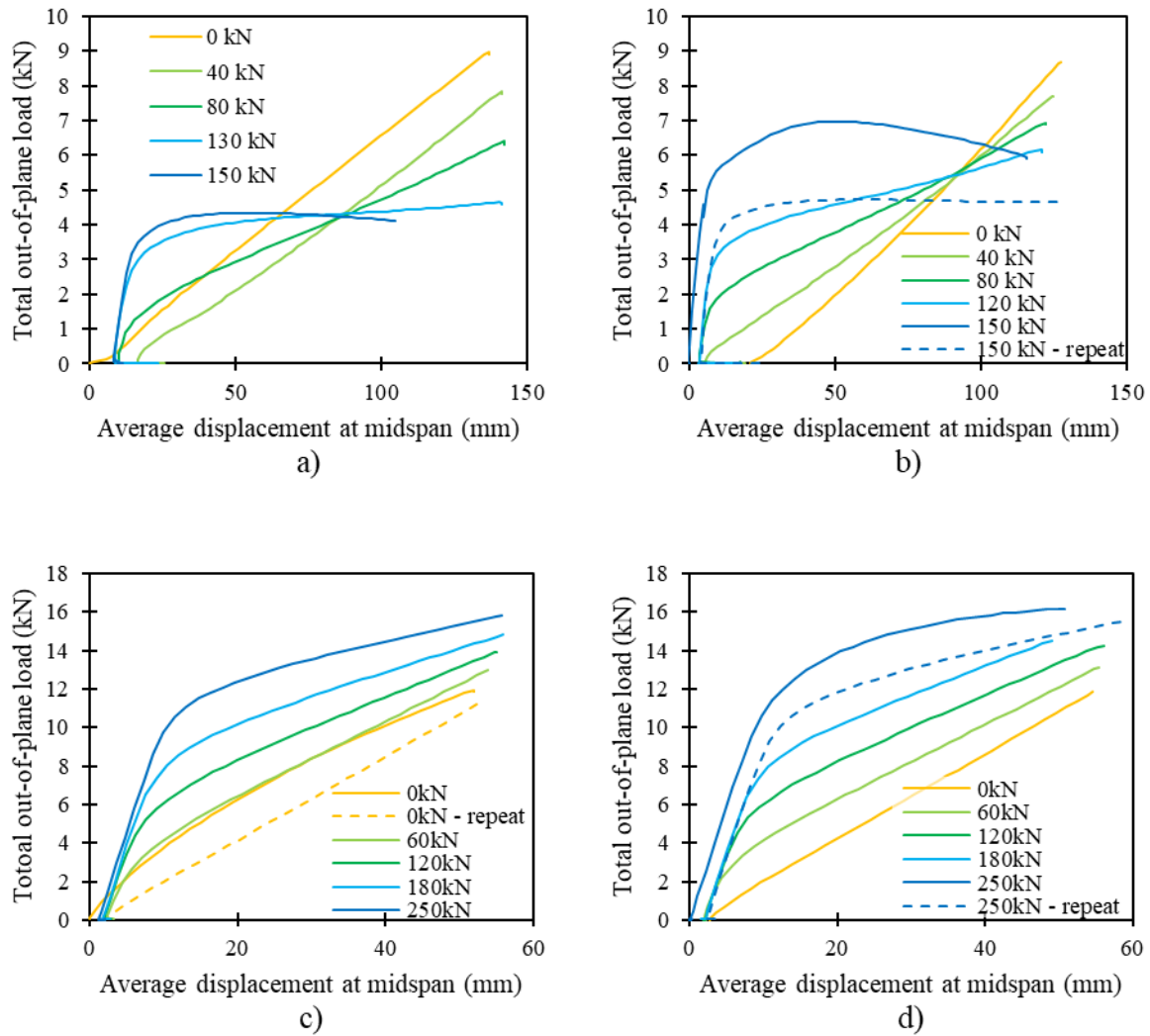
Figure 6.15: Load-displacement response with varying applied axial load: a) CH7800a; b) CH7800b; c) NH7800a; and d) NH7800b

The total moment-displacement response of walls with varying applied axial loads is illustrated in Figure 6.16. The total moment was calculated at the midspan by adding the effects of the out-of-plane loading to the effect of the imposed axial load and the self-weight of the top half of the wall (self weight applied at the top of the wall). The imposed axial load and self-weight contributed a moment due to the *P-Δ* effect. In all cases, increasing axial load resulted in increased moment resistance in the walls. The walls subjected to larger axial loads exhibited a strong bilinear response, the slope of both portions of the response are similar for subsequent loading cycles of a same wall; however, the length of the initial slope increases with increased axial load.

Chapter 6 – Analysis
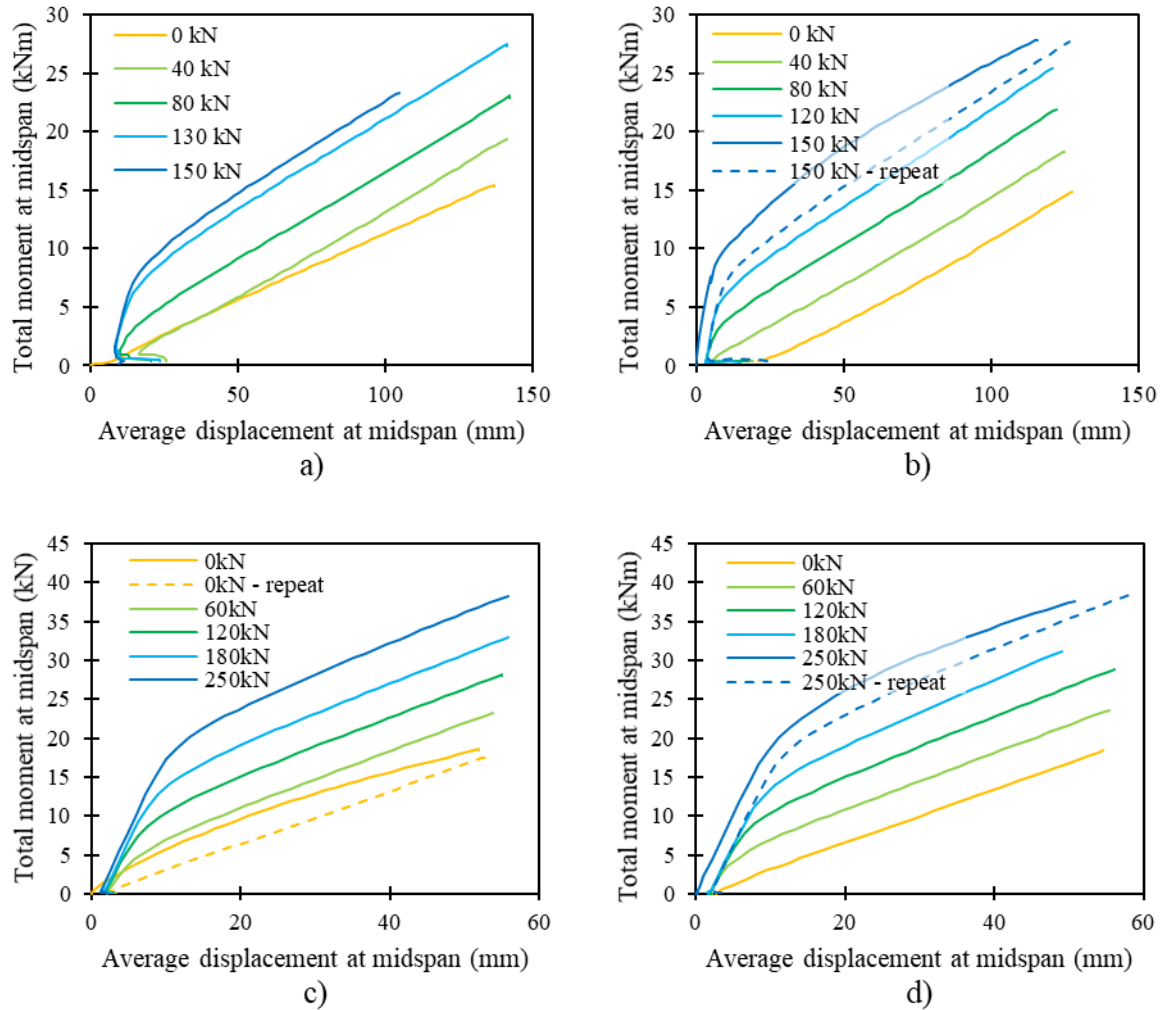
Figure 6.16: Moment-displacement response with varying applied axial load: a) CH7800a; b) CH7800b; c) NH7800a; and d) NH7800b

All four walls exhibited increased initial flexural stiffness and increased total moment resistance with increasing imposed axial load. The walls with NSM reinforcement had an increase in moment resistance of approximately 69% comparing the resistance at 0 kN and 140 kN of imposed axial loading; whereas the walls with conventional reinforcement had an increase in moment resistance of 84%. In absolute terms, all four walls exhibited an increased resistance of approximately 12 kNm. This increase is consistent with the effect of the axial load on increased moment resistance as shown in Equation (6.14), where the thickness t is 190 mm and the depth of the compression stress block a is approximately 10 mm.

Equation 6.14 $\qquad (M_r)_{axial\ load} = P\left(\frac{t}{2} - \frac{a}{2}\right)$

Chapter 6 – Analysis

6.4.2 Change in behaviour from first cycle to subsequent cycles

The walls were visibly undamaged at the start of each test; however, some level of cracking is likely to have occurred during the handling (lifting and moving) process prior to testing. Although efforts were made to minimize the stress imposed on the walls while moving them, noticeable dynamic sinusoidal bending was observed when moving the walls in the out-of-plane direction (necessary during the beginning and end of each wall move). The amplitude of this dynamic deformation is difficult to estimate, but it appears to have been on the order of several mm to a few cm – moreover, these dynamic effects were more pronounced while moving the less rigid conventionally reinforced walls, compared to the stiffer walls with NSM reinforcement. While moving the walls, efforts were made to ensure they were moved parallel to the strong axis whenever possible. Despite this stress history from handling, no visible cracks were identified prior to testing and a marked difference in behaviour was observed between the first loading cycle and subsequent loadings of each wall. The load resistance was greater, and the hysteresis loops were wider in the load-displacement response of the first loading cycle than for subsequent cycles as illustrated in Figure 6.17.
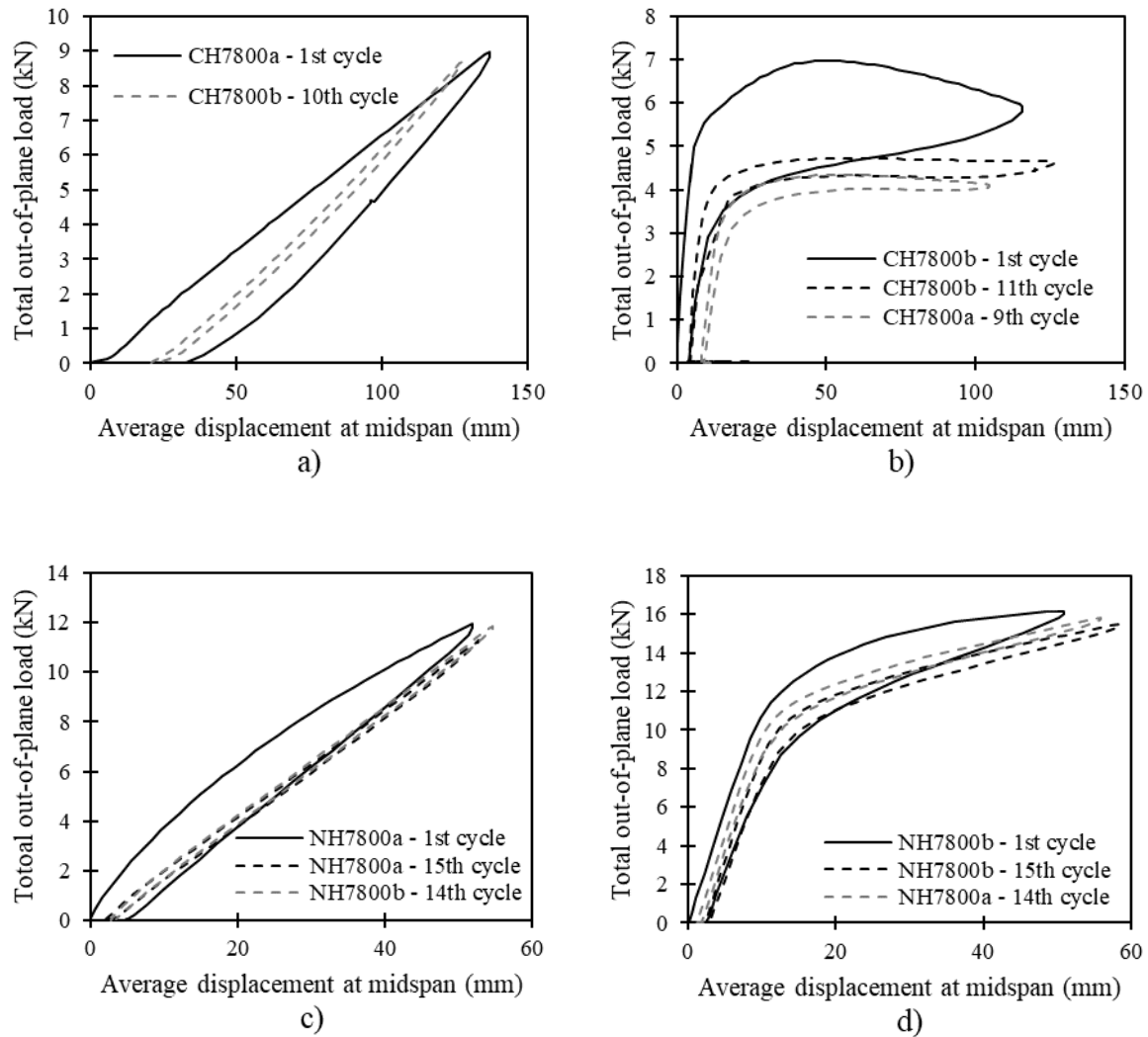
Figure 6.17: Load-displacement response of first and repeat loading cycles: a) wall CH7800a and CH7800b with no applied axial load; b) CH7800a and CH7800b with 150kN of applied axial load; c) NH7800a and NH7800b with no applied axial load; and d) NH7800a and NH7800b with 250kN of applied axial load

Wall CH7800a was loaded out of plane without any imposed axial load for its first loading cycle, whereas Wall CH7800b was loaded out of plane without imposed axial load for its 11th cycle. The slope of the response as well as the maximum resistance for both of these loading cycles is similar, as show in Figure 6.17 a), however a larger area is enclosed within the load-displacement response of CH7800a (first loading cycle).

Walls CH7800a and CH7800b were subjected to imposed axial loads of up to 150 kN. The out-of-plane load-displacement response of these walls at the maximum axial load level is shown in Figure 6.17 b). The

Chapter 6 – Analysis

loading cycle for Wall CH7800a occurred following eight loading cycles with lower levels of imposed axial load and was halted prematurely when the out-of-plane load resistance was observed to decrease with increasing displacement. When testing Wall CH7800b, the imposed axial load of 150 kN was applied for the first loading cycle. The maximum out-of-plane load resistance for this first loading cycle was 47% higher than that of the repeat cycle (11th cycle), performed following 9 elastic loading cycles with lower applied axial loads. All three load cycles performed on the conventionally reinforced walls with 150 kN of imposed axial load resulted in a decreasing trend in out-of-plane load resistance with increasing displacement and no signs of yielding in the reinforcing steel bars (elastic buckling). The first loading cycle of Wall CH7800b was characterized by a wide loop indicative of high levels of energy dissipation through initial damage to the masonry material. The repeat cycle for wall CH7800b had a similar shape and peak load resistance to that observed for wall CH7800a, with a much thinner loop suggesting that little additional damage was done to the walls during these subsequent loading cycles.

The difference between the initial and repeat loading cycles for Walls NH7800a and NH7800b (with 0 kN and 250 kN of imposed axial load, respectively) were more subtle, as illustrated in Figure 6.17 c) and d). However, greater energy dissipation (area enclosed within the loading/unloading curve) occurred during the first loading cycle, compared to subsequent cycles for each of the walls tested.

6.4.3   Flexural stiffness response with increasing applied axial load

In this section, data collected from strain gauges, as well as displacement transducers are used to examine the local and global flexural stiffness response of the 8 m tall RM walls with increasing applied axial load. These results are compared to the global flexural stiffness response prescribed by the CSA S304-14 (CSA Group 2019a) design provisions, as well as a simple rational analysis of the wall sections.

6.4.3.1   *Flexural stiffness calculated from surface strain*

The effective flexural stiffness of the 8 m tall walls can be determined by dividing the total moment (including secondary moment effects) by the curvature calculated, using measurements of the surface strain

Chapter 6 – Analysis

on the tension and compression sides, as described in Section 6.2.2. The resulting stiffness is the average stiffness over the gauge length of the instruments (400 mm, spanning 2 mortar joints), accounting for the contributions to curvature from the cracks (at mortar joints) as well as the crack-free regions (masonry units). A sample of the flexural stiffness response of Walls CH7800b and NH7800b calculated based on the surface strain measurement is provided in Figure 6.18. For all walls, there is a dramatic increase in the initial stiffness with increasing applied axial load. The walls also exhibit improved flexural stiffness with increasing applied axial load as the applied moment approaches the yield point (as the maximum reinforcement strain reaches 1800 μm/m).
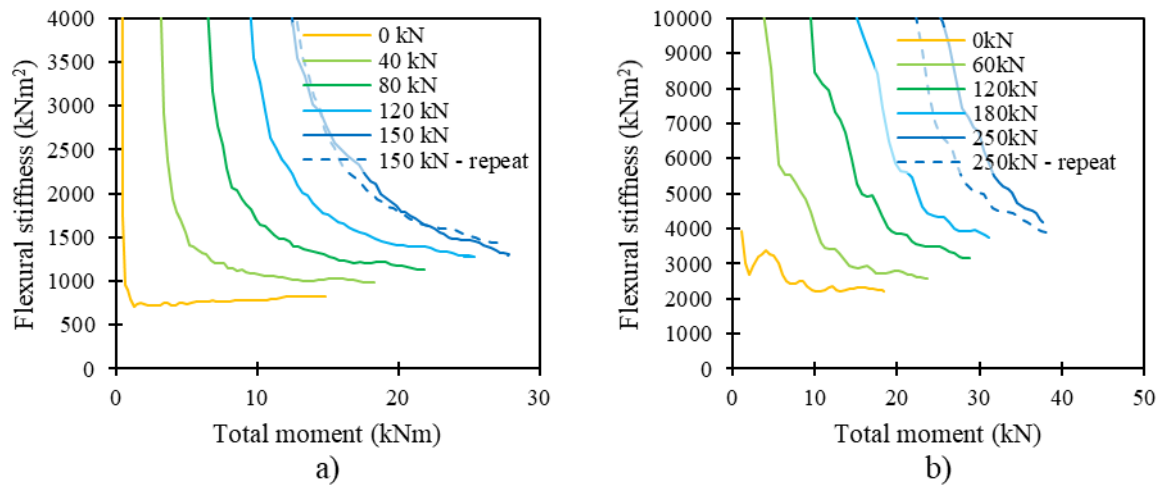
Figure 6.18: Flexural stiffness response calculated from the surface strain profile for various applied axial loads: a) CH7800b; and b) NH7800b

6.4.3.2 Flexural stiffness at mortar joints calculated from reinforcing bar strain

The flexural stiffness at mortar joints can be similarly calculated for the walls with NSM reinforcement since the reinforcing bars on both the tension and compression sides were fitted with strain gauges at the location of the mortar joints. However, for the walls with conventional reinforcement, the curvature cannot be calculated directly; instead, the curvature was calculated using a modified version of Method 1 which accounted for the effect of axial load as described in Section 6.2.1. The flexural stiffness was then determined by dividing the total moment, including the effect of the applied horizontal load and the *P-Δ* effects from the applied vertical load and self weight, by the calculated curvature. A sample of the stiffness

Chapter 6 – Analysis

response of Walls CH7800b and NH7800b, calculated based on the average of reinforcing bar strain measurements in the uniform moment region (middle 2 m), is provided in Figure 6.19. The flexural stiffness here is a lower bound, expressing the stiffness at a crack (mortar bed joint) where there is little or no tension stiffening effect. The shape of the stiffness response curve is similar to that calculated based on surface strain, and the increasing trends with increasing axial load are also apparent, however, the flexural stiffness values are lower throughout the range of applied moments. It is also notable that the stiffness response of the walls with conventional reinforcement (CH7800a and CH7800b) was not captured for low moments since the method used for calculating the curvature cannot be applied when the reinforcement strain is negative.
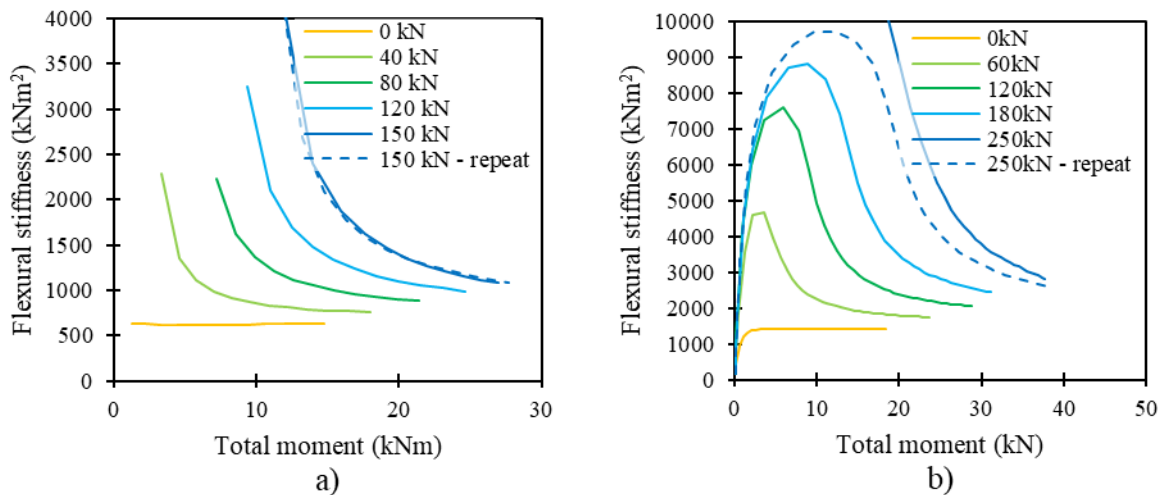
Figure 6.19: Flexural stiffness response calculated from the average reinforcing bar strain near the midspan for various applied axial loads: a) CH7800b; and b) NH7800b

6.4.3.3   Flexural stiffness back calculated based on applied loads and midspan displacement

The average effective flexural stiffness of the 8 m tall walls was also calculated based on the load and displacement response. The total moment in a wall is the sum of the primary moment and the secondary *P-Δ* moment as shown in Equation (6.15). For a simply supported wall with concentric axial loading and uniform flexural stiffness, Equation (6.16) (moment magnification equation) may be used with a C_m value of 1 due to the equal end moments, where P is the applied axial load, and P_{cr} (critical buckling load) is defined in Equation (6.17) for a wall with an effective height of kh (for these tests, $kh = 8000$ mm).

143

Chapter 6 – Analysis

Equation 6.15 $\qquad M_{tot} = M_p + P\Delta$

Equation 6.16 $\qquad M_{tot} = M_p \dfrac{C_m}{1 - \frac{P}{P_{cr}}}$

Equation 6.17 $\qquad P_{cr} = \dfrac{\pi^2 EI}{kh^2}$

Substituting Equation (6.15) and Equation (6.17) into Equation (6.16), and isolating the stiffness term *EI* yields Equation (6.18), in which all terms on the right-hand side are known or were measured directly throughout the wall tests.

Equation 6.18 $\qquad EI = \dfrac{P(kh)^2}{\pi^2 \left(1 - \frac{M_p}{M_p + P\Delta}\right)}$

For example, at the mid span, the primary moment M_p is the product of half of the total measured out-of-plane load and the shear span (3 m distance from a support to the location of one of the applied loads), the axial load *P* was constant and monitored throughout each loading cycle, and the average displacement *Δ* was measured using displacement transducers. A sample of the effective flexural stiffness response of Walls CH7800b and NH7800b, calculated based on the load and displacement measurements at midspan, is provided in Figure 6.20. The trends in the moment-stiffness response with increasing axial load are similar to those observed for the other methods of calculating the flexural stiffness.

Chapter 6 – Analysis
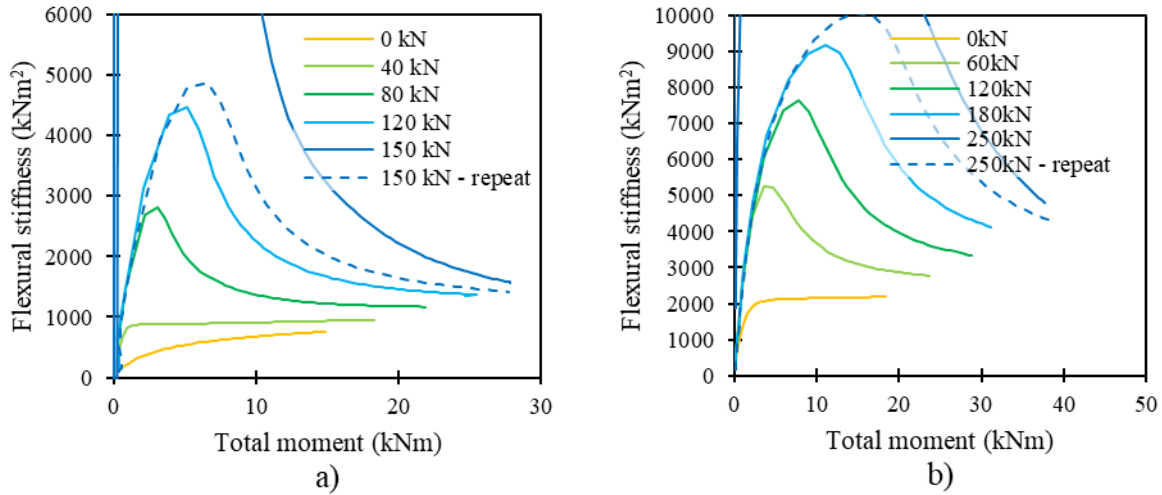
Figure 6.20: Flexural stiffness response calculated from the load and displacement at the midspan for various applied axial loads: a) CH7800b; and b) NH7800b

6.4.4 Discussion and fit of results with flexural stiffness formulations

The theoretical flexural stiffness of a RM wall section can be estimated through rational analysis. When no axial load is applied, the flexural stiffness of a cracked section is equal to the product of Young's modulus and the transformed moment of inertia of the cracked section regardless of the applied moment. For cases with applied axial load, the curvature of the section can be determined by applying conditions of equilibrium and strain compatibility for a given level of strain in the reinforcing steel. This process is similar to Method 1 for determining the curvature based on strain data as shown in Figure 6.5 and Equations (6.1) to (6.6) in Section 6.2. The flexural stiffness can then be determined by finding the resultant moment of the internal forces (axial load, reinforcement tension, compression force in the masonry flange and web) and dividing it by the curvature. The flexural stiffness calculated in this way will vary depending on the applied moment and axial load. A closed form solution can be derived for fully grouted walls; however, for the hollow walls in this experimental series, the curvature was determined iteratively when the depth to the neutral axis c is greater than the thickness of the masonry block flange t_f. For the conventionally reinforced walls, the contribution of the grouted cells is included; however, for the walls with NSM reinforcement there is no continuous cementitious material between the block flanges (mortar bedded face shells), therefore the block webs are not included in the calculation. A sample of the theoretical effective flexural stiffness response of

Chapter 6 – Analysis

the walls with conventional reinforcement and NSM reinforcement calculated based on a rational analysis of the sections is provided in Figure 6.21.
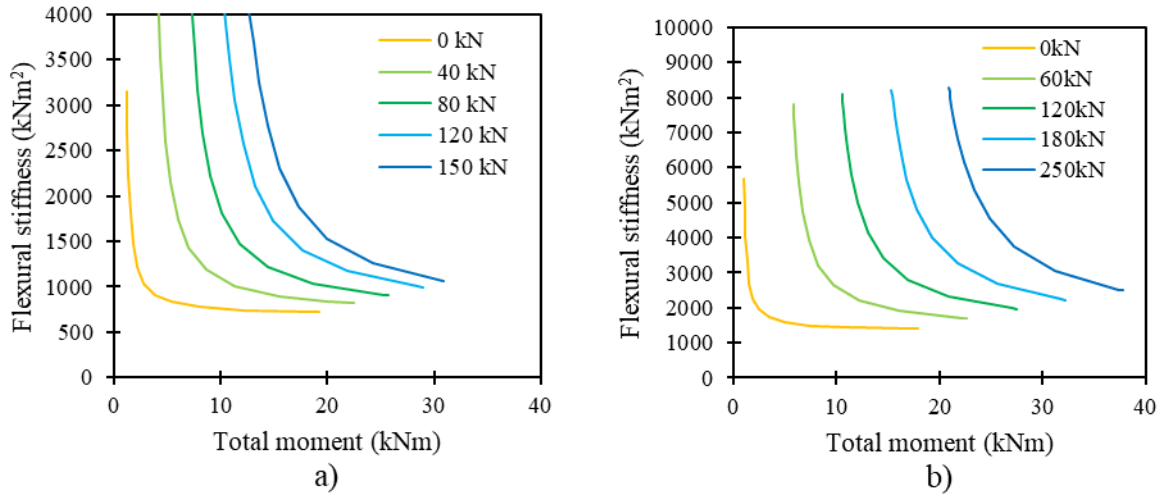
Figure 6.21: Theoretical flexural stiffness response calculated based on a rational section analysis at the midspan for various applied axial loads: a) Walls CH7800x; and b) Walls NH7800x

This rational analysis was found to be a good predictor of the flexural stiffness response at a crack (stiffness calculated from reinforcing bar strain), and a conservative estimate for the average flexural stiffness response (stiffness calculated from surface strain measurements, and displacement measurements) for the first loading cycle. Figure 6.22 illustrates the flexural stiffness response of each wall during their respective first loading cycle; it shows the contrasting responses that result from the calculation of the flexural stiffness response based on different instruments and using different methods. The flexural stiffness calculated based on the rational analysis seems to be a conservative estimate of the stiffness response, except for Wall CH7800a (as shown in Figure 6.22 a)) – for this case, the rational analysis overestimates the flexural stiffness, relative to what was calculated based on the displacement and strain responses, at low levels of applied moment.

Chapter 6 – Analysis
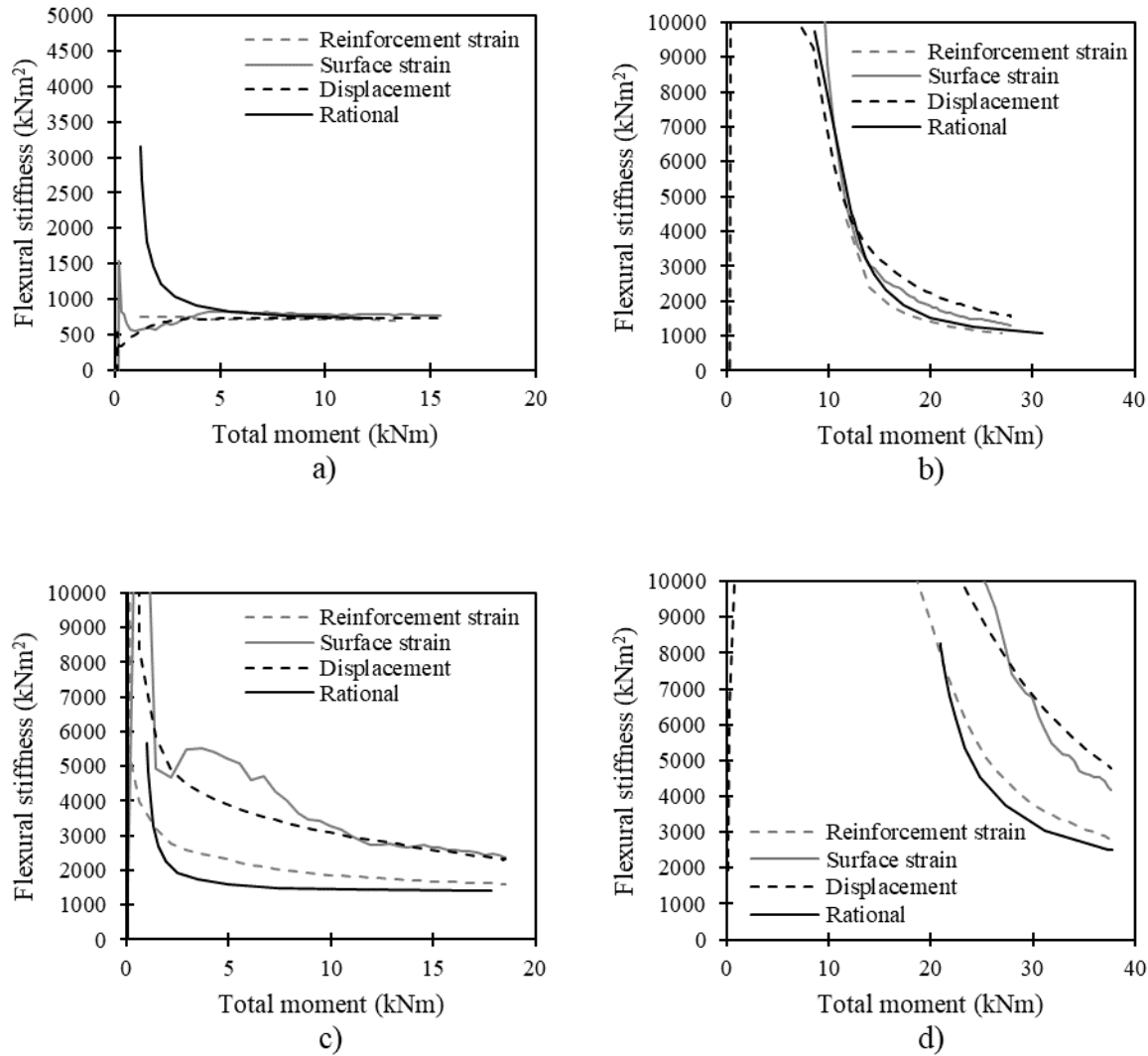
Figure 6.22: Flexural stiffness response for the first loading cycle of reinforced masonry walls: a) CH7800a - 0kN applied axial load; b) CH7800b – 150kN applied axial load; c) NH7800a – 0kN applied axial load; and d) NH7800b – 250kN applied axial load

During subsequent loading cycles, the rational section analysis no longer provides a conservative estimate of the effective flexural stiffness at low levels of applied moment. However, at moments approaching the yield moment, the flexural stiffness derived from the rational analysis provides a good estimate for the stiffness measured based on the curvature at the crack locations (calculated based in reinforcement strain) and is a conservative estimate of the global effective flexural stiffness (calculated based on displacement or average surface strain). Figure 6.23 provides a sample of the flexural stiffness response for Walls CH7800b and NH7800b for two intermediate levels of applied axial load, comparing the flexural stiffness

147

Chapter 6 – Analysis

response that is calculated through different methods based on data from different instruments. For these intermediate loading cases, the rational section analysis overestimates the flexural stiffness response of the walls for low applied moments but converges towards the stiffness at the mortar bed joints (cracks), as calculated using the strain gauge response, as the moment approaches the yield moment.
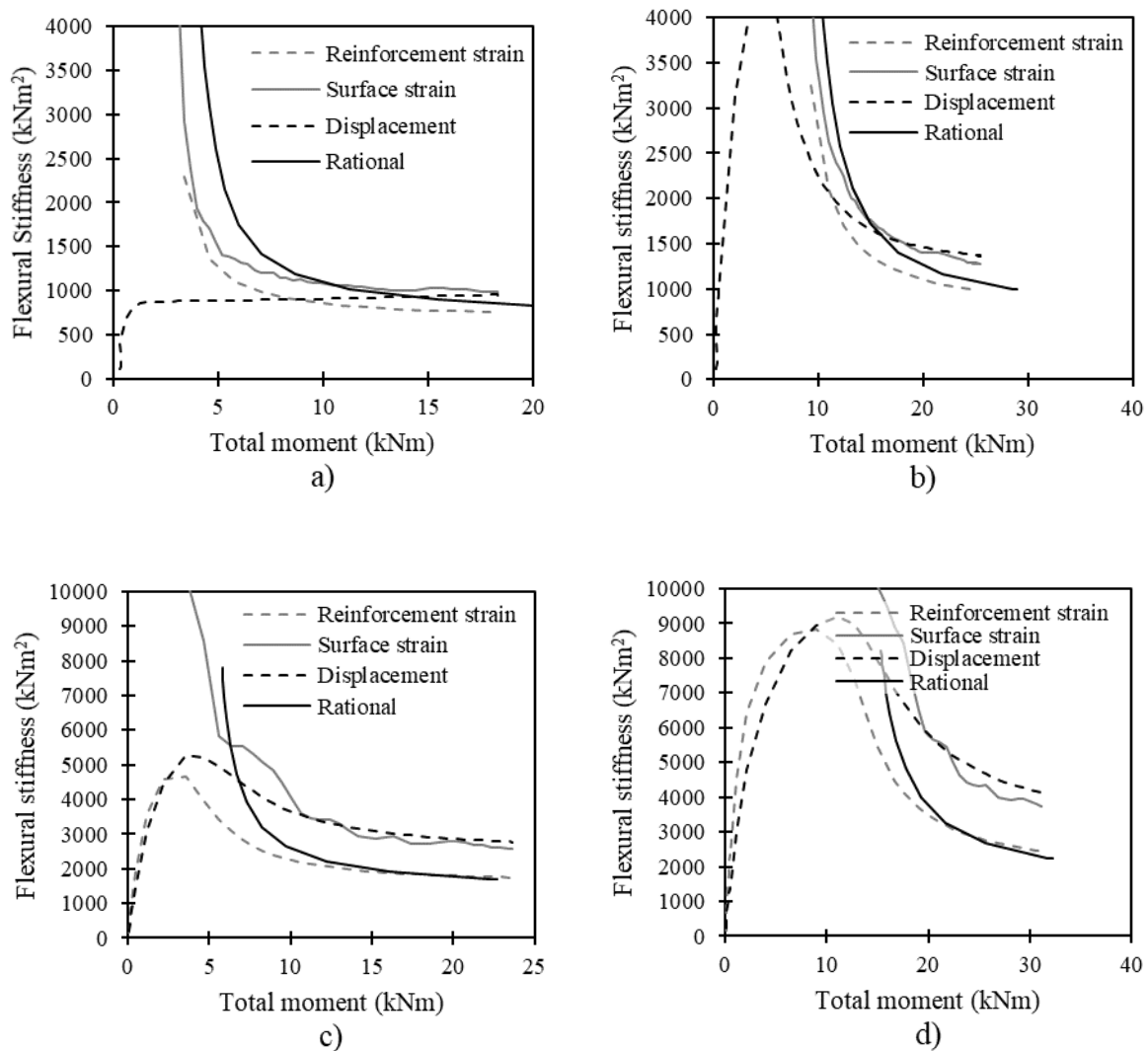
Figure 6.23: Flexural stiffness response for various loading cycles of RM walls: a) CH7800b - 40kN applied axial load; b) CH7800b – 120kN applied axial load; c) NH7800b – 60kN applied axial load; and d) NH7800b – 180kN applied axial load

The CSA S304 equation for flexural stiffness (Equation (6.13)) does not appear to provide consistently conservative stiffness values for low levels of applied axial load, particularly for walls with a stress history of high axial and out-of-plane loads. Figure 6.24 a) illustrates that neither the initial loading cycle of Wall

CH7800a, nor the 10th cycle of CH7800b (both with no applied axial load) exhibited the initial higher out-of-plane flexural stiffness based on the displacement at midspan (Equation (6.18)), predicted by the unfactored design equation (Equation 6.13). For NH7800a, the initial loading cycle of the wall exhibits high initial flexural stiffness, however upon reloading the wall without axial load (15th cycle), the design equation once again overestimates the stiffness at low levels of applied moment, as illustrated in Figure 6.24 b).
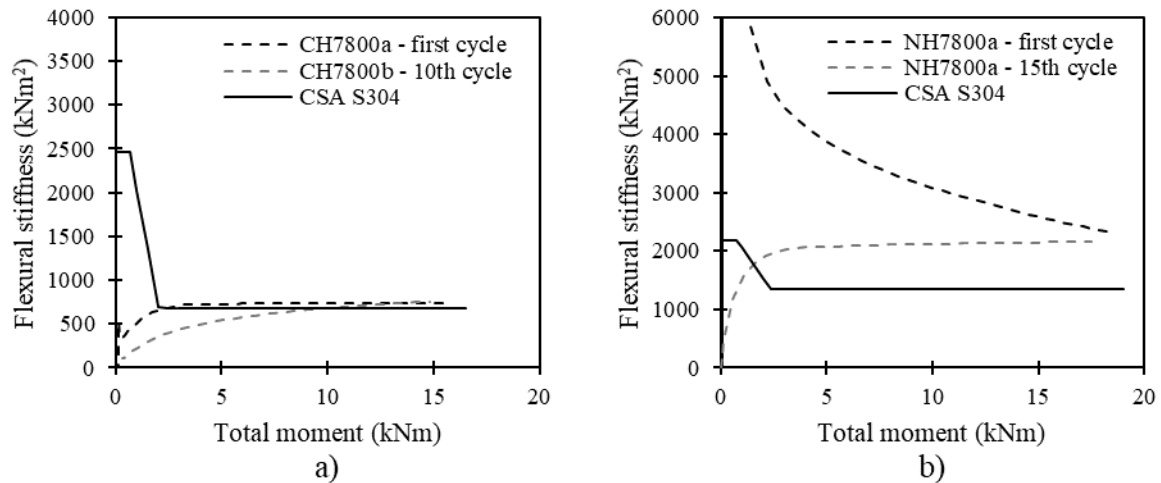
Figure 6.24: Moment-stiffness response with no imposed axial load comparing flexural stiffness calculated based on the displacement response and the unfactored CSA S304 formulation (CSA Group 2019a): a) CH7800a and CH7800b; b) NH7800a

For cases in which the walls were subjected to higher axial load, the CSA S304 design equation provides a conservative value for the flexural stiffness, even for walls with a stress history which includes high axial load and high out-of-plane displacement. However, the factor of safety (ratio of observed to calculated stiffness) appears inconsistent, as illustrated in Figure 6.25.

Chapter 6 – Analysis
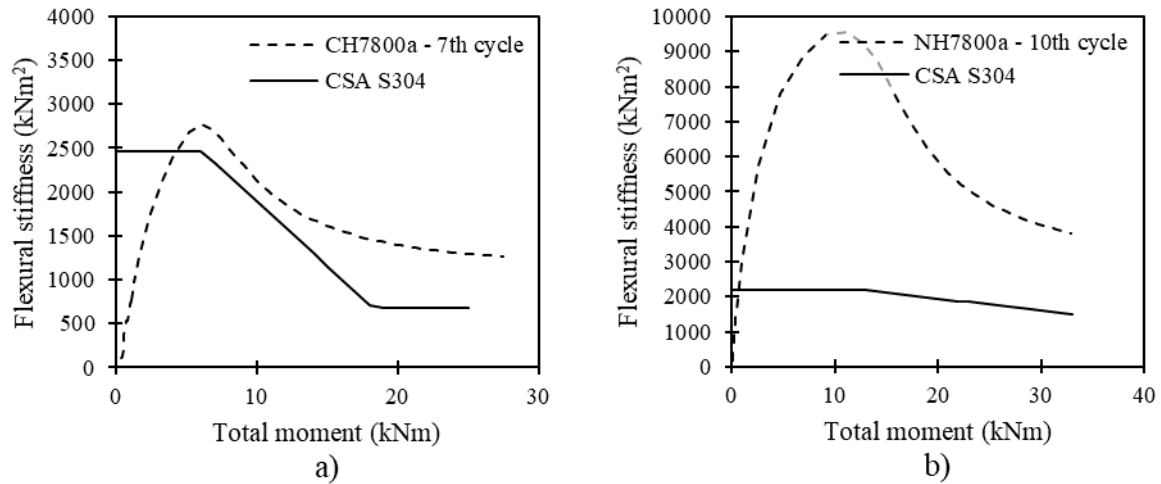
Figure 6.25: Moment-stiffness response comparing flexural stiffness calculated based on the displacement response and the CSA S304 formulation (CSA Group 2019): a) CH7800a with 130 kN applied axial load; b) NH7800a 180 kN applied axial load

In general, the CSA S304 equation allows little advantage to be gained from the higher flexural stiffness observed in walls subjected to high axial load and low out-of-plane moments and does not permit an adjustment of the lower-bound flexural stiffness (for cases of high applied moment) to account for increased stiffness from increased axial load. The moment-stiffness relation with increasing load expressed by the S304-14 equation (Equation (6.13)) is illustrated in Figure 6.26.
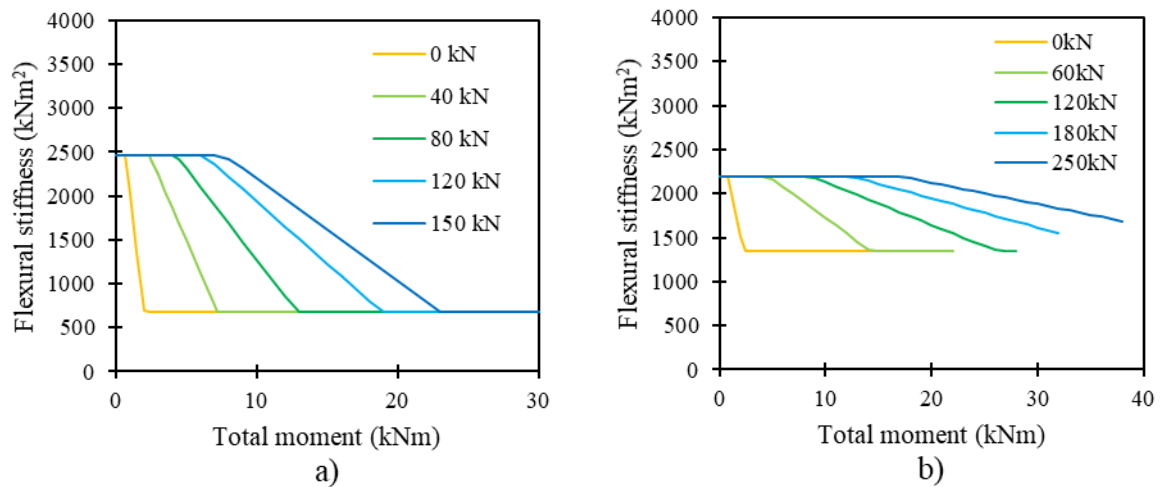
Figure 6.26: Moment-stiffness relation indicated by CSA S304 for various axial loads: a) Walls CH7800x; and b) Walls NH7800x

The flexural stiffness of each wall test at the point the maximum reinforcement strain reached 1800 μm/m (stiffness calculated based on the displacement at midspan – Equation 6.18) is tabulated in Table 6.5 for

150

Chapter 6 – Analysis

the conventionally reinforced walls and Table 6.6 for the walls with NSM reinforcement. In these tables, the experimental values can be compared to the value predicted by rational analysis and by analysis using the CSA S304-14 (CSA Group 2019a) design equation. Near the yield point of the reinforcing bars in tension, the rational analysis provides a conservative estimate of the flexural stiffness, while accounting for the beneficial effect of the axial load on the flexural stiffness; contrastingly, the design equation provides increasingly conservative stiffness values with increasing axial load.

Table 6.5: Flexural stiffness of conventionally reinforced walls at reinforcement strain of 1800 μm/m

Applied axial load (kN)	Stiffness from displacement CH7800a / CH7800b [repeat cycle] (kNm^2)	Stiffness from rational analysis (kNm^2)	Stiffness based CSA S304 (kNm^2)
0	726 / 757	719	683
40	888 / 952	816	683
80	1043 / 1163	908	683
120	- / 1363	995	683
130	1258 / -	1016	683
150	1446 / 1561 [1423]	1058	683

Table 6.6: Flexural stiffness of NSM reinforced walls at reinforcement strain of 1800 μm/m

Applied axial load (kN)	Stiffness from displacement NH7800a / NH7800b [repeat cycle] (kNm^2)	Stiffness from rational analysis (kNm^2)	Stiffness based CSA S304 (kNm^2)
0	2303 [2154] / 2185	1399	1341
60	2809 / 2769	1697	1341
120	3311 / 3329	1972	1341
180	3820 / 4124	2225	1549
250	4452 / 4793 [4276]	2496	1687

6.5   Axial Load-Moment Interaction

The maximum out-of-plane strength of each 8 m tall wall was not assessed for each axial load level; however, an increase in moment resistance was observed with increasing axial load for all cases. Figure 6.27 illustrates the interaction between the imposed axial load and total midspan moment at the maximum strain level of 1800 µm/m.

Chapter 6 – Analysis
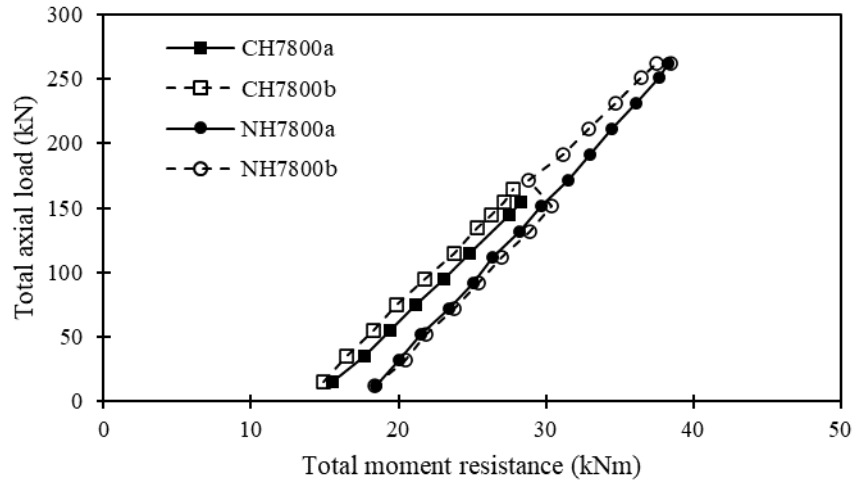
Figure 6.27: Axial load – moment resistance interaction for 8 m tall RM walls at max strain = 1800μm/m

An axial load moment interaction diagram can be developed for each wall at the yield point using the CSA S304-14 standard equation for the equivalent rectangular stress block (CSA Group 2019a) shown in Equation (6.19).

Equation (6.19) $\qquad \sigma_m = 0.85\chi\phi_m f'_m$

The uniform stress block is applied from the edge of the section in compression to a distance a, where a is determined using Equation (6.20) based on the distance c to the neutral axis.

Equation (6.20) $\qquad a = \beta_1 c$

The values in Table 6.7 were used to develop the interaction diagrams for the two walls. These are typical design values stated in CSA S304-14 (CSA Group 2019a) for 15 Mpa nominal strength masonry units, other than the material resistance factors (ϕ_m and ϕ_s) which were set to 1.0 to generate the diagram for the unfactored response. The strength, f'_m, of the masonry for Walls CH7800a and CH7800b was calculated as a weighted average of the values for the fully grouted and partially grouted masonry, as permitted by the standard, since these walls were only partially grouted.

The interaction diagram for the conventionally reinforced and NSM reinforced walls based on the CSA S304-14 design approach for the unfactored resistance is shown in Figure 6.28 a) and b), respectively. Each

Chapter 6 – Analysis

of these diagrams also include the experimental data for the test walls at a maximum reinforcement strain of 1800 μm/m. The maximum moment resistance of the walls for testing cycles that exceeded the yield resistance are also plotted on Figure 6.28.

Table 6.7: Typical design values for rectangular stress block for reinforced masonry

Parameter	CHxxxx	NHxxxx
f'_m	9.17 Mpa	10.0 Mpa
ε_m	0.003	0.003
β_1	0.8	0.8
f_y	400 Mpa	400 Mpa
E_s	200 000 Mpa	200 000 Mpa
ϕ_m	1	1
ϕ_s	1	1
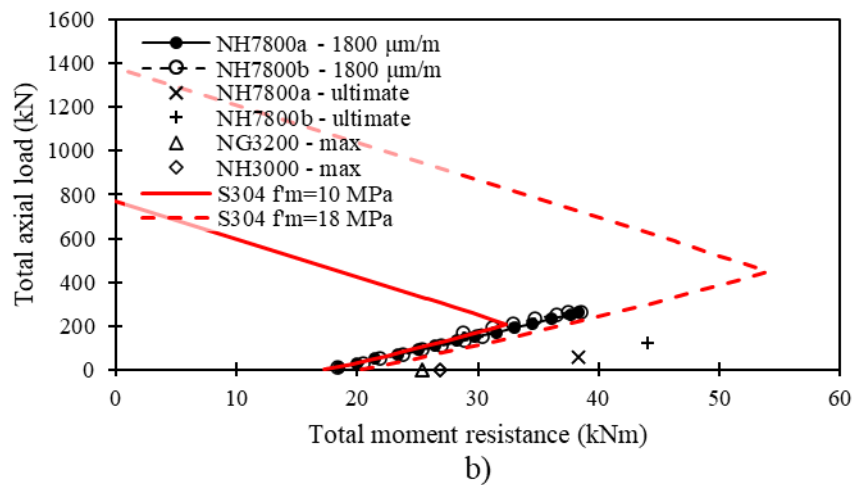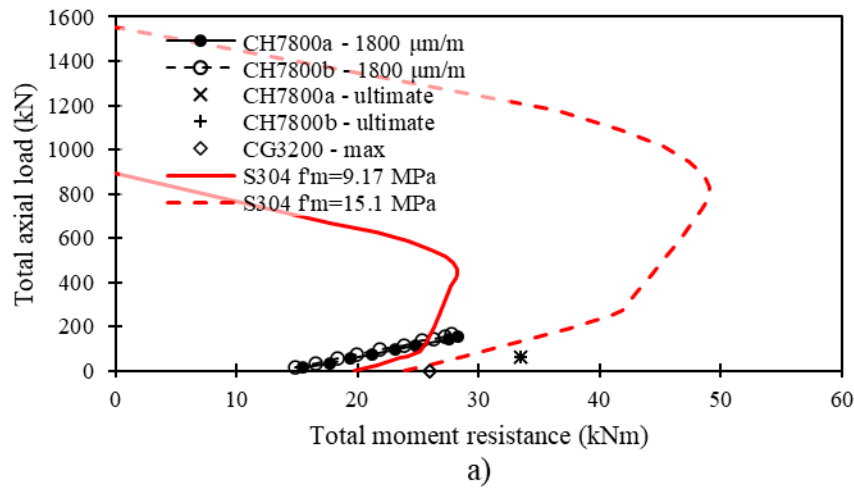
Figure 6.28: Axial load – moment interaction of 3 m tall and 8 m tall RM walls compared to unfactored design values: a) conventionally reinforced walls; and b) walls with NSM steel reinforcement

Chapter 6 – Analysis

These design values provide a conservative estimate of the compressive strength of the masonry material, and a good approximation of the resistance of the reinforcing steel. Although the interaction diagram based on the CSA S304-14 design approach is only applicable for walls at the ultimate limit state, the same trends are observed near the elastic limit state (maximum reinforcement strain of 1800 µm/m).

Alternately, the average masonry compression strength and steel reinforcement properties from the two testing series, shown in Table 6.8, can be used to generate similar interaction diagrams, also show in Figure 6.28 (dashed red line) following the same design equations from CSA S304-14 (CSA Group 2019a) as described above.

Table 6.8: Average prism strength and reinforcing bar strength from the testing series

Parameter	CHxxxx	NHxxxx
f'_m	15.08 Mpa	17.98 Mpa
ε_m	0.003	0.003
β_1	0.8	0.8
f_y	463 Mpa	463 Mpa
E_s	185 750 Mpa	185 750 Mpa
ϕ_m	1	1
ϕ_s	1	1

This graphic clearly demonstrates that the design equations provide a good estimate of moment resisting capacity of the walls for tension-controlled conditions (yielding of the steel reinforcement) for both conventionally reinforced slender RM walls, and those with NSM steel reinforcement. Additionally, the trend of increasing moment resistance with increasing axial load at 90% of the nominal yield strain of the reinforcing bars (1800 µm/m) matches the trend in the interaction diagram based on the standard equation.

6.6 Discussion of Flexural Stiffness Response

Accurately determining the flexural stiffness of an RM wall section for the calculation of secondary moment effects remains challenging. In this section, proposed methods for estimating the flexural stiffness are discussed. The viability of NSM steel bars as a method of improving the flexural stiffness and therefore the structural performance of slender RM walls is also discussed.

Chapter 6 – Analysis

6.6.1 Determining the flexural stiffness of slender RM walls

The CSA S304-14 equation for flexural stiffness, in most cases, provided a conservative estimate of the global flexural stiffness, calculated based on applied load and midspan displacement through the moment magnifier method and Equation (6.18), for the walls tested as part of the current experimental series; however, the level of conservatism is not consistent. Unconservative flexural stiffness values were found for low levels of applied moment, and over-conservatism is apparent for cases with high applied axial load and moment. Improving the design equation for flexural stiffness should consider the following conditions:

a) An accurate flexural stiffness value should be provided throughout the useful range

b) Cracked section properties should be used for consistency with the approach for calculation of flexural strength at the ultimate limit state

c) All practical reinforcement configurations should be accommodated within the approach

d) Ideally, the approach should be simple and practical

Measured against these criteria, the current CSA S304-14 equation does not provide a consistently accurate flexural stiffness value and allows the use of stiffness properties greater than the cracked stiffness, therefore it does not satisfy conditions a) and b). Condition c) is satisfied since the inputs of I_o (moment of inertia of the intact section) and I_{cr} (moment of inertial of the fully cracked section) may be defined, for any reinforced section, using a first principles approach. In more general terms, by using the *e/t* (eccentricity/thickness) ratio as the main variable, the equation is well suited for analysis of an interior wall subjected to eccentric axial load (for which the eccentricity remains constant and only the magnitude of the axial load will change); however for exterior walls, out-of-plane loads such as wind loads (or for interior walls subjected to seismic loads) will change the effective eccentricity depending on the load case. The simplicity of the equation, condition d), is a subjective matter.

The approach suggested by Liu and Hu (2007), presented in Chapter 2, and summarized as Equation (6.21), has the potential for greatly overestimating the flexural stiffness at high levels of applied moment. The current testing series has demonstrated that for low levels of applied axial load, the flexural stiffness of the

155

Chapter 6 – Analysis

walls converges towards the cracked stiffness with increasing moment. Furthermore, the cracked flexural stiffness of an RM section may often be less than 10% of the initial uncracked stiffness EI_o; however, for *e/t>0.4* (large applied moments), the proposed ratio of *EI_{eff}/EI_o* reaches 34% for the height to thickness ratio of the 8 m tall reinforced walls from this testing series. Furthermore, the equation does not account for the effect of reinforcing material, since EI_o is governed by the masonry material (if reinforcing bars are located at the centre of the section, they will not contribute to the I_o value). The benefit of even a heavily reinforced wall section may not be captured using this approach.

Equation 6.21
$$EI_{eff}/EI_o = \begin{cases} 0.7, \ 0 \le e/t \le 0.1 \\ 1 - [2.375 - (0.0175h/t)](e/t), \ 0.1 \le e/t \le 0.4 \\ [0.05 + 0.007h/t], \ e/t > 0.4 \end{cases}$$

The approached developed by Bilotta Rios and Cruz Noguez (2021), summarized as Equation (6.22), also has the potential to overestimate the effective flexural stiffness. The equation provides a solution unrelated to the cracked stiffness of the section, and higher stiffness values can be obtained by simply increasing the height of the wall (without increasing the wall thickness or reinforcement). Furthermore, stiffening effects that could arise based on the placement of the reinforcing bars (i.e., placing the bars in the centre of the cross section, or nearer to the outer surfaces) are not considered.

Equation 6.22

$$EI_{eff} = \begin{cases} 6.021x10^6P + 5.92x10^5A_s + 1.075x10^7f'_m + 1.0632x10^7\left(\frac{h}{t}\right) - 4.75x10^8, \quad \rho < 1.5 \\ 2.07x10^6P + 5.77x10^5A_s + 5.052x10^7f'_m + 2.157x10^7\left(\frac{h}{t}\right) - 6.602x10^8, \quad \rho \ge 1.5 \end{cases}$$

By inspection of the moment-stiffness response of the 3 m tall and 8 m tall RM walls in the current testing series, the flexural stiffness converges towards the cracked stiffness of the section with increasing applied moment, and the cracked stiffness is affected by the axial load. Through a rational analysis of the cracked section with an applied axial load and increasing applied moment, a rational moment-stiffness relation can be developed, however this relation over-estimates the flexural stiffness for repeated or subsequent loading

Chapter 6 – Analysis

cycles of an RM wall for low levels of applied axial load. It is therefore proposed that the cracked stiffness calculated through rational analysis at the onset of yielding in the reinforcing steel, and accounting for the effect of axial loading, be used as the effective flexural stiffness of RM walls. For lightly reinforced RM walls, the maximum compressive strain, ε_c, in the masonry at the onset of yielding of the reinforcement (ε_s = 0.002 m/m) is much lower than the maximum allowable strain of 0.003 m/m. For such cases, a linear stress distribution can be assumed as described in Method 1 for the determination of the curvature (Section 6.2). This method may be applied to a wall section, as illustrated in Figure 6.29, with an arbitrary distance d from the extreme compression fibre to the centroid of reinforcement in tension as demonstrated in Appendix C.
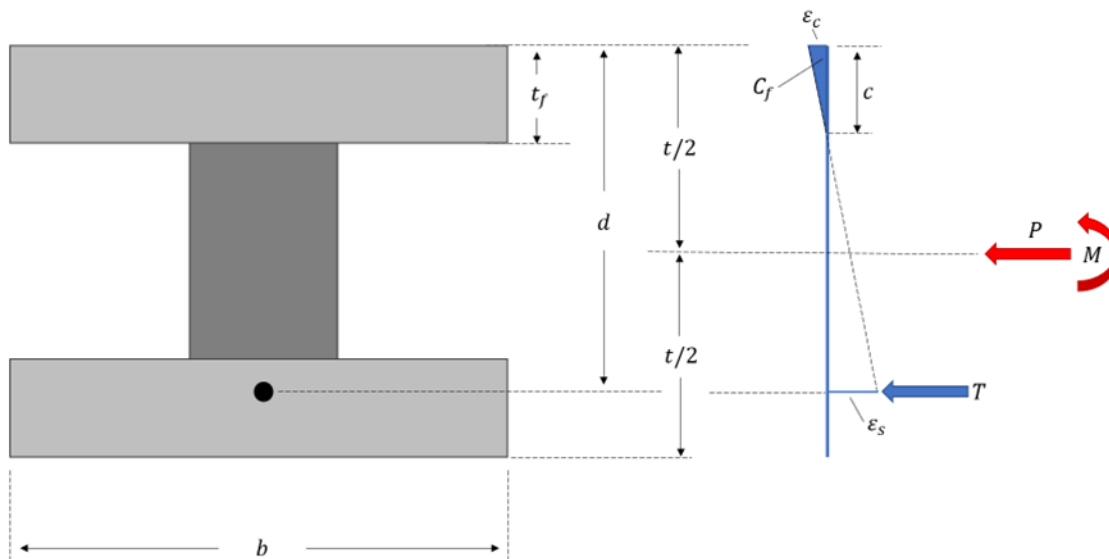
Figure 6.29: Reinforced wall section subjected to axial loading for determining the flexural stiffness

The closed-form solution presented in Appendix C is only valid for cases where the compression zone does not extend beyond the thickness of the face-shell of the masonry unit, and for fully grouted masonry sections. Conveniently, cases wherein the compressive zone exceeds the thickness of the face shell in compression corresponds to highly reinforced cases where most or all the cells within a wall section would be grouted. For cases that include compression within the grouted cells in partially grouted walls, or hollow

Chapter 6 – Analysis

sections in which the neutral axis falls within the hollow portion of the wall, a similar approach may be applied; however, the value c (depth to the neutral axis) may be determined through iteration rather than a closed-form equation.

This approach should provide a lower bound flexural stiffness value for RM walls subjected to out-of-plane loading. Although a higher flexural stiffness may be calculated using the rational analysis for lower levels of reinforcement strain, the current testing demonstrated that those values may not be conservative in cases of repeated loading cycles, or if an overloading event occurs (even if the yield moment resistance is not exceeded).

6.6.2   Improving the flexural stiffness of slender RM walls through NSM steel reinforcement

The testing presented in this report has demonstrated that walls with NSM reinforcement consistently exhibited improved flexural stiffness when compared to conventional RM walls. The similar flexural stiffness response of NH3200 and NH3000 (loading and reloading of Wall NH3200), as well as the cyclic loading tests of walls NH7800a and NH7800b, have demonstrated good flexural stiffness retention for this system. Aesthetically, the walls with NSM reinforcement developed narrower cracks at the yield point compared to the conventionally reinforced walls.

Although NSM-reinforced walls can be constructed without grouting the cells, the resulting system has a lower shear resistance than that of a grouted wall, as demonstrated by the lower displacement at failure of Wall NH3000 compared to Wall NG3200. Additionally, the vertical grooves required for the NSM reinforcement have contributed to the development of vertical failure planes at large displacements in the 3 m tall test walls. This ultimate failure mechanism was not observed during testing of the very slender 8 m tall walls; however, these were not tested to the point of ultimate failure.

The presence of the grooves within the masonry units may result in a reduction of the compressive strength, as was apparent for the prism tests that were completed alongside the tests of 3 m tall walls. This difference in strength, however, was not observed during the prism tests that accompanied testing of the 8 m tall walls,

Chapter 6 – Analysis

despite having been produced by the same manufacturer in the same moulds. No statistically significant difference in prism strength was observed during the initial testing of SRCMU prisms at the University of Manitoba (Sparling 2015). Further testing may be required to determine the effect of the grooves on the compressive strength, and refinement of the cross-sectional shape of the grooved masonry units (e.g., thickening the web around the groove) may reduce these effects. Under the test conditions discussed herein, any deficiencies in axial and shear strengths of the hollow NSM walls did not affect their elastic response.

Through analysis of the reinforcing bar strain readings, displacement readings, rational analysis, and through analysis by applying current CSA S304-14 masonry design provisions (CSA Group 2019a), the flexural stiffness of the walls with NSM reinforcement was shown to be equivalent to that of conventionally reinforced walls under low applied loads. The global flexural stiffness response of the walls was observed to trend toward or exceeds the theoretical uncracked stiffness (E_mI_o), upon initial loading, at load levels approaching zero. This contradicts findings by Al-Jaberi et al. (2019) who reported that initial flexural stiffness of 30% of the theoretical value is commonly reported in testing of masonry walls.

Under loads approaching the yield moment, the walls with NSM reinforcement exhibit twice the flexural stiffness of the walls with conventional reinforcement. Variability in flexural stiffness along the height of the walls was explored by studying the differences in curvature response at various heights and distances from the nearest bed joint. Although flexural stiffness decreases measurably at the location of bed-joints, the global displacement behaviour of the wall is well predicted by the stiffness response near the mid-span of the walls, at 45 mm from the nearest bed-joint, and by measuring the average curvature for the wall over a gauge length of 400 mm. Measuring the flexural stiffness at mortar joints near the mid-span (or calculating it through a rational analysis) generally provides a conservative estimate of the global flexural stiffness response of the wall as a whole.

The walls with NSM reinforcement exhibited good flexural stiffness retention. Under increasing applied moment, Walls NG3200, NH3200, and NH3000 maintained flexural stiffness significantly higher than the cracked stiffness (E_mI_{cr}) and better than the conventionally reinforced Walls CG3200 and CH3200. Under

Chapter 6 – Analysis

cyclic loading with varying levels of axial load, each of the 8 m tall RM walls (conventional and NSM reinforced), exhibited a global flexural stiffness response (stiffness calculated based on the displacement at midspan) lower than expected (based on a rational analysis of the cracked section and accounting for the effects of the axial load) when they were subjected to low out-of-plane loads. However, the rational analysis provided a conservative estimate of the flexural stiffness for increased levels of applied moment, which converged toward the flexural stiffness measured at a mortar joint near the midspan as the applied moment approached the yield moment.

Chapter 6 – Analysis

7 Application

Using reinforcing bar strains, displacement data, rational analysis, and S304-14 (CSA Group 2019a) design provisions indicate that existing methods for the analysis of reinforced CMU walls (for strength and flexural stiffness) are largely applicable to grooved CMU walls with NSM steel reinforcement. Each of these four techniques predict the high cracked flexural stiffness developed in walls with NSM reinforcement. This high flexural stiffness is conducive to the design and construction of slender masonry walls subjected to out-of-plane and axial loads, for which moment magnification effects may govern. The ductile out-of-plane response of the walls tested as part of this experimental program suggest they may also be useful as part of structural systems with a high ductility demand; given their modest out-of-plane flexural stiffness and strength, they would not likely be part of the main lateral force resisting system for a structure, yet their moderate out-of-plane ductile capacity suggests that they could withstand the ductile deformation demands of a structure without collapsing.

Furthermore, based on the testing reported herein, the S304-14 (CSA Group 2019a) provisions for flexural stiffness of reinforced masonry walls underestimate the extent to which tension stiffening effects contribute to the flexural stiffness under low-to-moderate out-of-plane flexural loads. The current standards formulation also does not account for the stiffening effect of increased axial load. A sectional analysis which accounts for the tension stiffening effect of the CMUs on the reinforcing steel, or provisions which would account for the stiffening effect of axial load, could result in a less conservative and more cost-effective approach for the determination of out-of-plane flexural stiffness for structural design.

This chapter provides a design example demonstrating the impact of the high out-of-plane flexural resistance developed by walls with NSM steel reinforcement for the design of the slender walls for warehouse buildings. The walls with NSM reinforcement can be constructed from narrower units and with less reinforcement than achievable with conventional reinforcement techniques; this could greatly reduce construction costs for slender RM walls. The effect of permitting a flexural stiffness formulation that

accounts for the stiffening effect of axial load is also highlighted. Practical considerations include how the shape of the masonry units may affect the ease of construction by a mason, as well as how the process of reinforcement could affect construction staging. Select durability considerations are also introduced in this section.

7.1 Design Example

Two structures are considered for the design examples herein. The first is a relatively small warehouse with 6 m tall exterior walls, and column spacing at 15 m on centre. The second is a large warehouse with 8 m tall exterior walls and column spacing at 18 m on centre to allow for larger equipment to drive between aisles. A conceptual view of the typical tributary area and elevation for the walls of each of these structures is provided in Figure 7.1.
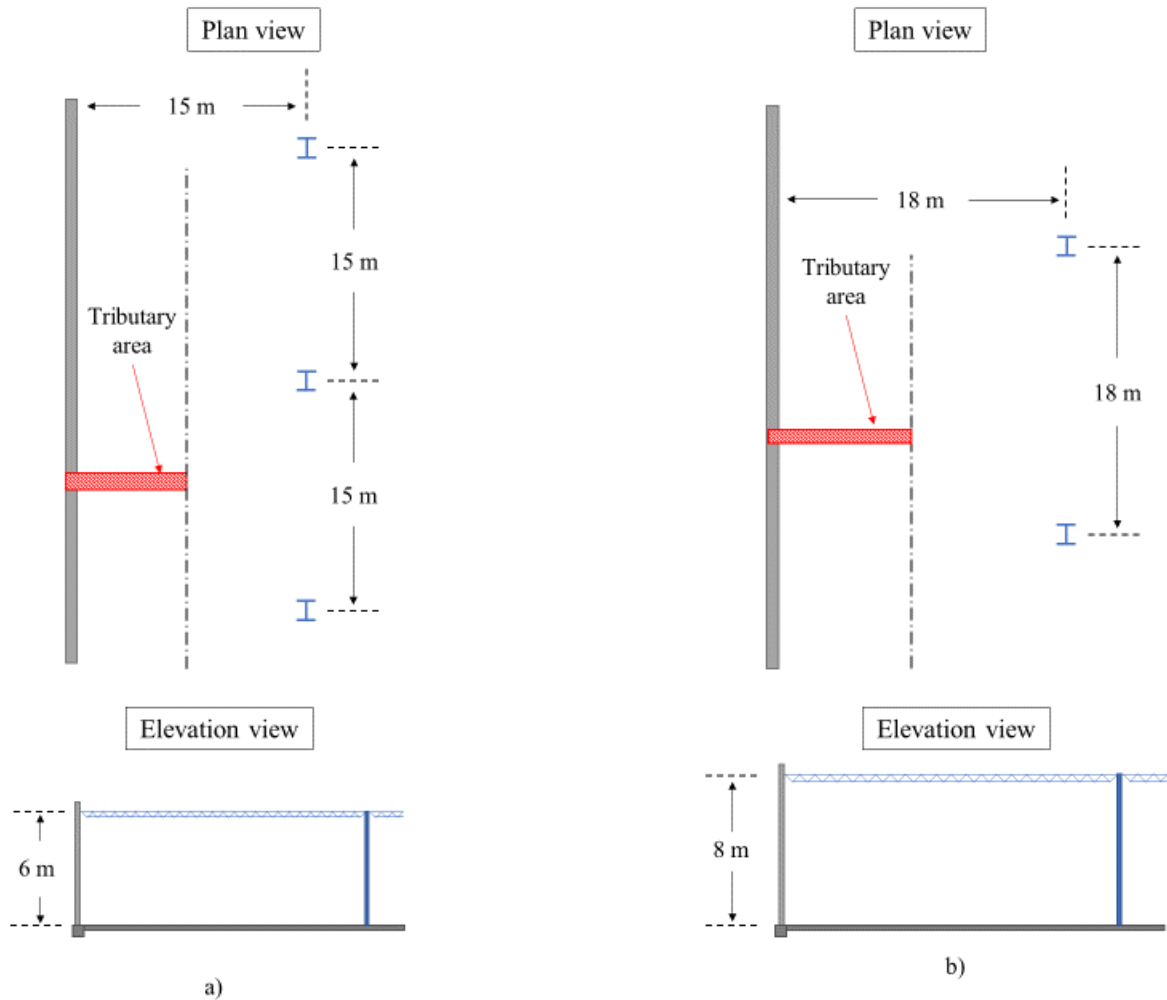
Figure 7.1: Typical layout and tributary area (1 m strip) supported by warehouse walls: a) 6 m tall warehouse; and b) 8 m tall warehouse

The complete design process, including assumptions and loading parameters prescribed by the 2015 National Building Code of Canada (NRC 2015) for North York, Ontario, is outlined in Appendix D. Based on this analysis, hollow SRCMU walls constructed from 200 mm, 15 MPa units (nominal block size and strength), reinforced with 10 M bars spaced at 400 mm on centre (such as those described in Chapters 4, 5, and 6) would be adequate for the construction of a small warehouse with 6 m tall walls, except that the total factored axial load exceeds the prescriptive limit on the axial load resistance of $0.1\phi_m f'_m A_e$ from CSA S304-14 (CSA Group 2019a). Given that the axial load resistance limit was put in place based on lack of experimental research on slender masonry walls, it is envisioned that this and other current research studies will lead to relaxation of this limitation; otherwise, the axial load capacity of these walls could be increased

through partial grouting or by using a higher strength unit (grouting one cell per metre length of the wall, or using 20 MPa strength units would be sufficient to meet the strength capacity limit).

Conventionally reinforced walls constructed from 200 mm, 15 MPa units (nominal block size and strength) reinforced with 20 M bars spaced at 600 mm on centre could only be constructed to a height of 4.5 m for a similarly loaded small warehouse structure. The analysis also shows that this type of wall would behave as an over-reinforced section (does not meet the maximum reinforcement requirement) and may not exhibit a ductile failure mechanism, given the base value for the masonry strength. This constraint could, however, be overcome if prism testing were used to confirm a higher value of f'_m following CSA S304-14 Annex D (CSA Group 2019a), or if higher strength units were used.

A fully-grouted SRCMU wall constructed from 200 mm units (nominal size), with NSM reinforcement in the form of 10M bars spaced at 200 mm on centre would be adequate for the exterior walls of a large 8 m tall warehouse. However, an f'_m value higher than the base value, arising from the use of 15 MPa units (nominal strength) would be needed to develop the required moment resistance. In this case 30 MPa units, providing an f'_m value of 13.5 MPa is sufficient. Achieving walls of this height with conventionally reinforced unit masonry would require the use of larger units. Using 250 mm (nominal size) CMUs, a sufficiently strong and rigid wall can be achieved if 20M reinforcing bars are placed in each cell; however, these bars would need to be placed in a staggered pattern such that the bars in tension (half of the bars) are placed at a depth of 150 mm from the compression face, as illustrated in Figure 7.2. Higher strength units (30 MPa nominal strength) would also be needed for this design to work.
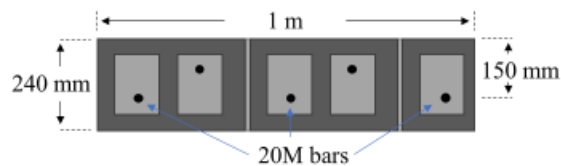
Figure 7.2: Staggered pattern of reinforcement for 1 m strip of RM wall constructed from 250 mm CMUs

Chapter 7 – Application

It is interesting to note for these walls that the use of higher strength masonry units has a large influence on the flexural strength and stiffness of the conventionally reinforced walls. This is because the change in the size of the masonry compression stress block at the ultimate limit state affects the moment arm of the reinforcement (distance from the centroid of the masonry compression stress block to the centroid of the reinforcement in tension). In conventionally reinforced walls (particularly in cases where reinforcement is placed in the centre of the unit cells), the moment arm of the reinforcement is quite small, and can therefore be greatly affected by small changes in the size of the compression zone. When NSM reinforcement is used, the moment arm of the reinforcement is larger, and the effect of the size of the compression zone is typically marginal.

For each of these design scenarios, the large applied axial loads included in the governing load combinations will likely have a significant effect on the flexural stiffness. As illustrated in Appendix D, the design height of the warehouse walls could be increased by approximately 500 mm without changing the reinforcement configurations if the stiffening effect of the axial load were accounted for, using the rational analysis method proposed in Chapter 6.

7.2   Practical Considerations

For a new construction method to be adopted, it is not sufficient for the new structural members to be stronger or otherwise better than existing methods, the construction process also needs to be practical and cost-effective in the field. During the construction of the test walls in the high bay laboratory, a few challenges were encountered, which need to be addressed before NSM reinforcement for new masonry walls can be deemed practical. These include concerns regarding the shape of the SRCMU blocks, as well as the reinforcement and construction staging.

7.2.1   SRCMU unit shape

During the construction of the masonry walls for the tests described in this dissertation, it was clear that the mason had difficulty maintaining a consistent head joint while keeping the vertical grooves clear of mortar

Chapter 7 – Application

when placing the SRCMU blocks. Some of the head joints were not fully filled during construction and had to be re-pointed before installing the NSM reinforcement as shown in Figure 7.3. Due to the presence of the partial groove on the ends of the SRCMU blocks, the mason had difficulty applying a full layer of mortar on those vertical edges; additionally, clearing excess mortar from the grooves after a block was placed occasionally dislodged mortar from the head joint, leaving an opening. A re-design of the masonry units could help address this issue.

a) b)
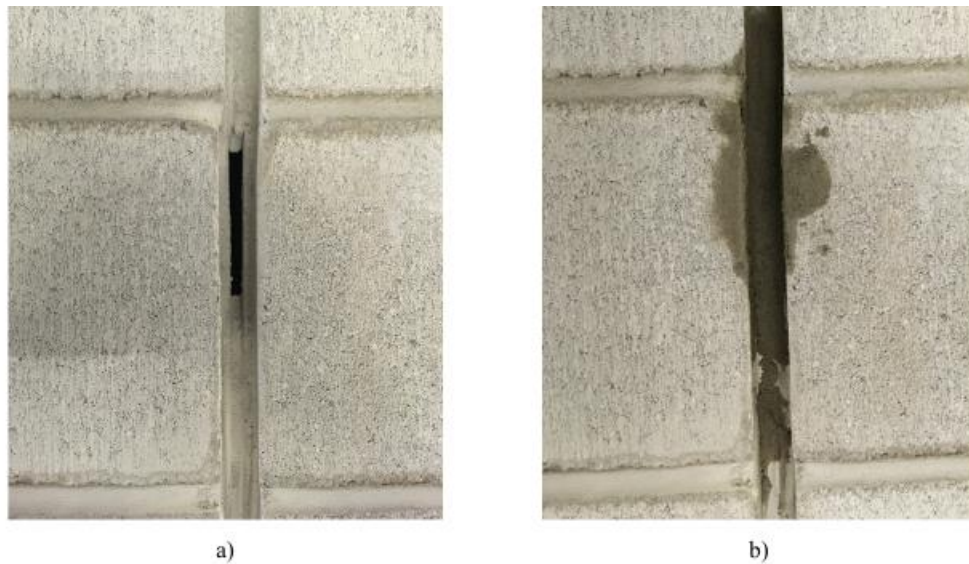
Figure 7.3: Mortar head joint of SRCMU wall: a) partially open head joint; and b) re-pointed head joint

The SRCMU blocks used in this testing series were manufactured using moulds modified from an existing block shape, as discussed in Chapter 4. This was done to reduce costs and accelerate manufacturing. If, however, a fully customized mould was to be fabricated, different shapes of the SRCMU could be considered. The possible block cross sections shown in Figure 7.4 each offer different benefits and disadvantages while facilitating the placement of vertical mortar head joints as well as vertical NSM reinforcement. Option a) 4-web unit, has the vertical grooves off-set by 100 mm from the position of the grooves in the original SRCMU; since these units have an additional web, they would be marginally heavier and more thermally conductive than current conventional CMUs. Options b) 2-web unit, also has the vertical grooves offset by 100 mm compared to the original SRCMU; however, the open-ended configuration could make it prone to breakage. Option c) 3-web unit, has the vertical grooves offset by

Chapter 7 – Application

50mm compared to the original SRCMU block and may also be more prone to breakage. To illustrate a few options of block configurations, only the stretcher-type units are shown in Figure 7.4. For each of these, edge units, corner units, and half-units would also be required, depending on the application.
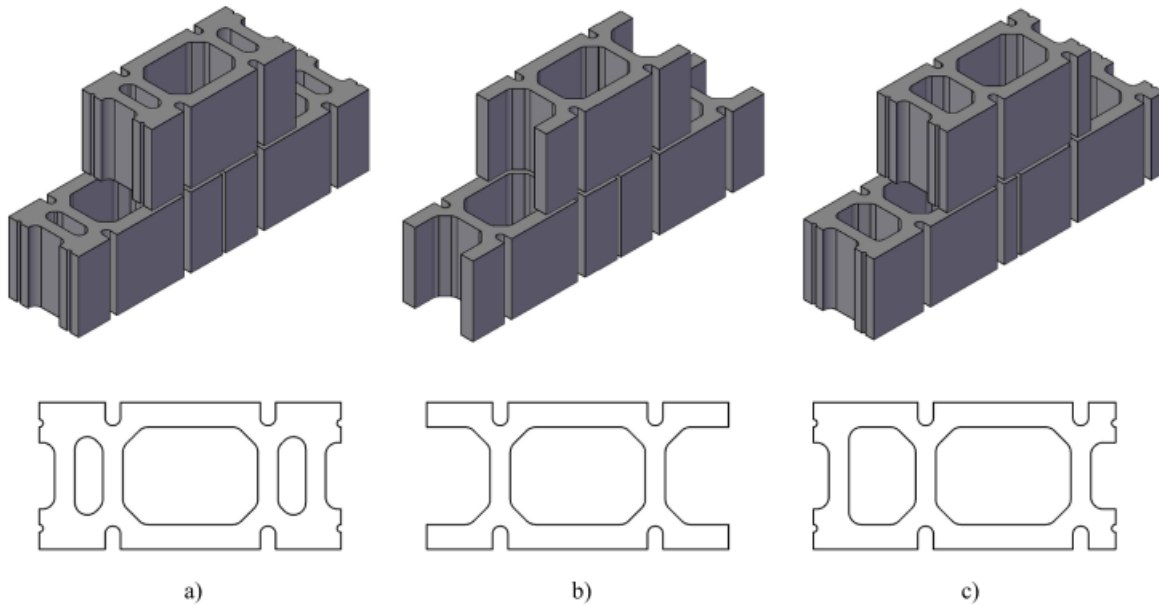
Figure 7.4: Possible unit shape options for SRCMU blocks: a) 4-web unit; b) 2-web unit; and c) 3-web unit

Each of the units illustrated in Figure 7.4 are based on a modular 190 mm x 190 mm x 390 mm CMU (200 mm nominal size) and include integral surface grooves spaced at 200 mm on centre. Option a), 4-web unit, maintains the geometry of conventional CMUs for the vertical edge faces (where the head joints are placed). When placed in running bond, the two central webs line up between subsequent courses of masonry, however the two end webs will obstruct the continuity of the hollow cells along the height of the constructed wall. The 4-web configuration would make the bare unreinforced unit more thermally conductive than conventional units; however, given that SRCMU walls with NSM reinforcement will not require as many grouted cells as conventional walls, such walls would likely still have improved thermal resistance.

Option b), the 2-web configuration, has protruding face shell components, similar to "H-blocks" (double open-ended masonry units) which are used in highly reinforced RM walls to improve the flow of grout through the wall section. When these blocks are placed in a running bond configuration, each of the webs, as well as the grooves for the NSM reinforcement, are aligned. This 2-web configuration would reduce

Chapter 7 – Application

thermal bridging through the units, as well as allow easy placement of additional reinforcing bars within the hollow cells, if required. These 2-web units could also be used in combination with option a) 4-web units and allow certain cells to be available for reinforcing bars, while others are obstructed by the more robust 4-web units.

The 3-web configuration, option c), provides a compromise between the 2- and 4- web units. Although two of the surface grooves are located near the corners of the block (where breakage could occur), they should be less prone to breakage than the 2-web units. They will also be less thermally conductive than the 4-web units. Two of the three webs of these units will be in alignment when subsequent courses of units are placed in a running bond pattern, and sufficient overlap of the cells is provided such that additional reinforcing bars could be placed within these cells, if needed. The position of the surface grooves, offset by 50 mm from the position of the grooves for the other unit configuration, would make it incompatible with the other two configurations.

7.2.2 Reinforcement

Modification to the joint reinforcement wire (ladders or trusses) is necessary to go around the surface grooves. For the purposes of this experimental study, the wire ladders were bent by hand during construction as shown in Figure 7.5; however galvanized steel wire ladders would need to be shaped by the manufacturer prior to hot-dip galvanization for exposed exterior wall applications. Concerns could also arise from the use of 10M reinforcing bars for the main longitudinal reinforcement of the walls. 10 M bars are very flexible and can accidentally be deformed during delivery and on-site handling – further modification to the surface grooves to accommodate a larger bar size (e.g., 15M) could be beneficial.

Chapter 7 – Application
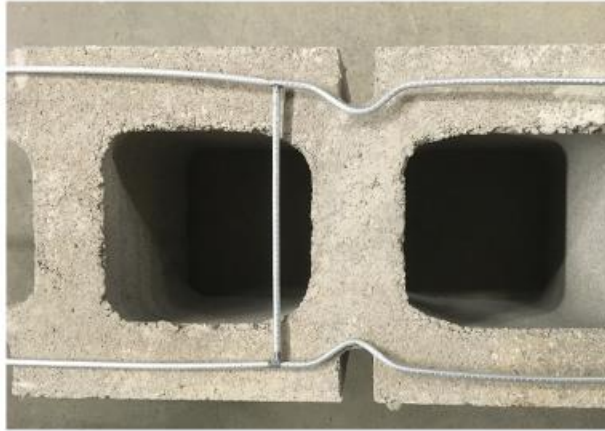
Figure 7.5: Deformed joint reinforcement ladder for SRCMU construction

7.2.3   Construction staging

Another concern that could arise during construction of SRCMU walls, particularly for slender walls, is that continuous NSM reinforcing bars are placed at the end of the construction process, leaving the walls without any vertical reinforcement until construction is completed. This is in contrast with conventional reinforcement, which is typically placed at intervals of 3 m in height to limit the height of grouting lifts. Additional bracing may be required during construction of walls that will be reinforced with NSM bars. In these cases, the speed of construction that can be achieved using NSM reinforcement (since work on the wall construction does not need to stop to allow grouting and reinforcement) could help mitigate the cost of additional bracing, if required. Additionally, if epoxy is used to bond the NSM reinforcement into the grooves, the full flexural strength of the walls could be developed very rapidly, as most structural epoxies achieve their design strength within a few days. Alternatively, a portion of the reinforcement may be placed using conventional means (grouted, embedded) during construction, for additional stability, before the NSM reinforcement is applied.

7.3   Durability

Long-term durability of RM walls with NSM steel reinforcement has yet to be studied in detail for new construction, although limited studies of the durability of NSM reinforcement are available. Fernandez et al (2018) studied the effect of accelerated ageing processes (salt crystallization and temperature cycling) on

Chapter 7 – Application

NSM Carbon Fibre Reinforced Polymer (CFRP) strips within concrete specimens and found that even very severe laboratory test conditions and real environmental exposure did not significantly decrease the strength of the NSM epoxy bonding. A different study by Al-Jaberi, Myers, and ElGawady (2018a) compared the durability of NSM CFRP and Glass Fibre Reinforced Polymer (GFRP) bars bonded in place using a cementitious paste. They found that the specimen reinforced with CFRP bars was more susceptible to degradation from the environmental exposure. Each of these studies only address the use of FRP reinforcement for NSM applications; however, relevant differences exist between FRP and steel reinforcement which could affect their long-term durability. It is also important to note that typical modern applications of reinforced concrete masonry walls shelter the loadbearing material from exposure to extreme temperature fluctuations as well as exposure to moisture. Although the susceptibility of concrete masonry with NSM steel reinforcement to bonding degradation will require further investigation, many of these concerns could be mitigated by proper detailing to prevent moisture ingress, and by placing insulating materials on the outer surface of the load bearing walls, as is common practice in Canada.

7.4   Fire Resistance

With regards to fire-resistance, RM walls are often used for the dual purposes of structural members and fire separations. The National Building Code of Canada (NRC 2015) provides a prescriptive fire rating for many materials including concrete block masonry. For 200 mm hollow CMU walls, the fire resistance rating for normal weight units is approximately 90 minutes. Fully grouted walls can also be used to easily achieve the maximum 4-hour fire-resistance rating. For most industrial buildings, however, the required fire resistance of load bearing walls is limited to the rating requirement of the supported elements, or 1 hour (whichever is greater); in the case of a single-storey warehouse, the roof may or may not require any fire-resistance rating. For concrete or masonry walls exposed to fire on one side only, there is no minimum concrete cover requirement; however, this likely assumes minimum covers required from CSA A23.3 (CSA 2019c) and achieved by conventional masonry construction following CSA S304 (CSA 2019a). Further research would be required to determine the fire resistance under loading of   RM walls with NSM

reinforcement; however, a thick plaster coating and/or Type X gypsum board covering could always be added to the wall system, where required, to achieve the necessary fire-resistance rating (as is common for steel construction).

Chapter 7 – Application

8   Conclusions

Three (3) m tall and 8 m tall, Reinforced Masonry (RM) walls were constructed and tested as part of this experimental series. The 3 m tall walls were tested in four-point out-of-plane loading, and the 8 m tall walls were tested in combined axial loading and four-point out-of-plane loading. Each of the walls tested had a nominal length of 1200 mm and were reinforced with the same total area of steel reinforcement. Testing of the 3 m tall walls was accompanied by Finite Element (FE) modeling and analysis. The testing compared the response of walls with conventional grouted reinforcement placed in the centre of the cross-section to walls with Near-Surface Mounted (NSM) steel reinforcement. Analysis of the response from testing focused on the flexural stiffness and its impact on secondary moment effects. This chapter provides a summary of major findings and conclusions.

8.1   Finite Element Analysis

Preliminary work towards developing an approach to FE modeling and analysis of hollow slender RM walls with NSM reinforcement was presented. The following conclusions may be drawn from the analysis work completed:

1) 3-dimensional FE model analysis may be used to accurately predict the load-displacement behaviour and yielding of a hollow RM wall.

2) A correction factor (shape factor) is needed to assign the appropriate material properties to the Concrete Masonry Units (CMU) within a masonry assembly for compression strength. The strength f'_c of the constituent concrete material of the CMU must be greater than the hollow prism strength.

3) Assigning the compressive strength of grout material determined from compressive tests of cylinders to the grout material of a masonry prism model led to the overestimation of the axial compressive strength and stiffness of the grouted prism.

Chapter 8 – Conclusions

4) A 44% reduction in the compressive strength of the constitutive material model for the CMU, and accompanying 24% decrease in Young's modulus, did not substantially affect the flexural stiffness, moment resistance, or ductility of the FE model of a 3 m tall hollow RM wall with NSM reinforcement.

5) Perfectly bonding the reinforcing truss elements to the FE model mesh of 1.2 m tall wall specimens and 3 m tall RM walls resulted in an acceptable response.

The following aspects of FE models will require additional research:

1) The FE models of 3 m tall masonry walls did not capture the ductility observed during testing. Further refinement of the modelling approach will be needed to allow the models to reflect the full plastic response observed during testing.

2) Refinement of the FE models for the grouted masonry prisms will be needed to capture the reduction in effective compressive strength from the interaction between the masonry unit and the grout.

3) The modelling approach presented in this dissertation results in highly complex models requiring large computational power to analyze; applying the approach to slender RM walls may not be currently feasible. The development of a less complex approach that can still capture the relevant structural behaviour would be desirable.

8.2   Response of 3 m Tall Walls

Testing of 3 m tall RM walls under conditions of four-point out-of-plane loading was used to compare the response of conventionally reinforced walls to walls with NSM steel reinforcement. Walls with the same total area of steel reinforcement, but different configurations and grouting were tested until failure. The following conclusions may be drawn based on the primary response from these tests:

1) Walls with conventional and NSM steel reinforcement configurations exhibited a defined elastic and extended period of plastic displacement prior to failure.

2) Each of the walls exhibited similar flexural strength ranging from 22.2 kNm to 25.9 kNm.

Chapter 8 – Conclusions

3) At low levels of applied loading, the grouted walls exhibited less displacement than similarly reinforced hollow walls.

4) At the global yield point, the displacement profile of the hollow and grouted walls with NSM reinforcement were nearly identical.

5) The fully grouted wall with conventional reinforcement failed by rupture of the reinforcing bars, whereas the hollow and grouted walls with NSM steel reinforcement failed by debonding of the reinforcement and fracture through the masonry material.

6) Strains in the tension reinforcement were lower for the grouted walls than the hollow walls under low loads; however, they converged as the moment approached the yield moment.

7) Strains in reinforcing bars near the compression face of walls with NSM steel reinforcement were lower for the grouted wall than for the hollow wall, and they diverged as the moment approached the yield moment.

8.3   Response of 8 m Tall Walls

Testing of 8 m tall RM walls with conventional and NSM steel reinforcement was conducted under conditions of combined axial loading and four-point out-of-plane loading. These walls were subjected to multiple cycles of out-of-plane loading within the elastic response range with different levels of applied axial load. During the final loading cycle, each wall was loaded until a displacement of at least twice the yield displacement was reached, while maintaining the applied axial load. The following conclusions may be drawn based on the primary response of these 8 m tall walls:

1) Each wall exhibited a strong recovery behaviour following the elastic loading cycles, recovering 80 to 95% of the displacement achieved when the maximum reinforcement strain reached 1800 µm/m.

2) Each wall exhibited a ductile behaviour when the yield strain in the reinforcing bars was exceeded.

3) The displacement at the onset of yielding for the walls with NSM steel reinforcement was approximately half that of the walls with conventional reinforcement.

Chapter 8 – Conclusions

4) The moment resistance was similar at the yield point for the walls with conventional and NSM steel reinforcement with 60 kN of applied axial load; however, the out-of-plane load resistance of the walls with NSM reinforcement was greater due to the reduced $P\text{-}\Delta$ effects.

5) The displacement ductility of the walls with NSM reinforcement, based on the out-of-plane load response, ranged from 1.3 to 1.5 for the walls with conventional reinforcement (60 kN applied axial load), and from 2.0 (120 kN applied axial load) to 2.6 (60 kN applied axial load) for the walls with NSM steel reinforcement.

6) A bi-linear response in the moment-displacement response developed for all walls with increasing applied axial load.

7) The walls with conventional reinforcement exhibited signs of elastic buckling under an applied load of 150 kN, whereas the walls with NSM steel reinforcement did not exhibit signs of buckling with 250 kN of axial load.

8) A sinusoidal curve was a good fit for the displaced shape of the walls.

9) More variability in the moment-strain response was observed for the walls with conventional reinforcement than for the walls with NSM steel reinforcement.

8.4   Analysis of Experimental results

Analysis of the response for testing the 3 m tall and 8 m tall walls, as well as the associated material testing, enabled a detailed study of the structural behaviour. The characteristics of the materials from the two experimental series were compared, and a detailed analysis of the flexural stiffness response of the masonry walls was conducted. The following conclusions may be drawn from comparing the response from the material testing with both series of RM wall tests:

1) Masonry prisms tested alongside the 3 m tall walls exhibited a difference in compressive strength between the prisms made from conventional masonry units and those made from the grooved Surface Reinforced Masonry Units (SRCMU) used in the construction of walls with NSM steel reinforcement;

Chapter 8 – Conclusions

however, this difference was not observed during the testing of the prisms that accompanied the 8 m tall wall tests.

2) The yielding properties of the 10M bars used to reinforce the 3 m tall walls exhibited a distinct yield plateau, whereas those used in the 8 m tall walls exhibited a curved stress-strain response. The latter was attributed to cold working (prior yielding) of the bars.

The following conclusions may be drawn from an analysis of the flexural stiffness response of 3 m tall RM walls:

1) The flexural stiffness of the masonry walls with NSM steel reinforcement was found to be lower at the horizontal mortar joints where horizontal cracks were observed to initiate.

2) The flexural stiffness was observed to be higher near the bottom of the walls, where axial load from self weight was higher.

3) The flexural stiffness calculated based on reinforcement strain data at 45 mm away from the nearest mortar bed joint agreed with the stiffness calculated based on the displacement response.

4) Both the CSA S304-14 standard equation for flexural stiffness and a rational analysis of the wall sections underestimate the observed flexural stiffness under conditions of low applied load; however, these values converge as the load approached the yield point.

The following conclusions may be drawn from analysis of the flexural stiffness response of 8 m tall RM walls:

1) The out-of-plane load resistance at 90% of the nominal yield strain in the reinforcement of the walls with conventional reinforcement decreased with increasing applied axial load, whereas the out-of-plane load resistance of the walls with NSM steel reinforcement increased with increasing applied axial load due to lower displacement and decreased P-Δ effects.

2) The moment resistance of each of the walls increased with increasing applied axial load.

Chapter 8 – Conclusions

3) The first loading cycle in the elastic range of each wall was characterized by a wide loop in the load-displacement response, whereas the response to subsequent cycles was characterized by thinner loops.

4) The flexural stiffness response of the walls determined based on the average surface strains on the compression and tension faces near the mid span agreed with the stiffness response determined based on displacement; the flexural stiffness response calculated based on the reinforcement strain at the location of mortar joints was lower.

5) The flexural stiffness response of the walls calculated based on a rational analysis of the section converged toward the stiffness response calculated based on the reinforcement strain at the mortar joints as the reinforcement strain approached 90% of the nominal yield strain.

6) During the first loading cycle, the flexural stiffness response of the walls calculated based on a rational analysis of the section provides a good estimate for the flexural stiffness response determined based on the reinforcement strain at the mortar joints; however, during subsequent loading cycles, the rational analysis overestimates the flexural stiffness response for conditions of low out-of-plane loads.

7) The CSA S304-14 standard equation for flexural stiffness provides a conservative estimate of the observed flexural stiffness response for most of the axial load conditions tested; however, it does not provide a consistently accurate value.

8) The axial load-moment resistance interaction at 90% of the nominal yield strain in the reinforcement matched the trend predicted based on the CSA S304-14 design equations for moment resistance at the ultimate limit state.

9) The calculation of the flexural stiffness using a rational analysis that accounts for the effect of axial load at the onset of yielding is proposed as a novel approach for the determination of flexural stiffness for the design of slender walls.

8.5   Application of the Research Findings

The purpose of this research was to supplement the literature on the structural behaviour of slender reinforced masonry walls, and to demonstrate the performance of RM walls with NSM steel reinforcement.

Chapter 8 – Conclusions

The potential impact of this research on building design was illustrated through a warehouse design example. The following conclusions may be drawn based on the design example for the assumed design conditions and site characteristics described in Chapter 7:

1) Given the same total area of reinforcing steel, lightly reinforced hollow masonry walls with NSM steel reinforcement can be constructed to a height approximately 1.5 m taller than walls with conventional reinforcement.

2) Fully grouted masonry walls with NSM steel reinforcement can be constructed using 190 mm wide concrete masonry units (CMU) to a height of up to 8 m; a similar wall reinforced with conventional methods would require the use of wider 240 mm units.

3) For the design scenarios considered, the use of the proposed approach for calculating flexural stiffness, which accounts for the effect of axial load, can be used to increase the design height of the walls by approximately 500 mm without changing the reinforcement or material properties.

Practical considerations that will require further investigation prior to adoption of NSM steel reinforcement for the construction of new buildings include the following:

1) The shape of the SRCMU masonry units used in this study made it difficult for the mason to maintain consistent vertical (head) joints. Changes to the block shape could help address this problem.

2) Modification to the joint reinforcement would be needed to prevent these wires from impeding the placement of NSM reinforcement.

3) Careful consideration of construction staging and temporary bracing would be necessary for the construction of slender walls with NSM steel reinforcement since these walls may be fully unreinforced until they reach their finished height.

Chapter 8 – Conclusions

4) Additional measures to ensure long-term durability and fire-resistance of the wall system may be required.

8.6 Final Remarks

The experimental work discussed in this dissertation incorporated the use of sophisticated instrumentation into the testing of full-scale reinforced masonry walls under loading conditions resembling field conditions. The displacement and curvature response of walls with NSM steel reinforcement shows that current methods of analysis for walls with conventional reinforcement are generally applicable to walls with NSM steel reinforcement. Although few reinforcement configurations and loading conditions were studied as part of this testing series, it appears that the high strength and flexural stiffness of RM walls with NSM steel reinforcement make them ideally suited for the construction of slender load-bearing walls such as the exterior walls of warehouse buildings.

9 Primary Contributions

This research project focused on full-scale, out-of-plane testing of reinforced concrete block masonry walls. The results presented herein complement the limited available experimental results from tests on very slender reinforced masonry walls subjected to combined axial and out-of-plane loads and include tests on walls reinforced using a novel approach for new construction: Near-Surface Mounted (NSM) steel reinforcement.

The main contributions arising from the research and outlined in this dissertation include the following:

- **Development of infrastructure for axial and out-of-plane load testing of reinforced masonry walls**

Steel frames were designed and constructed for testing full-scale reinforced masonry walls with and without axial load, which can accommodate walls with a height of up to 7.8 m. The axial loads applied during testing are the highest reported for full-scale tests on very slender reinforced masonry walls subjected to combined axial and out-of-plane loading.

- **Testing masonry walls with NSM steel reinforcement for new construction**

Reported herein are the first tests on full-scale Concrete Masonry Unit (CMU) walls reinforced with NSM steel bars. The out-of-plane flexural stiffness of CMU walls reinforced with NSM steel bars was compared to the stiffness of conventionally reinforced CMU walls. For walls with the same total area of flexural reinforcement, the walls with NSM reinforcement exhibited approximately twice the flexural stiffness of conventionally reinforced walls.

- **Detailed assessment of the flexural stiffness of reinforced masonry walls**

The flexural stiffness of the reinforced masonry walls tested was assessed using multiple methods with data collected from independent instrumentation. Subtle differences in the flexural stiffness response were observed depending on whether it was calculated using data from out-of-plane displacement, strain gauges located on reinforcing bars at the mortar joints, strain gauges located on reinforcing bars away from the

mortar joints, or average strains measured on the surface of the walls (tension and compression side) using a gauge length of 400 mm.

- **Influence of axial load on flexural strength and stiffness of reinforced masonry walls**

The interaction between axial load and flexural strength and stiffness of very slender (kh/t=42) reinforced masonry walls was assessed through cyclic out-of-plane loading with different superimposed axial loads, ranging from zero to 48% of their nominal axial compressive load capacity. Increased moment resistance and flexural stiffness were observed with increasing axial load for each of the walls tested. At 90% of the nominal yield stress of the steel reinforcing bars, the out-of-plane load resistance of the walls with NSM reinforcement increased with increasing axial load, whereas the resistance of the conventionally reinforced walls decreased with increasing axial load due to the greater secondary moment effects from the larger deflections (lower flexural stiffness).

- **Proposed method for slender reinforced masonry wall design and construction**

A sample design and analysis for the slender reinforced masonry exterior walls of a warehouse structure is used to illustrate the potential impact on design of the use of increased flexural stiffness due to imposed axial loads. The benefits of using the high stiffness of reinforced masonry walls with NSM steel reinforcement for the design of very slender reinforced masonry walls is also illustrated. Understanding of the structural response of reinforced masonry walls gained through the research presented herein may help improve the efficiency with which reinforced masonry structures are constructed, thereby reducing over-all usage of construction materials.

Chapter 9 – Primary Contributions

10 Future Work

Based on the research presented herein, the following areas require further examination:

1) Further work is needed toward the development of a FE analysis model that can predict the elastic and plastic response of slender RM walls with NSM steel reinforcement.

2) Testing of masonry prisms and masonry units as part of this experimental program yielded conflicting results regarding the effect of the shape of the grooved SRCMU masonry units, used for the construction of walls with NSM steel reinforcement, on the axial compressive strength. Further testing is required to determine whether the grooves of SRCMU masonry units affect the compressive strength of masonry walls.

3) The proposed method for determining the effective flexural stiffness for design of slender masonry walls should be validated against walls with other reinforcement configurations under a variety of axial and out-of-plane loading conditions. A similar approach to the testing presented in this dissertation should be adopted and multiple loading cycles should be applied within the elastic response range to capture the cracked stiffness response.

The following are additional proposed areas for future research:

1) Epoxy adhesives are expensive and carbon-intensive to produce. Other researchers have studied the use of cementitious pastes as an alternative to epoxy for bonding NSM reinforcement into grooves; however, so far these studies have been limited to applications of fibre-reinforced polymer (tapes, bars, or strands) as NSM reinforcement. Further research is needed to study the use of cementitious materials for the application of NSM steel reinforcement.

2) The shape of the SRCMU units used for the construction of the walls with NSM steel reinforcement made it difficult for the mason to maintain consistent vertical mortar joints between units. The development of a new masonry unit that would facilitate placement by a mason will require careful consideration of material usage and handling. Testing will be required to ensure they can be produced

using conventional block manufacturing techniques, and that they can withstand customary material handling during delivery and construction without excessive breakage, and to ensure an acceptable structural behaviour is achieved by the resulting masonry assemblies.

3) This testing series only considered the out-of-plane flexural behaviour of masonry walls. The effect of out-of-plane shear was not considered in the analysis of the response of the walls, and no tests with conditions of in-plane shear were conducted. Vertical NSM reinforcement may contribute significantly to in-plane shear resistance of masonry walls, however experimental testing will be required to characterize the response.

4) NSM reinforcement of masonry walls locates the reinforcing material very near to the surface, making it susceptible to deterioration. The environmental conditions to which the RM walls of new concrete masonry construction are subjected are different to those typical of retrofitting applications which constitute the focus of most existing literature on NSM reinforcement. Focused durability testing targeting the conditions typical of modern concrete unit masonry construction will be required.

11 Abbreviations and Notation

11.1 Abbreviations

The following abbreviations have been used throughout the text

BCEE	-	Bergeron Centre for Engineering Excellence
FE	-	Finite Element (computer analysis)
FRP	-	Fibre Reinforced Polymer
NSM	-	Near-Surface Mounted (reinforcement)
P-Δ	-	Secondary moment arising from axial load (P) and displacement (Δ)
RC	-	Reinforced Concrete
RM	-	Reinforced Masonry
SRCMU	-	Surface Reinforced Concrete Masonry Unit (Hashemian 2015)
URM	-	Unreinforced Masonry

11.2 Notation

The following notation has been used throughout the text, except as indicated for select equations from other works.

a	=	Depth of effective compression equivalent rectangular stress block
A_e	=	Effective area of the cross-section
A_s	=	Cross-sectional area of reinforcing steel
b	=	Length of a wall or wall section
c	=	Distance from the extreme compression fibre to the neutral axis of a section in flexure
C_m	=	Moment distribution factor
d	=	Depth from the extreme compression fibre to the centroid of reinforcement in tension

d_2 = Depth from the extreme compression fibre to the location of maximum tensile stress in the masonry material

e = Effective eccentricity M_{fp}/P_f

e_k = Kern eccentricity S_e/A_e

E = Young's modulus

E_m = Young's modulus of masonry

E_s = Young's modulus of reinforcing steel

$(EI)_{eff}$ = Effective flexural stiffness

$(EI)_s$ = Contribution of reinforcing steel bars to flexural stiffness

f'_c = Compressive strength of cementitious material

f'_m = Compressive strength of masonry material

ft = Modulus of rupture of cementitious material

f_y = Yield stress of steel

I_{cr} = Moment of inertia of the transformed cracked section

I_o = Moment of inertia of the effective cross section

k = Effective length factor for compression members

h = Unsupported height of a wall

M = Bending moment

M_{fp} = Factored primary moment

M_{ftot} = Total factored moment

P = Applied load

P_{cr} = Euler critical buckling load

P_f = Factored load

P_{rmax} = Maximum axial load resistance

S_e = Section modulus of A_e

t = Thickness of a wall

w = Distributed load (such as wind load)

β_d = Ratio of moment due to the factored dead load to the total factored moment

Δ = Displacement

Δ_y = Displacement at yielding

Δ_{max} = Maximum displacement

Δ_x = Displacement as a function of the position x

ε_m = Strain in the masonry material

ε_s = Strain of reinforcing steel

v = Poisson ratio

ρ = Reinforcement ratio (As/bt)

φ = Curvature of a structural section

ϕ_{er} = Resistance factor for flexural stiffness in the determination of slenderness effects

ϕ_m = Material resistance factor for masonry

12 References

Abboud, B. E., Hamid, A. A., and Harris, H. G. 1996 "Flexural Behavior of Reinforced Concrete Masonry Walls under Out-of-Plane Monotonic Loads." *ACI Structural Journal* 93(3): 327-335.

ACI Committee 551. 2021. "Pitfalls of Deviating from ACI 318 Slender Walls Provisions – Tech Note." *American Concrete Institute, PRC-551.3-21 Tech Note.*

ACI-SEASC Task Committee on Slender Walls. 1982. *Test Report on Slender Walls.* Los Angeles, CA.

Ahmed, A., Iskander, G., Bogoslavov, M., Isfeld, A., and Shrive, N. 2021. "Examining the Mode of Failure of Slender Concrete Block Walls." Paper presented at the *14th Canadian Masonry Symposium, Montreal, May 16-20, 2021.* Mississauga, ON: Canada Masonry Design Centre.

Al-Jaberi, Z., Myers, J. J., ElGawady, M. A. 2018a. "Environmental Effect on Reinforced Masonry Walls Strengthened with NSM and Cementitious Adhesive." Paper presented at the *10th Australasian Masonry Conference, Sydney, AUS, February 11-14, 2018,* 547-559.

———. 2018b. "Pseudo-Static Loading Comparison of Reinforced Masonry Walls Strengthened with FRCM or NSM FRP." *Construction and Building Materials* 167: 482-495. https://doi.org/10.1016/j.conbuildmat.2018.02.043

Alonso, A., Gonzalez, R., Cruz, C., and Tomlinson, D. 2021. "Pre-Test Analysis of the Effect of Rotational Base Stiffness on Loadbearing Slender Masonry Walls." Paper presented at the *14th Canadian Masonry Symposium, Montreal, May 16-20, 2021.* Mississauga, ON: Canada Masonry Design Centre.

Al-Saadi, N. T. K., Mohammed, A., and Al-Mahaidi, R. 2017. "Fatigue Performance of NSM CFRP Strips Embedded in Concrete using Innovative High-Strength Self- Compacting Cementitious Adhesive (HSSC-CA) made with Graphene Oxide." *Composite Structures* 163: 44–62. https://doi.org/10.1016/j.copmstruct.2016.12.015.

Amrhein, J. E. and Lee, D. E. 1984. *Design of Reinforced Masonry Tall Slender Walls*. San Francisco, CA: Wester States Clay Products Association.

Asplund, S. O. (1949). "Strengthening Bridge Slabs with Grouted Reinforcement." *Journal of the American Concrete Institute* 45 (1):397-406.

ASTM International. 2016. *Standard Test Methods for Tension Testing of Metallic Materials*, ASTM E8/E8M-16a, West Conshohocken, PA, USA.

Babaeidarabad, S., De Caso, F., and Nanni, A. 2014. "Out-of-Plane Behavior of URM Walls Strengthened with Fabric-Reinforced Cementitious Matrix Composite." *Journal of Composites for Construction* 18(4): 04013057. https://doi.org/10.1061/(ASCE)CC.1943-5614.0000457.

Bean Popehn, J. R., Schultz, A. E., and Drake, C. R. (2007). "Behavior of Slender, Posttensioned Masonry Walls under Transverse Loading." *ASCE Journal of Structural Engineering* 133 (11): 1541-1550. https://doi.org/10.1061/(ASCE)0733-9445(2007)133:11(1541)

Bilotta Rios, M. and Cruz Noguez, C. 2021. "Evaluation of Second-Order Effects in Slender Reinforced Masonry Walls." Paper presented at the *14th Canadian Masonry Symposium, Montreal, May 16-20, 2021*. Mississauga, ON: Canada Masonry Design Centre.

Borri, A., Castori, G., Corradi, M., and Sisti, R. 2014. "Masonry Wall Panels with GFRP and Steel-Cord Strengthening Subjected to Cyclic Shear: An Experimental Study." *Construction and Building Materials* 56: 63–73. https://doi.org/10.1016/j.conbuildmat.2014.01.056.

Chapter 12 – References

Borri, A., Corradi, M., Giannantoni, A., Speranzini, E., and Giannantoni, A. 2009. "Rubble Stone Masonry Strengthened using "Reticolatus" System." *Conservation News – Journal of the Association of Monument Conservators*, 26: 147–158. Available from https://repozytorium.biblos.pk.edu.pl/resources/33677

Carney, P., and Myers, J. J. 2003. "Shear and Flexural Strengthening of Masonry Infill Walls with FRP for Extreme Out-of-Plane Loading." Paper presented at the *Architectural Engineering Conference (AEI), Austin, TX, September 17-20, 2003*: American Society of Civil Engineers. https://doi.org/10.1061/40699(2003)45.

Casacci, S., Gentilini, C., Di Tommaso, A., and Oliveira, D. V. 2019. "Shear Strengthening of Masonry Wallettes Resorting to Structural Repointing and FRCM Composites." *Construction and Building Materials* 206: 13-34. https://doi.org/10.1016/j.conbuildmat.2019.02.044.

Červenka Consulting. 2016. *ATENA 3D Engineering*. V. 5.3. PC.

Chen, J. F., Chen, G. M., and Teng, J. G. 2016. "Challenges in the numerical simulation of debonding failure in FRP-strengthened RC structures." Paper presented at the *6th International Conference on Structural Engineering, Mechanics and Computation, Cape Town, RSA, September 5-7 2016: CRC Press.*

CSA Group. 2019a. *Design of Masonry Structures,* CSA S304-14 (R2019), Mississauga, ON.

———. 2019b. *Mortar and Grout of Unit Masonry*, CAN/CSA-A179-14 (R2019), Mississauga, ON.

———. 2019c. *Design of Concrete Structures*, CSA A23.3:19, Mississauga, ON.

da Porto, F., Mosele, F. and Modena, C. 2011. "Cyclic out-of-plane behaviour of tall reinforced masonry walls under P–Δ effects." *Engineering Structure* 33 (2): 287-297. https://doi.org/10.1016/j.engstruct.2010.10.004

Chapter 12 – References

Dawe, J. L. and Aridru, G. G. 1993. "Prestressed Concrete Masonry Walls Subjected to Uniform Out-of-Plane Loading." *Canadian Journal of Civil Engineering* 20: 969-979. https://doi.org/10.1139/l93-128

De Lorenzis, L., and Teng, J. G. 2007. "Near-Surface mounted FRP reinforcement: An Emerging Technique for Strengthening Structures." *Composites Part B: engineering* 38 (2): 119-143. https://doi.org/10.1016/j.compositesb.2006.08.003.

Derakhshan, H., Lucas, W., Visintin, P., and Griffith, M. C. 2018. "Laboratory Testing of Strengthened Cavity Unreinforced Masonry Walls." *ASCE Journal of Structural Engineering* 144(3): 04018005. https://doi.org/10.1061/(ASCE)ST.1943-541X.0001987

Dizhur, D., Griffith, M., and Ingham, J. 2014. "Out-of-Plane Strengthening of Unreinforced Masonry Walls using Near Surface Mounted Fibre Reinforced Polymer Strips." *Engineering Structures* 59: 330-343. http://dx.doi.org/10.1016/j.engstruct.2013.10.026

Dona, M., Minotto, M., Verlato, N., da Porto, F. 2019. "Proposal of Simplified Design Methods to Evaluate Second-Order Effects in Tall Reinforced Masonry Walls." Paper presented at the *13th North American Masonry Conference, Salt Laske City, UT, June 16-16, 2019.* Longmont, CO: The Masonry Society.

Dona, M., Tecchio, G., da Porto, F. 2018. "Verification of second-order effects in slender reinforced masonry walls." *Materials and Structures* 51: 69. https://doi.org/10.1617/s11527-018-1196-x

Drysdale, R. G., and Hamid, A. A. 2005. *Masonry Structures Behavior and Design.* Canadian Edition. Mississauga, ON: Canada Masonry Design Centre.

Drysdale, R. G. and Sallam, S. E. A. 1976. "Design of Masonry Walls and Columns for Combined Axial Load and Bending Moment." Paper presented at the *1st Canadian Masonry Symposium, Calgary, AB, June 7-10, 1976.*

Chapter 12 – References

Dutrisac, H., and Banting, B. 2021. "Towards the Harmonization of Canadian and American Masonry Structures Design Standards." *CSA Group*. Available: https://www.csagroup.org/article/research/towards-the-harmonization-of-canadian-and-american-masonry-structures-design-standards/

Entz, J., Cruz Noguez, C., Guzman Sanchez, O., and Banting, B. 2017. "Tall Masonry Walls with In-Line Boundary Elements." Paper presented at the *13th Canadian Masonry Symposium, Halifax NS, June 4-7, 2017*

Fernandez, P., Sena-Cruz. J., Xavier, J., Silva, P., Pereira, E., Cruz, J. 2018. "Durability of Bondin NSM CFRP-Concrete Systems Under Different Environmental Conditions." *Composites Part B* 138: 19-34. https://doi.org/10.1016/j.compositesb.2017.11.022

Galal, K., and Sasanian, N. 2010. "Out-of-Plane Flexural Performance of GFRP-Reinforced Masonry Walls." *Journal of Composites for Construction* 14(2): 162-174. https://doi.org/10.1061/(ASCE)CC.1943-5614.0000061.

Galati, N., Tumialan, G., and Nanni, A. 2006. "Strengthening with FRP Bars of URM Walls Subject to Out-of-Plane Loads." *Construction and Building Materials* 20 (1-2): 101-110 https://doi.org/10.1016/j.conbuildmat.2005.06.047

Gonzalez, R., Alonso, A., Cruz, C., and Tomlinson, D. 2021. "Numerical Study of the Response of Reinforced Slender Masonry Walls with Various Reinforcement Arrangements." Paper presented at the *14th Canadian Masonry Symposium, Montreal, May 16-20, 2021*. Mississauga, ON: Canada Masonry Design Centre.

Hashemian, F. *Surface reinforced concrete masonry units*. US Patent Application 15/107,043, filed January 16, 2015, and published January 19, 2017.

Chapter 12 – References

Hatzinikolas M. A. and Korany, Y. 2005. *Masonry Design for Engineers and Architects*. Edmonton, AB: Canadian Masonry Publications.

Hatzinikolas, M., Longworth, J., and Warwaruk, J. 1978. "Concrete Masonry Walls." *University of Alberta, Structural Engineering Report No. 70.*

Isfeld, A. C., Hagel, M. D., and Shrive, N. G. 2019. "Finite Element Analysis of Hollow Concrete Block Masonry Walls." Paper presented at the *13th North American Masonry Conference, Salt Laske City, UT, June 16-16, 2019.* Longmont, CO: The Masonry Society.

Johnston, B. G., ed. 1966. *The Column Research Council Guide to Design Criteria for Metal Compression Members.* 2nd Ed. New York: John Wiley and Sons.

Konthesingha, K. M. C., Masia, M. J., Petersen, R. B., and Page, A. W. 2015. "Experimental Evaluation of Static Cyclic In-Plane Shear Behavior of Unreinforced Masonry Walls Strengthened with NSM FRP Strips." *Journal of Composites for Construction*, 19 (3): 04014055. https://doi.org/10.1061/(ASCE)CC.1943-5614.0000512.

Liu, Y., and Dawe, J. L. 2003 "Analytical Modeling of Masonry Load-Bearing Walls." *Canadian Journal of Civil Engineering* 30: 795-806. https://doi.org/10.1139/l03-036

Liu, Y., and Hu, K. 2007. "Experimental Study of Reinforced Masonry Walls Subjected to Combined Axial Load and Out-of-Plane Bending." *Canadian Journal of Civil Engineering* 34: 1489-1494. https://doi.org/10.1139/L06-167

MacGregor, J. G., Breen, J. E., and Pfrang, E. O. 1970. "Design of Slender Concrete Columns." *American Concrete Institute Journal* 67 (1): 6-28.

Mahmood, T., Gheni, A., and ElGawady, M. 2021. "Out-of-Plane Seismic Behavior of Reinforced Fully Grouted Masonry Walls Subjected to High Axial Loads" Paper presented at the *14th Canadian Masonry Symposium, Montreal, May 16-20, 2021.* Mississauga, ON: Canada Masonry Design Centre.

Maljaee, H., Ghiassi, B., and Lourenco, P. B. 2018. "Bond Behaviour in NSM-Strengthened Masonry." *Engineering Structures* 166: 302-313. https://doi.org/10.1016/j.engstruct.2018.03.091

Marcus, B., Ziegert, S., Paganoni, S., Mahdy, H., and Muhammad, S. 2019. "Conservation and Structural Stabilization of al Hayla Tower in the Liwa Oasis, Abu Dhabi." *Journal of Architectural Conservation* 25 (1-2): 104-116. https://doi.org/10.1080/13556207.2019.1619985.

Mohsin, E. and Elwi, A. E. 2003. "Effect of Implied Fixity at Masonry Block Wall-Support Interface on Stability of Load Bearing Walls." Paper presented at the *9th North American Masonry Conference, Clemson, SC, June 1-4, 2003.* Longmont, CO: The Masonry Society.

Mufti, A. A., Bakht, B., Banthia, N., Benmokrane, B., Desgagne, G., Eden, R., Erki, M.-A., Karbhari, V., Kroman, J., Lai, D., Machida, A., Neale, K., Tadros, G., and Taljsten, B. 2007. "New Canadian Highway Bridge Design Code Design Provisions for Fibre-Reinforced Structures." *Canadian Journal of Civil Engineering* 34(3): 267-283. https://doi.org/10.1139/L06-137.

National Research Council of Canada. 2015. *National Building Code of Canada 2015: Volume 1*, Ottawa, ON.

Parvin, A., and Shah, T. S. 2016. "Fiber Reinforced Polymer Strengthening of Structures by Near-Surface Mounting Method." *Polymers* 8(8): 298. https://doi.org/10.3390/polym8080298

Pettit, C., Entz, J., Sanchez, O. G., Cruz-Noguez, C. and Banting, B. 2019. "Tall Masonry Walls with In-Line Cage Reinforcing." Paper presented at the *13th North American Masonry Conference, Salt Laske City, UT, June 16-16, 2019.* Longmont, CO: The Masonry Society.

Chapter 12 – References

Priestley, M. J. N., and Park, R. 1987. "Strength and Ductility of Concrete Bridge Columns Under Seismic Loading." *ACI Structural Journal* 84(1): 61-76.

Rashid, R., Oehlers, D. J., and Seracino, R. 2008. "IC Debonding of FRP NSM and EB Retrofitted Concrete: Plate and Cover Interaction Tests." *ASCE Journal of Composites for Construction* 12(2): 260-167. https://doi.org/10.1061/(ASCE)1090-0268(2008)12:2(160).

Salem, S., Ezzeldin, M., El-Dakhakhni, W., and Tait, M. 2021. "Behaviour of Load-Bearing Reinforced Masonry Walls Under Out-of-Plane Loading." Paper presented at the *14th Canadian Masonry Symposium, Montreal, May 16-20, 2021*. Mississauga, ON: Canada Masonry Design Centre.

Sentrop, J. T. *Building block.* US Patent US1661739, filed June 10, 1926, and issued March 6, 1928.

Sparling, A. J. J. 2015. "The Development of a Hollow Concrete Masonry System for use with Near-Surface Mounted Reinforcement." M.Sc. thesis, Department of Civil Engineering, The University of Manitoba, Winnipeg, MB.

Sparling, A., and Palermo, D. 2021. "Out-of-Plane Cyclic Response of Slender Reinforced Masonry Walls Subjected to Increasing Axial Load." Paper presented at the *14th Canadian Masonry Symposium, Montreal, May 16-20, 2021*. Mississauga, ON: Canada Masonry Design Centre.

———.2022. "Response of Full-Scale Slender Masonry Walls with Conventional and NSM Steel Reinforcement Subjected to Axial and Out-of-Plane Loads." *ASCE Journal of Structural Engineering* (Submitted January 2022)

Sparling, A., Palermo, D., and Hashemian, F. 2017. "Finite Element Analysis of SRCMU Masonry Walls with NSM Reinforcement in Out-of-Plane Flexure." Paper presented at the *13th Canadian Masonry Symposium, Halifax, NS, June 4 – 7, 2017*. Mississauga, ON: Canada Masonry Design Centre.

Chapter 12 – References

———. 2018. "Out-of-Plane Flexural Response of Hollow Masonry Walls with Near-Surface Mounted Reinforcement." In proceedings of the 10th *International Masonry Conference, Milan, ITA, July 9 – 11, 2018.* Whyteleafe, UK: International Masonry Society.

———. 2019. "Flexural Testing of a Concrete Masonry Unit Wall with Near-Surface Mounted Steel Reinforcement." Paper presented at the *13th North American Masonry Conference, Salt Lake City, UT, June 16 – 19, 2019*. Longmont, CO: The Masonry Society.

———. 2021. "Out-of-Plane Flexural Testing and Stiffness Response of Concrete Masonry Walls with NSM Steel Reinforcement." *Canadian Journal of Civil Engineering* 48: 749-762. https://doi.org/10.1139/cjce-2019-0685.

Sustersic, H., Stubbs, D., Peterson, R., Bennett, R., Pettit, C., Flisak, B., Erdogmus, E., Thompsong, J., Banting, B., Cruz-Noguez, C. 2021. "Parametric Studies on Reinforced Masonry Walls Resisting Out-of-Plane Loads: A Comparison of CSA S304-14 and TMS 402-16." Paper presented at the *14th Canadian Masonry Symposium, Montreal, May 16-20, 2021.* Mississauga, ON: Canada Masonry Design Centre.

The Masonry Society. 2016. *Building Code Requirements and Specification for Masonry Structures,* TMS 402/602-16, Longmont, CO.

Valluzzi, M. R., Binda, L., and Modena, C. 2005. "Mechanical Behaviour of Historic Masonry Structures Strengthened by Bed Joint Structural Repointing." *Construction and Building Materials* 19(1): 63-73. https://doi.org/10.1016/j.conbuildmat.2004.04.036.

Yokel, F. Y., Mathey, R. G., and Dikkers, R. D. 1970. "Compressive Strength of Slender Concrete Masonry Walls." *U.S. National Bureau of Standards, Building Science Series 33.*

Chapter 12 – References

Appendices

Appendix A   Construction of 3 m Tall RM Walls: Sample Photos

A.1   Preparation for wall construction

Half-units, shown in Figure A.1 were saw cut from full-sized masonry units prior to construction of the masonry walls. These units were used at the ends of alternating courses as the walls were constructed such that a running bond pattern (50% offset of units of subsequent courses of masonry) could be achieved. These half-units were also used for the construction of alternating courses of masonry prisms that were prepared for axial load testing.

Figure A.1: Half-units cut from the full-length CMUs and SRCMUs

A.2   Wall construction

The mortar used for the construction of the masonry walls was mixed by hand in a wheelbarrow as shown in Figure A.2. The first course of masonry was laid on a bed of mortar, for levelling, as shown in Figure A.3. The walls were constructed one at a time in perpendicular orientations so that they could be braced against each-other. Mortar filled the vertical grooves of the SRCMUs during construction as shown in

Appendix A – Construction of 3 m Tall RM Walls: Sample Photos

Figure A.4. The partial vertical grooves at the ends of the units had to be buttered with mortar to ensure a proper head joint was formed, and mortar from the bed joints also flowed into the central grooves of the units. This excess mortar was cleared from the grooves as shown in Figure A.5 and Figure A.6.

Figure A.2: Mortar mixed by hand in a wheelbarrow

Figure A.3: The first course of masonry laid on a bed of mortar

Appendix A – Construction of 3 m Tall RM Walls: Sample Photos

Figure A.4: Mortar filling vertical grooves of SRMUs during construction

Figure A.5: Mortar being cleared from grooves using a piece of 3/8" plywood

Appendix A – Construction of 3 m Tall RM Walls: Sample Photos

Figure A.6: Grooves in alignment and cleared of mortar

The mason worked from a free-standing mobile scaffold while building the free-standing walls, one at a time. Three and a half walls were constructed in one working day as shown in Figure A.8. A total of five walls were built, one of these was coated with a polymer membrane for a test unrelated to the current study. The walls were braced against each other at the top, for stability, until testing as shown in Figure A.9.

Appendix A – Construction of 3 m Tall RM Walls: Sample Photos

Figure A.7: Mason working on a freestanding platform

Figure A.8: Masonry walls at the end of the first day of construction

Appendix A – Construction of 3 m Tall RM Walls: Sample Photos

Figure A.9: Completed walls braced against each-other for stability

A.3   Reinforcement of Masonry Walls

The masonry grout was mixed in a vertical axis concrete mixer in batches as shown in Figure A.10 a), and the reinforcement was placed in the hollow cells before grouting. The epoxy for the NSM reinforcement was mixed by hand in a tray as shown in Figure A.10 b) and piped into the grooves using a re-sealable plastic bag. To apply the NSM reinforcement, a bead of epoxy was first applied in the grooves as shown in Figure A.11. A reinforcing bar was then pressed into place, and a topping layer of epoxy applied as shown in Figure A.12. Finally, the epoxy was recessed by pressing in a strip of foam.

Appendix A – Construction of 3 m Tall RM Walls: Sample Photos
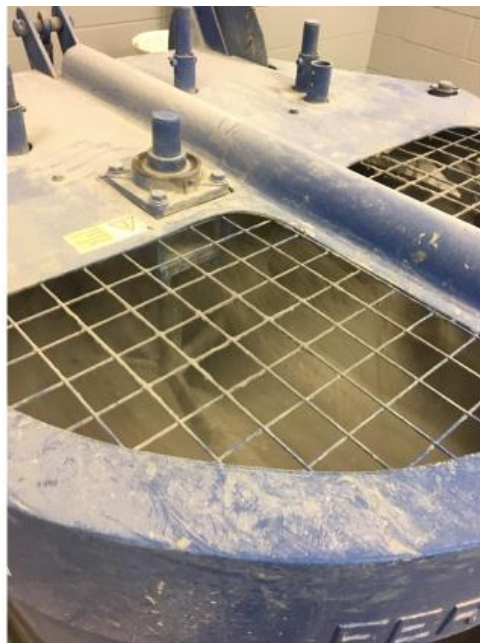
Figure A.10: Mixing of binders: a) masonry grout; and b) sanded epoxy

Figure A.11: Application of base layer of epoxy for NSM reinforcement

Appendix A – Construction of 3 m Tall RM Walls: Sample Photos
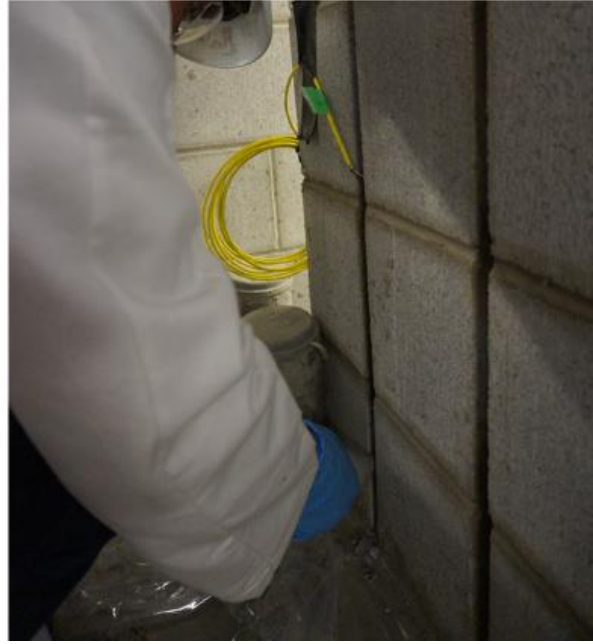
Figure A.12: Installation of NSM steel bars
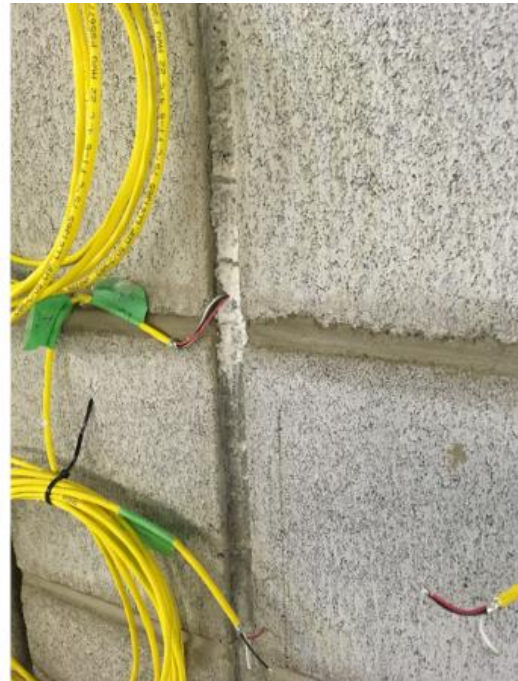
Figure A.13: Recessing of epoxy

Appendix A – Construction of 3 m Tall RM Walls: Sample Photos

Appendix B Construction of 8 m Tall RM Walls: Sample Photos

B.1 Construction Drawings for Slender RM Walls

The drawings in Figure B.1 and Figure B.2 provide an overview of the construction staging and reinforcement process. Lap splices of the 20M bars used for the reinforcement of Walls CH7800a and CH7800b were 800 mm long.

Figure B.1: Grouted reinforcement placement: a) Walls NH7800a and NH7800b; and b) Walls CH7800a and CH7800b

Appendix B – Construction of 8 m Tall RM Walls: Sample Photos

Figure B.2: Staging for the placement of reinforcement for Walls CH7800a and CH7800b

B.2   Construction of Slender RM Walls

The first course of masonry units was laid on November 20th, 2019, as shown in Figure B.3. The walls were built in one line to allow the mason to build all four walls concurrently using the same mason's line (efficiency of construction time). Figure B.4 shows how a lead was constructed at the ends of the line of walls to facilitate the concurrent construction of all four walls. As the walls grew in height, scaffolding was necessary to continue construction. Figure B.5 shows the walls during the second stage of construction, and Figure B.6 shows the free-standing scaffolding used; these figures also illustrate how the walls were braced against steel columns, which were themselves anchored into the laboratory strong floor. The masonry prisms for axial load testing were constructed by the mason during the second stage of construction as shown in Figure B.7. A mason's apprentice helped with the construction of the final stage of the wall construction as shown in Figure B.8. The final units were placed on November 28th, 2019. The height approached the upper limit of available space in the high bay lab (when fully retracted, the bottom of the crane hook reaches 9 m above the main floor area).

Appendix B – Construction of 8 m Tall RM Walls: Sample Photos

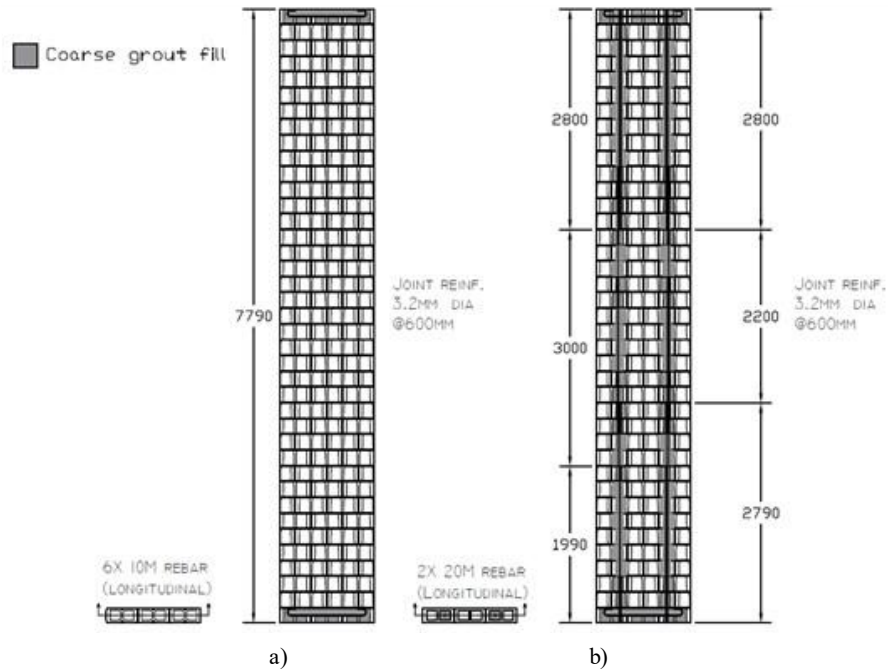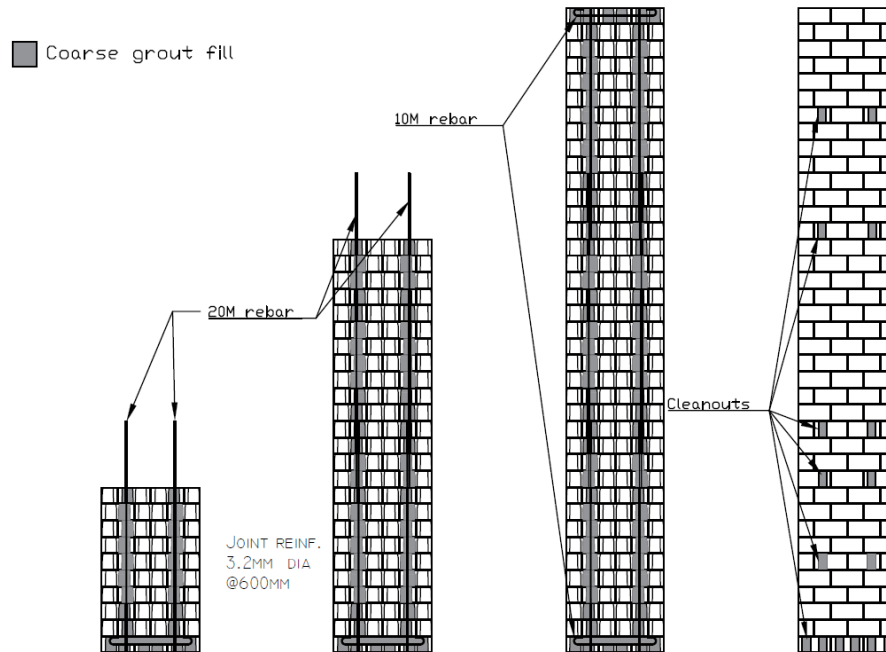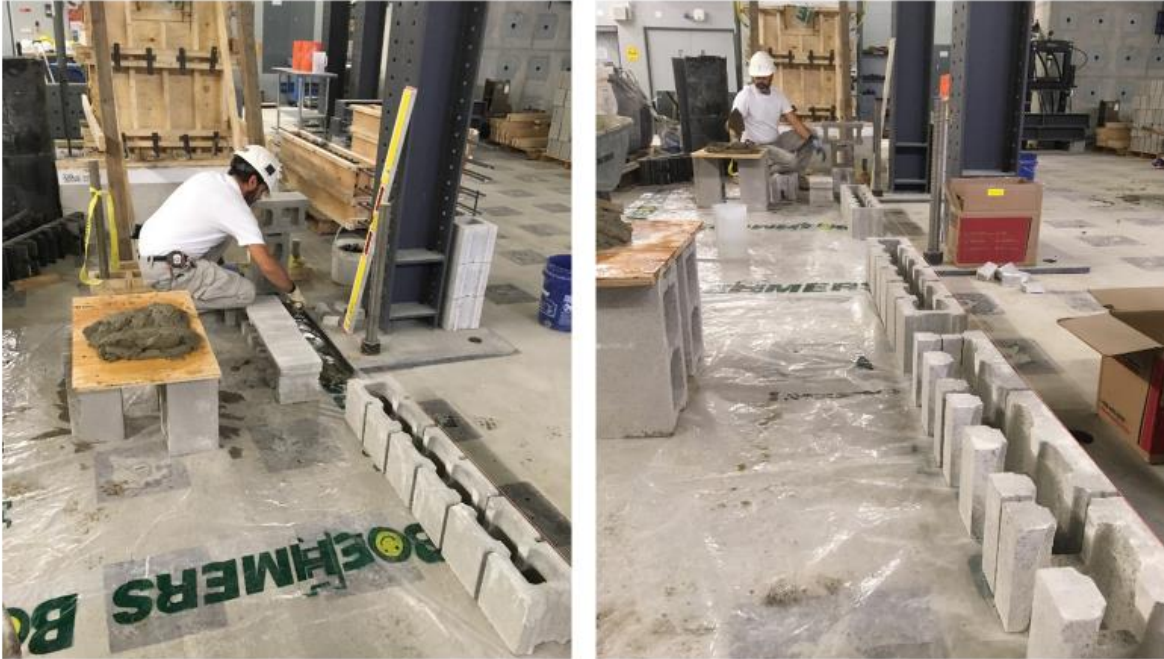*Figure B.3: Placement of the first course of masonry units*

Figure B.4: Construction in a single line

Appendix B – Construction of 8 m Tall RM Walls: Sample Photos
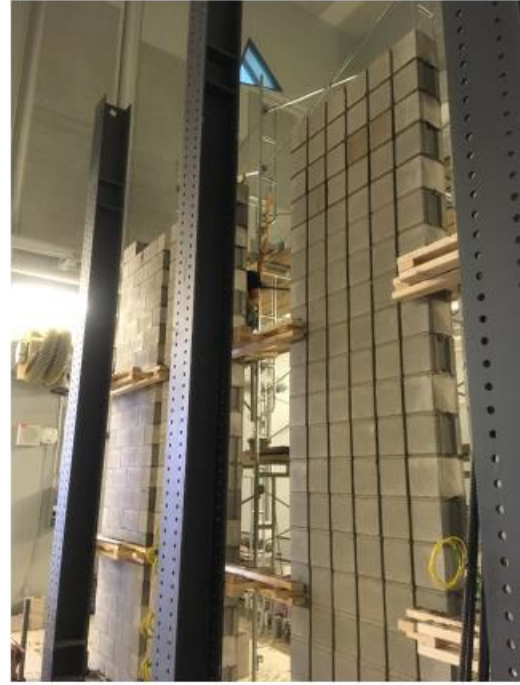
Figure B.5: Second stage of slender wall construction

Figure B.6: Scaffolding for the second stage of wall construction

Appendix B – Construction of 8 m Tall RM Walls: Sample Photos

Figure B.7: Construction of masonry prisms from conventional masonry units

Figure B.8: Third stage of slender wall construction

B.3   Conventional Reinforcement of Slender Walls

Steel ladder joint reinforcement, shown in Figure B.9, was placed every 3rd course (600 mm on centre) of each wall during construction. Bar positioner and clean-out openings in the walls facilitated positioning of

209

the conventional reinforcement prior to grouting as shown in Figure B.10. For the first stage of construction, the walls were built to 2 m in height. Reinforcing bars for walls CH7800a and CH7800b were threaded through the bar positioners to the base of the wall as shown in Figure B.11. For subsequent construction stages, the reinforcement was lap spliced, and continued to the top of the preceding wall stage as shown in Figure B.12. Instrumentation wire connected to the strain gauges mounted on the reinforcing bars were routed to exit the wall at either end at the top of each stage. For the top course of masonry of the conventionally reinforced walls, flashing was placed in the cells of the units that did not contain vertical reinforcing bars as shown in Figure B.13. This permitted grout to be poured into the cells with vertical reinforcement, as well as across the top course of masonry which had depressed webs (knock-outs) to allow the placement of a hooked 10M bar as reinforcement. Grout was poured into the reinforced cells from the top, as shown for the final construction stage in Figure B.14.

Figure B.9: Ladder-type joint reinforcement used in construction

Appendix B – Construction of 8 m Tall RM Walls: Sample Photos

Figure B.10: Details to facilitate placement of grouted reinforcing bars: a) clean-out holes; and b) bar positioner

Figure B.11: Positioning of conventional reinforcing bars after the first stage of construction

Appendix B – Construction of 8 m Tall RM Walls: Sample Photos
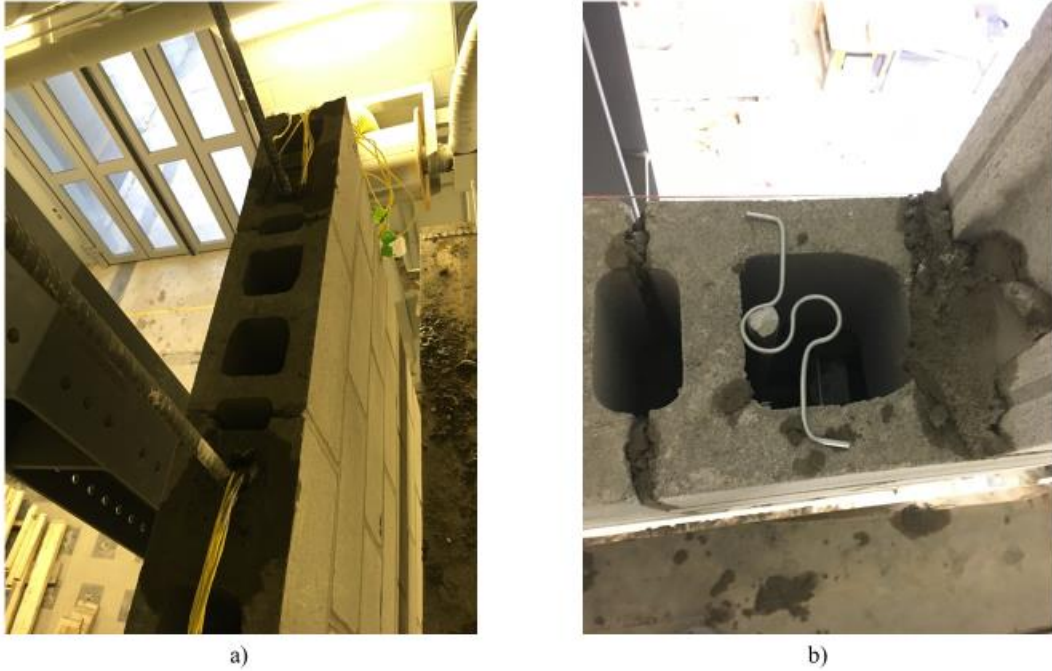
Figure B.12: Conventional reinforcement: a) grouting of second stage of construction; and b) bar positioner to align the lap splice with the reinforcement for the third stage
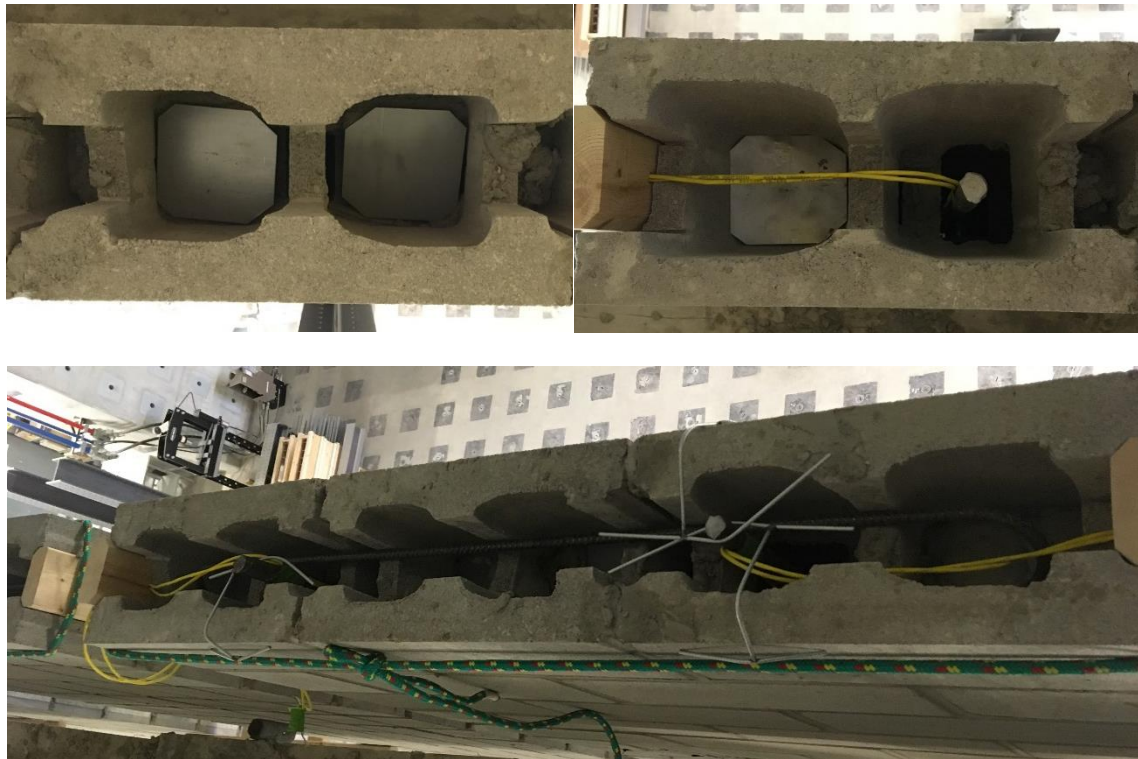

Figure B.13: Positioning of reinforcement and flashing to allow grouting of the top course of masonry: Conventional wall

Appendix B – Construction of 8 m Tall RM Walls: Sample Photos

Figure B.14: Grouting third stage of slender masonry walls

B.4   Reinforcement of slender walls SRCMU walls

For the walls with NSM reinforcement (Walls NH7800a and NH7800b) grout and reinforcement was placed in the top and bottom courses of masonry similarly to the walls with conventional reinforcement. For the grouting and reinforcement of the top course, flashing was inserted into each cell as shown in Figure B.15. The NSM steel bars were placed using a similar technique to that used for the 3 m tall walls, except that the overhead crane was used to raise and hold the bars in place during installation as shown in Figure B.16.

Appendix B – Construction of 8 m Tall RM Walls: Sample Photos

Figure B.15: Reinforcement and flashing for grouting of top course of masonry: SRCMU wall

Figure B.16: Placement of NSM reinforcement using overhead crane

214

Appendix B – Construction of 8 m Tall RM Walls: Sample Photos

B.5   Moving slender RM walls

After they were reinforced, the walls were moved using the overhead crane and a pair of long lifting straps in a symmetrical "choke" configuration above their mid-height as shown in Figure B.17. This configuration was applied each time the walls were moved.

Figure B.17: Lifting of slender reinforced masonry wall

Appendix B – Construction of 8 m Tall RM Walls: Sample Photos

Appendix C   Flexural Stiffness at Onset of Yielding: Rational Method

The internal reaction of a Reinforced Masonry (RM) section subjected to an axial load P as well as out of plane flexure is illustrated in Figure C.1. In this section, tensile stresses and strains are assumed positive and compressive stresses and strains are negative. The axial load P is positive when it causes compression in the RM section.
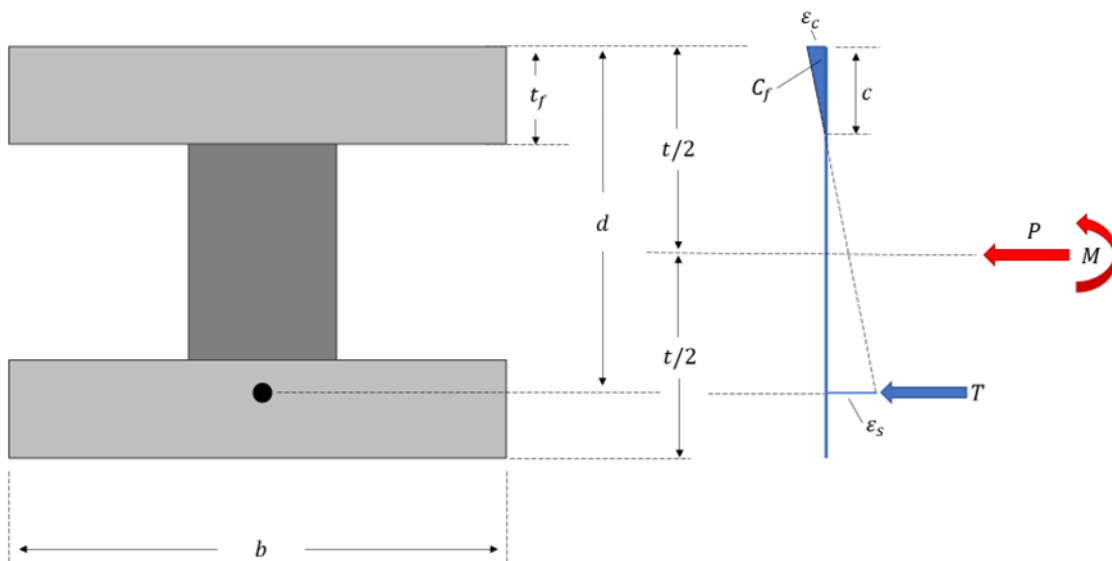

Figure C.1: Reinforced wall section subjected to axial loading for determining the flexural stiffness

The following equations demonstrate how the effective flexural stiffness EI_{eff} may be derived from conditions of equilibrium of forces and strain compatibility at the onset of yielding of the reinforcing steel bars ($\varepsilon_s = 0.002$ m/m). This closed-form solution is only applicable for fully grouted walls, and cases of partially grouted walls in which the depth of the compression zone c does not extend beyond the thickness of the face shell (where $c \leq t_f$).

Condition of strain compatibility:

$$\varepsilon_c = \varepsilon_s - \varphi d$$

Appendix C – Flexural Stiffness at the Onset of Yielding: Rational Method

$$\varphi = \frac{\varepsilon_s}{d - c}$$

$$\varepsilon_c = \varepsilon_s - \frac{\varepsilon_s d}{d - c}$$

Definitions (where $c \leq t_f$ or the wall is fully grouted):

$$C_f = \frac{\varepsilon_c E_c bc}{2}$$

$$T = A_s E_s \varepsilon_s$$

Equilibrium of forces:

$$0 = P + T + C_f$$

Substitute defined forces:

$$0 = P + A_s E_s \varepsilon_s + \left(\varepsilon_s - \frac{\varepsilon_s d}{d - c}\right)\left(\frac{E_c bc}{2}\right)$$

Simplify and isolate c:

$$0 = P + A_s E_s \varepsilon_s + \left(\frac{\varepsilon_s E_c bc}{2}\right) - \frac{\varepsilon_s d E_c bc}{2(d - c)}$$

$$\frac{d\varepsilon_s E_c bc}{2(d - c)} = P + A_s E_s \varepsilon_s + \left(\frac{\varepsilon_s E_c bc}{2}\right)$$

$$d\varepsilon_s E_c bc = \left(2(d - c)\right)P + \left(2(d - c)\right)A_s E_s \varepsilon_s + \left(2(d - c)\right)\left(\frac{\varepsilon_s E_c bc}{2}\right)$$

$$d\varepsilon_s E_c bc = 2dP - 2Pc + 2dA_s E_s \varepsilon_s - 2A_s E_s \varepsilon_s c + d\varepsilon_s E_c bc - \varepsilon_s E_c bc^2$$

$$c^2 (\varepsilon_s E_c b) + c(2P + 2A_s E_s \varepsilon_s) = 2dP + 2dA_s E_s \varepsilon_s$$

$$c^2 \left(\frac{\varepsilon_s E_c b}{2}\right) + c(P + A_s E_s \varepsilon_s) - d(P + A_s E_s \varepsilon_s) = 0$$

Appendix C – Flexural Stiffness at the Onset of Yielding: Rational Method

Set the following:

$$x = \frac{\varepsilon_s E_c b}{2}$$

$$y = P + A_s E_s \varepsilon_s$$

$$z = -d(P + A_s E_s \varepsilon_s)$$

Solve using the quadratic formula where:

$$c = \frac{-y + \sqrt{y^2 - 4xz}}{2x}$$

For $c \leq t_f$ or for fully grouted wall sections, the moment resistance M is calculated as:

$$M = -C_f \left(d - \frac{c}{3}\right) - P\left(d - \frac{t}{2}\right)$$

The effective flexural stiffness EI_{eff} is the moment divided by the curvature:

$$EI_{eff} = \frac{(d - c)M}{\varepsilon_s}$$

Appendix C – Flexural Stiffness at the Onset of Yielding: Rational Method

Appendix D   Design Example: Warehouse Walls

The design process outlined herein has been developed for illustration purposes only. The calculations highlight select differences between the potential flexural resistance performance of NSM steel reinforcement compared to conventional reinforcement for RM walls.

D.1   Design parameters:

D.1.1   Building description:

Two sizes and layout of warehouse buildings are considered in this section: a "Small warehouse" and a "Large warehouse". Select characteristics or these structures necessary for a preliminary design are described in this section and illustrated in Figure D.1 and Figure D.2.

Small warehouse

      6 m tall exterior walls with 1 m parapet

      15 m clear span between the walls and interior support columns

      Small characteristic length ($l_c < 70$) [for snow load calculation]

Large warehouse:

      8 m tall exterior walls with 1 m parapet

      18 m clear span between the wall an interior support column

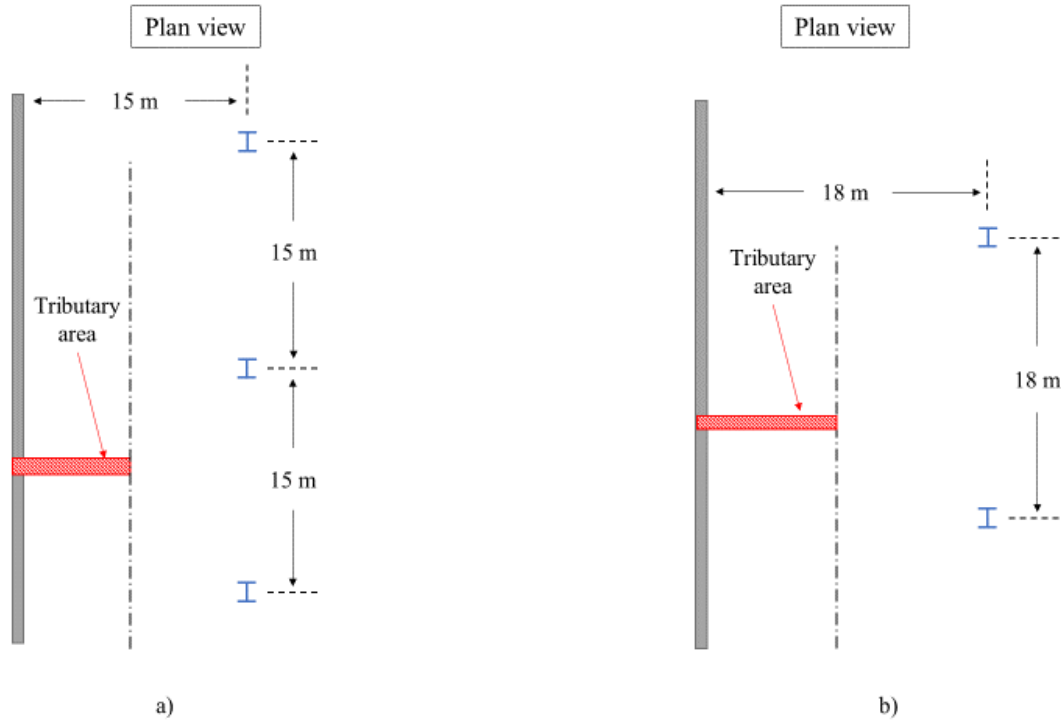   Very large characteristic length ($l_c > 600$) [for snow load calculation]

Appendix D – Design Example: Warehouse Walls

Figure D.1: Typical layout and tributary area of warehouse wall: a) small warehouse, and b) large warehouse

Figure D.2: Typical elevation of warehouse wall: a) small warehouse, and b) large warehouse

D.1.2 Building location

For the purposes of this preliminary design and comparison, the warehouses were assumed to be located in North York, ON, in an urban environment with limited sheltering from wind effects.

D.1.3 Design wall

The design wall features the following characteristics, illustrated in Figure D.3:

- 1 m length of wall supporting half of the roof span from the wall to the interior row of support columns

Appendix D – Design Example: Warehouse Walls

- 90 mm wide clay brick veneer, supported at grade (on grade beam) and tied to the block wall backup
- Open web steel joist (OWSJ) roof system with light steel decking
- Roof load applied on 75 mm ledger
- Simple support conditions: dowelled connection to the foundation at the base, rigid roof diaphragm at top
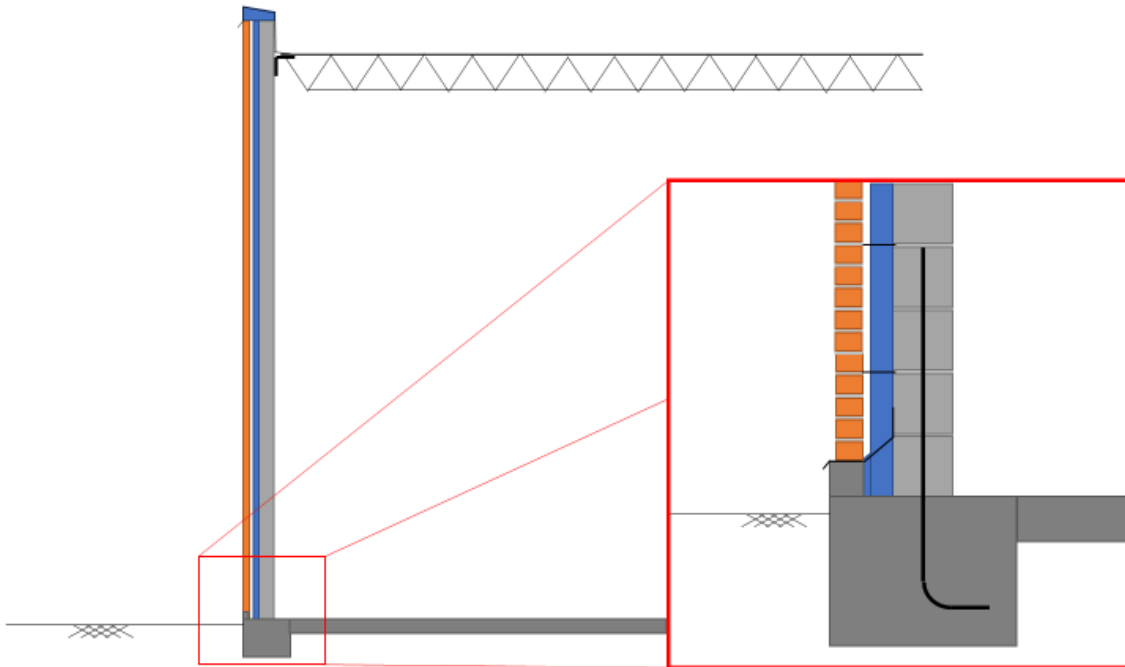

Figure D.3: Characteristics of design wall

D.2   Dead Loads

D.2.1   Masonry units

All masonry units were assumed to be normal weight. The following recommended dead load values from Drysdale and Hamid (2005) were assumed for the designs and consider the thickness of the walls.

190 mm CMU – Hollow wall: 2.2 kPa

190 mm CMU – Fully grouted wall: 4.12 kPa

240 mm CMU – Fully grouted wall: 5.22 kPa

Appendix D – Design Example: Warehouse Walls

90 mm clay brick – Cored units: 1.32 kPa [brick veneer is self-supporting, only contributes to loading for seismic cases]

D.2.2 Roofing

The following loads for the roofing structure were assumed, based on a long spanning light steel truss and decking system.

Open web steel joist system: 1 kPa

Decking and ballast: 1 kPa

Mechanical: 0.5 kPa

D.2.3 Total deal load

The deadload, D, is calculated at the mid-height for walls of height, h, supporting a clear span, s, as follows:

190 mm CMU – Hollow wall: $D = 2.2*(h/2+1) + 2.5*(s/2) = (2.2h/2 + 2.5*(s/2) + 2.2)$ kN/m

190 mm CMU – 1/3 grouted wall: $D = 2.84*(h/2+1) + 2.5*(s/2) = (2.84h/2 + 2.5*(s/2) + 2.84)$ kN/m

190 mm CMU – Fully grouted wall: $D = 4.12*(h/2+1) + 2.5*(s/2) = (4.12h/2 + 2.5*(s/2) + 4.12)$ kN/m

240 mm CMU – Fully grouted wall: $D = 5.22*(h/2+1) + 2.5*(s/2) = (5.22h/2 + 2.5*(s/2) + 5.22)$ kN/m

D.3 Live Loads

All live loads are taken as prescribed by Part 4 of the 2015 National Building Code of Canada (National Research Council of Canada 2015).

D.3.1 Roof occupancy load

Occupancy: L=1 kPa [NBCC Table 4.1.5.3.]

D.3.2 Snow load

$S = I_s [S_s(C_bC_wC_sC_a)+S_r)$ [NBCC Sentence 4.1.6.2.(1)]

Appendix D – Design Example: Warehouse Walls

$I_s = 1$ [Importance factor assumed to be normal]

$S_s=1.2$ kPa [1 in 50 year ground snow load for North York, ON]

$S_r=0.4$ kPa [1 in 50 year associated rain load]

$C_b = 2$ [basic roof snow load factor for a very large warehouse – $l_c > 600$]

$C_b = 1$ [assumed basic roof snow load factor for a small warehouse – $l_c < 70$]

$C_w=1$ [conservative assumption of wind exposure factor]

$C_s = 1$ [slope factor for a flat roof]

$C_a = 1$ [accumulation factor – local accumulations above 1 are possible, however the effect on the wall load would be minimal]

Snow load for very large warehouse: S= 1.2*2+0.4 = 2.8 kPa

Snow load for small warehouse: S= 1.2+0.4 = 1.6 kPa

D.3.3   Wind load

Note that uplift effects of the wind on the roof structure were neglected as they would generally benefit the loadbearing wall structure. When loaded in the out-of-plane direction, the walls are not part of the lateral force resisting system for the building and are therefore considered secondary members, subject to higher localized loads.

$p = I_w q C_e C_t C_g C_p$ [NBCC Sentence 4.1.7.3.(1)]

$p_i = I_w q C_{ei} C_t C_{gi} C_{pi}$ [NBCC Sentence 4.1.7.3.(3)]

$I_w=1$ [Importance factor assumed to be normal]

$q = 0.44$ kPa [1 in 50 year reference wind velocity pressure for North York, ON]

$C_e = 1$ [exposure factor, conservatively assumed to be 1]

Appendix D – Design Example: Warehouse Walls

$C_t = 1$ [topographic factor for flat topography]

$C_g = 2.5$ [gust factor for secondary structural members]

$C_p = \pm0.9$ [external pressure coefficient for secondary members away from the building corners]

$C_{ei} = 1$ [exposure factor for internal pressure, conservatively assumed to be 1]

$C_{gi} = 2$ [internal gust effect factor for building with numerous overhead doors]

$C_{pi} = -0.45$ or $+0.3$ [internal pressure coefficient assuming openings are wind resistant and closed during storms]

For maximum outward single curvature:

p=0.44*2.5*-0.9 = -.99 kPa

and

p_i = 0.44*2*0.3 = 0.264 kPa

Wind load: $W = p - p_i = $ -1.25kPa

D.3.4   Seismic load

Note that the seismic loads determined here are for the exterior walls acting as secondary loadbearing members. Site class C is assumed for the soil conditions.

$V_p = 0.3*F_aS_a(0.2)I_ES_pW_p$ [NBCC Sentence 4.1.8.18.(1)]

$F_a = 1$ [site coefficient for Site Class C]

$S_a(0.2) = 0.195$ [5% damped spectral response acceleration for a period of 0.2s for North York, ON]

$I_E = 1$ [Importance factor assumed to be normal]

$S_p = C_pA_rA_x/R_p$ [horizontal force factor]

Appendix D – Design Example: Warehouse Walls

$C_p = 1$ [component factor for interior and exterior walls]

$A_r = 1$ [component force amplification factor for interior and exterior walls]

$A_x = 2$ [height factor, maximum value for the top of the structure]

$R_p = 2.5$ [component response modification factor for interior and exterior walls]

$S_p = 2/2.5 = 0.8$

W_p = deadload of masonry + brick veneer [weight of the component, distributed according to the weight]

Seismic load 190 mm CMU hollow: $E = V_p = 0.3*0.195*0.8* (2.2 + 1.32) = 0.165$ kPa

Seismic load 190 mm CMU 1/3 grouted: $E = V_p = 0.3*0.195*0.8* (2.84 + 1.32) = 0.195$ kPa

Seismic load 190 mm CMU grouted: $E = V_p = 0.3*0.195*0.8* (4.12 + 1.32) = 0.255$ kPa

Seismic load 240 mm CMU grouted: $E = V_p = 0.3*0.195*0.8* (5.22 + 1.32) = 0.306$ kPa

D.4 Load Combinations

A limited number of the load cases prescribed in Part 4 of the 2015 National Building Code of Canada (National Research Council of Canada 2015) were selected as the most likely to govern the reinforcement requirements of the walls in out-of-plane flexure. The orientation and location of application of the loads comprising the load cases are illustrated in Figure D.4, and the considered load combination cases are listed as follows:

Case 3: $1.25D + 1.5S + 0.4W$

Case 4: $1.25D + 1.4W + 0.5S$

Case 5: $D + E + 0.5L + 0.25S$

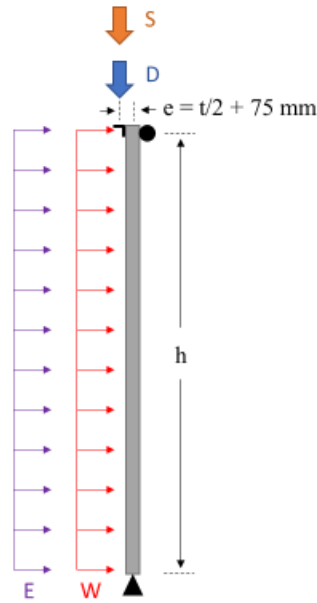Appendix D – Design Example: Warehouse Walls

Figure D.4: Orientation and location of applied loads

Note that, to simplify the analysis, all vertical loads were conservatively assumed to be applied at the edge of the ledger (75 mm from the inner face of the wall).

D.5   Example factored load calculation

The factored axial load and factored applied moment at midspan of the hollow wall with NSM reinforcement is shown here for the 6 m tall warehouse structure (small warehouse). The applied loads were calculated similarly for the other design conditions considered. Note that the maximum moment was assumed to occur at mid-span and therefore the dead load includes the weight of the masonry above the midspan (weight of half of the wall plus the weight of the parapet).

D = 2.2*(6 m)/2 + 2.5*((15 m)/2) + 2.2 = 27.55 kN/m

S = 1.6 kPa * (15 m)/2 = 12.0 kN/m

W = 1.25 kPa

E = 0.165 kPa

Appendix D – Design Example: Warehouse Walls

Case 3:

$M_{fp} = (1.25D + 1.5S)*e/2 + 0.4(Wh^2/8)$

$M_{fp} = (1.25*27.55 + 1.5*12)*0.17/2 + 0.4* 1.25*6^2/8$

$M_{fp} = 6.7$ kNm/m

$P_f = 1.25D + 1.5S$

$P_f = 1.25*27.55 + 1.5*12$

$P_f = 52.4$ kN/m

Case 4:

$M_{fp} = 11.3$ kNm/m

$P_f = 40.4$ kN/m

Case 5:

$M_{fp} = 6.6$ kNm/m

$P_f = 34.3$ kN/m

D.6 Example moment and axial load resistance calculation

The factored axial load resistance, the factored moment resistance, and the factored total applied moment at midspan of the hollow wall with NSM reinforcement is shown here for the 6 m tall warehouse structure (small warehouse) for load combination **Case 3**. The axial load and moment resistance were calculated similarly for the other wall designs presented.

D.6.1 Assigned material and geometric properties

$t_f = 36.2$ mm [face shell thickness – design value from Drysdale and Hamid (2005)]

Appendix D – Design Example: Warehouse Walls

f'_m = 10 MPa [maximum compressive stress for masonry – design value from CSA S304-14 for hollow wall constructed from 15 MPa concrete units with type S mortar]

ϕ_m = 0.6 [material resistance factor for masonry in compression - design value from CSA S304-14]

d = 170 mm [depth to reinforcement – specified design value]

t = 190 mm [actual thickness of concrete masonry unit]

b = 1000 mm [width of section for 1 m strip of wall]

b_w = 0.01 mm [width of grouted cells per 1 m strip of wall – arbitrarily small for fully hollow wall]

kh = 6 m [effective height of the wall – specified design value]

A_s = 250 mm^2 [area of steel in tension per 1 m strip of wall – specified design value]

f_y = 400 MPa [yield stress of steel reinforcement – specified design value]

ϕ_m = 0.85 [material resistance factor for reinforcing steel - design value from CSA S304-14]

E_s = 200 000 MPa [Young's modulus of reinforcing steel]

ϕ_{er} = 0.75 [resistance factor for member flexural stiffness for the determination of slenderness effects - design value from CSA S304-14]

D.6.2   Calculated section properties

$A_e = tb_w + (b-b_w)2t_f = 72400$ mm^2/m [effective area of the section]

$I_o = bt^3/12 - (b-b_w)(t-2t_f)^3/12 = 436*10^6$ mm^4/m [uncracked moment of inertia, neglecting the steel reinforcement]

$S_e = I_o2/t = 4.59*10^6$ mm^3/m [section modulus]

$e_k = S_e/A_e = 63.4$ mm [kern eccentricity]

Appendix D – Design Example: Warehouse Walls

$E_m = 850f'_m = 8500MPa$ [Young's modulus of masonry – CSA S304-14]

$n = E_s/E_m = 23.5$ [modular ratio]

D.6.3   Cracked moment of inertia

The location of the neutral axis, c, which results in equilibrium within the fully cracked section, was determined through iteration.

$c = 39.33$ mm [distance from the extreme compression fibre to the neutral axis – determined iteratively]

$\varepsilon_c = 0.0003$ m/m [strain in the extreme compression fibre of the masonry section – arbitrary value within the elastic range of the masonry material]

$\phi = \varepsilon_c/c = 7.627*10^{-6}$ m^{-1} [section curvature]

$\varepsilon_{c2} = \varepsilon_c - \phi\, t_f = 0.0000239$ m/m [strain at inner side of face shell – from strain compatibility]

$\varepsilon_s = \varepsilon_c - \phi\, d = -0.000996$ m/m [reinforcing bar strain – from strain compatibility]

Check of c-value:

$T_s = A_s n \varepsilon_s = -5.86$ N/MPa [tension in reinforcing steel]

$C_w = b_w c \varepsilon_c/2 = 0$ N/MPa [compression in the grouted region of the wall, including the face shell]

$C_f = (b - b_w)t_f(\varepsilon_{c2} + \varepsilon_c)/2 = 5.86$ N/MPa [compression in the face shell for the un-grouted region –

for $c > t_f$]

$T_s + C_w + C_f = 0$ [section is in equilibrium when c = 39.33]

$I_w = b_w c^3/3 = 0$ [moment of inertia contribution from the grouted region of the wall, including the face shell]

$I_f = (b-b_w)t_f^3/12 + (b-b_w)t_f(c-t_f/2)^2 = 20.3*10^6$ mm^4 [moment of inertia contribution from the face shell from the ungrouted region – for $c > t_f$]

Appendix D – Design Example: Warehouse Walls

$I_s = nA_s(c-d)^2 = 100.4*10^6$ mm^4 [moment of inertia contribution from the reinforcing steel]

$I_{cr} = I_w + I_f + I_s = 120.7*10^6$ mm^4/m [cracked moment of inertia of the RM wall section]

D.6.4 Effective flexural stiffness

The effective flexural stiffness of the wall section is determined here using the formulation from CSA S304-14 (CSA Group 2019).

$e = M_{fp}/P_f = 192.6$ mm [virtual eccentricity of the factored loads]

$(EI)_{eff} = E_m(0.25I_o - (0.25I_o-I_{cr})(e-e_k)/2e_k) = 1\ 026$ kNm^2 [effective flexural stiffness – where $(EI)_{eff}$ must be no greater than $0.25E_mI_o$, and no less than E_mI_{cr}]

D.6.5 Total factored moment

The total factored moment on the section at midspan accounts for the displacement using the moment magnifier method.

$\beta_d = 0.42$ [ratio of factored dead load to total factored moment]

$C_m = 0.6$ [factor relating moment diagram to uniform moment case – 1.0 if lateral loads contribute more than 50% of the total moment at midspan, 0.6 otherwise]

$P_{cr} = \pi^2\phi_{er}(EI)_{eff}/((1+0.5\beta_d)(kh)^2) = 174.5$ kN [critical buckling load]

$M_{ftot} = M_{fp}C_m(1-P_f/P_{cr}) = 6.71$ [total factored moment – cannot be less than M_{fp}]

D.6.6 Factored moment resistance

The moment resistance calculated here applies the material resistance factors for masonry and reinforcing steel from CSA S304-14 and accounts for the effect of the factored axial load P_f on the section (P-M interaction).

Appendix D – Design Example: Warehouse Walls

$a = (P_f + A_s\phi_s f_y)/(0.85b\phi_m f'_m) = 26.94$ mm [rectangular stress block if $a < t_f$]

OR

$a = (P_f + A_s\phi_s f_y - (b-b_w)t_f 0.85\phi_m f'_m)/ (0.85b_w\phi_m f'_m)$ [rectangular stress block if $a > t_f$]

$c = a/0.8 = 33.69$

$C_{mf} = a0.85(b-b_w)\phi_m f'_m = 137.4$ kN [compression force in the masonry face shell where there are no grouted cells – if $a<t_f$]

OR

$C_{mf} = t_f 0.85(b-b_w)\phi_m f'_m = 137.4$ kN [factored compression force in the masonry face shell where there are no grouted cells – if $a>t_f$]

$C_{mw} = a0.85b_w\phi_m f'_m = 0$ [factored compression force in grouted region of wall, including the face shell]

$M_r = C_{mf}(d-a/2) + C_{mw}(d-a/2) - P_f(d-t/2) = 17.6$ kNm [factored moment resistance – if $a < t_f$]

D.6.7   Factored axial load resistance and maximum reinforcement check
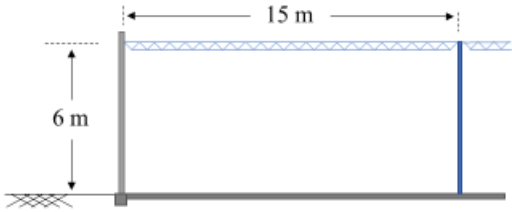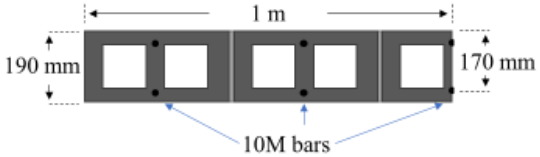
For wall with $h/t > 30$, the factored axial load is limited as follows

$P_f > P_r = 0.1\phi_m f'_m A_e = 43.4$ MPa [axial load resistance limited to 10% of the factored axial stress]

$c/d < 600/(600+fy) \rightarrow 0.198 < 0.6$ [maximum reinforcement check – ensures a ductile mode of failure]
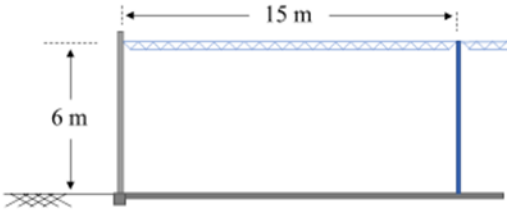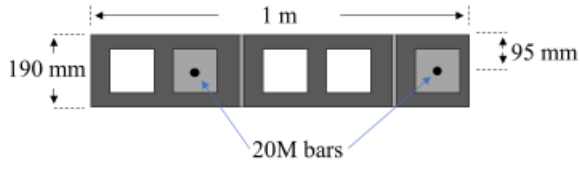
Appendix D – Design Example: Warehouse Walls

D.7 Summary of factored load and factored resistance

Table D.1: Summary design results for hollow CMU wall with NSM reinforcement

Building parameters	Wall parameters
Effective unsupported wall height = 6 m span between wall and columns = 15 m Small warehouse 	f'_m = 10 MPa A_s = 250 mm²/m t = 190 mm d = 170 mm

Case 3	
Factored loads	Factored resistance
M_{ftot} = 6.7 kNm/m P_f = 52.4 kN/m	M_r = 17.6 kNm/m $0.1\phi_m f'_m A_e$ = 43.4 kNm/m c/d = 0.2 < 0.6

Case 4	
Factored loads	Factored resistance
M_{ftot} = 14.8 kNm/m P_f = 40.4 kN/m	M_r = 16.7 kNm/m $0.1\phi_m f'_m A_e$ = 43.4 kNm/m c/d = 0.18 < 0.6

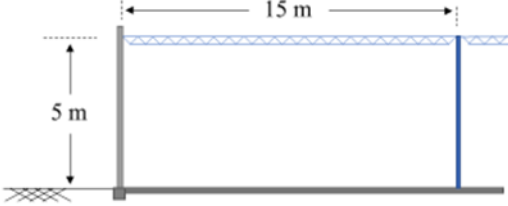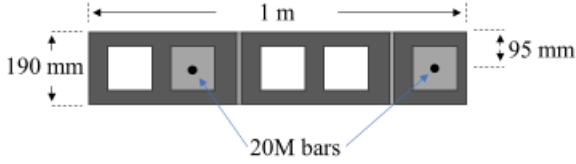| Case 5	
Factored loads	Factored resistance
M_{ftot} = 6.6 kNm/m P_f = 34.4 kN/m	M_r = 16.3 kNm/m $0.1\phi_m f'_m A_e$ = 43.4 kNm/m c/d = 0.17 < 0.6

Note: For load case 3, the maximum axial load is exceeded for a very slender wall – this clause of the S304 standard may, however, be overly conservative. This clause could be satisfied by increasing the strength of the units used (increasing the f'_m value)

Appendix D – Design Example: Warehouse Walls

Table D.2: Summary design results for hollow CMU wall with conventional reinforcement

Building parameters	Wall parameters
Effective unsupported wall height = 6 m span between wall and columns = 15 m Small warehouse 	$f'_m = 9.17$ MPa $A_s = 500$ mm^2/m $t = 190$ mm $d = 95$ mm

Case 3	
Factored loads	Factored resistance
$M_{ftot} = 10.7$ kNm/m $P_f = 55.6$ kN/m	$M_r = 15.3$ kNm/m $0.1\phi_m f'_m A_e = 61.4$ kNm/m c/d = 0.95 > 0.6

Case 4	
Factored loads	Factored resistance
$M_{ftot} = 30.7$ kNm/m $P_f = 43.6$ kN/m	$M_r = 15.0$ kNm/m $0.1\phi_m f'_m A_e = 61.4$ kNm/m c/d = 0.85 > 0.6

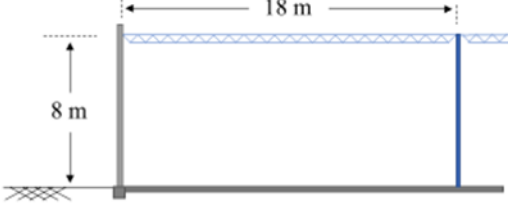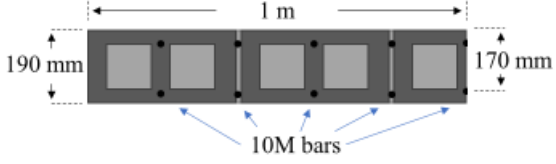| Case 5	
Factored loads	Factored resistance
$M_{ftot} = 8.9$ kNm/m $P_f = 36.9$ kN/m	$M_r = 14.8$ kNm/m $0.1\phi_m f'_m A_e = 61.4$ kNm/m c/d = 0.79 > 0.6

Note: In this application, the section is over-reinforced, and the moment resistance is inadequate for the Case 4 load combination. Furthermore, since c/d > 0.6, the calculated moment resistance M_r, which assumes yielding in the steel, is not valid. The wall must be made shorter, or a different reinforcement configuration is needed.

Appendix D – Design Example: Warehouse Walls

Table D.3: Summary design results for hollow CMU wall with conventional reinforcement

Building parameters	Wall parameters
Effective unsupported wall height = 5 m span between wall and columns = 15 m Small warehouse 	$f'_m = 9.17$ MPa $A_s = 500$ mm^2/m $t = 190$ mm $d = 95$ mm

Case 3	
Factored loads	Factored resistance
$M_{ftot} = 6.1$ kNm/m $P_f = 53.9$ kN/m	$M_r = 15.3$ kNm/m $0.1\phi_m f'_m A_e = 61.4$ kNm/m c/d = 0.94 > 0.6

Case 4	
Factored loads	Factored resistance
$M_{ftot} = 12.6$ kNm/m $P_f = 41.9$ kN/m	$M_r = 14.9$ kNm/m $0.1\phi_m f'_m A_e = 61.4$ kNm/m c/d = 0.84 > 0.6

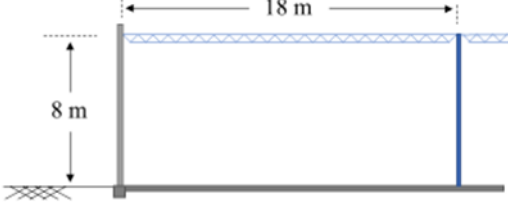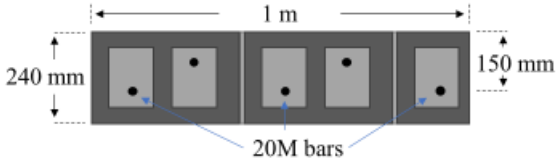| Case 5	
Factored loads	Factored resistance
$M_{ftot} = 6.6$ kNm/m $P_f = 35.4$ kN/m	$M_r = 14.7$ kNm/m $0.1\phi_m f'_m A_e = 61.4$ kNm/m c/d = 0.78 > 0.6

Note: In this application, the section is still over-reinforced, however, the moment resistance is adequate for all load combinations. Increasing the CMU strength to 20 MPa units (nominal unit strength) is sufficient to reduce the c/d ratio to below 0.6 for all load combination cases and results in a small increase in the moment resistance.

Appendix D – Design Example: Warehouse Walls

Table D.4: Summary design results for grouted CMU wall with NSM reinforcement

Building parameters	Wall parameters
Effective unsupported wall height = 8 m span between wall and columns = 18 m Large warehouse 	f'_m = 17.5 MPa A_s = 500 mm^2/m t = 190 mm d = 170 mm
Case 3	
Factored loads	Factored resistance
M_{ftot} =13.0 kNm/m P_f = 91.7 kN/m	M_r = 33.8 kNm/m $0.1\phi_m f'_m A_e$ = 200.0 kNm/m c/d = 0.22 < 0.6
Case 4	
Factored loads	Factored resistance
M_{ftot} = 29.3 kNm/m P_f = 66.5 kN/m	M_r = 32.1 kNm/m $0.1\phi_m f'_m A_e$ = 200.0 kNm/m c/d = 0.19 < 0.6
Case 5	
Factored loads	Factored resistance
M_{ftot} = 11.2 kNm/m P_f = 53.9 kN/m	M_r = 31.2 kNm/m $0.1\phi_m f'_m A_e$ = 200.0 kNm/m c/d = 0.18 < 0.6

Note: Using the NSM reinforcement system, a wall up to 8 m tall can be constructed using 20 cm (nominal size) masonry units.

Appendix D – Design Example: Warehouse Walls

Table D.5: Summary design results for grouted CMU wall with Conventional reinforcement

Building parameters	Wall parameters
Effective unsupported wall height = 8 m span between wall and columns = 18 m Large warehouse 	f'_m = 13.5 MPa A_s = 750 mm^2/m t = 240 mm d = 150 mm

Case 3	
Factored loads	Factored resistance
M_{ftot} = 18.8 kNm/m P_f = 98.6 kN/m	M_r = 41.0 kNm/m $0.1\phi_m f'_m A_e$ = 194.4 kNm/m c/d = 0.43 < 0.6

Case 4	
Factored loads	Factored resistance
M_{ftot} = 36.6 kNm/m P_f = 73.3 kN/m	M_r = 39.2 kNm/m $0.1\phi_m f'_m A_e$ = 194.4 kNm/m c/d = 0.40 > 0.6

Case 5	
Factored loads	Factored resistance
M_{ftot} = 14.0 kNm/m P_f = 59.4 kN/m	M_r = 38.2 kNm/m $0.1\phi_m f'_m A_e$ = 194.4 kNm/m c/d = 0.38 < 0.6

Note: Placing the bars at the centre of the wall resulted in an over-reinforced condition (c/d > 0.6) – the staggered reinforcement increases the flexural stiffness while decreasing the stress in the masonry in compression. Only the bars nearest the extreme tension fibre were used in the calculation of moment resistance and stiffness.

D.8 Proposed formulation for calculation of flexural stiffness

The proposed formulation for the determination of flexural stiffness of RM walls outlined in Appendix C, which accounts for the effect of axial load on the section stiffness, could have a beneficial effect in design by reducing the total factored moment. For example, by using the properties of the example wall from Table D.4, the effective flexural stiffness at the onset of yielding can be calculated accounting for the axial load effect for load combination **Case 4** (the governing load case), as follows:

$x = \varepsilon_s E_m b/2 = 0.002*14\ 875*1000/2 = 14\ 875$

$y = P + A_s E_x \varepsilon_s = 66\ 475 + 500*200\ 000*0.002 = 622\ 475$

Appendix D – Design Example: Warehouse Walls

z = -d(P + A$_s$E$_x$ε$_s$) = -170*(66 475 + 500*200 000*0.002) = -45 300 750

$$c = \frac{-y+\sqrt{y^2-4xz}}{2x} = 46.95 \text{ mm}$$

φ = 0.002/(170 - 46.95) = 1.625*10^{-5} mm^{-1}

ε$_c$ = -1.625*10^{-5} * 46.95 = -7.63*10^{-4} m/m

C$_f$ = -7.63*10^{-4} * 14 875 * 1000 * 46.95 / 2 = -266 kN

M = -(-266 000)*(170 – 46.95/3) – 66 475 * (170 - 190/2) = 36.1 kNm

EI$_{eff}$ = M / φ = 36 100 000 / 1.625*10^{-5} = 2 220 kNm^2

For this load case, the calculated EI$_{eff}$ value is approximately 10% greater than the (EI)$_{eff}$ value calculated based on the CSA S304-14 formulation of 2 006 kNm^2.

If this value is substituted into the critical buckling load equation, the same increase in P$_{cr}$ results.
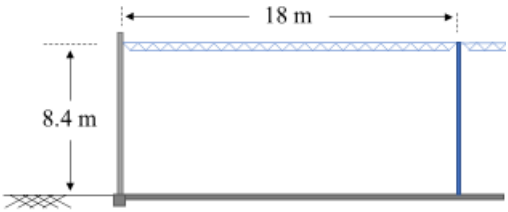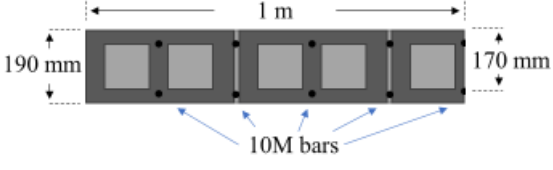
P$_{cr}$ = π^{2}φ$_{er}$EI$_{eff}$ / ((1+0.5β$_d$)(kh)^2)

Using this value in the moment magnifier equation will also reduce the total factored moment
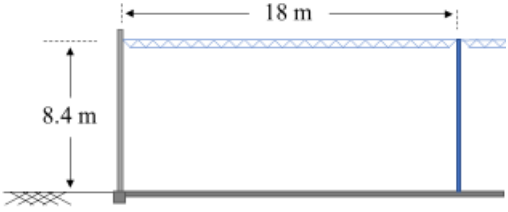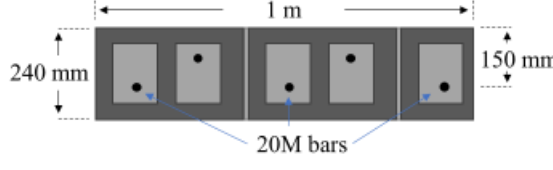
M$_{ftot}$ = M$_{fp}$C$_m$(1-P$_f$/P$_{cr}$)

In the case of the fully grouted wall with NSM reinforcement from Table D.4, the wall height could be increased by 5% as illustrated in Table D.6.

Appendix D – Design Example: Warehouse Walls

Building parameters	Wall parameters
Effective unsupported wall height = 8.4 m span between wall and columns = 18 m Large warehouse 	f'$_m$ = 17.5 MPa A$_s$ = 500 mm^2/m t = 190 mm d = 170 mm
Case 4	
Factored loads	Factored resistance
M$_{ftot}$ = 33.8 kNm/m [(EI)$_{eff}$ = 2005.6 kNm^2] M$_{ftot}$ = 31.9 kNm/m [EI$_{eff}$ = 2227.0 kNm^2] P$_f$ = 67.5 kN/m	M$_r$ = 32.2 kNm/m 0.1ϕ_mf'$_m$A$_e$ = 200.0 kNm/m c/d = 0.20 < 0.6

Similar results may be achieved with the conventionally reinforced wall, as illustrated in Table D.7.

Building parameters	Wall parameters
Effective unsupported wall height = 8.4 m span between wall and columns = 18 m Large warehouse 	f'$_m$ = 13.5 MPa A$_s$ = 750 mm^2/m t = 240 mm d = 150 mm
Case 4	
Factored loads	Factored resistance
M$_{ftot}$ = 43.3 kNm/m [(EI)$_{eff}$ = 1977.5 kNm^2] M$_{ftot}$ = 39.3 kNm/m [EI$_{eff}$ = 2221.0 kNm^2] P$_f$ = 74.7 kN/m	M$_r$ = 39.3 kNm/m 0.1ϕ_mf'$_m$A$_e$ = 194.4 kNm/m c/d = 0.40 > 0.6

Appendix D – Design Example: Warehouse Walls